

In presenting the dissertation as a partial fulfillment of the requirements for an advanced degree from the Georgia Institute of Technology, I agree that the Library of the Institution shall make it available for inspection and circulation in accordance with its regulations governing materials of this type. I agree that permission to copy from, or to publish from, this dissertation may be granted by the professor under whose direction it was written, or, in his absence, by the dean of the Graduate Division when such copying or publication is solely for scholarly purposes and does not involve potential financial gain. It is understood that any copying from, or publication of, this dissertation which involves potential financial gain will not be allowed without written permission.

A STUDY OF LATTICE VIBRATIONS THROUGH  
THE TEMPERATURE DEPENDENCES OF X-RAY BRAGG INTENSITIES

A THESIS

Presented to

The Faculty of the Graduate Division

by

Robert Merle Nicklow


In Partial Fulfillment

of the Requirements for the Degree

of Doctor of Philosophy in the School of Physics

Georgia Institute of Technology


April, 1964



38  
12T

A STUDY OF LATTICE VIBRATIONS THROUGH  
THE TEMPERATURE DEPENDENCES OF X-RAY BRAGG INTENSITIES

Approved:

  
\_\_\_\_\_  
\_\_\_\_\_  
\_\_\_\_\_

Date approved by Chairman: 8 May 1964

## ACKNOWLEDGEMENTS

The author wishes to thank Dr. R. A. Young not only for suggesting the thesis topic and providing the author many hours of constructive consultation concerning the research, but also for his continued guidance and encouragement throughout the author's graduate career. The financial support of this research by the Office of Naval Research is gratefully acknowledged. The author also wishes to thank Dr. F. Moser of the Eastman Kodak Company for providing him with single crystal samples of ultra-pure silver chloride, and Drs. Chris Walker and Henderson Cole for providing him with some results of their own research.

And finally, the author wishes to thank his wife whose patience and encouragement made the completion of this thesis possible, and Mrs. Jo Ann Gable for typing the thesis.

## TABLE OF CONTENTS

	Page
ACKNOWLEDGEMENTS . . . . .	ii
LIST OF TABLES . . . . .	vi
LIST OF FIGURES . . . . .	viii
SUMMARY . . . . .	x
Chapter	
I. INTRODUCTION . . . . .	1
General Problem	
Background	
Brief Outline of Theory and X-ray Methods used Previously	
Specific Problem Pursued	
II. THEORY . . . . .	12
X-ray Diffraction Intensities and Normal Modes	
One Atom per Lattice Point	
Vibrational Spectrum and Debye's Assumptions	
Anharmonic Contributions to M	
Temperature Derivative of Intensity	
$dM/dT$ for a General Spectrum	
$dM/dT$ for a Debye Spectrum	
Dependence of $\Theta$ on Experimental Methods	
Moments Method	
Two Atoms per Lattice Point	
Individual Temperature Factors for an NaCl Type	
Lattice and Their Relation to the Frequency	
Spectrum	
Temperature Derivatives of $M_1$ and $M_2$	
Contributions of $M_1$ and $M_2$ to $d(\ln I)/dT$	
$A_0$ versus $\sin^2 \theta / \lambda^2$ . Character and the Determination	
of $B_1$ and $B_2$ Separately	
III. EXPERIMENTAL PART . . . . .	55
Summary of Experimental Procedure	
Apparatus	
X-Ray Apparatus	
Temperature Control Apparatus	

## TABLE OF CONTENTS (Continued)

Chapter	Page
Temperature Determination	
Samples	
Sample Preparation	
Silver Chloride	
Potassium Chloride	
Aluminum	
Sample Mounting	
Intensity Measurement Considerations	
Geometry	
Background Determination	
Data Collection Procedures	
Sample Alignment	
I versus T	
B <sub>0</sub> versus T	
Data Reduction	
Definition of A and A <sub>0</sub>	
Corrections to I versus T Data	
IV. RESULTS AND DISCUSSIONS . . . . .	98
Aluminum	
Potassium Chloride	
Silver Chloride	
Determination of Observed Values of B <sub>1</sub> ' and B <sub>2</sub> '	
Determination of Calculated Values of B <sub>1</sub> ' and B <sub>2</sub> '	
Comparison of Calculated and Observed Values for	
B <sub>1</sub> and B <sub>2</sub>	
Debye Θ Values	
Moments Expansion of Data	
V. CONCLUSIONS AND RECOMMENDATIONS . . . . .	139
Appendixes	
A. THERMAL DIFFUSE SCATTERING . . . . .	144
B. CALCULATION OF $(\partial B / \partial T)_V$ FOR ALUMINUM . . . . .	180
C. CALCULATION OF INDIVIDUAL TEMPERATURE FACTORS FOR	
SILVER AND CHLORINE IN AgCl . . . . .	187
D. ALUMINUM A VALUES AND CORRECTIONS . . . . .	194

## TABLE OF CONTENTS (Continued)

Appendixes	Page
E. POTASSIUM CHLORIDE A VALUES AND CORRECTIONS . . . . .	201
F. SILVER CHLORIDE A VALUES AND CORRECTIONS . . . . .	207
GLOSSARY . . . . .	218
REFERENCES . . . . .	222
VITA . . . . .	225

## LIST OF TABLES

Table		Page
1.	List of AgCl Samples . . . . .	68
2.	List of KCl Samples . . . . .	70
3.	List of Al Samples . . . . .	70
4.	List of Adhesives . . . . .	72
5.	Comparison of Measured and Calculated TDS Contributions . . . . .	94
6.	Aluminum A Values and Corrections at 290° K . . . . .	102
7.	Potassium Chloride A Values and Corrections at 290°K. . . . .	112
8.	Silver Chloride A Values and Corrections at 290°K . . . . .	117
9.	Calculated and Measured Temperature Derivatives of $B_1$ and $B_2$ for AgCl . . . . .	127
10.	Calculated Values of $B_1$ and $B_2$ for AgCl . . . . .	127
11.	Frequency Spectrum Moments for KCl . . . . .	135
12.	Data Used to Calculate $\sigma$ . . . . .	179
13.	Frequency Spectrum of Aluminum in Tabular Form . . . . .	182
14.	Calculated Values for $(\partial B / \partial T)_V$ for Aluminum . . . . .	186
15.	Calculated Values for $B_{Ag}$ and $B_{Cl}$ for AgCl . . . . .	193
16.	Aluminum A Values and Corrections at 240°K . . . . .	195
17.	Aluminum A Values and Corrections at 200°K . . . . .	196
18.	Aluminum A Values and Corrections at 160° K . . . . .	197
19.	Aluminum A Values and Corrections at 140° K . . . . .	198
20.	Aluminum A Values and Corrections at 120° K . . . . .	199



## LIST OF TABLES (Continued)

Table		Page
21.	Aluminum A Values and Corrections at $100^{\circ}$ K . . . . .	200
22.	Potassium Chloride A Values and Corrections at $240^{\circ}$ K. .	202
23.	Potassium Chloride A Values and Corrections at $200^{\circ}$ K. .	203
24.	Potassium Chloride A Values and Corrections at $160^{\circ}$ K. .	204
25.	Potassium Chloride A Values and Corrections at $140^{\circ}$ K. .	205
26.	Potassium Chloride A Values and Corrections at $120^{\circ}$ K. .	206
27.	Silver Chloride A Values and Corrections at $240^{\circ}$ K . . .	208
28.	Silver Chloride A Values and Corrections at $200^{\circ}$ K . . .	210
29.	Silver Chloride A Values and Corrections at $160^{\circ}$ K . . .	212
30.	Silver Chloride A Values and Corrections at $140^{\circ}$ K . . .	214
31.	Silver Chloride A Values and Corrections at $120^{\circ}$ K . . .	216

## LIST OF FIGURES

Figure		Page
1.	The Function $f(x)$ . . . . .	33
2.	Dependence of $A_0$ on $\phi$ . . . . .	52
3.	Dependence of $A_0$ on $\phi$ for Small $ \Delta B' $ . . . . .	53
4.	Gas Train . . . . .	58
5.	Equipment . . . . .	61
6.	Equipment . . . . .	62
7.	Crystal Cutting Methods . . . . .	67
8.	Sample Shaping Method . . . . .	69
9.	$\omega$ -scan with Balanced Filters . . . . .	75
10.	Crystal Oscillation Apparatus . . . . .	79
11.	Typical Intensity versus Temperature Run . . . . .	81
12.	Dependence of $A_{LPf}$ for Al on $\sin^2\theta/\lambda^2$ at Several Temperatures . . . . .	86
13.	Dependence of $A_{LPf}$ for KCl on $\sin^2\theta/\lambda^2$ at Several Temperatures . . . . .	87
14.	Dependence of $A_{LPf}$ for AgCl on $\sin^2\theta/\lambda^2$ at Several Temperatures . . . . .	88
15.	Dependence of $A_{TDS}$ on $\phi$ at 300°K for Al . . . . .	96
16.	Dependence of $A_{TDS}$ on $\phi$ at 300°K for KCl and AgCl . . . . .	97
17.	Dependence of Intensity on Temperature for (h00) Reflections of Aluminum Sample No. 2 . . . . .	99
18.	Dependence of A on $\sin^2\theta/\lambda^2$ at 290°K for Al . . . . .	101
19.	Dependence of Aluminum Debye $\Theta$ on Temperature . . . . .	104

## LIST OF FIGURES (Continued)

Figure		Page
20.	Comparison of Calculated and Measured Values of $\Theta(\text{x-ray})$ for Al . . . . .	106
21.	Dependence of A on $\sin^2\theta/\lambda^2$ at 290°K for KCl . . . . .	111
22.	Dependence of Potassium Chloride Debye $\Theta$ on Temperature . . . . .	114
23.	Dependence of $A_0$ on $\sin^2\theta/\lambda^2$ at 290°K for AgCl . . . . .	119
24.	Dependence of $ F(\text{obs}) / F(\text{cal}) $ on $\phi$ for AgCl Sample No. 18 . . . . .	121
25.	Dependence of $m_1B'_1 + m_2B'_2$ on Temperature for AgCl . . . . .	130
26.	Dependence of AgCl Debye $\Theta$ on Temperature . . . . .	132
27.	Dependence of $(\partial B/\partial T)_V(V_0/V)^{2\gamma}$ and $(\partial B/\partial T)_V(V_0/V)^{2\gamma} +$ $a_1(T')^{-2}$ on Temperature for KCl . . . . .	137
28.	X-ray Scattering Viewed in Reciprocal Space . . . . .	149
29.	Present Experimental Geometry in Direct Space . . . . .	151
30.	Present Experimental Geometry in Reciprocal Space . . . . .	152
31.	Direct Space Source of Typical Component of $w(z)$ . . . . .	157
32.	Typical Component of $w(z)$ . . . . .	158
33.	Intensity Distribution in X-ray Target Projection . . . . .	161
34.	The Function $w(z)$ for a Spherical Sample . . . . .	162
35.	Fraction of Crystal Volume Which Contributes to TDS . . . . .	164
36.	Aluminum Vibration Spectrum . . . . .	181

## SUMMARY

New experimental and analytical techniques have been developed for the study of thermal vibrations through measurements of the temperature dependences of Bragg intensities. These techniques have been applied to the study of thermal vibrations in Al, KCl, and AgCl in the 100 to 300° K temperature range. These techniques involve the collection of precision intensity data at temperature intervals which are small enough to allow useful determination of the slope and curvature of the intensity versus temperature data. From these slopes it is possible to obtain meaningful values for the temperature derivatives,  $dB/dT$ , of the Debye-Waller factors for both a monatomic lattice and for each type of atom individually in an NaCl type lattice. These results have been related in a straightforward way to the frequency spectrum and have been used for the determination of  $\Theta(\text{x-ray})$  as a function of temperature for both the monatomic and diatomic cases. A value for  $\Theta(\text{x-ray})$  so obtained at a given temperature is absolute in the sense that it does not depend on the values which are appropriate to other temperatures.

Comparison of the intensity versus temperature results obtained for Al in this study with calculations based on Walker's vibration spectrum for Al indicate that  $dB/dT$  is sensitive both to anharmonicity and to certain details in the character of the low and, possibly, intermediate frequency portion of the vibrational spectrum. A five percent increase of the frequencies in the transverse branch of Walker's spectrum, suggested by the neutron inelastic scattering results of Brockhouse and Stewart, makes a significant improvement in the agreement between our

calculated and observed results for  $\Theta(\text{x-ray})$ . When thermal expansion effects on the elastic spectrum are also included, the calculated  $\Theta(\text{x-ray})$  versus temperature curve is in excellent agreement with our experimental curve. Anharmonic effects other than thermal expansion were not found to be significant in Al in the 100 to 300° K temperature range.

The experimental results obtained for AgCl show that  $d(B_{\text{Ag}})/dT$  is larger than  $d(B_{\text{Cl}})/dT$  by approximately 20 - 30% in the 100 to 300° K temperature range. This result is in substantial agreement with our calculations which are based on Cole's dispersion curves for AgCl and on Brillouin's expression for the wave vector dependence of the atomic vibrational amplitude ratio in a one-dimensional diatomic lattice. According to these calculations the optic modes contribute significantly to  $d(B_{\text{Cl}})/dT$  and to the temperature dependence of  $\Theta(\text{x-ray})$ . However, these contributions were not well determined. Therefore, no attempt was made to estimate the size of anharmonic effects, other than thermal expansion, in the AgCl even though the temperature dependence of  $\Theta(\text{x-ray})$  could not be accounted for by thermal expansion alone.

For KCl it is found that between 200 and 300° K  $\Theta(\text{x-ray})$  agrees well with the high temperature value calculated by Blackman and has a temperature dependence which is fully accounted for by thermal expansion effects on a Debye spectrum. As the temperature decreases below 200° K,  $\Theta(\text{x-ray})$  increases more than can be accounted for by thermal expansion alone. This increase is presumably due to differences between the real vibration spectrum of KCl and the Debye spectrum.

As expected, for all three materials  $\Theta(\text{elastic}) > \Theta(\text{x-ray})$  at the temperatures where they could be compared. The discrepancy (according to

Blackman) between theory and experiment which once existed for KCl, viz.,  $\Theta(\text{x-ray}) > \Theta(\text{elastic})$ , has been removed by our data. At room temperature  $\Theta(C_V)$  is approximately 25% larger than  $\Theta(\text{x-ray})$  for AgCl. This large difference is presumably due to the existence of optic branches in AgCl which represent a high frequency peak in the vibrational spectrum and which contribute more to  $\Theta(C_V)$  than to  $\Theta(\text{x-ray})$ .

Attempts to fit the x-ray data with an expansion in terms of the moments of the frequency spectrum failed. Possible reasons for this failure are pointed out.

The intensity versus temperature data were obtained from small (maximum diameter  $\sim 0.5$  mm) approximately spherical single crystal samples with a counter adapted Weissenberg camera and a Philip's x-ray unit. MoK $\alpha$  radiation, balanced filters, and a scintillation counter were used throughout the work. The geometry used was such that all parts of the sample could "see" all parts of the x-ray target and the counter intercepted all of the diffracted beam. The bulk of the data consisted of measurements of peak heights versus temperature. The desired integrated intensity versus temperature information was obtained from these data and measurements of the temperature dependence of the ratio of integrated intensity to peak height. The integrated intensities used for the determination of this ratio were obtained by the  $\omega$ -scan technique. All the data were obtained from zero layer reflections. Control of the sample temperature was achieved by means of a gas stream directed onto the sample.

A rather extensive investigation of the thermal diffuse scattering (TDS) contributions to the Bragg intensities measured in this

study was made. Particularly examined were the possible effects of all experimental parameters, e.g., sample size and shape, beam divergence and inhomogeneity, counter window size, etc., on the TDS contributions. Expressions have been derived which can be used to determine both the one and two phonon contributions to the Bragg peak intensity. The results of specially devised experimental tests indicate that TDS contributions in this study were determined to within 5 to 15%.

Our own review treatment of the theory relating thermal vibrations to Bragg intensities is presented and some extensions of the theory are made in the process. Specifically treated are the cases of primitive and non-primitive (e.g. face-centered) cubic Bravais lattices containing both one and two atoms per lattice point. Expressions which relate the temperature slope of intensity to the temperature derivatives of the Debye-Waller factors for these crystal structures, and which relate these temperature derivatives to the frequency spectrum and  $\Theta(\text{x-ray})$ , are presented and discussed. Anharmonic contributions to the Debye-Waller factor are discussed. The analytical method developed for separating the contributions of the two atom types in an NaCl type structure to the observed slopes of intensity versus temperature curves is described.

## CHAPTER I

### INTRODUCTION

#### General Problem

This study is concerned with the general question of what information about the thermal vibrations of the atoms in a crystal lattice can be determined from the temperature dependences of Bragg intensities and how, both experimentally and analytically, one obtains this information. As is discussed in the following paragraphs, the temperature dependence is of particular interest because of the opportunities such measurements provide for the determination of thermal vibration information with greater accuracy than is possible from other types of x-ray measurements.

#### Background

In the Born and Von Karman<sup>1</sup> theory of the thermal vibrations of the atoms in a crystal, later generalized by Born and Begbie<sup>2</sup>, the vibrations are harmonic and can be described in terms of a superposition of independent plane waves. The vibrational frequency spectrum of these waves has been of considerable interest for many years because of its importance to many branches of solid state physics. Thermal vibrations, and hence the vibrational spectrum, are related to, and can be investigated to some extent by, measurements of specific heats, electric and thermal resistivities, and elastic properties among other things. The most nearly complete information about thermal vibrations that can be obtained experimentally is that obtained from measurements of the inelastic scattering of x-rays (thermal diffuse



scattering) and of cold neutrons. Such measurements can, in principle, yield the entire vibrational spectrum. However, they are tedious to make because of the low intensities involved, and in the x-ray case are subject to large and usually not well known corrections. Thus, measurements of other solid state properties, such as those mentioned above, can be of considerable value in the study of thermal vibrations since they can be made relatively easily and often with high precision. However, the information obtained is less nearly complete than that obtained from the inelastic scattering experiments.

As has already been implied, thermal vibrations are also related to the temperature dependences of x-ray diffraction maxima (Bragg reflections or peaks) intensities. Measurements of this temperature dependence should provide information about thermal vibrations and the vibrational spectrum which would supplement usefully the information obtained from other sources. However, a search of the literature reveals that very little really useful information has been obtained from such measurements. In a recent review article, Herbst<sup>3</sup> comes to the same conclusion and states that although x-ray diffraction methods have been used fairly widely, difficulties in interpretation remain and, to date, such methods have not given unambiguous results. No valid reason for these difficulties is apparent. With present day experimental techniques x-ray intensities can be measured with high precision, and, at least in principle, the study of thermal vibrations with such measurements should be straightforward. Therefore, it seemed desirable that the present investigation be undertaken.

#### Brief Outline of Theory and X-Ray Methods used Previously

The influence of thermal vibrations on the intensities of Bragg reflections was first investigated by Debye<sup>4</sup>. The result, in the form due to

Waller, is a standard part of x-ray diffraction theory. To the extent that the thermal vibrations are harmonic, the theory shows that the observed intensity,  $I$ , diffracted from a particular set of Bragg planes of a cubic, monatomic crystal lattice is related to  $I_0$ , the intensity that would be observed if there were no thermal vibrations, by

$$I = I_0 e^{-2M}, \quad (1-1)$$

where

$$M = 8\pi^2 \overline{u_n^2} \sin^2 \theta / \lambda^2 = B \sin^2 \theta / \lambda^2. \quad (1-2)$$

Here  $M$  is the Debye-Waller temperature factor,  $\theta$  is the Bragg angle,  $\lambda$  is the x-ray wavelength, and  $\overline{u_n^2}$  is the mean square displacement of each atom in the direction  $\vec{n}$  perpendicular to the planes.

The mean square displacement, and hence  $B$ , is related to the absolute temperature,  $T$ , and to an integral involving the vibrational spectrum in the manner described in Chapter II. However, as normally used, the Debye-Waller theory employs a Debye (parabolic) spectrum which is characterized by a maximum cutoff frequency,  $\nu_m$ , and a characteristic Debye temperature  $\Theta = h\nu_m/k$  (where  $h$  is Planck's constant,  $k$  is Boltzmann's constant).  $B$  then becomes a relatively simple function of only  $T$  and  $\Theta$ . The relationship of  $B$  to the true vibrational spectrum is of particular interest in the present study. In much of the work, however, it is convenient to express our results in terms of an assumed Debye spectrum. Such a spectrum provides a single thermal parameter,  $\Theta$ , which can be measured many different ways, e.g., from

specific heats and elastic constants. Casting the present x-ray results in terms of  $\Theta$  facilitates simple comparison of our thermal vibration results with those obtained from different experimental techniques. Additionally, except for the relatively few TDS studies, essentially all reported x-ray diffraction investigations of thermal vibrations are interpreted only to the point of yielding values for  $\Theta$ .

For the determination of  $\Theta$  from x-ray measurements, one of two methods is commonly used<sup>5</sup>. One method involves isothermal intensity measurements from Bragg peaks occurring at different scattering angles,  $2\theta$ , and makes use of the dependence of  $M$  on  $\sin^2\theta/\lambda^2$ . From equation (1-1) it follows that a plot of  $\ln(I/I_0)$  versus  $\sin^2\theta/\lambda^2$  is a line which has a slope  $-2B$ . A value for  $\Theta$  can then be determined from the measured value for  $B$ . However, there are a number of problems associated with the use of such a plot. The Bragg reflections are superimposed on a nonuniform background of thermal diffuse scattering (TDS) which has a maximum at the same positions as the Bragg reflections. The TDS intensity is also a function of  $\sin^2\theta/\lambda^2$ . Thus, the true Bragg intensity must be obtained by subtraction of a calculated TDS correction from the observed intensity. The importance of this correction varies with the material investigated. For single crystal measurements on NaCl, Nilsson<sup>6</sup> estimates that the application of this correction reduces Renninger's<sup>7</sup> measured  $\Theta$  from  $319^\circ$  K to  $302^\circ$  K. There is also a problem associated with an accurate calculation of  $I_0$  which is also, usually strongly, dependent on angle. For the case of a monatomic single crystal and a particular experimental arrangement,  $I_0$  is given by

$$I_0 = K \frac{1 + \cos^2 2\theta}{\sin 2\theta} A E f^2 \quad (1-3)$$

Here  $\theta$  is the Bragg angle,  $K$  is a constant,  $A$  is an absorption factor whose dependence on angle is often not well known,  $E$  is the extinction factor whose value varies with angle and depends on the usually not well known perfection of the sample, and  $f$  is the atomic scattering factor which depends on angle and is obtained theoretically from imperfectly known electron distributions in the atoms. Further, tabulated values of  $f$  often require corrections for anomalous dispersion<sup>5</sup> and accurate application of this correction is itself difficult. For these reasons the determination of accurate values for  $B$  and  $\theta$  from isothermal x-ray measurements is very difficult, if not impossible.

The other x-ray method sometimes used for the determination of  $\theta$  involves measurements of intensities at different temperatures. Although TDS corrections are still required, an accurate determination of  $I_0$  (see equation (1-3)) is not since the dependences of  $A$ ,  $E$ , and  $f$  on temperature are usually quite small. For this reason intensity versus temperature methods are much preferred over isothermal methods for the study of thermal vibrations. In addition, the particular methods we have used, which are mentioned briefly later in this chapter, have some advantages over the usual intensity versus temperature studies reported in the literature. Usually the ratio of the intensity,  $I_1$ , of a particular Bragg peak measured at temperature  $T_1$  to the intensity,  $I_2$ , of the same peak measured at  $T_2$  is obtained. Then it follows from equation (1-1) and the dependence of  $B$  on  $T$  and  $\theta$  that

$$\ln (I_2/I_1) = 2 [B(T_1, \theta) - B(T_2, \theta)] \sin^2 \theta / \lambda^2, \quad (1-4)$$

where for simplicity TDS and the small dependence of  $\sin^2 \theta / \lambda^2$  and  $I_0$  on

temperature has been neglected. If  $\Theta$  is assumed temperature independent, it can be determined from equation (1-4). The main disadvantage of this method is that  $\Theta$  is not independent of temperature because of both (1) the differences between the true vibrational spectrum and the Debye approximation and (2) the fact that the vibrations are not harmonic so  $B$  has an additional temperature dependence due to anharmonicity (see Chapter II). Thus,  $\Theta(T_1)$  and  $\Theta(T_2)$  should appear in the above equation. A measurement of the ratio  $I_2/I_1$  is not sufficient to determine both  $\Theta(T_1)$  and  $\Theta(T_2)$ <sup>8</sup>. Only if  $\Theta(T_1)$  or  $\Theta(T_2)$  is known from some independent experiment, which is usually not the case, can equation (1-4) be solved for the unknown  $\Theta$ .

Chipman<sup>8</sup> has suggested a method with which one can determine  $\Theta$  versus  $T$  from measurements of intensity ratios. However, the method requires that some assumptions be made about the expected shape of a  $\Theta$  versus  $T$  curve. Since the form of a curve of  $\Theta$  versus  $T$  for a given solid depends on the usually unknown shape of the frequency spectrum and anharmonicity, results obtained with Chipman's method are somewhat ambiguous<sup>3</sup>. Further, in so far as we are aware, all reported measurements of x-ray intensities at different temperatures, were made at temperatures which were separated by rather large ( $50^\circ - 100^\circ$ ) temperature intervals. Thus, the determination of the detailed dependence of  $\Theta$  on  $T$  from x-ray measurements has not been reported in the literature. This situation contrasts with the detailed  $\Theta$  versus  $T$  curves usually obtained from specific heat and elastic constant measurements.

So far, only monatomic cubic crystal structures have been mentioned. However, it is also of interest to study the thermal vibrations of each kind of atom in more complex polyatomic structures. For a crystal structure

which contains more than one type of atom, there is a Debye-Waller factor,  $M_i$ , associated with the atomic scattering factor,  $f_i$ , of each kind of atom. It is theoretically possible to relate a certain linear combination of the  $M_i$ 's of the individual atoms to an integral involving the vibrational spectrum. Thence, the  $M_i$ 's can be related to a  $\Theta$  which can be compared with  $\Theta$ 's obtained from measurements of specific heats, elastic constants, etc. Also, the knowledge of the individual atomic vibrational amplitude, such as can be obtained with diffraction methods, would be of considerable value in examinations of the validity of theoretical models for the vibrations in complex crystal structures. For example, Brillouin<sup>9</sup> has derived an expression for the wave vector dependence of the ratio of the vibrational amplitude of one atom type to that of another for the case of a diatomic one-dimensional lattice. This expression has been used by Cole<sup>10</sup> for the interpretation of his TDS measurements for AgCl although no examination of its validity for a three-dimensional lattice appears in the literature. (This point is mentioned in the analysis of the present results.)

Isothermal x-ray intensity measurements have been used for the determination of  $M_i$  for each atom in a polyatomic crystal, but we know of no attempts to use such data to investigate the frequency spectrum. Neither do we know of any previous attempts to use x-ray intensity versus temperature measurements as described above to determine a  $\Delta B_i$  (of equation (1-4)) for each kind of atom in such crystals. Most measurements of this kind have been interpreted in terms of a  $\Delta \bar{B}$  where it is assumed either that  $\bar{B}$  is some average of the individual  $B_i$ 's or that all  $B_i = \bar{B}$  so that equations of the form (1-1) and (1-4) can be used<sup>3,7</sup>. It is then not clear what the relationship of the resulting values for  $\Theta$  is to those obtained from other experimental techniques.

### Specific Problem Pursued

The specific problem pursued in the present work was (a) the development of the experimental and analytical techniques described in Chapters II and III for the study of thermal vibrations through measurements of the temperature dependences of Bragg intensities, and (b) the application of these techniques to the study of thermal vibrations in Al, KCl, and AgCl in the 100° to 300° K temperature range.

These techniques involved the collection of precision intensity data at temperature intervals which were small enough (5-15°) to permit useful determination of the slope,  $dI/dT$ , of the intensity versus temperature data. The advantages of the intensity versus temperature method were thus exploited.

From the temperature slopes the determination of the temperature dependence of  $dM/dT$  for the monatomic case and of  $dM_i/dT$  for each type of atom in the diatomic case was possible. These results have been related in a straightforward way to the vibrational spectrum and, hence, have been used for the determination of the dependence of  $\Theta$  on temperature, for both the monatomic and diatomic cases, without the necessity of assumptions regarding the expected shape of a  $\Theta$  versus  $T$  curve.

The 100 to 300° K temperature range was chosen because it was expected that the harmonic assumption would be more nearly valid at low temperatures and hence the simple theories should apply better. Thus, as is the case in low temperature studies of specific heats, it was hoped that some information about the vibrational spectrum could be obtained. The possible existence of anharmonicity was also specifically investigated.

The particular materials studied, Al, AgCl, and KCl, were chosen for several reasons:

1. Since a study of thermal vibrations by means of the temperature dependences of Bragg intensities was being attempted, it was desired that all atomic positions should be fully determined by symmetry so that no part of the observed changes in intensity would be due to changes in atomic positions. The structure of Al and the NaCl type structure of KCl and AgCl satisfy this condition.

2. It was desired that the experimental and analytical techniques developed in this work be applied both (a) to monatomic materials, for which the data analysis was expected to be straightforward, and (b) to diatomic materials, in which the possibility existed for the study of the thermal vibrations of more than one type of atom. It was felt, however, that more than two types of atoms would be excessive for the present work.

3. Aluminum was chosen for study because its vibrational spectrum had been particularly well determined by Walker<sup>11</sup> from TDS measurements. Thus, it was possible for us to interpret the data in terms of the correct, or at least approximately correct\*, spectrum rather than only the Debye spectrum. It was felt that such an interpretation would provide a particularly meaningful comparison of theory with experiment.

4. KCl was chosen because the atomic weights of K and Cl are nearly equal and the ions are isoelectronic. Hence, its structure and diffraction properties closely approximate the ideal simple cubic lattice for which the Debye theory was developed. Comparison between experiment and Debye's theory in the case of KCl therefore was expected to provide an interesting test of the validity of the theory in a near-ideal situation. Further, a

---

\*The results of Walker's TDS experiments have been verified in most of the essential details by inelastic scattering of cold neutrons<sup>12</sup>.



detailed analysis of specific heat measurements for KCl has been reported recently<sup>13</sup> and it was desirable to compare the specific heat results with those obtained from x-ray measurements.

5. It was thought that AgCl would be a particularly interesting material to study because of (a) the presence of two types of atoms with considerably different masses, (b) the presence of some co-valent bonding character which might produce vibrational anisotropy, and (c) the possibility of comparing our data with theoretical calculations based on Cole's TDS measurements and Brillouin's expression for the atomic vibrational amplitude ratio. It was hoped that such a comparison would shed some light on the validity of Brillouin's expression for a three-dimensional lattice.

In Chapter II the theory relating thermal vibrations to Bragg intensities is presented in some detail. This section starts with a pedagogical review treatment of existing theory<sup>5</sup> and then proceeds to a discussion of the several extensions which we found necessary. Specifically treated are the cases of primitive and non-primitive (e.g., face-centered) cubic Bravais lattices containing both one and two atoms per lattice point. Expressions which relate the temperature slope of intensity to the temperature derivatives of the Debye-Waller factors for these crystal structures, and which relate these temperature derivatives to the vibrational spectrum and  $\Theta$ , are presented and discussed. Anharmonic contributions to the Debye-Waller factor are discussed. An analytical method for separating the contributions of the two atom types in an NaCl type structure to the observed slope of intensity versus temperature curves is described. The relationship of the Debye  $\Theta$  obtained from intensity versus temperature measurements to those obtained

from specific heat and elastic constant measurements is briefly discussed and, finally, a method for determining the moments of the vibrational spectrum from the temperature derivative of the Debye-Waller factor is presented.

In Chapter III the experimental methods of this study are described. Because the results of the present study were expected to depend critically on the accuracy of the measurements, one of the major problems of this work was the determination of changes in intensity with near maximum precision in a reasonable length of time. Considerable effort was expended in the examination of such accuracy-affecting factors as the various instrumental factors, matters of technique, and the contribution of TDS to the apparent Bragg intensities. A detailed examination and computation of TDS contributions was necessary because no reported work which can be applied to the particular experimental techniques used in the present work is known. The details of this work are discussed in Appendix A. There we present a treatment of TDS theory which includes a review of James<sup>5</sup> treatment of the case of a simple cubic monatomic lattice and our extension of the theory to the cases of non-primitive cubic Bravais lattices containing both one and two atoms per lattice point. The comparison of the TDS computations with specially designed experimental measurements is discussed in Chapter III.

In Chapter IV the results obtained for Al, KCl, and AgCl are presented and discussed. In Chapter V the conclusions to be drawn from this work are presented.

## CHAPTER II

## THEORY

X-Ray Diffraction Intensities and Normal Modes

According to the kinematic<sup>+</sup> theory of x-ray diffraction the intensity of x-rays scattered from a single crystal that contains  $N$  Bravais unit cells, each of which contains  $p$  atoms, is proportional to  $PP^*$ , where<sup>++</sup>

$$P = \sum_{n=1}^N \sum_{j=1}^p f_j \left( \frac{|\vec{S}|}{\lambda} \right) e^{i\kappa \vec{S} \cdot \vec{R}_{nj}} \quad (2-1)$$

Here  $f_j$  is the atomic scattering factor of atom  $nj$ ,  $\kappa$  equals  $2\pi/\lambda$ ,  $\lambda$  is the x-ray wavelength,  $\vec{R}_{nj}$  is the position vector of atom  $nj$  referred to an arbitrary origin, and  $\vec{S} = \vec{s} - \vec{s}_0$  is the diffraction vector where  $\vec{s}_0$  and  $\vec{s}$  are unit vectors in the direction of the incident and scattered radiation, respectively.  $|\vec{S}| = 2 \sin \theta$ , where  $\theta$  is the Bragg angle and  $2\theta$  is the total angular deflection of the scattered x-rays from the incident direction. It is convenient to let  $\vec{R}_{nj} = \vec{r}_n + \vec{\rho}_j + \vec{u}_{nj}$ , where  $\vec{r}_n$  is the position vector of some reference point in the cell  $n$ ,  $\vec{\rho}_j$  is the

---

<sup>+</sup>Multiple reflections within the crystal are ignored.

<sup>++</sup>It is assumed that the charge distribution can be decomposed to a sum of spherical distributions located at each atom.

position vector of the equilibrium position of atom  $n_j$  referred to that point, and  $\vec{u}_{n_j}$  is the instantaneous displacement of atom  $n_j$  from its equilibrium position. The vector  $\vec{r}_n$  is given by  $n_1\vec{a} + n_2\vec{b} + n_3\vec{c}$  where  $n_1$ ,  $n_2$ , and  $n_3$  are integers and  $\vec{a}$ ,  $\vec{b}$ , and  $\vec{c}$  are the translation vectors of the lattice. From equation (2-1) one obtains<sup>+</sup>

$$PP^* = \sum_{n,m=1}^N \sum_{j,\ell=1}^p f_j f_\ell e^{i\kappa\vec{S} \cdot (\vec{r}_n - \vec{r}_m)} e^{i\kappa\vec{S} \cdot (\vec{\rho}_j - \vec{\rho}_\ell)} e^{i\kappa\vec{S} \cdot (\vec{u}_{n_j} - \vec{u}_{m\ell})} \quad (2-2)$$

The thermal vibrational displacements of the atoms from their equilibrium positions are not independent since the displacement of one atom affects those of its neighbors because interatomic forces exist. However, if it is assumed that the potential energy of the solid can be expressed as a quadratic function of the components of the displacements, a normal mode analysis of the vibrations can be made. The details of such an analysis have been described by a number of authors<sup>2,14,15</sup> and will not be repeated here. The result of most interest for the present study is that  $\vec{u}_{n_j}$  can be expressed as a superposition of independent plane waves with average amplitudes determinable from standard statistical mechanical results. Each wave has associated with it a wave vector  $\vec{k}$ , a polarization unit vector  $\vec{e}$ , and an angular frequency  $\omega$ . If each unit cell contains  $q$  lattice points with  $s$  atoms per lattice point, there are  $Nq$  distinct wave vectors. For each wave vector there are in general three different polarization vectors, for each of which, in turn,

---

<sup>+</sup>It is assumed that the electron cloud of each atom follows the nucleus as it is displaced from its equilibrium position (adiabatic assumption).

there are  $s$  values of  $\omega$ . A plot of  $\omega$  as a function of  $|\vec{k}|$  for any given direction of  $\vec{k}$  will yield  $3s$  dispersion curves. For three of the curves, called the acoustical branch,  $\omega$  goes to zero as  $|\vec{k}|$  goes to zero. The other  $3s-3$  modes have frequencies which do not go to zero for any value of  $\vec{k}$  and are called the optical vibration modes.

One can thus write the instantaneous displacement  $\vec{u}_{nj}$  in the following form,

$$\vec{u}_{nj} = \sum_{\vec{k}} \sum_{\alpha=1}^{3s} \vec{e}(\vec{k}, \alpha) a_j(\vec{k}, \alpha) \cos \left[ \omega(\vec{k}, \alpha)t - \vec{k} \cdot (\vec{r}_n + \vec{p}_j) + \delta(\vec{k}, \alpha) \right] \quad (2-3)$$

where  $\alpha$  identifies the branch and  $\delta(\vec{k}, \alpha)$  is a phase angle. The amplitudes,  $a_j(\vec{k}, \alpha)$  are in general complex quantities because different atoms associated with the same lattice point may vibrate not only with different amplitudes but with different phases as well. After substitution of equation (2-3) into the factor  $\exp [i\vec{S} \cdot (\vec{u}_{nj} - \vec{u}_{ml})]$ , it is necessary to average the resulting expression over a time, such as that of an observation, which is long compared to the period of the vibrations. Since the duration of the interaction between the radiation and the thermal vibrations is short compared to the period of the vibrations, all possible configurations of the atoms are averaged over. The details of this averaging process have been described by Born and Sarginson<sup>16</sup> and, in somewhat different form, by James<sup>5</sup>. The result, written in a form similar to that obtained by James, is

$$\begin{aligned} \left\langle e^{i\kappa\vec{S} \cdot (\vec{u}_{nj} - \vec{u}_{m\ell})} \right\rangle = \exp \left[ -1/4 \sum_{\vec{k}, \alpha} (\kappa\vec{S} \cdot \vec{e}(\vec{k}, \alpha))^2 \left( \left\langle a_j^2(\vec{k}, \alpha) \right\rangle + \left\langle a_\ell^2(\vec{k}, \alpha) \right\rangle \right. \right. \\ \left. \left. - 2 \left\langle a_j(\vec{k}, \alpha) a_\ell(\vec{k}, \alpha) \right\rangle \cos \left\{ \vec{k} \cdot (\vec{r}_n - \vec{r}_m) + \vec{k} \cdot (\vec{\rho}_j - \vec{\rho}_\ell) \right\} \right) \right] \end{aligned} \quad (2-4)$$

James derived the expression for  $\langle \exp [i\kappa\vec{S} \cdot (\vec{u}_{nj} - \vec{u}_{m\ell})] \rangle$  for the case of only one atom per lattice point for which  $a_j(\vec{k}, \alpha) = a_\ell(\vec{k}, \alpha)$ . Equation (2-4) is the result of our extension of James' derivation to the case of more than one atom per lattice point for which it is possible that  $a_j(\vec{k}, \alpha) \neq a_\ell(\vec{k}, \alpha)$ .

The term in equation (2-4) containing the cosine function leads to a description of the inelastic scattering\* of x-rays into directions which can be considerably different from those contributing to the intensity maxima (Bragg' peaks) of the diffracted x-rays. This inelastic scattering is called thermal diffuse scattering (TDS) and is peaked, though not as sharply, in the same directions as the Bragg scattering. Its contribution to the measured diffraction peak intensity is not always negligible. However, to simplify the discussion, TDS will be ignored for the present and will be discussed separately in Chapter III and Appendix A.

---

\*The change in energy of the inelastically scattered x-ray photon due to its interaction with one of the normal vibration modes is quite small and usually ignored. However, the change in momentum is not small and hence scattering in directions other than the diffraction maxima results.

The factors in equation (2-2) which do not contain the instantaneous displacements,  $\vec{u}_{nj}$ , need not be averaged since they do not depend on time. Therefore, substitution of equation (2-4) without the cosine term into (2-2) leads to

$$\langle PP^* \rangle = \sum_{n,m}^N \sum_{j,\ell}^p f_j f_\ell e^{i\kappa \vec{S} \cdot (\vec{r}_n - \vec{r}_m)} e^{i\kappa \vec{S} \cdot (\vec{\rho}_j - \vec{\rho}_\ell)} e^{-(M_j + M_\ell)} \quad (2-5)$$

where, for instance,

$$M_j = 1/4 \sum_{\vec{k}, \alpha} (\kappa \vec{S} \cdot (\vec{e}(\vec{k}, \alpha)))^2 \langle a_j^2(\vec{k}, \alpha) \rangle \quad (2-6)$$

Rearranging the terms in equation (2-5), one obtains

$$\langle PP^* \rangle = \left\{ \sum_{n,m=1}^N e^{i\kappa \vec{S} \cdot (\vec{r}_n - \vec{r}_m)} \right\} \left\{ \sum_{j,\ell=1}^p \left( f_j e^{-M_j} \right) \left( f_\ell e^{-M_\ell} \right) e^{i\kappa \vec{S} \cdot (\vec{\rho}_j - \vec{\rho}_\ell)} \right\} \quad (2-7)$$

or

$$\langle PP^* \rangle = I_o(\vec{S}/\lambda) \left| \sum_{j=1}^p f_j e^{-M_j} e^{i\kappa \vec{S} \cdot \vec{\rho}_j} \right|^2 \quad (2-8)$$

where

$$I_o(\vec{S}/\lambda) = \left| \sum_{n=1}^N e^{i\kappa \vec{S} \cdot \vec{r}_n} \right|^2 = \left| \sum_{n=1}^N e^{2\pi i (\vec{S}/\lambda) \cdot \vec{r}_n} \right|^2 \quad (2-9)$$

$I_0(\vec{S}/\lambda)$  is called the interference function and, as is shown in standard texts on x-ray diffraction<sup>5</sup>, has appreciable values only when

$$(\vec{S}/\lambda) \cdot \vec{r}_n = \text{integer}, \quad (2-10)$$

and hence defines the positions of the Bragg peaks. The set of vectors,  $\vec{H}$ , that satisfy,  $\vec{H} \cdot \vec{r}_n = \text{integer}$ , are usually considered the position vectors of a three-dimensional periodic array of points known as the reciprocal lattice. The use of the reciprocal lattice to describe the geometrical aspects of x-ray diffraction will be considered later when we discuss the contribution of TDS to the Bragg peaks.

The mean square amplitudes  $\langle a_j^2(\vec{k}, \alpha) \rangle$  are related to the mean energy,  $E(\nu(\vec{k}, \alpha))$ , of a simple harmonic oscillator having a frequency  $\nu(\vec{k}, \alpha) = \omega(\vec{k}, \alpha)/2\pi$  as follows,<sup>17</sup>

$$E(\nu(\vec{k}, \alpha)) = N 2\pi^2 \nu^2(\vec{k}, \alpha) \sum_{j=1}^p m_j \langle a_j^2(\vec{k}, \alpha) \rangle, \quad (2-11)$$

where

$$E(\nu(\vec{k}, \alpha)) = h\nu(\vec{k}, \alpha) (n(\nu(\vec{k}, \alpha)) + 1/2) \quad , \quad (2-12)$$

and

$$n(\nu(\vec{k}, \alpha)) = \left( e^{h\nu(\vec{k}, \alpha)/kT} - 1 \right)^{-1} \quad (2-13)$$

The sum in equation (2-11) is taken over all the atoms in a unit cell,



$N$  is the number of unit cells,  $m_j$  is the mass of atom  $j$ ,  $h$  is Planck's constant,  $k$  is Boltzmann's constant, and  $T$  is the absolute temperature.

To discuss the effect of thermal vibrations on the intensity of x-ray diffraction peaks in more detail, one finds it convenient to consider separately those crystal structures which have only one atom per lattice point and those which have two or more. In addition only cubic Bravais unit cells will be considered.

#### One Atom Per Lattice Point

For a cubic unit cell with one atom per lattice point, equation (2-11) can be rewritten as follows

$$\langle a^2(\vec{k}, \alpha) \rangle = \frac{E(v(\vec{k}, \alpha))}{2\pi^2 N' m v^2(\vec{k}, \alpha)} , \quad (2-14)$$

where  $N' = qN$  = total number of atoms. Equation (2-8) then takes the form

$$\langle PP^* \rangle = I_0(\vec{S}/\lambda) |F|^2 e^{-2M} , \quad (2-15)$$

where

$$F = \sum_j f_j e^{i\kappa \vec{S} \cdot \vec{\rho}_j} , \quad (2-16)$$

and

$$M = \frac{1}{8\pi^2 N' m} \sum_{\vec{k}, \alpha} \left\{ \kappa \vec{S} \cdot \vec{e}(\vec{k}, \alpha) \right\}^2 \frac{E(v(\vec{k}, \alpha))}{v^2(\vec{k}, \alpha)} . \quad (2-17)$$

From equations (2-3) and (2-6) it can be seen that  $M$  is proportional to the mean square of the projection of the vibrational amplitude of each atom along  $\vec{S}$ . In the case of harmonic vibrations with all atoms at positions of cubic symmetry,  $M$  is required to be independent of the direction of  $\vec{S}$ . For this case it can be shown<sup>18,19</sup> that  $\{\kappa\vec{S}\cdot\vec{e}(\vec{k},\alpha)\}^2$  can be replaced by its average value, equation (2-18), and taken outside the summation sign in equation (2-17).

$$\{\kappa\vec{S}\cdot\vec{e}(\vec{k},\alpha)\}_{\text{ave}}^2 = \frac{16\pi^2}{3} \frac{\sin^2 \theta}{\lambda^2} \quad (2-18)$$

$M$  can therefore be simplified to

$$M = \frac{2}{3N'm} \left( \frac{\sin \theta}{\lambda} \right)^2 \sum_{\vec{k}, \alpha} \frac{E(\nu(\vec{k}, \alpha))}{\nu^2(\vec{k}, \alpha)} \quad (2-19)$$

#### Vibrational Spectrum and Debye's Assumptions

The sum over  $\vec{k}$  and  $\alpha$  in equation (2-19) is usually replaced by an integral over all the normal mode frequencies by introduction of the frequency distribution function,  $g(\nu)$ . Then  $g(\nu)d\nu$  is defined as the number of normal modes having frequencies between  $\nu$  and  $\nu + d\nu$  and is normalized such that

$$\int_0^{\nu_m} g(\nu) d\nu = 3N' \quad , \quad (2-20)$$

where  $\nu_m$  is the maximum frequency in the vibrational spectrum.

In terms of  $g(\nu)$  equation (2-19) becomes

$$M = \frac{2}{m} \left( \frac{\sin \theta}{\lambda} \right)^2 \int_0^{\nu_m} E(\nu) \nu^{-2} g(\nu) d\nu \bigg/ \int_0^{\nu_m} g(\nu) d\nu \quad (2-21)$$

Actual vibrational spectra are so complex that approximate forms are of considerable practical importance in calculating quantities related to thermal vibrations such as  $M$ , specific heats, etc. The approximation most widely used is that introduced by Debye<sup>20</sup>. In this approximation one obtains the dependence of  $g(\nu)$  on  $\nu$  by assuming that a crystal can be treated as an isotropic continuous solid in which all waves of a given branch,  $\alpha$ , are propagated with the same speed, independent of their direction or wavelength. The following form is then obtained for  $g(\nu)$ ,

$$g(\nu) = 4\pi \left( \frac{1}{\nu_l^3} + \frac{2}{\nu_t^3} \right) V \nu^2 = a \nu^2 \quad (2-22)$$

In an isotropic solid the three modes for each  $\vec{k}$  correspond to one longitudinally and two transversely polarized waves. Hence in equation (2-22)  $\nu_l$  and  $\nu_t$  correspond to the velocity of the longitudinal and transverse waves, respectively.  $V$  is the volume of the crystal. The atomic nature of a real crystal sets a lower limit for the wavelength of the waves. Since the velocities of transverse and longitudinal waves are generally different, there are different upper limits to the frequencies for waves having different polarizations. An average maximum frequency is chosen by requiring

$$\int_0^{\nu_m} a \nu^2 d\nu = 3N' \quad , \quad (2-23)$$

and hence

$$v_m = (9N'/a)^{1/3} \quad (2-24)$$

Substitution of equation (2-22) into (2-21) leads to

$$M = \frac{6h}{m} \left( \frac{\sin \theta}{\lambda} \right)^2 \frac{1}{v_m^3} \int_0^{v_m} \left( \frac{1}{e^{hv/kT} - 1} + \frac{1}{2} \right) v dv \quad (2-25)$$

where equations (2-12) and (2-13) have also been used. Changing the integration variable to  $\xi = hv/kT$  and introducing the Debye characteristic temperature  $\Theta = hv_m/k$ , one obtains

$$M = \frac{6h^2 T}{mk\Theta^2} \left\{ \phi(x) + \frac{x}{4} \right\} \frac{\sin^2 \theta}{\lambda^2} \quad (2-26)$$

where

$$x = \Theta/T \quad \text{and}$$

$$\phi(x) = \frac{1}{x} \int_0^x \frac{\xi d\xi}{e^\xi - 1} \quad (2-27)$$

The function  $\phi(x)$  must be evaluated numerically\*. It is found to approach 1 as  $x$  approaches 0 and to approach 0 as  $x$  approaches infinity.

No real solid is expected to satisfy the assumptions described above which lead to equation (2-26). Approximate vibrational spectra have

---

\* A table of  $\phi(x)$  can be found in "International Tables for X-Ray Crystallography", edited by John S. Kasper and Kathleen Lonsdale (The Kynoch Press, Birmingham, England, 1959), Vol. II, p. 264.

been determined experimentally for a few solids (e.g., Al by Walker<sup>11</sup>) and are found to be appreciably different from the simple parabolic form in equation (2-22). However, as is pointed out by several authors<sup>3,21</sup>, the detailed differences between the true spectrum and the parabolic approximation often do not severely affect properties, such as  $M$  and the thermal vibration contribution to the specific heat, which are based on the integral over the entire spectrum. Thus in spite of the obvious shortcomings of the Debye theory,  $\Theta$  is a widely used semi-empirical parameter which provides a convenient means for comparing theory with experiment. Experimentally determined  $\Theta$ 's are usually found to depend on temperature and on the experimental technique used. Such variations in  $\Theta$  can usually be traced to the differences between the true spectrum and the parabolic approximation and to anharmonic effects. Expected differences between  $\Theta$ 's determined by different experimental techniques will be discussed briefly later.

#### Anharmonic Contributions to $M$

One underlying assumption on which the derivation of equations (2-3) and (2-4) is based is that the potential energy of the crystal can be expanded as a series in terms of the displacements,  $\vec{u}_{nj}$ , of the atoms from their equilibrium positions, and that such a series can be terminated at the term which is quadratic in the displacements. The thermal vibrations of an atom can then be written as a superposition of simple harmonic vibrations as given by equation (2-3). The frequencies,  $\omega(\vec{k}, \alpha)$ , are then determined by the second order derivatives of the potential energy with respect to the displacements, taken at the equilibrium positions  $\vec{r}_n + \vec{\rho}_j$ .

This harmonic assumption is not consistent with the fact that all solids exhibit thermal expansion<sup>22</sup>. Thus it is necessary to consider the effect on  $M$  of anharmonicity, i.e. the inclusion of higher order terms in the expansion of the potential energy.

The effect on  $M$  of including the third and fourth order terms of the potential energy expansion has been considered recently by Hahn and Ludwig<sup>23</sup> and by Maradudin and Flinn<sup>24</sup> for the classical (high temperature) case. A quantum mechanical treatment which is valid for all temperatures has been developed by H. Hahn<sup>25</sup>. The results obtained by the above authors are: (1) The frequencies which appear in equation (2-19) are temperature dependent since the points at which the second order derivatives of the potential energy are evaluated, i.e. the equilibrium positions of the atoms, vary with temperature due to thermal expansion. (2) In addition to equation (2-19) there is a term which represents the anharmonic corrections to the mean square amplitude of vibration of an atom and which is related to the third and fourth order derivatives of the potential energy with respect to the displacements. At high temperatures this term is proportional to the square of the absolute temperature. (3) There is an additional term which represents the thermal average of the fourth power of an atomic displacement and which is related to the third and fourth order derivatives of the potential energy. This term is proportional to the cube of the absolute temperature and is not isotropic, although for a cubic crystal, it possesses cubic symmetry<sup>24</sup>.

The dependences of the normal mode frequencies on temperature via thermal expansion has been investigated by Maradudin<sup>26</sup>. His result for a completely general force law between the atoms is complex. For the

case of a face-centered cubic lattice with nearest neighbor, central force interactions, the result is considerably simplified and becomes

$$\nu(\vec{k}, \alpha) = \tilde{\nu}(\vec{k}, \alpha) \left\{ 1 - \frac{\epsilon(T)}{24} \frac{[\phi'''(r_0)]^2}{[\phi''(r_0)]^3} \right\} \quad (2-28)$$

Here  $\phi(r)$  is the potential energy of interaction between two atoms separated by a distance  $r$ , the primes denote derivatives with respect to  $r$ ,  $\epsilon(T)$  is the vibrational energy per atom, and  $\tilde{\nu}(\vec{k}, \alpha)$  is the frequency which is obtained when the equilibrium separation of neighboring atoms is  $r_0$ , the separation which corresponds to the minimum of the potential energy.

The assumptions which lead to equation (2-28), e.g., nearest neighbor interactions are rather drastic and the simplified expression still contains some unknown quantities such as the second and third order derivatives of  $\phi(r)$ . Therefore, instead of equation (2-28), we have used an empirical approach to estimate the effect of thermal expansion on the normal mode frequencies  $\nu(\vec{k}, \alpha)$ . If it is assumed that this effect is independent of  $\vec{k}$  and  $\alpha$ , then according to Grüneisen's theory of thermal expansion one has<sup>14</sup>

$$\frac{d \ln \nu}{d \ln V} = -\gamma \quad (2-29)$$

where  $V$  is the crystal volume and  $\gamma$  is the Grüneisen constant which is assumed to be the same for all  $\nu(\vec{k}, \alpha)$  and which at low temperatures is given approximately by

$$\gamma \approx \beta V / K C_v \quad (2-30)$$

Here  $\beta$  is the volume coefficient of thermal expansion,  $K$  is the compressibility, and  $C_v$  is the specific heat at constant volume. If a Debye frequency spectrum is also assumed, it follows that (see reference 14)

$$\frac{d \ln \Theta}{d \ln V} = -\gamma \quad (2-31)$$

Integrating equations (2-29) and (2-31) one obtains

$$v_T = v_o (V_o/V_T)^\gamma \text{ and } \Theta_T = \Theta_o (V_o/V_T)^\gamma \quad (2-32)$$

where  $T$  is the absolute temperature and  $o$  represents some arbitrary reference temperature<sup>\*</sup>. Since values of  $\gamma$  for many solids, or the quantities needed to calculate it, can be found in the literature, the corresponding estimation of the temperature dependence of  $v(\vec{k}, \alpha)$  and  $\Theta$  is a simple matter.

Several weak points of this empirical approach should be pointed out, however. (1) The use of the crystal volume,  $V$ , in the above equations means that the possibility that thermal expansion of the crystal in different directions may have different effects on any given frequency,  $v(\vec{k}, \alpha)$ , is being ignored. Although we know of no reported theoretical analysis of this point, it would seem that such differences would be negligible when the thermal expansion is isotropic as it is for cubic structures such as those studied in this work. (2) Recent generalizations of Grüneisen's theory by Blackman<sup>29</sup> and by Barron<sup>30</sup> for several

<sup>\*</sup>The use of equation (2-31) in the form shown above was first suggested by Paskin<sup>27</sup>. However this equation also follows directly from an expression derived earlier by Zener and Belinsky<sup>28</sup>.



simple models of a solid show that the effects of thermal expansion on the normal mode frequencies are not necessarily independent of  $\vec{k}$  and  $\alpha$ , i.e., there is a  $\gamma(\vec{k}, \alpha)$  for each frequency, where

$$-\gamma(\vec{k}, \alpha) = \frac{d \ln v(\vec{k}, \alpha)}{d \ln V} \quad (2-33)$$

The single  $\gamma$  in equations (2-29) and (2-31) is found by the above authors to be a certain average over the individual  $\gamma(\vec{k}, \alpha)$ 's, which average in general will vary with temperature if the individual  $\gamma(\vec{k}, \alpha)$ 's are different from one another. Experimentally determined values of  $\gamma$  sometimes do vary with temperature. However, this variation is small for many solids. In fact, Grüneisen's theory with a single temperature independent  $\gamma$  describes quite adequately the measured thermal expansion of both Al and AgCl in the 100 to 300° K temperature range<sup>31</sup>. Thus, one might expect that although the individual  $\gamma(\vec{k}, \alpha)$ 's are possibly different\*, the net effect of the temperature dependence of all the normal mode frequencies on properties such as thermal expansion and  $M$ , which are based on an integral over the entire frequency spectrum, can be approximated reasonably well by the use of a single  $\gamma$ . Since the determination of individual  $\gamma(\vec{k}, \alpha)$ 's is at best only now becoming an experimental possibility, and since the temperature dependence of the normal mode frequencies is expected to represent a small contribution to the total temperature dependence of  $M$ , at least at low temperatures, it is felt that the

---

\* It is interesting to note that since the terms in the brackets on the right side of equation (2-28) do not depend on  $(\vec{k}, \alpha)$ , the individual  $\gamma(\vec{k}, \alpha)$ 's are all equal for the case of a face-centered cubic lattice with nearest neighbor central force interactions.

empirical approach just described is a reasonable first approximation to use. The fact that this approach is an approximation whose accuracy is difficult for one to determine should be borne in mind, however.

For the other anharmonic contributions to  $M$ , the dependence on temperature and the normal mode frequencies is extraordinarily complicated except at high temperatures ( $T > \Theta$ )<sup>25</sup>. Even at high temperatures the dependence on the normal mode frequencies is complicated unless simplifying assumptions, such as those used for equation (2-28), are made. The general expression for the anharmonic term proportional to  $T^2$ , as given by Hahn and Ludwig<sup>23</sup>, is

$$\begin{aligned} \frac{(kT)^2}{2N'm} \sum_{\vec{k}, \alpha} \frac{(\vec{S} \cdot \vec{e}(\vec{k}, \alpha))^2}{\omega^4(\vec{k}, \alpha)} \left[ \sum_{\substack{\vec{k}', \alpha' \\ \alpha', \alpha''}} \frac{|\phi_{\alpha, \alpha', \alpha''}^{\vec{k}, \vec{k}', \vec{k}''}|^2}{\omega^2(\vec{k}', \alpha') \omega^2(\vec{k}'', \alpha'')} \right. \\ \left. - \sum_{\vec{k}', \alpha'} \frac{\phi_{\alpha, \alpha, \alpha'}^{\vec{k}, -\vec{k}, \vec{k}', -\vec{k}'}}{\omega^2(\vec{k}', \alpha')} \right] \quad (2-34) \end{aligned}$$

The superscripts and subscripts on the  $\phi$ 's denote the normal mode wave vectors and the branches of the dispersion curves respectively. The first term in equation (2-34) is proportional to the square of the coefficient of the third order term in the expansion of the potential energy and the second term is proportional to the coefficient of the fourth order term. For example,

$$\phi_{\alpha, \alpha', \alpha''}^{\vec{k}, \vec{k}', \vec{k}''} = \frac{1}{N_m^{3/2}} \sum_{\substack{r, s, t \\ i, j, l}} \phi_{i, j, l}^{r, s, t} e_i e_j e_l \exp \{i(\vec{k} \cdot \vec{R}_r + \vec{k}' \cdot \vec{R}_s + \vec{k}'' \cdot \vec{R}_t)\} \\ (e_j = e_j(\vec{k}; \alpha)) \quad (2-35)$$

Here  $\phi_{ijl}^{rst}$  is the third derivative of the potential energy,  $\phi$ , where, for instance, the superscript  $r$  and subscript  $i$  means that the first derivative of  $\phi$  is taken with respect to the  $i^{\text{th}}$  component ( $i = x, y, z$ ) of the displacement of the atom whose position vector is  $\vec{R}_r$ , etc., and  $e_i$  is the  $i^{\text{th}}$  component of the polarization vector.

The complexity of anharmonic expressions such as equations (2-34) and (2-35) make it extremely difficult to calculate expected anharmonic contributions to  $M$  with much certainty. These expressions do give, however, the temperature dependence expected at high temperatures (where these effects are presumably most significant) a knowledge of which may permit the determination of these anharmonic contributions from experimental measurements of  $M$  (or of  $dM/dT$ , as discussed later) as a function of temperature. Since the contribution of the third and fourth order derivatives of the potential energy are of different sign, the experimental determination of merely the sign of the expression (2-34) could be useful for testing the validity of theoretical models of the interatomic potential in a given solid.

The anharmonic terms which depend on the cube of the absolute temperature and which are not isotropic are even more complex than expression (2-34). Maradudin and Flinn<sup>24</sup> show that for the case of a nearest neighbor-central force model of a face-centered cubic crystal

the dependence of these terms on the components of  $\vec{S}$  is given by the following expression:

$$a(S_x^4 + S_y^4 + S_z^4) + b(S_x^2 S_y^2 + S_y^2 S_z^2 + S_x^2 S_z^2) \quad (2-36)$$

where  $a$  and  $b$  are complicated functions of the normal mode frequencies and wave vectors and are given by Maradudin and Flinn. These authors find that (2-36) is quite negligible for the above crystal model with the elastic and thermal expansion properties of lead. (2-36) may not be negligible for all solids, however, and may lead to a measurable anisotropy in  $M$ . From expression (2-36) it follows that if the  $x$ - $y$ - $z$  axes are chosen to be along the  $\vec{a}$ ,  $\vec{b}$ , and  $\vec{c}$  axes of the cubic unit cell, the differences between values for  $M$  corresponding to different crystallographic directions would be largest for the  $[100]$ ,  $[110]$ , and  $[111]$  directions. In the present study we have investigated the possible anisotropy of  $M$  by obtaining data for these crystallographic directions.

One additional point concerning anharmonic effects should be mentioned. It has been implicitly assumed that the potential energy has no explicit dependence on temperature. We know of no reported theoretical investigation of this point; however, such a dependence would result if the energies of the bonding electrons were to vary with temperature, and it seems reasonable that they could. Such an effect would lead to a temperature dependence of the normal mode frequencies even when the crystal is held at constant volume. However, to simplify the following discussion it will be assumed that  $(\partial v(\vec{k}, \alpha) / \partial T)_v = 0$ , where the subscript  $v$  means that the temperature derivative is taken at constant volume.

### Temperature Derivative of Intensity

We now consider the diffracted intensity observed when  $\vec{S}/\lambda$  satisfies equation (2-10) and combine all the quantities<sup>+</sup> which relate the observed intensity to  $\langle PP^* \rangle$  into  $I_0$ . The integrated intensity  $I$  of an x-ray diffraction (Bragg) peak of a monatomic cubic crystal is then,

$$I = I_0 e^{-2M} \quad . \quad (2-37)$$

Thus

$$\ln I = \ln I_0 - 2M \quad , \quad (2-38)$$

and if one assumes for the moment that  $I_0$  is independent of temperature then,

$$-\frac{1}{2} \frac{d}{dT} (\ln I) \approx \frac{dM}{dT} \quad . \quad (2-39)$$

### $\frac{dM}{dT}$ for a General Spectrum

Neglecting for the moment anharmonic effects other than thermal expansion, with  $M$  given by equation (2-19) one obtains

$$\frac{dM}{dT} = \frac{2h}{2mN} \left( \frac{\sin \theta}{\lambda} \right)^2 \sum_{\vec{k}, \alpha} \left\{ \frac{h(1 + T\gamma(\vec{k}, \alpha)\beta)}{kT^2} n^2(v(\vec{k}, \alpha)) e^{hv(\vec{k}, \alpha)/kT} \right.$$

---

<sup>+</sup>For example, L.P., absorption, TDS, incident intensity, all systematic errors, etc.

$$+ (\gamma(\vec{k}, \alpha) - 2/3) \beta \left( \frac{n(v(\vec{k}, \alpha)) + 1/2}{v(\vec{k}, \alpha)} \right) \} \quad (2-40)$$

where equation (2-12) has been substituted for  $E(v(\vec{k}, \alpha))$  and  $n(v(\vec{k}, \alpha))$  is given in equation (2-13). Here  $\beta = (1/V)(dV/dT)$  is the volume coefficient of thermal expansion and equation (2-33) was used to determine  $dv(\vec{k}, \alpha)/dT = -\gamma(\vec{k}, \alpha)v(\vec{k}, \alpha)\beta$ . The term containing  $2/3$  arises from the effect of thermal expansion on  $(\sin \theta)^2/\lambda^2$ . The terms which contain  $\gamma(\vec{k}, \alpha)$  and  $\beta$  arise from thermal expansion and the resulting dependence of  $v(\vec{k}, \alpha)$  on volume. Although they are not expected to be negligible, they are so small that most of the information about the vibrational spectrum would be obtained from the temperature derivative of  $M$  at constant volume,

$$\left( \frac{\partial M}{\partial T} \right)_V = \frac{2h^2}{3mN'kT^2} \left( \frac{\sin \theta}{\lambda} \right)^2 \sum_{\vec{k}, \alpha} n^2(v(\vec{k}, \alpha)) e^{hv(\vec{k}, \alpha)/kT} \quad (2-41)$$

which, written in terms of  $g(v)$ , becomes,

$$\left( \frac{\partial M}{\partial T} \right)_V = \left( \frac{\partial B}{\partial T} \right)_V \left( \frac{\sin^2 \theta}{\lambda^2} \right) = \frac{2h^2}{3mN'kT^2} \left( \frac{\sin \theta}{\lambda} \right)^2 \int_0^{v_m} \frac{e^{hv/kT} g(v) dv}{(e^{hv/kT} - 1)^2} \quad (2-42)$$

where we have substituted the expression given in equation (2-31) for  $n(v(\vec{k}, \alpha))$ .

$\frac{dM}{dT}$  for a Debye Spectrum

With  $M$  given by equation (2-26), one obtains

$$\frac{dM}{dT} = \frac{6h^2}{mk\Theta^2} [f(x) + g(x)] \left( \frac{\sin \Theta}{\lambda} \right)^2, \quad (2-43)$$

where

$$f(x) = 2\phi(x) - \frac{x}{e^x - 1}, \quad (2-44)$$

$$g(x) = \beta T [(\gamma - 2/3)\{\phi(x) + \frac{x}{4}\} + \gamma f(x)], \quad (2-45)$$

and equation (2-31) was used to determine  $d\Theta/dT = -\gamma\Theta\beta$ .

As shown in Figure 1,  $f(x)$  is a slowly varying function of  $x$ ; changing only from 1 to 0.46 as  $x$  changes from 0 to 7, i.e., as  $T$  changes from  $\infty$  to  $\Theta/7$ . The term containing  $f(x)$  in equation (2-43) is equivalent to what would be obtained by integrating over a Debye spectrum in equation (2-42). Thus, for a Debye spectrum,

$$\left( \frac{\partial M}{\partial T} \right)_v = \left( \frac{\partial B}{\partial T} \right)_v \left( \frac{\sin \Theta}{\lambda} \right)^2 = \frac{6h^2}{mk\Theta^2} f(x) \left( \frac{\sin \Theta}{\lambda} \right)^2 \quad (2-46)$$

The expression for  $f(x)$  obtained by inserting a Debye spectrum in equation (2-42) is,

$$f(x) = \frac{1}{x} \int_0^x \frac{\xi e^{\xi} d\xi}{(e^{\xi} - 1)^2}. \quad (2-47)$$

The expression in equation (2-44) was used to obtain the  $f(x)$  vs  $x$  plot shown in Figure 1 since tables of  $\phi(x)$  were readily available and  $x(e^x - 1)^{-1}$  is easily calculated.

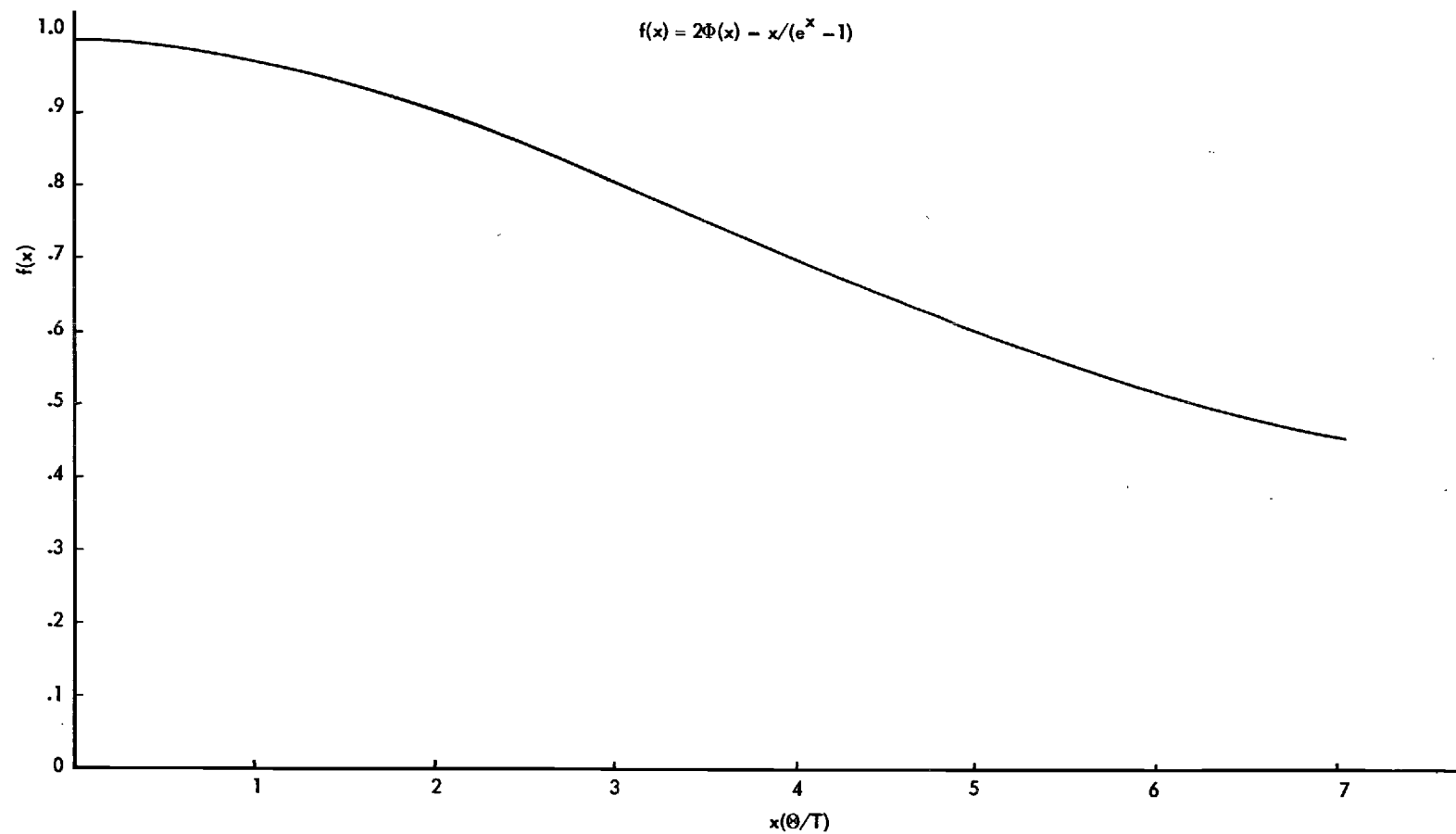


Figure 1. The Function  $f(x)$ .



The term containing  $g(x)$  results from thermal expansion. It is equivalent to the corresponding term in equation (2-40) with  $\gamma(\vec{k}, \alpha) = \gamma$  and with a Debye spectrum introduced.  $g(x)$  is small compared to  $f(x)$ ; normally being no larger than 10 per cent of  $f(x)$  at  $300^\circ$  K for the materials we have studied. The dependence of  $g(x)$  on  $x$  turns out to be small since  $\{\phi(x) + \frac{x}{4}\}$  increases while  $f(x)$  decreases with increasing  $x$ . Thus the temperature dependence of  $g(x)$  is governed primarily by the product  $\beta T$  and the size of  $\gamma$ .

Since  $f(x)$  and, to a lesser extent,  $g(x)$  depend on  $x$ , the determination of  $\Theta$  from an experimentally measured  $dM/dT$  requires an iterative procedure at low temperatures ( $T \leq \Theta$ ). At high temperatures,  $T \gg \Theta$ ,  $\{\phi(x) + \frac{x}{4}\}$  and  $f(x)$  are both nearly one and are very insensitive to  $\Theta$ , so that iterations are not required.

The integrand appearing in equation (2-42) is the vibrational spectrum multiplied by a function which "weights" the frequencies of the spectrum differently at different temperatures. Thus if  $g(v)$  departs significantly from the Debye approximation, it is possible that the  $\Theta$  (hereafter denoted  $\Theta(x\text{-ray})$ ) which makes the right side of equation (2-46) equal to the right side of equation (2-42) will vary with temperature. In addition,  $g(v)$  itself will vary with temperature due to the dependence of the frequencies on temperature, which dependence is primarily a volume dependence. Hence, a  $\Theta(x\text{-ray})$  obtained from a measured  $dM/dT$  can vary with temperature both due to thermal expansion effects on  $g(v)$  and due to the probable difference between the real spectrum and the Debye approximation.

The use of equations (2-39) and (2-43) allows a determination of  $dM/dT$  and of  $\Theta(\text{x-ray})$  as a function of temperature directly from the temperature dependence of a single given Bragg reflection, and allows this to be done (as mentioned earlier in Chapter I) without the use of any assumptions regarding the expected shape of a  $\Theta(\text{x-ray})$  vs  $T$  curve. Of course, the results we obtain for  $\Theta(\text{x-ray})$  do depend on the assumptions we have made concerning the effects of thermal expansion on the normal mode frequencies. Fortunately, these assumptions affect the experimentally determined  $\Theta(\text{x-ray})$  only through its dependence on  $g(x)$ , (see equation (2-43)) which, as already mentioned, is small compared to  $f(x)$ . An error in  $\Theta(\text{x-ray})$  and its temperature dependence will result if the additional anharmonic terms in  $M^+$  are significant but not explicitly accounted for. Presumably, the significance of these terms can be determined from the temperature dependence of  $\Theta(\text{x-ray})$  at high temperatures. For example, at high temperatures, the difference between the real spectrum and the Debye approximation should not affect the temperature dependence of  $\Theta(\text{x-ray})$  since  $f(x) = 1$  at these temperatures. Thus, if the temperature dependence of  $\Theta(\text{x-ray})$  is not accounted for by equation (2-32) (assuming that this equation is valid), then these additional anharmonic terms are significant.

#### Dependence of $\Theta$ on Experimental Methods

The methods used most frequently for the determination of  $\Theta$  are those which involve measurements of  $M$  (or of  $\Delta M$ ), as was discussed in Chapter I, of specific heats, and of elastic constants. Differences

---

<sup>+</sup>The terms which vary as  $T^2$  and  $T^3$  in  $M$  vary respectively as  $T$  and  $T^2$  in  $dM/dT$ .

between  $\Theta$ 's so determined have been discussed by Blackman<sup>21</sup> and by Herstein<sup>3</sup>, and are due to the fact that the above properties weight the frequencies of the spectrum differently.

The limiting form of the true spectrum at very low frequencies is parabolic<sup>21</sup>. As only the very lowest frequencies are excited in measurements of elastic constants,  $\Theta(\text{elastic})$  will be that appropriate to a parabola which fits correctly this part of the true spectrum. Deviations of the true spectrum from the Debye approximation will not influence the shape of the  $\Theta(\text{elastic})$  versus  $T$  curve.

Although higher frequencies in the spectrum play a more important role in determining  $M$ , or  $dM/dT$ , than elastic constants,  $dM/dT$  is still primarily determined by the low frequency range of the spectrum. This fact can be seen easily by writing equation (2-42) for the case of high temperatures, i.e., when  $h\nu_m/kT \ll 1$ . One obtains in this case:

$$\left(\frac{\partial M}{\partial T}\right)_v = \frac{2k}{3mN'} \left(\frac{\sin \theta}{\lambda'}\right)^2 \int_0^{\nu_m} \frac{g(\nu) d\nu}{\nu^2} \quad (2-48)$$

Thus, even at high temperatures, where all of the frequencies in the spectrum are excited, the low frequencies are relatively much more important to  $(\partial M/\partial T)_v$  since they are heavily weighted by the  $\nu^{-2}$  factor in the integrand of equation (2-48). As the temperature is lowered, the low frequencies become even more important to  $(\partial M/\partial T)_v$  since the high frequencies become less excited, and as  $T$  approaches zero,  $\Theta(\text{x-ray})$  approaches  $\Theta(\text{elastic})$ . For  $T \neq 0$  one expects  $\Theta(\text{x-ray})$  to be less than  $\Theta(\text{elastic})$  if the true spectrum rises above its initial parabolic shape.

This is because the parabola that fits the true spectrum best over an appreciable part of the frequency range will be steeper and thus have a smaller value of  $\nu_m$ , than the parabola chosen to fit the limiting shape of  $g(\nu)$  at the very lowest values of  $\nu$ . The rule  $\Theta(\text{x-ray}) < \Theta(\text{elastic})$  seems to be a general one since most frequency spectra have peaks in the lower frequency range<sup>19</sup>.

In terms of  $g(\nu)$  the formula for  $C_v$ , the specific heat at constant volume, can be written:

$$C_v = \frac{h^2}{kT^2} \int_0^{\nu_m} \frac{\nu^2 e^{h\nu/kT} g(\nu) d\nu}{(e^{h\nu/kT} - 1)} \quad (2-49)$$

The factor which weights the frequencies of the spectrum is seen to be the factor appropriate to  $(\partial M / \partial T)_v$  (see equation (2-42)) multiplied by  $\nu^2$ . Thus, the higher frequencies play a more important role in determining  $C_v$  than  $(\partial M / \partial T)_v$ . For example, at high temperatures ( $h\nu_m/kT \ll 1$ ) equation (2-49) becomes

$$C_v = k \int_0^{\nu_m} g(\nu) d\nu \quad , \quad (2-50)$$

and all the frequencies of the spectrum are equally weighted, in contrast to the situation, discussed above, for the high temperature expression for  $(\partial M / \partial T)_v$ . The importance of high frequencies to  $C_v$  makes predictions concerning comparisons of  $\Theta(C_v)$  with  $\Theta(\text{x-ray})$  and  $\Theta(\text{elastic})$  difficult at intermediate temperatures. At low temperatures, the low

frequencies are heavily weighted for all three types of measurements and for  $T = 0$  one expects  $\Theta(C_v) = \Theta(\text{elastic}) = \Theta(\text{x-ray})$ . At high temperatures one would expect  $\Theta(C_v)$  to be larger than  $\Theta(\text{x-ray})$  and  $\Theta(\text{elastic})$  if there is a high density of high frequencies in  $g(\nu)$ . For example, Batterman and Chipman<sup>32</sup> have recently shown that the large differences, 20 per cent, found between  $\Theta(C_v)$  and  $\Theta(\text{x-ray})$  in Ge and Si, with  $\Theta(C_v)$  being the larger, are due to the existence of a large number of high frequency optical modes in the frequency spectra of these materials. One would expect a similar situation to exist for AgCl where the large difference in the masses of the two ions leads one to expect the existence of a large gap between the acoustical and optical frequencies<sup>10</sup>.

#### Moments Method

The "moments method", which has been used some in the analysis of specific heat data<sup>13</sup>, appears not to have received any consideration for the analysis of x-ray intensity versus temperature data. This method appears to be equally useful for the analysis of either type of data; especially when thermal vibration information obtained from these two experimental techniques are to be compared. The method involves the use of a Maclaurin expansion of the mean energy of a linear harmonic oscillator in powers of  $(h\nu/kT)$  where  $\nu$  is the oscillator frequency. If one writes the mean energy as

$$E(\nu) = h\nu(n(\nu) + 1/2)$$

with  $n(\nu)$  given in equation (2-13), this expansion takes the form

$$E(\nu) = kT \left[ 1 - \sum_{n=1}^{\infty} (-1)^n \frac{B_n}{(2n)!} \left( \frac{h\nu}{kT} \right)^{2n} \right] \quad (2-51)$$

where  $B_n$  are Bernoulli numbers<sup>21</sup>, the first six of which are

$$B_1 = 1/6, \quad B_2 = 1/30, \quad B_3 = 1/42$$

$$B_4 = 1/30, \quad B_5 = 5/66, \quad B_6 = 691/2730.$$

The expansion is convergent for  $(h\nu/kT) < 2\pi$ . In terms of either the maximum frequency,  $\nu_m$ , of the vibrational spectrum or the Debye  $\Theta$ , the expansion is convergent only for temperatures,  $T$ , such that

$$T > \frac{h\nu_m}{2\pi k} = \Theta/2\pi$$

Insertion of equation (2-51) into equation (2-19) yields for  $M$ ,

$$M = \frac{2}{3N'm} \left( \frac{\sin \theta}{\lambda} \right)^2 \sum_{\vec{k}, \alpha} \frac{kT}{v^2(\vec{k}, \alpha)} \left[ 1 - \sum_{n=1}^{\infty} (-1)^n \frac{B_n}{(2n)!} \left( \frac{h\nu(\vec{k}, \alpha)}{kT} \right)^{2n} \right] \quad (2-52)$$

The temperature derivative of the expression in equation (2-52) yields two terms; one is equal to  $(\partial M / \partial T)_V$  and the other arises from the dependence of the frequencies,  $\nu(\vec{k}, \alpha)$ , on volume. The thermal expansion contribution is small, so we assume that it can be determined with sufficient accuracy by the corresponding term obtained when a Debye spectrum is used, i.e., by the  $g(x)$  term in equation (2-43). Assuming that the term proportional to  $g(x)$  has been subtracted from a measured  $dM/dT^*$ , we consider only  $(\partial M / \partial T)_V = (\partial B / \partial T)_V \sin^2 \theta / \lambda^2$  in what follows. One obtains,

---

\*We are also assuming here that a  $\Theta$  has already been calculated from the measured  $dM/dT$ .

$$\left(\frac{\partial B}{\partial T}\right)_V = \frac{2}{3N'm} \sum_{\vec{k}, \alpha} \frac{k}{v^2(\vec{k}, \alpha)} \left[ 1 + \sum_{n=1}^{\infty} (-1)^n \frac{2n-1}{(2n)!} B_n \left( \frac{h\nu(\vec{k}, \alpha)}{kT} \right)^{2n} \right] \quad (2-53)$$

where we have assumed  $(\partial v(\vec{k}, \alpha)/\partial T)_V = 0$ . The frequencies which appear in equation (2-53) still depend on temperature through their dependence on volume. This additional temperature dependence can be eliminated through the use of equation (2-32), if we assume that the use of a single Grüneisen constant is valid. That is, we let  $v(\vec{k}, \alpha) = v_0(\vec{k}, \alpha)(V_0/V)^\gamma$ , where  $v_0(\vec{k}, \alpha)$  is the normal mode frequency at some temperature  $T_0$ . We also let

$$T' = T(V_0/V)^{-\gamma} \quad (2-54)$$

and define the  $n^{\text{th}}$  moment of the vibrational spectrum at temperature  $T_0$  as

$$\mu_n^0 = \frac{1}{3N'} \sum_{\vec{k}, \alpha} v_0^n(\vec{k}, \alpha) = \frac{1}{3N'} \int_0^{v_m} v^n g_0(v) dv \quad (2-55)$$

Then equation (2-53) becomes

$$\left(\frac{V_0}{V}\right)^{2\gamma} \left(\frac{\partial B}{\partial T}\right)_V = \frac{2k}{m} \left[ \mu_{-2}^0 + \sum_{n=1}^{\infty} (-1)^n \frac{2n-1}{(2n)!} B_n \left( \frac{h}{kT'} \right)^{2n} \mu_{2(n-1)}^0 \right] \quad (2-56)$$

or

$$\left(\frac{V_0}{V}\right)^{2\gamma} \left(\frac{\partial B}{\partial T}\right)_V = a_0 - a_1(T')^{-2} + a_2(T')^{-4} - a_3(T')^{-6} + \dots \quad (2-57)$$

where

$$a_0 = (2k/m)\mu_{-2}^0$$

and

$$a_n = \frac{2n-1}{(2n)!} B_n \left(\frac{h}{k}\right)^{2n} \left(\frac{2k}{m}\right) \mu_{2(n-1)}^0 \quad (2-58)$$

Now  $a_1$  is known because it does not depend on the vibrational spectrum since  $\mu_0^0 = 1$ . Thus, one can fit, using a high speed computer, experimentally determined values for  $(V_0/V)^{2\gamma}(\partial B/\partial T)_V + a_1(T')^{-2}$  to the expansion  $a_0 + a_2(T')^{-4} - a_3(T')^{-6} + \dots$  to estimate the coefficients  $a_n$ . The results, along with the recursion formula, equation (2-58) can then be used to yield values for the various moments of the vibrational spectrum.

The expansion which is appropriate for  $C_V$  is given by<sup>21</sup>:

$$C_V = 3N'k \sum_{\vec{k}, \alpha} \left[ 1 + \sum_{n=1}^{\infty} (-1)^n \frac{2n-1}{(2n)!} B_n \left( \frac{h\nu(\vec{k}, \alpha)}{kT} \right)^{2n} \right] \quad (2-59)$$

As can be seen by comparison of equation (2-59) with equation (2-53), each term in the expansion for  $(\partial B/\partial T)_V$  is proportional to the corresponding term in the expansion of  $C_V$  divided by  $\nu^2(\vec{k}, \alpha)$ . Therefore,



where  $\mu_{2n}$  appears in the expansion for  $C_v$ ,  $\mu_{2(n-1)}$  appears in the expansion for  $(\partial B/\partial T)_v$ . This means that a term proportional to  $\mu_{-2}$  occurs in  $(\partial B/\partial T)_v$  but not in  $C_v$ . Except for this term, the same moments occur in the expansions for both  $C_v$  and  $(\partial B/\partial T)_v$  although they do not multiply the same power of the temperature. Therefore, in addition to giving specific information about the vibrational spectrum, the analysis of experimentally determined values for  $(\partial B/\partial T)_v$  by the moments method yields results (except for  $\mu_{-2}$ ) which are directly comparable to those obtained from a similar analysis of specific heat data. However, problems which were encountered in our attempts to perform such an analysis indicated that either the experimental precision obtainable by present day x-ray techniques is not sufficiently high or the thermal expansion corrections suggested above are not sufficiently valid to allow meaningful determinations of the vibrational spectrum moments except possibly  $\mu_{-2}$ . These problems are discussed in Chapter IV.

### Two Atoms per Lattice Point

#### Individual Temperature Factors for an NaCl Type Lattice and Their Relation to the Vibrational Spectrum

For the case of more than one atom per lattice point, equation (2-8) takes the form

$$\langle PP^* \rangle = I_0(S/\lambda) |F|^2, \quad (2-60)$$

where

$$F = \sum_j f_j e^{-M_j} e^{\frac{2\pi i}{\lambda} \vec{S} \cdot \vec{\rho}_j}, \quad (2-61)$$

and where  $M_j$  is given by equation (2-6). For an NaCl type lattice with  $\vec{S}/\lambda$  satisfying equation (2-10),  $F$  takes the form<sup>5</sup>,

$$F = 4(f_1 e^{-M_1} \pm f_2 e^{-M_2}) \quad , \quad (2-62)$$

where for AgCl (or for KCl) the subscript 1 represents the  $\text{Ag}^+$  (or  $\text{K}^+$ ) ion and the subscript 2 represents the  $\text{Cl}^-$  ion. The plus sign in equation (2-62) corresponds to Bragg reflections which have all even Miller indices and the minus sign to those reflections which have all odd Miller indices. (No reflections with mixed indices are allowed.)

The relation of  $M_1$  and  $M_2$  to the vibrational spectrum is obtained, neglecting anharmonic effects, by combining equations (2-6) and (2-11). If  $M_j$  is multiplied by  $m_j$ ; the mass of atom  $j$ , and summed over  $j$ , then from equation (2-6) one obtains,

$$\sum_{j=1}^p m_j M_j = \frac{1}{4} \sum_{\vec{k}, \alpha} \{ \kappa \vec{S} \cdot \vec{e}(\vec{k}, \alpha) \}^2 \sum_{j=1}^p m_j \langle a_j^2(\vec{k}, \alpha) \rangle \quad . \quad (2-63)$$

Substitution of equation (2-11) into the right side of (2-63) gives,

$$\sum_{j=1}^p m_j M_j = \frac{1}{4} \sum_{\vec{k}, \alpha} \{ \kappa \vec{S} \cdot \vec{e}(\vec{k}, \alpha) \}^2 \frac{E(v(\vec{k}, \alpha))}{2\pi^2 N v^2(\vec{k}, \alpha)} \quad (2-64)$$

Now for an NaCl lattice,

$$\sum_{j=1}^p m_j M_j = 4(m_1 M_1 + m_2 M_2) \quad , \quad (2-65)$$

which when substituted into equation (2-64) yields,

$$m_1 M_1 + m_2 M_2 = \frac{1}{6N} \left( \frac{\sin \theta}{\lambda} \right)^2 \sum_{\vec{k}, \alpha} \frac{E(\nu(\vec{k}, \alpha))}{\nu^2(\vec{k}, \alpha)} \quad , \quad (2-66)$$

where we have made use of equation (2-18) and have set  $\kappa = 2\pi/\lambda$  and

$|\vec{S}| = 2\sin \theta$ . Insertion of the vibrational spectrum,  $g(\nu)$ , into equation (2-66) yields,

$$m_1 M_1 + m_2 M_2 = 4 \left( \frac{\sin \theta}{\lambda} \right)^2 \frac{\int_0^{\nu_m} E(\nu) \nu^{-2} g(\nu) d\nu}{\int_0^{\nu_m} g(\nu) d\nu} \quad . \quad (2-67)$$

and for a Debye spectrum,

$$m_1 M_1 + m_2 M_2 = \frac{12h^2 T}{k\Theta^2} \left\{ \phi(x) + \frac{x}{4} \right\} \left( \frac{\sin \theta}{\lambda} \right)^2 \quad (2-68)$$

A result equivalent to equation (2-67) was derived by Blackman<sup>19</sup> in a slightly different manner than that used above. Thus we see that neither  $M_1$  nor  $M_2$  is simply related to the vibrational spectrum, but their sum, weighted by the masses of the appropriate atoms, is.

Expressions can be obtained which relate  $M_1$  or  $M_2$  separately to the normal modes, however additional information is required, as is shown below, and the insertion of the vibrational spectrum into these expressions leads to little or no simplification. According to Laval<sup>17</sup> (also see Slater<sup>33</sup>) we can define a set of complex numbers  $C_j(\vec{k}, \alpha)$  such that

$$a_j(\vec{k}, \alpha) = C_j(\vec{k}, \alpha) a(\vec{k}, \alpha) \quad (2-69)$$

and

$$\sum_{j=1}^p |C_j(\vec{k}, \alpha)|^2 m_j = m' \quad (2-70)$$

where  $m'$  is the total mass of the atoms in the unit cell. Thus the differences in the vibrational amplitudes and phases of different atoms are contained in the  $C_j(\vec{k}, \alpha)$ 's and  $\langle a^2(\vec{k}, \alpha) \rangle$  is related to  $E(v(\vec{k}, \alpha))$  by,

$$2\pi^2 N m' v^2(\vec{k}, \alpha) \langle a^2(\vec{k}, \alpha) \rangle = E(v(\vec{k}, \alpha)) \quad (2-71)$$

Substitution of equations (2-69) and (2-71) into (2-6) leads to,

$$M_1 = \frac{1}{4} \sum_{\vec{k}, \alpha} \left\{ \kappa \vec{S} \cdot \vec{e}(\vec{k}, \alpha) \right\}^2 \frac{|C_1(\vec{k}, \alpha)|^2 E(v(\vec{k}, \alpha))}{2\pi^2 N m' v^2(\vec{k}, \alpha)} \quad (2-72)$$

It is convenient, for future discussion, to define a quantity

$$\Gamma(\vec{k}, \alpha) = C_2(\vec{k}, \alpha) / C_1(\vec{k}, \alpha) \quad (2-73)$$

which in the present experiment is the ratio of the  $Cl^-$  ion vibrational amplitude to that for the  $Ag^+$  (or  $K^+$ ) ion.  $\Gamma(\vec{k}, \alpha)$  is negative for the optic modes, where adjacent atoms vibrate out of phase, and it is positive for the acoustic modes, where adjacent atoms vibrate in phase<sup>10</sup>.

In terms of  $\Gamma(\vec{k}, \alpha)$   $M_1$  becomes

$$M_1 = \frac{1}{6N} \left( \frac{\sin \theta}{\lambda} \right)^2 \sum_{\vec{k}, \alpha} \frac{E(v(\vec{k}, \alpha))}{(m_1 + |\Gamma(\vec{k}, \alpha)|^2 m_2) v^2(\vec{k}, \alpha)}, \quad (2-74)$$

where again we have substituted the appropriate expression for  $\{\kappa \vec{S} \cdot \vec{e}(\vec{k}, \alpha)\}^2$ .

As we have indicated,  $\Gamma(\vec{k}, \alpha)$  is a function of the mode. Brillouin<sup>9</sup> has derived  $\Gamma(\vec{k}, \alpha)$  for the case of a one-dimensional diatomic chain with only nearest-neighbor interactions. Even for this "simple" case,  $\Gamma(\vec{k}, \alpha)$ , for a given  $m_1$  and  $m_2$ , is a rather complicated function of  $k$  (see appendix C). Thus the dependence of  $M_1$  (a similar result would apply to  $M_2$ ) on the normal modes is considerably complicated by the presence of  $\Gamma(\vec{k}, \alpha)$ , whose functional form for a general three-dimensional lattice is unknown. Thus it appears that the use of equations (2-67) and (2-68) would permit the better investigation of the vibrational spectrum. However, experimentally determined values for  $M_1$  and  $M_2$  (or of  $dM_1/dT$  and  $dM_2/dT$ ) could also be of considerable value in testing, for instance, the applicability of Brillouin's expression for  $\Gamma(\vec{k}, \alpha)$  to a three-dimensional lattice.

#### Temperature Derivatives of $M_1$ and $M_2$

The relationship between the vibrational spectrum and the temperature derivatives of  $M_1$  and  $M_2$  is essentially the same as that already discussed for the case of one atom per lattice point. For example when a Debye spectrum is assumed one obtains from equation (2-68)

$$m_1 M'_1 + m_2 M'_2 = \frac{12h^2}{k\theta^2} [f(x) + g(x)] \left( \frac{\sin \theta}{\lambda} \right)^2, \quad (2-75)$$

where the prime indicates the temperature derivative of the primed quantity. If a Debye spectrum were not assumed, the right side of equation (2-75) would be proportional to the right side of equation (2-40). Here it has been assumed that thermal expansion effects on the normal mode frequencies are the same as that already discussed for the monatomic case. For the moment other anharmonic effects have been neglected. Actually the anharmonic terms for the diatomic solid are not necessarily the same as discussed for the monatomic case. Different atom-types may have different anharmonic character in their vibrations, especially if they have different vibrational amplitudes. For simplicity, however, it will be assumed that even if the anharmonic terms are not the same size for  $M_1'$  and  $M_2'$ , the temperature dependence is the same for both.

The thermal motions of the two atom types in an NaCl type lattice are not in general identical. If the difference is negligible, i.e., if  $M_1 \approx M_2 = M$  and  $M_1' \approx M_2' = M'$ , equations (2-67), (2-68) and (2-75) reduce to the corresponding equations discussed earlier for the monatomic case with  $m$  replaced by  $(m_1 + m_2)/2$ . The experimental determination of  $dM/dT$  also would proceed exactly as already discussed in the monatomic case since  $e^{-M_1} = e^{-M_2} = e^{-M}$ , which can be taken outside the parenthesis in equation (2-62). It should be pointed out, however, that even if  $M_1 \approx M_2$  at, say, room temperature, they may not be equal at some other temperature, that is,  $M_1'$  is not necessarily equal to  $M_2'$ . Thus it is desirable to investigate the possibility of experimentally determining both  $M_1'$  and  $M_2'$  from intensity versus temperature measurements.

Contributions of  $M_1'$  and  $M_2'$  to  $d(\ln I)/dT$

We combine into  $K$  all quantities which relate the observed integrated intensity to  $|F|^2$ . From equation (2-62) we can write,

$$I = 16K \left( f_1 e^{-M_1} \pm f_2 e^{-M_2} \right)^2 \quad (2-76)$$

It is convenient to rewrite this expression in the following form,

$$I = 16K f_1^2 e^{-2M_1} \left( 1 \pm f e^{-\Delta M} \right)^2 \quad (2-77)$$

where

$$f = f_2/f_1 \text{ and } \Delta M = M_2 - M_1.$$

We assume for the moment that  $K$ ,  $f_1$ ,  $f$ , and  $\sin^2 \theta/\lambda^2$  are independent of temperature. Then,

$$-\frac{1}{2} \frac{d}{dT} (\ln I) \approx M_1' \pm \frac{f e^{-\Delta M}}{1 \pm f e^{-\Delta M}} (\Delta M') \quad (2-78)$$

Denoting the right side by  $A_0 (\sin^2 \theta/\lambda^2)^*$ , one obtains, in terms of  $B_1'$  and  $B_2'$ ,

$$A_0 = B_1' \pm (\Delta B') \left( \frac{1}{e^{\Delta M}/f \pm 1} \right), \quad (2-79)$$

---

\*This agrees with the general definition of  $A_0$  given in Chapter III.

where  $\Delta B' = B_2' - B_1'$ . Thus we see that  $B_1'$ ,  $B_2'$  and  $\Delta M$  all contribute to the temperature derivative of the intensity of a given Bragg peak. It is possible, however, to separate the individual contributions of  $B_1'$  and  $B_2'$  to  $A_0$  with the help of the analytic methods discussed in the following paragraphs.

#### $A_0$ Versus $\sin^2\theta/\lambda^2$ Character and the Determination of $B_1'$ and $B_2'$ Separately

From equation (2-79) and the definition of  $\Delta M$ , it follows that if the vibrational amplitudes of the two atom types in an NaCl type structure are different,  $A_0$  will vary with  $\sin^2\theta/\lambda^2$ . The purpose of the following discussion is, therefore, to investigate the use of an  $A_0$  versus  $\sin^2\theta/\lambda^2$  plot to determine, separately,  $B_1'$  and  $B_2'$ . To this end it is desirable that the possible distinguishing characteristics of an  $A_0$  versus  $\sin^2\theta/\lambda^2$  plot be determined along with the manner in which these characteristics depend on the sizes and signs of  $\Delta B'$  and  $\Delta B$ , where  $\Delta M = (\Delta B) \sin^2\theta/\lambda^2$ . Observations about the expected character of  $A_0$  versus  $\sin^2\theta/\lambda^2$  would also facilitate fitting curves to the experimental data, especially including curve fitting done with the use of a high-speed computer, should it be necessary.

Intuitively it is expected that the lighter atoms will have the larger vibrational amplitude so that for  $f < 1$ , (as it is according to the above definition), then  $\Delta B > 0^*$ . The actual situation will depend, however, in a complicated way on the interatomic forces so that the following discussion will cover both the case  $\Delta B < 0$  as well as the

\*The designation 1 and 2 for the atoms is completely arbitrary and will not affect any following conclusions. The case of  $\Delta B > 0$  and  $f < 1$  is redundant with  $\Delta B < 0$  and  $f > 1$ .



case  $\Delta B \geq 0$ . For the purpose of simplification, however, it is assumed that  $\Delta B'$  and  $\Delta B$  have the same sign, as would be expected, although it is not totally unreasonable for  $\Delta B'$  and  $\Delta B$  to have different signs.

In addition to equation (2-79) it is desirable that the first and second derivatives of  $A_o$  with respect to  $\sin^2 \theta / \lambda^2$  be known. Letting  $\sin^2 \theta / \lambda^2 = \phi$  and taking  $d(\Delta B)/d\phi = dB'_1/d\phi = dB'_2/d\phi = 0^+$ , one obtains from equation (2-79),

$$\frac{dA_o}{d\phi} = \mp \frac{(\Delta B') (\Delta B) \frac{e^{\Delta B \phi}}{f}}{\left( \frac{e^{\Delta B \phi}}{f} \pm 1 \right)^2} \quad (2-80)$$

and

$$\frac{d^2 A_o}{d\phi^2} = - (\Delta B) \frac{dA_o}{d\phi} \left( \frac{\frac{e^{\Delta B \phi}}{f} \mp 1}{\frac{e^{\Delta B \phi}}{f} \pm 1} \right) \quad (2-81)$$

Several observations can now be made:

1.  $A_o$  varies with  $\phi$  in a manner which depends on whether the Miller indices are even or odd such that

$$A_o \xrightarrow{\phi \rightarrow \infty} \text{smaller of } B'_1 \text{ and } B'_2, \quad (2-82)$$

\*+ Actually  $f$  may vary with angle although the dependence is expected to be small. For example for  $\text{AgCl}$   $f$  varies only + 3 percent from  $\phi = 6 \times 10^{14} \text{ cm}^{-2}$  to  $\phi = 80 \times 10^{14} \text{ cm}^{-2}$ . Thus we will set  $df/d\phi = 0$  also.

$$A_0 \xrightarrow{\phi \rightarrow 0} \frac{B'_1 + B'_2}{1 + \phi} \quad (2-83)$$

Since  $\phi$  will generally be known fairly well, both  $B'_1$  and  $B'_2$  may be separately determined by extrapolation of either  $A_0$  (even) or  $A_0$  (odd) first to  $\phi = \infty$  and then to  $\phi = 0$ .

2. If only  $\Delta B'$  is zero,  $A_0$  for the even and odd parity cases will be equal and independent of  $\phi$ .

3. If only  $\Delta B$  is zero, or if  $(\Delta B)\phi \ll 1$  for the entire experimentally observable range of  $\phi$ ,  $A_0$  for the even and odd parity cases will be respectively independent, or essentially independent, of  $\phi$ . For this case  $B'_1$  and  $B'_2$  can be separately determined without extrapolations by comparing  $A_0$  (even) with  $A_0$  (odd).

4. If, as has been assumed,  $\Delta B'$  and  $\Delta B$  have the same sign, the slope of  $A_0$  versus  $\phi$  is never negative for the case of odd parity and is never positive for the case of even parity.

5. A singularity (odd parity case) or an inflection point (even parity case) occurs at

$$\phi = \frac{\ln \phi}{\Delta B} \quad (2-84)$$

For  $\Delta B > 0$  these points will not occur in the observable positive range of  $\phi$  for  $\phi < 1$ . However for  $\Delta B < 0$  the case when the heavy atom has the larger amplitude, these points will occur in the positive and possibly observable range of  $\phi$ . Additional observations are made more easily by means of a qualitative sketch of  $A_0$  versus  $\phi$ . Figures 2 and 3 are such sketches. From an analytic point of view the distinguishing

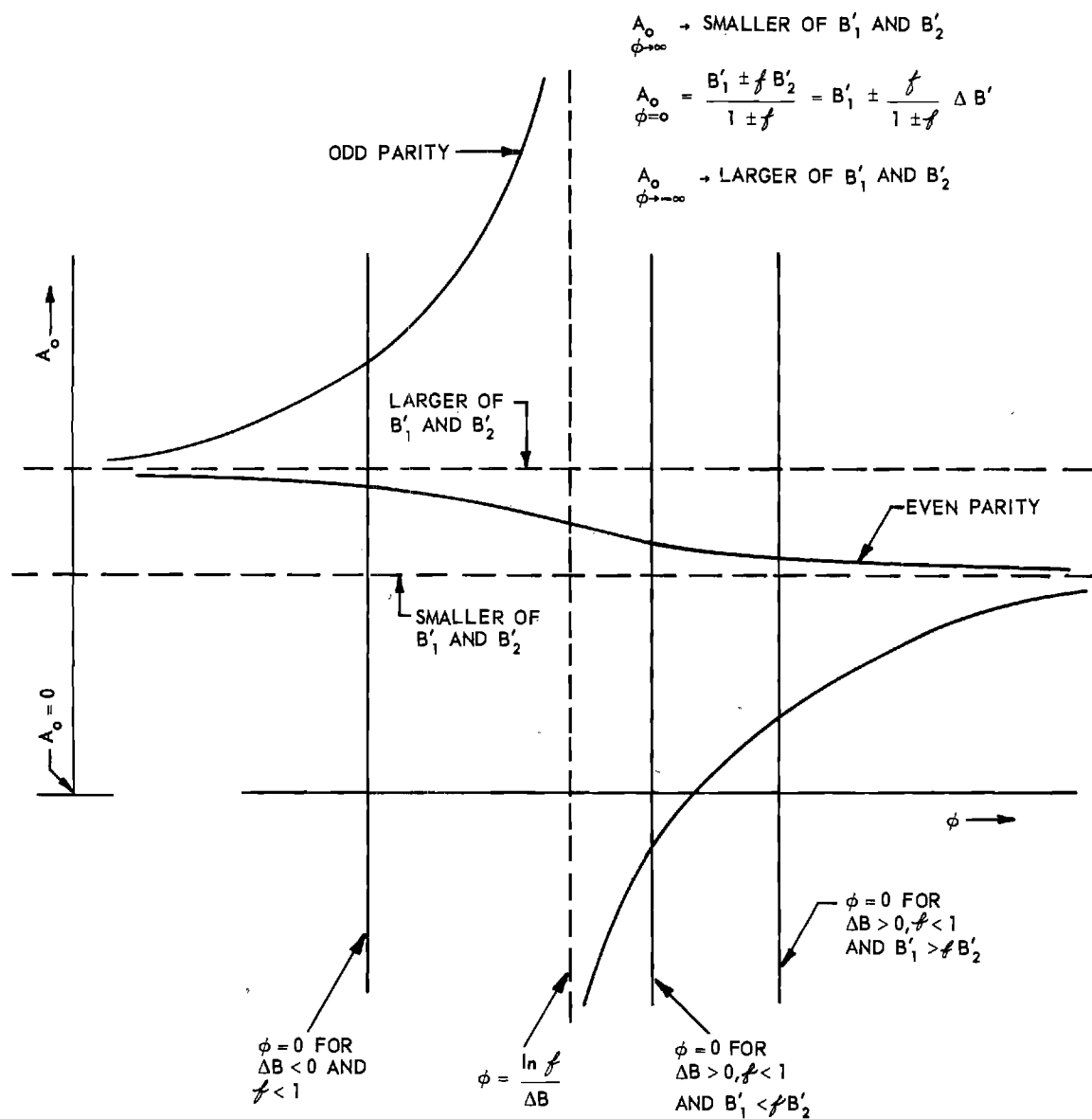


Figure 2. Dependence of  $A_0$  on  $\phi$ .

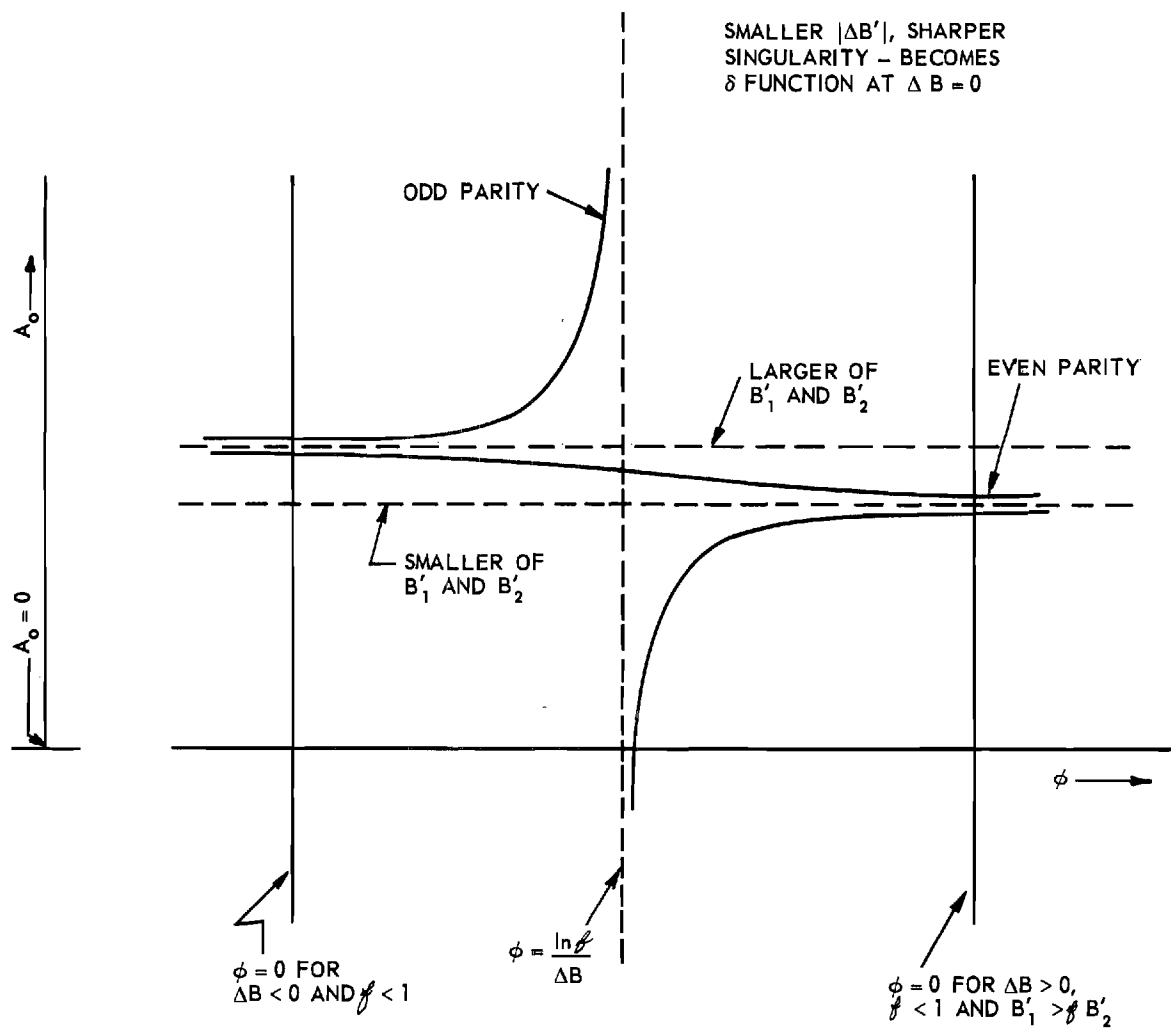


Figure 3. Dependence of  $A_0$  on  $\phi$  for small  $|\Delta B'|$ .

features of  $A_0$  versus  $\phi$  are the singularities and points of inflection; the sketches are therefore made with reference to these points as fixed points. The point  $\phi = 0$  is then treated as a dependent variable in the sketches.

Further observations follow with the aid of the sketches:

- (1)  $A_0$  (even) lies between  $B_1'$  and  $B_2'$  for all  $\phi$ , approaching the smaller from above as  $\phi$  tends to infinity.
- (2) For  $\Delta B > 0$  and  $f < 1$ ,  $A_0$  (odd) is smaller than  $A_0$  (even) for all observable values of  $\phi$  and approaches  $A_0$  (even) as  $\phi$  tends to infinity.  $A_0$  (odd) can even be negative for some positive values of  $\phi$ ; the requirement being  $B_1' < f B_2'$ .
- (3) For  $\Delta B < 0$  and  $f < 1$ ,  $A_0$  (odd) is first larger and then smaller than  $A_0$  (even) as  $\phi$  increases if the singularity lies within the observable range of  $\phi$ .
- (4) As  $\Delta B \rightarrow 0$  (see Figure 3)
  - (a) the singularity becomes sharper and moves toward either  $+\infty$  or  $-\infty$  depending on the sign of  $\Delta B$ , and
  - (b) the dependence of  $A_0$  (even) on  $\phi$  becomes smaller.

Figures 2 and 3 along with the foregoing discussion indicate that an experimental  $A_0$  versus  $\phi$  plot can have enough character to be of considerable help in the interpretation of intensity versus temperature data obtained from a crystal having an NaCl type structure. The usefulness of such a plot is demonstrated in Chapter IV in the analysis of the data for AgCl.

## CHAPTER III

## EXPERIMENTAL PART

Summary of Experimental Procedure

The intensity versus temperature data were obtained from small (maximum diameter  $\sim 0.5$  mm) approximately spherical single crystal samples with a counter-adapted Weissenberg camera and a Philip's x-ray unit. MoK $\alpha$  radiation, balanced filters, and a scintillation counter were used throughout the work. The geometry used was such that all parts of the sample could "see" all parts of the x-ray target and the counter intercepted all of the diffracted beam. The bulk of the data consisted of measurements of peak heights\* versus temperature. The desired integrated intensity versus temperature information was obtained from these data and measurements of the temperature dependence of  $B_0$  (ratio of integrated intensity to peak height). The integrated intensities used for the determination of  $B_0$  were obtained by the  $\omega$ -scan technique (rotation of the sample about the Weissenberg spindle axis with the counter held stationary). The samples were so mounted that all the data were obtained from zero layer reflections. Control of the sample temperature was achieved by means of a gas stream directed onto the sample. The gas stream temperature was determined with a well calibrated chromel-alumel thermocouple. The next several sections give detailed information on matters of apparatus and technique.

---

\*By peak height is meant the maximum intensity of a plot of intensity versus angle obtained for a Bragg reflection.

## Apparatus

### X-Ray Apparatus

The x-ray apparatus used in the present work includes a Philips x-ray generator, scintillation counter, associated scaling, pulse height discrimination (PHD), and recording circuits, and a Supper Weissenberg camera adapted for use with a counter. The counter adaptor is of Georgia Tech design and construction<sup>34</sup>. It provides a stable mounting for the counter with both coarse and fine adjustments in azimuth and elevation about the sample position as center (see figures 5 and 6). A scintillation counter was chosen, in preference to a gelger or proportional counter, partly because of its high counting efficiency for MoK $\alpha$  radiation but mainly because of the uniform response ( $\pm 1/4\%$  or better) across the window. This uniformity is important because the diffracted beam does not always impinge at exactly the same place on the counter window.

The x-ray generator and associated circuits are supplied with regulated voltage ( $\pm 1/4\%$  or better) and a separate beam current stabilizer. The overall stability of the x-ray generator and detection apparatus was generally better than  $\pm 1\%$  as determined experimentally. Although the long term (one to two hours) stability was somewhat beam current dependent (improving, for instance, from  $\pm 2\%$  to  $\pm 1/2\%$  as the current was changed from 20 ma to 10 ma with no PHD and a  $\bar{M}\bar{o}$  tube operated at 50 KV), data for the low intensity reflections were obtained at the higher current settings. This decrease in machine stability was generally compensated by the fact that the low intensity reflections occur at large values of  $\sin^2\theta/\lambda^2$  and hence exhibit a

correspondingly large temperature dependence. Analysis of data obtained from both high and low intensity reflections yielded substantially the same results.

The linearity of the response of the overall detection equipment to counting rate was checked by the multiple absorber technique. Pieces of Al foil were used as absorbers. It was found that with the PHD in the circuit the response was linear to within 1% up to counting rates of 20,000 counts per second.

All the data were obtained with  $\text{MoK}_\alpha$  radiation ( $\lambda = 0.709 \text{ \AA}$ ). This relatively short wavelength was used in order that reciprocal lattice points (relp) comparatively far out in reciprocal space could be observed. (All observations are limited, by the wavelength used, to a sphere in reciprocal space which is centered at the origin and has a radius equal to twice the reciprocal wavelength.) Data extending as far out in reciprocal space as possible are desired for several reasons: (1) the magnitude of the temperature effect for "far out" reflections is enhanced due to the dependence of  $M$  on  $\sin^2\theta/\lambda^2$  (see theory), (2) other  $\sin^2\theta/\lambda^2$  dependent effects, such as TDS or such as that possible for an NaCl type structure (see theory), can be detected more easily if the data extend over a large range of  $\sin^2\theta/\lambda^2$ , and (3) more independent observations are thereby made available.

#### Temperature Control Apparatus

Control of the sample temperature was achieved by means of a gas stream, approximately 1/2 inch in diameter, directed onto the sample. The gas train is shown in Figure 4. The liquid nitrogen container was a standard 25 liter Linde dewar. Nitrogen gas at liquid



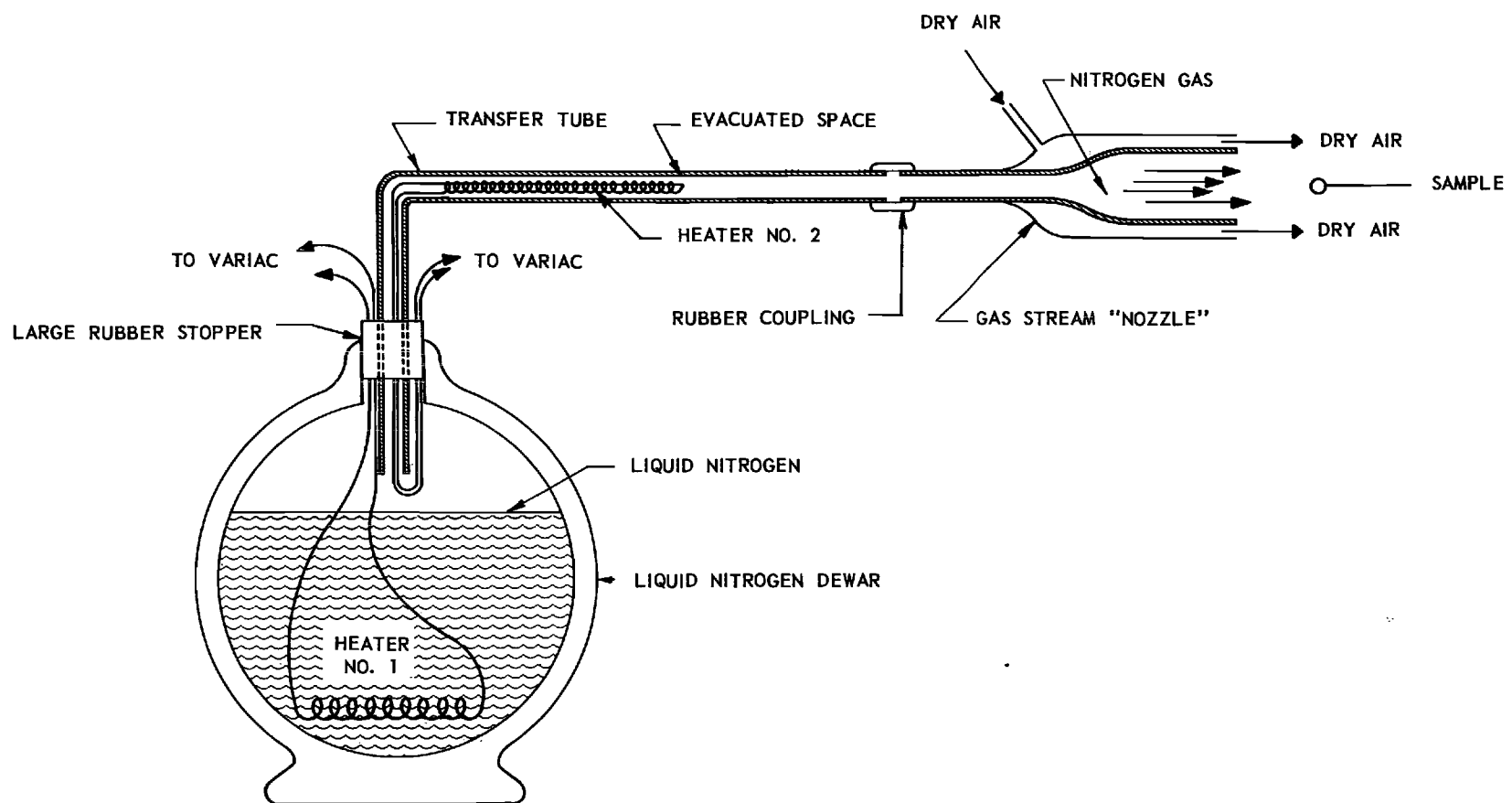


Figure 4. Gas Train.

nitrogen temperature ( $\sim 78^{\circ}$  K) was obtained by vaporizing liquid nitrogen with electrical heater no. 1. This heater was a coil of no. 18 kanthal wire which had a resistance of approximately 5 ohms when immersed in liquid nitrogen. Under normal operating conditions this heater dissipated approximately 125 watts to give a calculated gas flow rate of about 25 liters per minute at liquid nitrogen temperature.

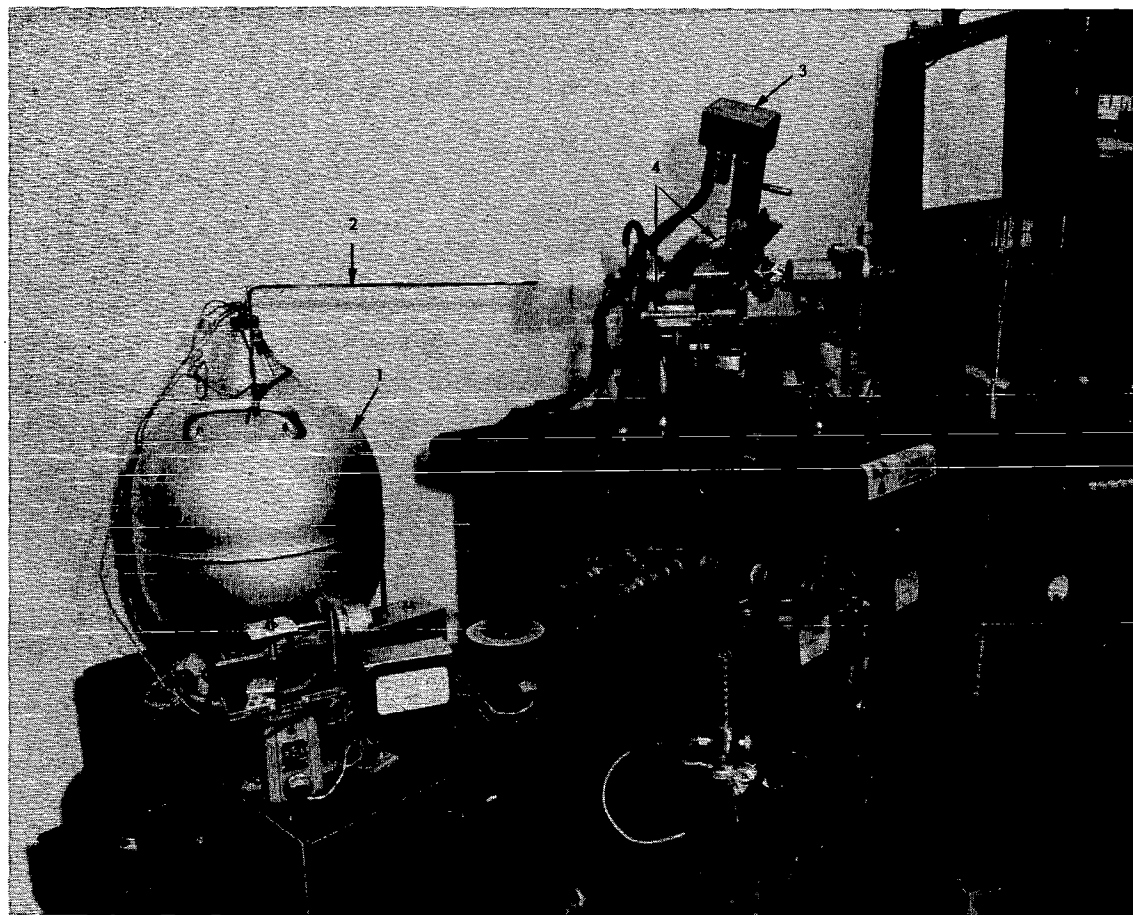
The escaping gas was collected in a glass transfer tube and directed onto the sample with the gas stream "nozzle" as shown in Figure 4. The gas stream was directed to flow co-axially with the Weissenberg spindle axis. With this geometric arrangement the nozzle could be brought to within 1 mm of the sample without obstructing either the incident or diffracted beams in the zero layer. The transfer tube and the inner conductor of the nozzle had double walls with an evacuated space between them, shown cross hatched in Figure 4, to minimize the conduction of heat to the cold stream. Heat leaks were satisfactorily small. Moisture never condensed on the outer surface of the transfer tube and the lowest temperature of the gas obtained at the nozzle exit (more than two feet from the liquid nitrogen container) was between  $85$  and  $90^{\circ}$  K. An annular stream of dry, room temperature air surrounded the cooling stream (see Figure 4) to minimize turbulence and, hence, sample frosting due to moisture in the room air.

The temperature of the gas stream could be varied between  $90$  and  $350^{\circ}$  K by variation of the voltage applied to electrical heater no. 2, located inside the transfer tube. This voltage was supplied by a stepless auto-transformer and could be continuously and linearly increased or decreased by driving the auto-transformer shaft with a synchronous

(Haydon) motor. The heater was a coil (coiled lengthwise along the transfer tube to minimize obstruction of the gas stream) of no. 36 copper wire which had a resistance of approximately 110 ohms at room temperature. For this resistance the maximum gas stream temperature, 350° K, corresponded to nearly the maximum of the variac voltage output. Copper wire was used because of its favorably high thermal coefficient of resistance. The heat dissipated by this heater, and hence the gas stream temperature, was more nearly a linear function of the applied voltage,  $V$ , than the power equation  $P = V^2/R$  indicates because the heater resistance,  $R$ , increased significantly with an increase in temperature. Therefore it was possible to vary the gas stream temperature at a nearly constant rate by constant rate variation of the auto-transformer setting with the synchronous motor.

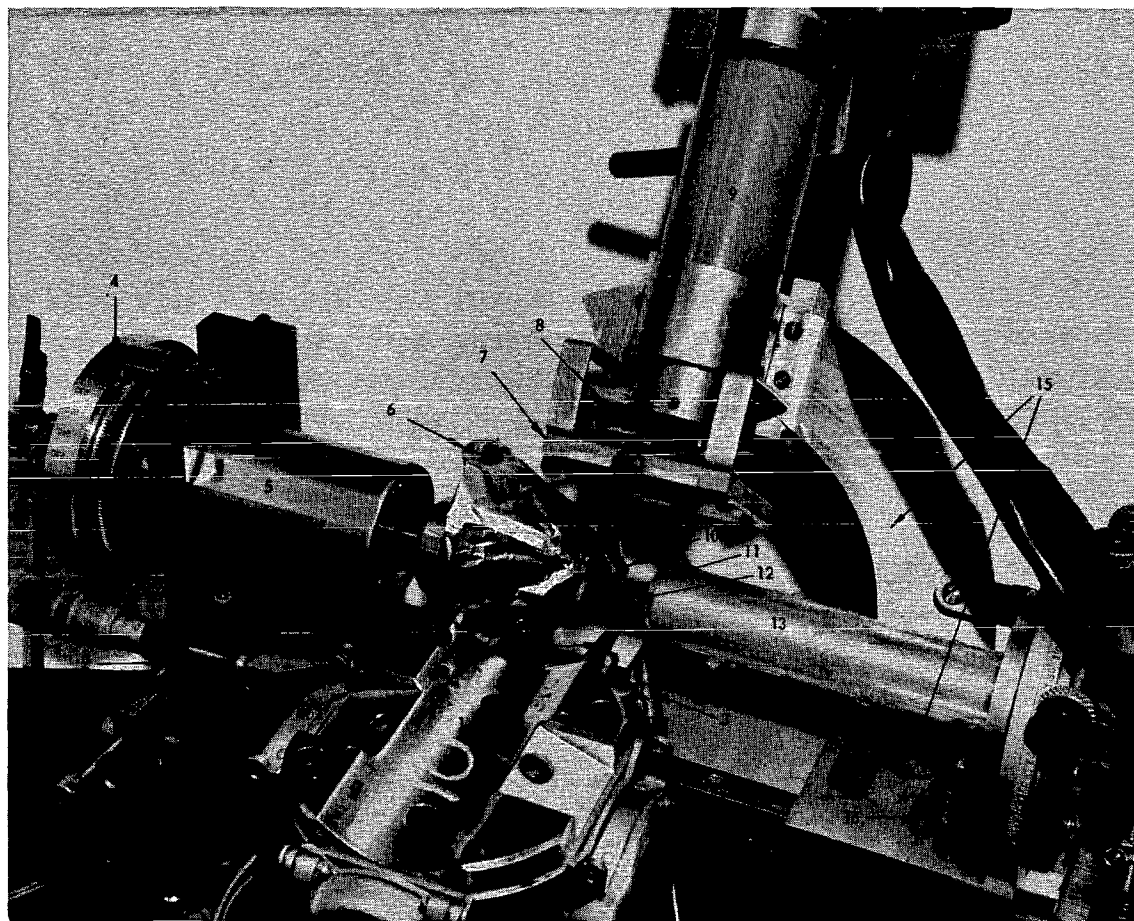
To keep heaters no. 1 and no. 2 from being damaged because of over-heating, a protective electrical circuit was incorporated into the cold stream system. This circuit consisted of a thermistor, placed in the nitrogen gas stream in the nozzle, which was connected in series with a variable resistor, a battery, and a relay. When the nitrogen gas temperature became higher than some preselected temperature (selectable by adjustment of the variable resistor) the thermistor resistance decreased to the point at which the current flow in the circuit was sufficiently large to actuate the relay and thereby to shut off the power to both heaters.

Figure 5 shows the entire experimental setup, including the low temperature apparatus. Figure 6 is a close up view of the region surrounding the sample. The aluminum foil wrapped around the goniometer



- |                          |                                     |
|--------------------------|-------------------------------------|
| 1. LIQUID NITROGEN DEWAR | 6. SAMPLE OSCILLATION APPARATUS     |
| 2. TRANSFER TUBE         | 7. DETECTION CIRCUIT PANEL          |
| 3. SCINTILLATION COUNTER | 8. X-RAY GENERATOR                  |
| 4. COUNTER ADAPTER       | 9. DRY AIR SUPPLY                   |
| 5. WEISSENBERG CAMERA    | 10. TEMPERATURE CONTROL ELECTRONICS |

Figure 5. Equipment.



- |   |                           |                                       |
|---|---------------------------|---------------------------------------|
| 1. X-RAY TUBE HEAD                      | 6. GONIOMETER HEAD SHIELD | 11. GLASS MOUNTING FIBER              |
| 2. THERMOCOUPLE POSITIONER              | 7. APERTURE SUPPORT       | 12. SAMPLE                            |
| 3. THERMOCOUPLE SUPPORT                 | 8. BALANCED FILTERS       | 13. COLD STREAM NOZZLE                |
| 4. $\omega$ SCALE OF WEISSENBERG CAMERA | 9. SCINTILLATION COUNTER  | 14. COLLIMATOR                        |
| 5. WEISSENBERG SPINDLE HOUSING          | 10. BRASS MOUNTING PLUG   | 15. COUNTER ADAPTER                   |
|   |                           | 16. $\omega$ SCALE OF COUNTER ADAPTER |

Figure 6. Equipment.

head had room temperature-dry air blown on it from behind to help shield the goniometer head and Weissenberg spindle housing from the cold gas. Thermal expansion of these parts of the apparatus was thereby minimized.

#### Temperature Determination

The temperature of the gas stream was determined with a specially calibrated chromel-alumel thermocouple having 3-mil diameter leads. It was placed  $< 1$  mm from the sample. The small wire diameter was found necessary for the elimination of significant heat conduction along the leads. That the thermocouple actually measured the gas stream temperature was demonstrated several ways. The indicated temperature did not depend on whether the thermocouple leads were situated perpendicular to the gas stream, so that about  $1/4$  inch of the leads was in the stream, or whether several inches of the leads were parallel to and in the stream. Thus heat conduction along the leads was negligible. Temperature measurement errors due to the effects of radiation from objects at room temperature were also shown to be negligible. The indicated temperature did not depend on whether the thermocouple junction was in its normal position outside the nozzle or whether it was placed inside the nozzle where it was essentially surrounded by a surface at the gas stream temperature. Temperature measurements made with the sample removed indicated that at the sample position the temperature of the gas stream, throughout a region several times the size of the sample, was within  $1/2^{\circ}$  K of the temperature indicated by the thermocouple in its normal position. The reference junction of the thermocouple was always immersed in a room temperature water bath whose temperature was monitored by a standard laboratory thermometer.

As will be discussed later, the intensity measurements on which all of the intensity vs temperature analyses are based were made under dynamic conditions, i.e., as the temperature was changing. The thermocouple output was displayed on a Brown strip chart recorder just before and just after each intensity measurement. The temperature corresponding to the intensity measurement was obtained by interpolation. That the lag of the sample temperature behind the gas stream, or thermocouple, temperature was insignificant is indicated by the lack of a measurable hysteresis in the intensity vs temperature data obtained while cooling and then while heating a sample.

Besides being convenient, temperature control by means of a gas stream has some additional advantages over other possible methods. The moving gas is a nearly perfectly agitated fluid bath with effectively infinite heat capacity and with excellent heat transfer properties. Thus for the small, approximately spherical samples used the surface of the sample was held at the gas stream temperature. An estimate of the thermal gradients which existed in the sample was not attempted. However the lack of hysteresis in the intensity vs temperature data, mentioned earlier, indicates that thermal gradients were satisfactorily small. In addition, work done with similar gas stream geometry and quartz specimens at  $575^{\circ}\text{C}$  indicated that the sample temperature in that case was uniform to within  $1^{\circ}\text{K}^{35}$  or less. The largest uncertainty in sample temperature is estimated to be  $\pm 1^{\circ}\text{K}$  and arises from the interpolation of the thermocouple output readings on the Brown recorder. The uncertainty in temperature increments was substantially smaller, however, because of the nearly constant rate at which the gas stream temperature was varied and because the recorder chart advanced at a constant rate.

### Samples

As mentioned in Chapter I, the materials studied in this work were Al, KCl, and AgCl. Aluminum samples were prepared from a single-crystal rod of about 99.9% purity. Potassium chloride samples were prepared from optical-grade single-crystal material obtained from the Harshaw Chemical Company. Silver chloride samples were prepared from ultrapure single-crystal material kindly provided by F. Moser\* of the Eastman Kodak Company and from optical-grade single-crystal material obtained from the Harshaw Chemical Company. Data were obtained from at least two samples of each material in order that the results obtained be indicative of the material studied rather than of a particular sample. No residual darkening of the KCl and AgCl samples due to exposure to x-rays was observed.

Some attempt was made to shape the samples into approximations of spheres. There are several reasons that justify such an effort. The combination of an irregularly shaped sample and non-uniform x-ray source illumination can cause the top of a diffraction peak to have more than one maximum. Variations in peak shape will affect the relationship between peak height and integrated intensity and hence complicate the determination of  $B_0$ . Also the amount of absorption of x-rays in an irregularly shaped sample is dependent on the sample orientation. Since thermal expansion causes the Bragg angle,  $\theta$ , and, hence, the optimum sample orientation to be temperature dependent, the absorption correction for an irregularly shaped sample would be temperature dependent. This

---

\*The preparation and purity of ultrapure AgCl are described by N. R. Nail, F. Moser, P. E. Goddard, and F. Urbach, Rev. Sci. Instr. 28, 275 (1957).



situation would considerably complicate the interpretation of intensity vs temperature data. In addition, an irregularly shaped sample would cause the cross-fire in the incident beam to be dependent on sample orientation and hence on the Bragg reflection being observed. This situation would complicate the calculation of TDS corrections to the intensity vs temperature data (see Appendix A and the end of this chapter for a discussion of TDS corrections).

### Sample Preparation

#### Silver Chloride

At room temperature AgCl is so subject to plastic flow that considerable care must be taken in cutting and shaping it. In fact, it was shown by Laue photographs that all mechanical methods tried hopelessly distorted the single crystals.

In order to avoid distortion, etching techniques had to be used. Two methods for cutting AgCl samples from large "parent" single crystals have been used successfully. They both involve the use of a standard photographic "hypo" solution (sodium thiosulfate) which is an excellent etchant for AgCl. In one method, Figure 7(a), a 5-mil thick circular saw is rotated with a small motor (Dremel "Moto-Tool"). The rotating saw is kept wet with hypo as the crystal is advanced onto the saw slowly enough so that the cut is made solely by etching. The saw itself does not actually touch the crystal; the teeth in the saw are useful for carrying the hypo to the crystal. The other method, Figure 7(b), is similar in principle and makes use of a string saw arrangement. The saw is a continuous piece of string which is passed over several pulleys made of

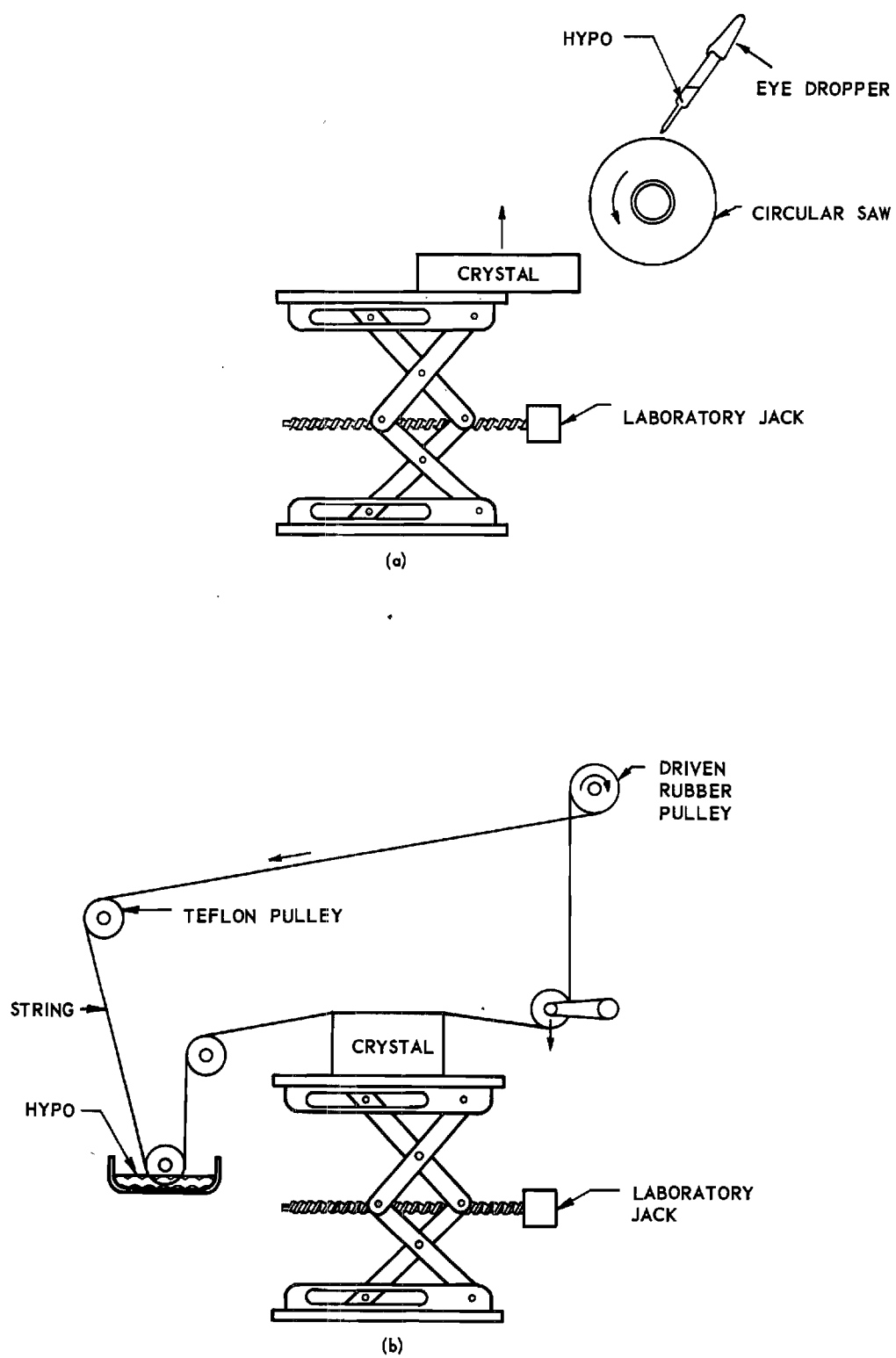


Figure 7. Crystal Cutting Methods.

teflon and over one which is made of rubber and driven by a Haydon motor. The string is wet in a hypo solution before it passes over the crystal; cutting of the crystal consists of controlled etching. The string is advanced onto the crystal by the weight of a pulley which rests on top of the string at a point just past the crystal.

The small cubes which were cut from the parent crystals by the methods just described were made approximately spherical by a shaping technique which also involved etching with hypo. The crystal to be shaped was fastened to a shaft rotated by the Dremel Moto-Tool. The rotating crystal was brought into contact with an ink blotter placed on end in a beaker half filled with hypo as indicated in Figure 8. The "high spots" on the crystal were etched off by contact with the hypo-soaked blotter. Thus any portion of the crystal could be given a fairly circular cross section. Through remounting of the crystal several times and repetition of the process a fairly spherical sample could be obtained.

The AgCl samples used in the present work are described in Table 1.

Table 1. List of AgCl Samples

<u>Sample No.</u>	<u>Size</u>	<u>Source</u>
7	0.14 mm ave. dia.	Harshaw Chemical Company
11	0.14 mm ave. dia.	Eastman Kodak Company
17	0.50 mm ave. dia.	Harshaw Chemical Company
18	0.47 mm ave. dia.	Harshaw Chemical Company

#### Potassium Chloride

KCl is not subject to plastic flow at room temperature so it was not necessary for us to resort to etching techniques for cutting and

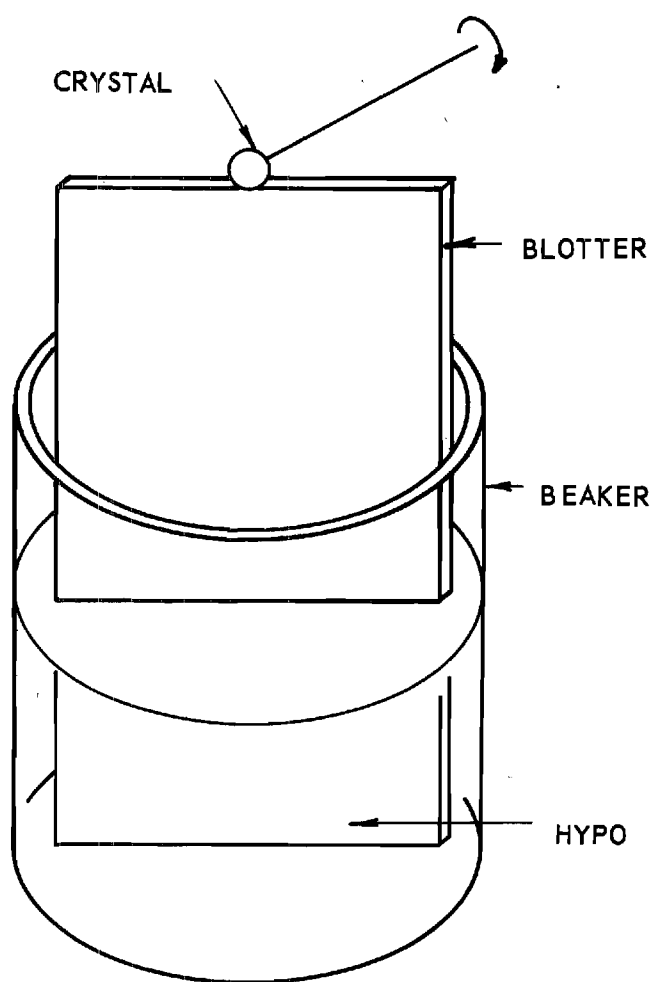


Figure 8. Sample Shaping Method.

shaping of the KCl samples. Small cubic crystals could be obtained from a large parent crystal by cleavage, as KCl cleaves readily on 100 faces. The small cubic crystals were then ground to a nearly spherical shape, with a diameter of approximately 2 mm, by being tumbled in an air stream on the periphery of a cylindrical cavity lined with diamond dust. The sphere was etched in water to a diameter of approximately 0.5 mm to remove surface distortions caused by the grinding. The KCl samples used are described in Table 2.

Table 2. List of KCl Samples

<u>Sample No.</u>	<u>Size</u>	<u>Source</u>
1	0.61 mm ave. dia.	Harshaw Chemical Company
2	0.50 mm ave. dia.	Harshaw Chemical Company
3	0.36 mm ave. dia.	Harshaw Chemical Company

### Aluminum

Small Al cubes, approximately 2 mm on a side, were sawed from the rod of single crystal material with a jewelers saw. It was found that etching these cubes in a solution of HCl + HNO<sub>3</sub> yielded sufficiently spherical samples for our purposes. As for the KCl samples, the etching removed any surface distortions caused by mechanical shaping. The Al samples are described in Table 3.

Table 3. List of Al Samples

<u>Sample No.</u>	<u>Size</u>	<u>Source</u>
2	0.35 mm ave. dia.	Georgia Tech
4	0.52 mm ave. dia.	Georgia Tech

The sharpness of the  $\omega$ -scans of the reflections of the KCl and Al samples indicated that preparation induced residual strains in these samples were not a problem.

#### Sample Mounting

In order that heat conduction problems be minimized, the shaped crystals were mounted on glass fibers approximately 1 cm in length with any one of several adhesives. The glass fiber was first affixed, with wax, to a small brass plug which fits the goniometer head. The following procedure was used to mount a sample:

The glass fiber is held in a vertical position by attachment of the brass plug, with clay, to the vertical side of any convenient object. The sample is then placed on the adhesive side of Scotch tape which is in turn taped, adhesive side up, to a rectangular metal weight. The weight is placed on a laboratory microjack (such as illustrated in Figures 7(a) and 7(b)) positioned so that the sample lies directly under the end of the glass fiber. With a second fiber the adhesive is applied both to the sample and to the end of the mounting fiber. The jack is then raised to bring the fiber and sample into contact. The whole operation is monitored through a stereomicroscope.

Since the shaped samples have no distinguishing exterior characteristics which aid in mounting the sample in a desired orientation, re-mounting of a sample was sometimes necessary because the desired orientation could not be achieved with the first mounting or because the alignment required excessively large goniometer arc displacements.

Remounting of a sample was facilitated by the use of a series of two pairs of adhesives. Either member of a pair is insoluble in the solvent of the other member. Table 4 lists these adhesives.

Table 4. List of Adhesives

<u>Adhesive</u>	<u>Soluble In</u>
Formvar	ethylene dichloride
polyvinyl alcohol	H <sub>2</sub> O
collodion	amyl acetate
mucilage	H <sub>2</sub> O

For remounting, the sample was placed below a brass plug and fiber as usual, but it was held in a known orientation by the goniometer head. The second member of the adhesive pair was then used to make a joint between the new fiber and sample. When the second adhesive hardened, the first fiber was removed by dissolution of the first adhesive.

#### Intensity Measurement Considerations

The integrated intensity corresponds to the total power diffracted during one complete passage of a reciprocal lattice point (relp) either into or out of the Ewald sphere of reflection as the crystal is rotated with a constant angular velocity. Most formulas for intensity are based on this measure. In the present study we need only to follow the changes in the total intensity associated with a given relp as the temperature is changed. Neither the total intensity itself nor its value relative to that for any other relp need be determined. Thus for the sake of speed, measurement of peak height may be considered adequate for the collection of nearly continuous intensity versus temperature data.

Of course occasional measurements of  $B_0$  at different temperatures are also desired to insure that the measured changes of the peak height are, or can be corrected to yield, adequate measures of the changes of the integrated intensity.

### Geometry

The geometry used in the present study was such that all parts of the sample could "see" all parts of the x-ray target. This broad beam geometry was chosen to minimize variations in peak height (or  $B_0$ ) resulting from nonuniform illumination of the x-ray target and small temperature induced sample displacements and misalignments. In addition this geometry yields broad diffraction peaks which results in extensive overlap of the  $K\alpha_1$  and  $K\alpha_2$  components of the peak. Hence the percent variations in the overall peak width (and  $B_0$ ) resulting from the thermal expansion induced variations in the  $K\alpha_1$  and  $K\alpha_2$  doublet separation are minimized.

The counter window was large enough so that all of the diffracted beam was detected during measurement of either peak height or integrated intensity. A lead aperture was placed between the counter and sample (see Figure 6). Its purpose was to limit the "view" of the counter to the sample and its immediate neighborhood, thereby minimizing background contributions (I misc) resulting from scattering of the incident beam by air and the exit end of the collimator<sup>36</sup>.

### Background Determination

The proper determination of background intensities is the subject of an extensive study made recently in connection with the present



research work<sup>36</sup>. It turns out that measurements of peak heights and integrated intensities by the  $\omega$ -scan method are particularly susceptible to errors arising from harmonic, including both sub-harmonic and non-integral harmonic, contributions arising from the Bremstrahlung on which the characteristic  $K\alpha$  radiation of interest is superimposed. For the purposes of the present work, the balanced filter technique offers the best compromise between high intensity and discrimination against unwanted wavelengths. It is preferred here for reasons of speed and of insensitivity to nonuniformity in both the x-ray target illumination and in effective sample reflectivity due to absorption and shape. Two filters are said to be balanced when they both have the same absorption for wavelengths lying outside the region between their closely spaced absorption edges, which ordinarily are chosen to bracket the  $K\alpha$  wavelength. Thus the difference between two intensity measurements, one with each filter, is due entirely to wavelengths in the interval between the absorption edges (pass-band region).

Proper peak and background measurements with balanced filters require at least four separate measurements, one on and one off the peak with each filter<sup>36</sup>. Figure 9 shows a sketch of a diffraction peak obtained by rotation of the sample about the Weissenberg spindle axis with the counter held stationary. One curve is shown for each filter. The  $\beta$  filter and  $\alpha$  filter have absorption edges on the short wavelength and long wavelength side of the  $K\alpha$  characteristic respectively. The small peak at B is usually almost entirely due to harmonic contributions. The use of the intensity at C,  $I_C$ , as the whole background would miss this contribution. On the other hand, the use of  $I_B$  as the whole background

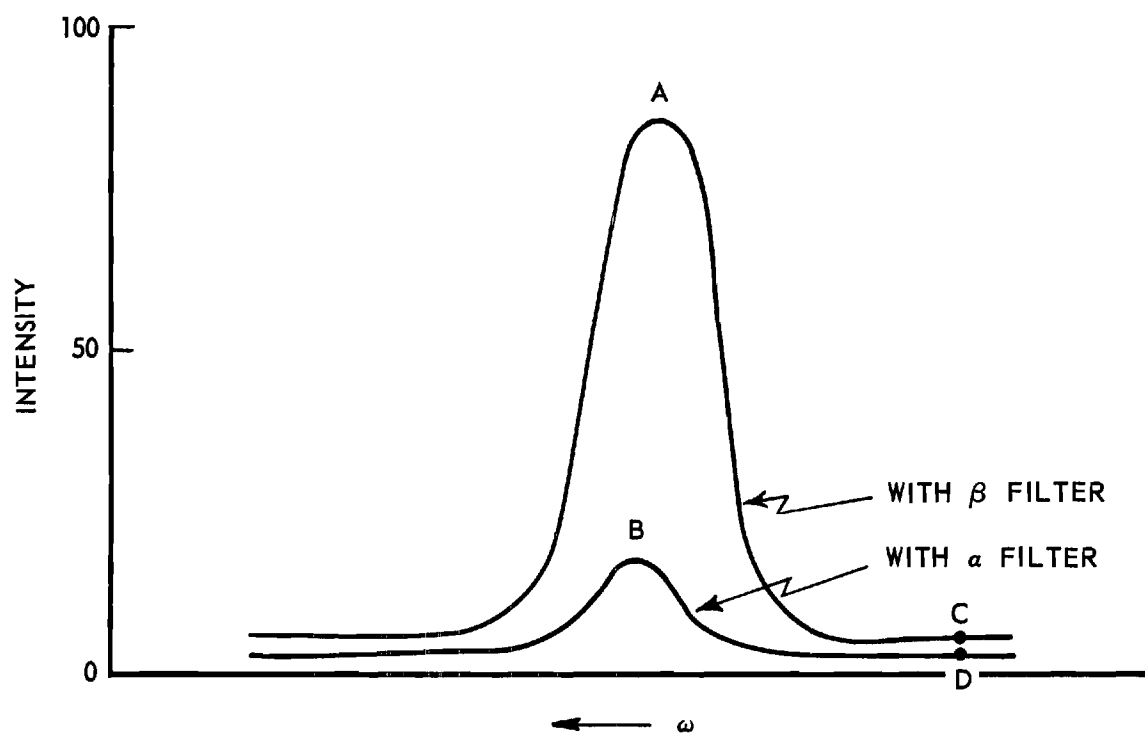


Figure 9.  $\omega$ -scan with Balanced Filters.

would miss some of the angle-independent background ( $I_C - I_D$ ) which is due to non-Bragg scattering of pass-band wavelengths. It is composed of  $I(\text{misc})$  and TDS. Our best corrected peak height is given by  $I = (I_A - I_C) - (I_B - I_D)$ . The contribution from TDS of pass-band wavelengths is only partially accounted for by these four measurements since it also peaks at the Bragg peak position. However, the TDS contribution to the peak height can be calculated adequately as is shown later. An analogous procedure with obvious modifications must be followed when one obtains integrated intensities.

For  $\text{MoK}\alpha$  radiation the filter materials are zirconium and either yttrium or strontium. In the present work we have used a  $\text{Zr-Y}_2\text{O}_3$  filter pair which was carefully balanced with a procedure described elsewhere<sup>37</sup>. It is impossible to obtain a perfect balance for all wavelengths in the x-ray tube spectrum. Thus the filters were balanced to within 1% at wavelength near and on both sides of their K absorption edges, i.e. near the  $\text{MoK}\alpha$  wavelength. Possible imbalance at wavelengths far from the  $\text{K}\alpha$  was rendered unimportant by the use of electronic pulse height discrimination. The filter pair was mounted in front of the counter window on a bar which could slide in a groove in a cap which fits over the front of the counter (see Figure 6). One changes from one filter to the other by sliding the bar until a spring loaded ball riding on the edge of the bar falls into an indentation, thereby positioning the filter reproducibly in the diffracted beam. Significant effects due to the fluorescence of the  $\alpha$ -filter were absent. Any fluorescent radiation from the  $\alpha$ -filter which reaches the counter merely introduces a scale factor which will not affect the intensity versus temperature results.

### Data Collection Procedures

The samples were aligned so that the  $[110]$  direction was coaxial with the spindle axis of the Weissenberg. With this alignment all three principal crystallographic directions,  $[001]$ ,  $[1\bar{1}0]$ , and  $[1\bar{1}1]$  are in the zero layer. This alignment is preferred for several reasons:

1. If the observed reflections are confined to the zero layer, the gas stream nozzle can be brought close (within  $< 1$  mm) to the sample without obstructing the incident and diffracted beams.
2. TDS calculations are greatly simplified for zero layer as compared to upper layer reflections.
3. The  $[hhh]$  reciprocal lattice row contains reflections having both all odd and all even Miller indices. Thus it may be possible to determine the difference in the vibration amplitudes of the different atom types in an NaCl structure (see theory) without the possible complication of (crystallographic) directionally dependent anharmonic effects.
4. The possible anisotropy of  $M$  due to anharmonic effects (see theory) may be most easily detected by comparing data obtained from reflections in these principal crystallographic directions.

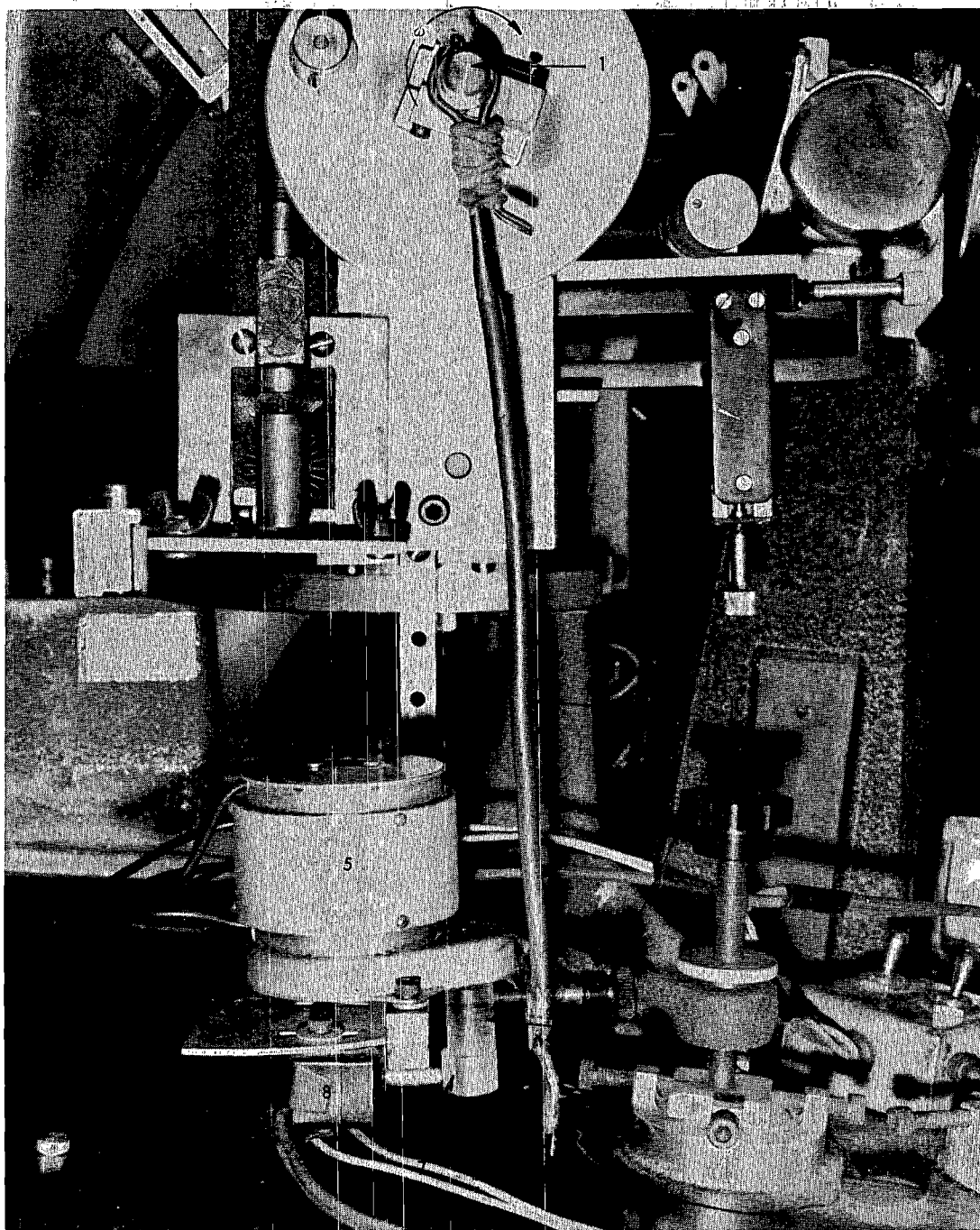
The alignment procedures used have been described in detail elsewhere<sup>38</sup>. Briefly they can be described as follows. The counter elevation angle ( $\Upsilon$ ) is set to zero, the counter azimuth angle ( $\nu$ ) is set equal to the Bragg angle,  $\theta$ , for some  $(hh0)$  reflection (usually the  $(220)$ ), and the Weissenberg table is rotated by  $\theta$ . The goniometer arc settings are then systematically changed until the reflection is found, i.e. until the  $(220)$  Bragg plane normal is made coincident with the spindle axis so that a beam is diffracted into the counter. The arc settings are then

adjusted until the diffracted intensity is a maximum at each of four spindle settings separated by  $90^\circ$ . This procedure will fail if the sample has been mounted too far out of alignment. The sample must then be remounted. In such cases, precession photographs were often used for determination of the crystal orientation in the first mounting.

### I vs T

As mentioned earlier the integrated intensity versus temperature information desired was obtained from measurements of peak height versus temperature subsequently corrected, when necessary, for the temperature dependence of  $B_0$ . Since thermal expansion causes the peak position to be a function of temperature, continual readjustment of the crystal orientation to the optimum diffracting position is required as the temperature is varied. Manual optimization of the sample position at each temperature was shown to be inferior to a motorized method. The sample was made to oscillate ( $\omega$ -oscillation) through a small angle including the optimum position by means of the motor and cam arrangement shown in Figure 10. The maximum intensity recorded during each oscillation was then the desired peak height.

This method of optimizing the sample orientation made it possible partially to automate data-taking procedures. Two flat surfaces were cut  $\sim 180^\circ$  apart on a cylindrical extension of the piece of lucite from which the cam was made. The flat surfaces were positioned to arrive at the micro-switch plunger, normally depressed by the lucite cylinder, when the crystal was at one end of its oscillating travel, and hence was off the peak maximum position. The micro-switch plunger was then released thereby switching the Brown strip chart recorder from the rate



- |                             |                                |
|-----------------------------|--------------------------------|
| 1. WEISSENBERG SPINDLE AXIS | 5. SYNCHRONOUS MOTOR           |
| 2. MANUAL SPINDLE DRIVE     | 6. LUCITE CAM                  |
| 3. LEVER                    | 7. FLAT CUT IN LUCITE CYLINDER |
| 4. SCREW                    | 8. MICRO-SWITCH                |

Figure 10. Crystal Oscillation Apparatus.

meter output to the output of the thermocouple. During a run, the output of the autotransformer which supplied power to heater no. 2 (see Figure 4) was varied continuously by variation of the variac setting with a synchronous motor. Thus the top of the Bragg peak and temperature readings could be alternately displayed on the recorder chart as the crystal temperature was being continuously varied from  $90^{\circ}$  to  $300^{\circ}$  K or vice versa. The results of a typical intensity versus temperature run are shown in Figure 11. The temperatures at the peak positions were obtained by interpolation. Background measurements on and off the peak (B, C, and D in Figure 9) were usually taken at the beginning and end of each run. Occasional background readings made during runs indicated that the background at each temperature could be determined satisfactorily by a linear interpolation between measurements made at the temperature extremes.

#### $B_0$ vs T

For the determination of  $B_0$  at a given temperature, the area of a peak was obtained by collection, on a count register, of the total number of counts obtained during a continuous  $\omega$ -scan from background on one side of the peak to background on the other side. One scan was made with each member of the balanced filter pair.

$B_0$  was determined at room temperature and at approximately  $100^{\circ}$  K for the (400), (600), and (10,00) reflections for at least one sample of each material studied. Essentially no ( $< 1\%$ ) change in  $B_0$  for the (400) and (600) reflections were observed.  $B_0$  for the (10,00), however, was several percent larger at room temperature than at  $100^{\circ}$  K for each sample on which  $B_0$  measurements were made.

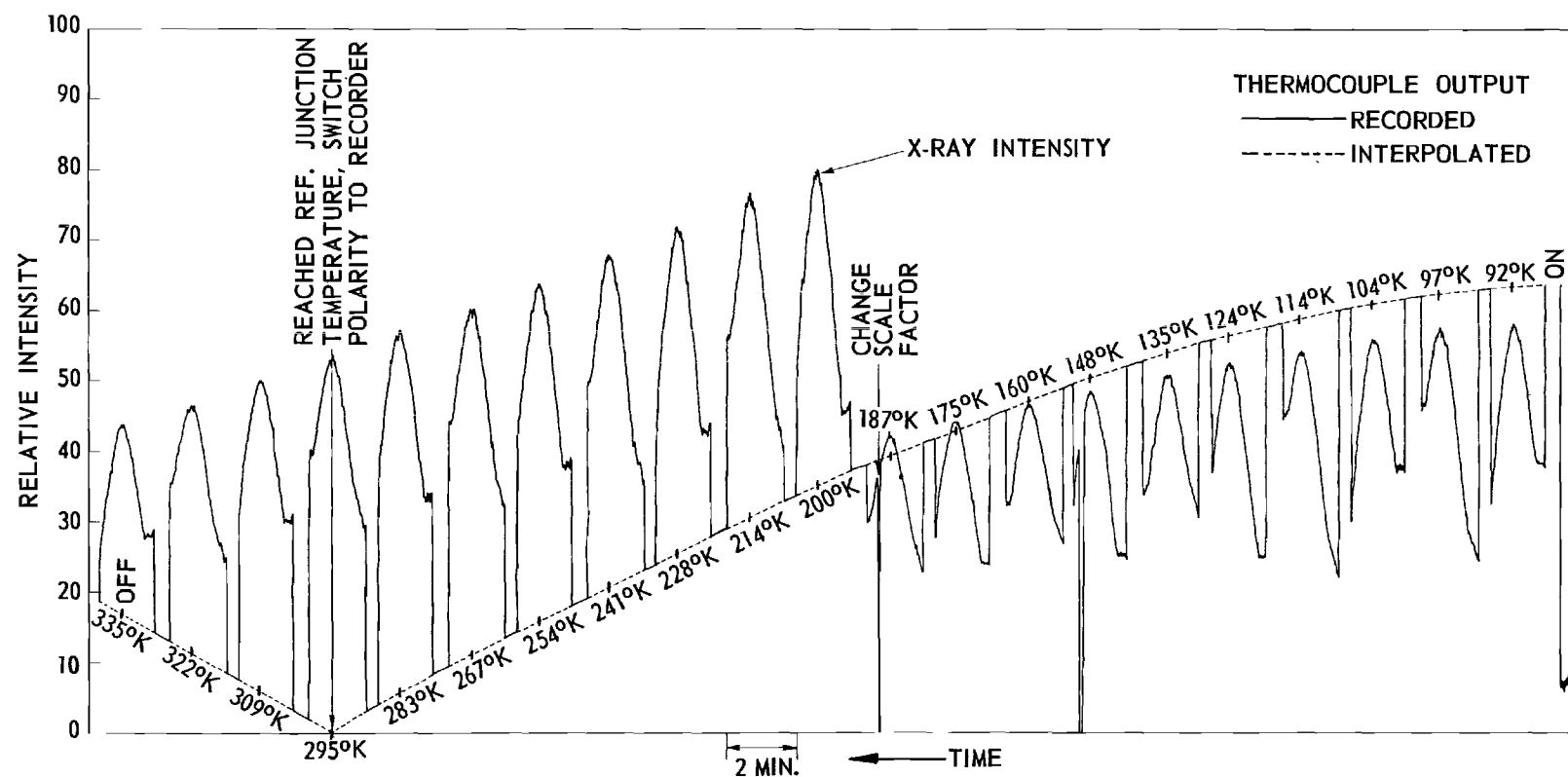


Figure 11. Typical Intensity Versus Temperature Run.



The major contributions to the temperature variation of  $B_0$  are expected to be TDS and the variation in the  $K\alpha_1$  and  $K\alpha_2$  doublet separation due to thermal expansion. Both of these would have a larger effect at large Bragg angles,  $\theta$ , such as that for the (10,00) reflections. The expected effect of the variation of the  $\alpha$ -doublet separation is opposite to that observed however. That is, the observed variations in  $B_0$  indicated a "sharpening up" of the peak as the temperature was reduced, such as that expected from TDS contributions, whereas a "sharpening up" would result only as the temperature was raised if the  $\alpha$ -doublet separation were the only contribution.

Therefore it may be assumed that the major contribution to the temperature dependence of  $B_0$  arises from TDS and that the variation in the  $\alpha$ -doublet separation was rendered insignificant by the broad beam geometry used. Since the peak height data were to be corrected for TDS contributions, no  $B_0$  versus  $T$  corrections were applied to the observed peak height versus temperature data. The apparent validity of this procedure is indicated by the good agreement between results obtained from the (10,00) reflection and other reflections, such as the (400) and (600)\*.

#### Data Reduction

##### Definition of A and $A_0$

In order to compare easily the intensity versus temperature results obtained from different Bragg reflections, we found it convenient

---

\* In addition since good agreement was found between the results obtained for the [100], [110], and [111] directions, no examination of the directional dependence of the temperature dependence of  $B_0$  was made.

to eliminate the obvious  $\sin^2\theta/\lambda^2$  dependence of  $d(\ln I)/dT$  (see for instance equations (2-39), (2-43), and (2-78)) and to define the quantity A;

$$A = - 1/2 (\sin^2\theta/\lambda^2)^{-1} \frac{d}{dT} \ln I(\text{obs}) \quad , \quad (3-1)$$

where  $I(\text{obs})$  denotes the observed intensity. There are "small" contributions to the temperature dependence of  $I(\text{obs})$  in addition to the temperature factor. Although these contributions are discussed separately in the following paragraphs, they are mentioned here briefly as an aid to understanding how they all contribute to A. Consider the case of a monatomic cubic crystal\*. For this case the observed integrated intensity can be written (see equations (1-1), and (1-3))

$$I(\text{obs}) = C \frac{1+\cos^2\theta}{\sin 2\theta} f^2(\theta) e^{-2M} (1 + \epsilon_{\text{TDS}}) \quad , \quad (3-2)$$

where all temperature independent factors are included in C, the TDS contribution is contained in  $\epsilon_{\text{TDS}}$ , and the other factors have been defined earlier. The quantities which are shown to depend on  $\theta$  in equation (3-2) depend on temperature since  $\theta$  varies because of thermal expansion. Denoting the Lorentz and polarization factor  $(1 + \cos^2 2\theta)/(\sin 2\theta)$ , by (L.P.), and  $\sin^2\theta/\lambda^2$  by  $\phi$  one obtains

$$- \frac{1}{2\phi} \frac{d}{dT} \ln I(\text{obs}) = \frac{1}{\phi} \frac{dM}{dT} - \frac{1}{2\phi} \frac{d}{dT} \ln \left[ (\text{L.P.}) f^2 \right] - \frac{1}{2\phi} \frac{d}{dT} \ln (1 + \epsilon_{\text{TDS}}) \quad (3-3)$$

---

\*The general situation is essentially the same for an NaCl type structure. Any differences will be pointed out.

or

$$A = A_0 + A_{LPf} + A_{TDS} \quad (3-4)$$

where

$$A_{LPf} = -\frac{1}{2\phi} \frac{d}{dT} \ln \left[ (L.P.) f^2 \right] \quad , \quad (3-5)$$

$$A_{TDS} = -\frac{1}{2\phi} \frac{d}{dT} \ln \left( 1 + \epsilon_{TDS} \right) \quad , \quad (3-6)$$

and for the special case treated here,

$$A_0 = \frac{1}{\phi} \frac{dM}{dT} \approx \frac{dB}{dT} \quad . \quad (3-7)$$

$A_0$  represents the contribution to  $A$  resulting from only the temperature factor. For an NaCl type lattice,  $A_0$  is not as simple as shown above but depends on the temperature factors of both atom types as indicated in equation (2-79).  $A_{LPf}$  and  $A_{TDS}$  represent corrections which must be applied to the measurements of  $A$  in order to obtain the quantity of interest in the present study, viz.  $A_0$ . These corrections are discussed in more detail below.

#### Corrections to I vs T Data

$A_{LPf}$ . For a monatomic cubic crystal, one obtains

$$A_{LPf} = +\frac{\alpha}{2\beta} \left\{ \frac{1}{(L.P.)} \frac{d(L.P.)}{d\beta} + \frac{2}{f} \frac{df}{d\beta} \right\} \quad (3-8)$$

where  $\beta = \sin \theta / \lambda$  and  $\alpha$  is the linear coefficient of thermal expansion. It was found convenient to take the derivatives with respect to  $\beta$  because  $f$  is usually found tabulated along with  $\beta$  and (L.P.) is usually found tabulated along with  $\sin \theta = \beta \lambda$ . The derivatives were obtained graphically.

For the case of an NaCl type lattice some assumptions which were used should be pointed out. If it is not assumed that  $f_1$  and  $f$  are independent of temperature as was done to obtain equation (2-78), one finds that the contribution to  $A_{LPf}$  of the atomic scattering factors  $f_1$  and  $f_2$  is

$$= \frac{1}{2\phi} \left( \frac{1}{f_1} \frac{df_1}{dT} + \frac{df/dT}{e^{\Delta M} + f} \right) \quad (3-9)$$

Since  $A_{LPf}$  represents a small correction, we set  $e^{\Delta M} = 1$  in equation (3-9). When this assumption is made equation (3-9) simplifies and  $A_{LPf}$  for an NaCl type lattice becomes the same as equation (3-8) with  $f$  replaced by  $f_1 + f_2$ . It also turned out that the difference between  $A_{LPf}$  for reflections having odd Miller indices and for reflections having even Miller indices was less than 1/2% of the  $A$  values obtained for AgCl (as mentioned in Chapter IV no KCl data were obtained from reflections having odd Miller indices). Thus the  $A_{LPf}$  correction used for both types of AgCl reflections was that obtained by replacing  $f$  with  $f_1 + f_2$  in equation (3-8)\*. Figures 12, 13, and 14 are plots of  $A_{LPf}$  versus  $\sin^2 \theta / \lambda^2$  for Al, KCl, and AgCl respectively and for MoK $\alpha$  radiation.

\*The atomic scattering factors for Al, K<sup>+</sup>, Ag<sup>+</sup>, and Cl<sup>-</sup> were obtained from International Tables for X-ray Crystallography, edited by Caroline H. Macgillavry, Gerard D. Rieck, and Kathleen Lonsdale (The Kynock Press, Birmingham, England, 1962), Vol. III, p. 201.

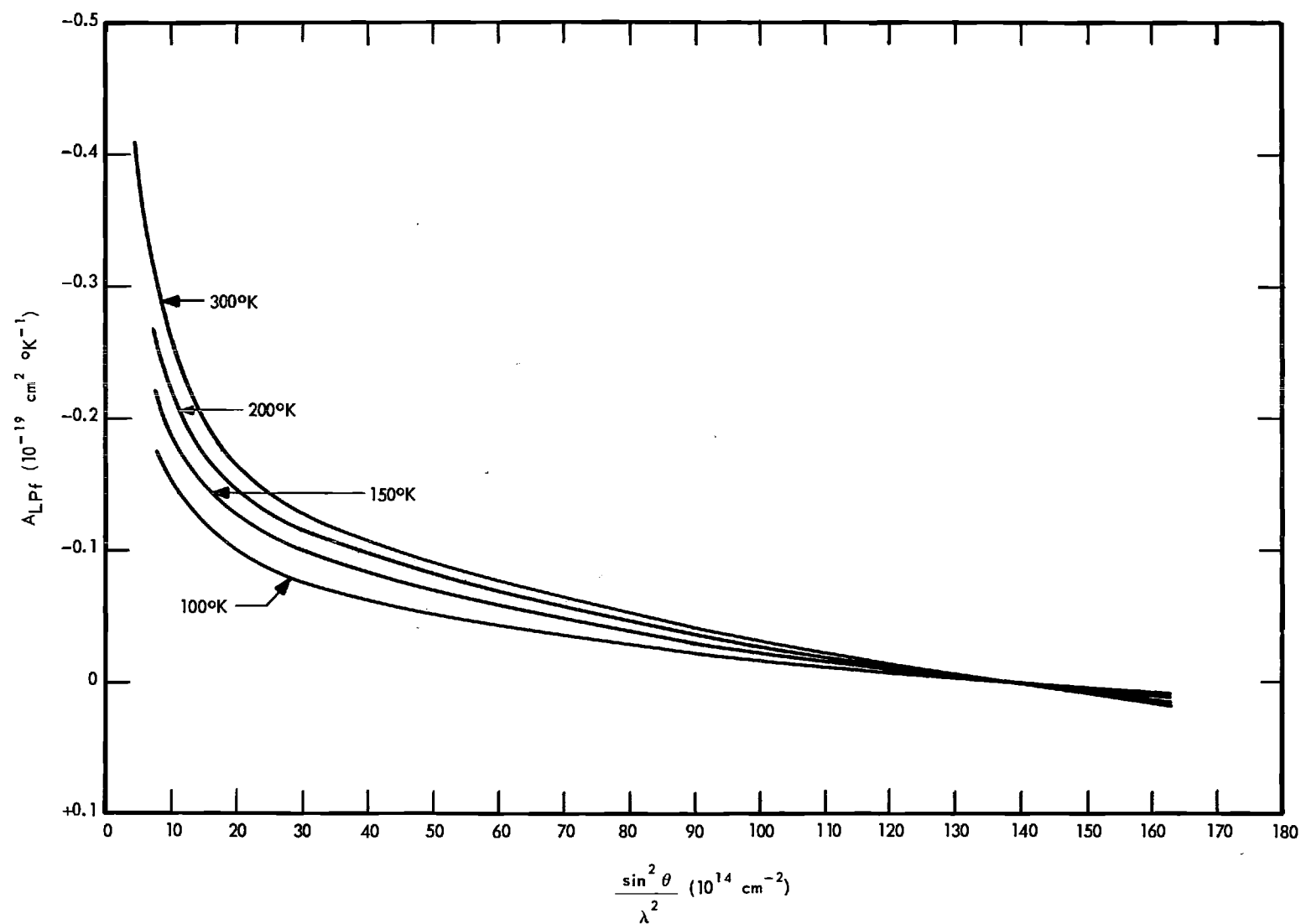


Figure 12. Dependence of  $A_{LPf}$  for Al on  $\sin^2 \theta / \lambda^2$  at Several Temperatures.

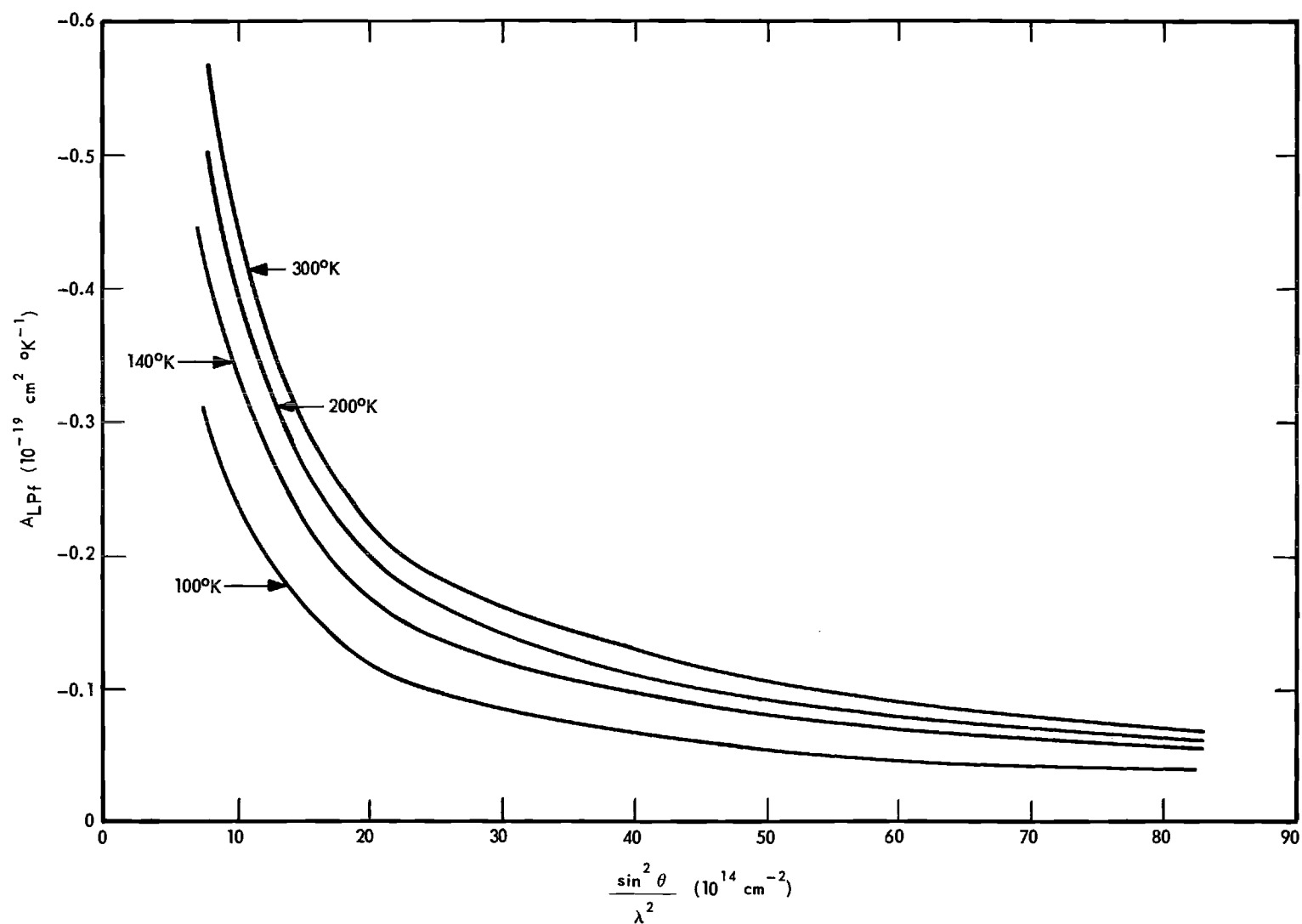


Figure 13. Dependence of  $A_{LPf}$  for KCl on  $\sin^2 \theta / \lambda^2$  at Several Temperatures.

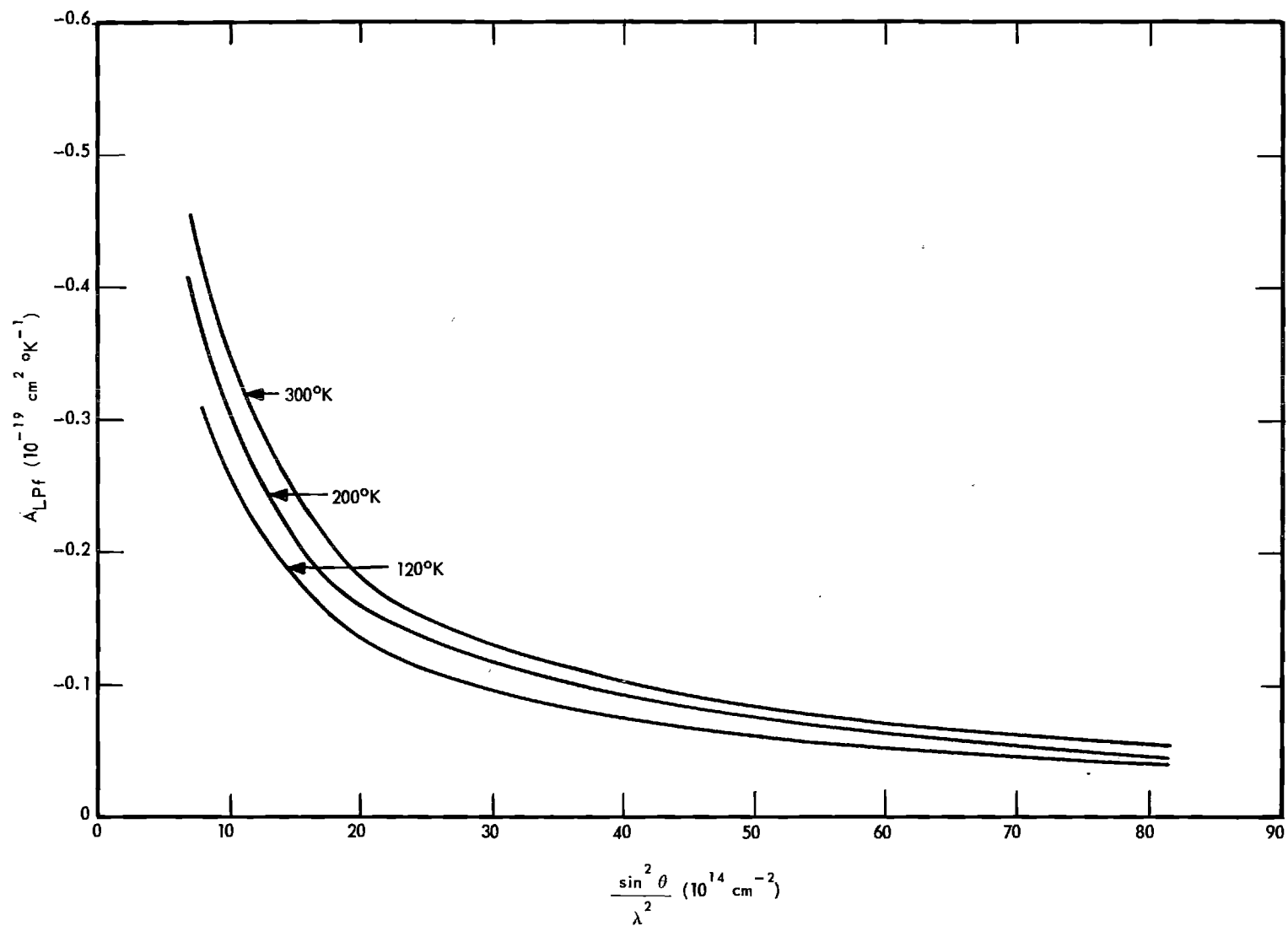


Figure 14. Dependence of  $A_{LPf}$  for AgCl on  $\sin^2 \theta / \lambda^2$  at Several Temperatures.

Thermal Diffuse Scattering and A<sub>TDS</sub>. It is well known that thermal diffuse scattering can contribute significantly to the measured intensity of an x-ray diffraction peak<sup>6,39,40,41</sup>. It is apparent from the work of the authors referred to above that an accurate determination of the TDS contribution to the measured peak intensity depends on the particular experimental technique used. We know of no work which can be directly applied to the experimental technique we have used in the present study.

Thus, although the work referred to above is helpful in pointing out the necessity of TDS corrections, we have found it necessary to make a rather extensive study of the possible effects of all experimental parameters, e.g. sample size and shape, beam size and divergence, counter window size, etc., on the TDS corrections. The development of these corrections has necessitated a thorough review and synthesis of existing TDS theory followed by some recasting and extension of it. This necessarily extensive discussion, and the resulting statement and solution of the specific problems in the present research, are put in Appendix A because of their length. For continuity of the present discussion, we shall discuss only briefly in the following paragraphs the general approach used in making the TDS corrections, the results obtained, and an experimental test of the calculations. It should be pointed out that the calculations made were of the TDS contributions to a peak height measurement. However the temperature independence of  $B_0$  discussed earlier indicates that the contributions obtained are also probably adequate corrections to some  $\omega$ -scan integrated intensity measurements.

The general approach to the problem is most easily discussed by means of a specific case. For simplicity consider the first order (or one phonon)



scattering from a monatomic-cubic crystal. According to the general theory of thermal diffuse scattering (see Appendix A), the diffuse intensity corresponding to a point in reciprocal space a distance  $|\vec{g}|$  from some reciprocal lattice point  $(hkl)$  is proportional to  $J_1$  and

$$J_1 = \frac{N|F(hkl)|^2 e^{-2M}}{m} \phi \sum_{\alpha=1}^3 \cos^2(\theta(\vec{S}, \vec{e})) E(v(\vec{g}, \alpha)) / v^2(\vec{g}, \alpha) \quad , \quad (3-10)$$

where  $\vec{k} = 2\pi\vec{g}$ ,  $|\vec{g}| = 1/\Lambda$ ,  $\Lambda$  is the wavelength of the normal mode wave,  $\theta(\vec{S}, \vec{e})$  is the angle between  $\vec{S}$  and the polarization vector  $\vec{e}(\vec{g}, \alpha)$  and the other quantities in equation (3-10) have been defined earlier in Chapter II.

In a peak height measurement only that TDS which corresponds to points in reciprocal space that are in the immediate neighborhood of the relp under investigation is observed. Thus the following approximations were made:

1. The wave vectors,  $\vec{g}$  which contribute to TDS in the vicinity of a relp are relatively small and correspond to long wavelength normal modes. For these modes the dispersion curves are linear and pass through  $v(\vec{g}, \alpha) = |\vec{g}| = 0$ . It should be a good approximation to set  $v(\vec{g}, \alpha) = |\vec{g}|V_\alpha$ , where  $V_\alpha$  is the velocity of the waves in branch  $\alpha$  for  $|\vec{g}| \rightarrow 0$ .  $V_\alpha$  is determinable from measured elastic constants.

2.  $\cos^2(\theta(\vec{S}, \vec{e}))$  was replaced by an average value  $1/3$ , the value obtained when all possible orientations of  $\vec{e}$  with respect to  $\vec{S}$  occur with equal probability\*.

---

\*This assumption is discussed in Appendix A.

3. Since  $|\vec{g}|$  and, hence  $v(\vec{g}, \alpha)$ , is small, to a good approximation  $h\nu(\vec{g}, \alpha) \ll kT$ , and hence  $E(v(\vec{g}, \alpha)) \approx kT$  for temperature between  $100^\circ$  and  $300^\circ$  K.

With these assumptions  $J_1$  becomes

$$J_1 = \frac{N|F(hkl)|^2 e^{-2M}}{3m} \phi \quad kT \sum_{\alpha=1}^3 \frac{1}{v_\alpha^2} \left( \frac{1}{|\vec{g}|^2} \right) \quad (3-11)$$

The total one phonon scattering observed during a peak height measurement was then obtained by integration of the function  $|\vec{g}|^{-2} = g^{-2}$  throughout the region in reciprocal space "seen" by the detector. The size of this region is determined both by the size of the detector window and the maximum crossfire in the incident beam in the plane of incidence. This crossfire is determined by the sizes of both the sample and the x-ray target projection.

Actually, the integration of  $J_1$  is not as straightforward as just implied. The diffuse intensity will depend on the intensity incident on the crystal and, according to equation (3-11), on the number,  $N$ , of contributing unit cells in the crystal. Thus before the integration of  $J_1$  could be carried out, it was found necessary to determine a function  $w(\vec{g})$  which would weight each point in the reciprocal lattice seen by the counter according to (1) how much of the crystal volume could contribute to each point and (2) the point on the x-ray target from which the scattered ray originated. In general, the function  $w(\vec{g})$  depends on the sample shape and on the variation of illumination across the x-ray target.

The calculations of the TDS contributions for more complex cases, e.g. second order (or two phonon) scattering and/or two atoms per unit cell, were carried out in a manner similar to that just discussed. Third and higher order scattering processes were assumed negligible. Also the contribution of the optic modes to the diffuse scattering near the relps in KCl and AgCl was assumed negligible, although it may be significant farther away. The result obtained for the total intensity observed during a peak height measurement is given by the following equation,

$$I(\text{obs}) = I_0 (1 + \sigma T \mathcal{Q}_1 + (1/2) \sigma^2 T^2 \mathcal{Q}_2) \quad (3-12)$$

The first term is the intensity due to the true Bragg peak, the second term is the one phonon TDS intensity, and the third term is the two phonon TDS intensity.  $\mathcal{Q}_1$  and  $\mathcal{Q}_2$  are complicated functions of  $2\theta$  and of the sample size, x-ray target size, and counter window size (see Appendix A). The derivation of these functions required a knowledge of the sample shape and of the illumination variations across the x-ray target.  $T$  is the absolute temperature and  $\sigma$  for the monatomic cubic crystal is given by

$$\sigma = \frac{a^3 k}{3m} \sum_{\alpha=1}^3 \frac{1}{V_{\alpha}^2}, \quad (3-13)$$

where  $a$  is the lattice parameter,  $k$  is Boltzmann's constant,  $m$  is the mass of the atoms in the lattice, and  $V_{\alpha}$  is defined above. For KCl and

AgCl,  $m$  in equation (3-13) is replaced by  $m_1 + m_2$ . Calculations of  $\sigma$  for Al, KCl, and AgCl are described in Appendix A.

Experimental Verification of TDS Calculations. In order to test experimentally the validity of the intensity expressions derived in Appendix A, we made measurements of the intensity both on and  $1.5^\circ$  off (in  $\omega$ ) the (10,00) reflection of AgCl sample no. 18 at several temperatures. To eliminate the temperature dependence of  $I_0$  in equation (3-12), the quantity compared with theory was the ratio,  $R$ , of the peak intensity to the intensity observed  $1.5^\circ$  off the peak. Measurement of this ratio should also eliminate Compton scattering contributions since they are slowly varying functions of angle. One and one-half degrees was far enough from the actual diffraction peak so that it does not contribute significantly to the measured intensity but near enough so that a measurable amount of TDS was present. Since nearly all of the intensity above background at  $1.5^\circ$  off the peak is presumably due to TDS, comparisons of measured and calculated ratios,  $R$ , should provide a sensitive check of our TDS calculations. The background was measured  $5^\circ$  off the peak. Calculations of  $\mathcal{I}_1$  and  $\mathcal{I}_2$  on,  $1.5^\circ$  off, and  $5^\circ$  off the (10,00) peak of AgCl were made with equations (A-30), (A-31), (A-33), (A-38), (A-39), and (A-40) respectively and with the appropriate experimental parameters. We get

$$\text{ON PEAK: } \mathcal{I}_1 = 21.3 \times 10^6 \text{ cm}^{-1}, \quad \mathcal{I}_2 = 10.2 \times 10^{14} \text{ cm}^{-1}$$

$$1.5^\circ \text{ OFF PEAK: } \mathcal{I}_1 = 3.5 \times 10^6 \text{ cm}^{-1}, \quad \mathcal{I}_2 = 8.2 \times 10^{14} \text{ cm}^{-1}$$

$$5^\circ \text{ OFF PEAK: } \mathcal{I}_1 = 0.3 \times 10^6 \text{ cm}^{-1}, \quad \mathcal{I}_2 = 1.5 \times 10^{14} \text{ cm}^{-1}$$

With  $\sigma = 4.68 \times 10^{-27} \text{ cm}^3 \text{ O}_2 \text{ K}^{-1}$  and  $\phi = 0.91 \times 10^{16} \text{ cm}^{-2}$  one obtains, after subtracting background,

$$\text{ON PEAK:} \quad I = I_0(1 + 7.9T \times 10^{-4} + 6.4T^2 \times 10^{-7}) \quad (3-14)$$

$$1 \frac{1}{2}^\circ \text{ OFF PEAK:} \quad I = I_0(1.2T \times 10^{-4} + 4.8T^2 \times 10^{-7}) \quad (3-15)$$

The experimental results for R are compared with the calculations in Table 5.

Table 5. Comparison of Measured and Calculated TDS Contributions

$T(^{\circ}\text{K})$	$R(\text{calc})$	$R(\text{obs})$
88	71.4	$55 \pm 1$
185	30.8	$29.6 \pm 0.6$
301	16.5	$16.3 \pm 0.3$

The agreement is seen to be quite good except at  $88^\circ \text{ K}$ . This is probably due to the fact that no Bragg peak tail was included in the calculations of the "off peak" intensity. If as little as 0.4 percent of the Bragg peak intensity is assumed to contribute to the off peak intensity,  $R(\text{calc})$  at  $88^\circ \text{ K}$  is reduced to 56, at  $185^\circ \text{ K}$  to 28, and at  $301^\circ \text{ K}$  to 15.7, each of which is within 5 percent of the measured ratios. Other comparisons made of calculated ratios with those measured imply that if no Bragg peak tail contributes to the intensity  $1.5^\circ$  off the peak, the calculated TDS corrections are at most 15% too small. Such an error would produce approximately a 1 percent error in  $A_0$  because an error of  $y\%$  in the calculated TDS corrections produces less than  $0.1y\%$  error in  $A_0$ . Thus we conclude that equation (3-12) adequately represents the TDS contributions to the measured Bragg intensities in the present study.

It is of interest to point out how large the TDS contribution can get. At  $300^{\circ}$  K equation (3-14) yields the results that 19 percent of the measured Bragg peak intensity for the (10,00) of AgCl and the present experimental geometry is due to one-phonon scattering while 5 percent is due to two-phonon scattering. That is, roughly one-fourth of the measured intensity is due to TDS!

A<sub>TDS</sub>. From equations (3-6) and (3-12) one obtains,

$$A_{TDS} = \frac{-1/2(\sigma Q_1 + \sigma^2 Q_2 T \phi)}{1 + \sigma Q_1 T \phi + \sigma^2 Q_2 T^2 \phi^2 / 2} \quad (3-16)$$

The expressions obtained for  $Q_1$  and  $Q_2$  are rather complicated functions of  $2\theta$ . Thus rather than calculate  $A_{TDS}$  for each Bragg peak, it was calculated for only a few values of  $2\theta$  and then plotted against  $\phi$ .  $A_{TDS}$  for each Bragg peak was then obtained by interpolation. In Figure 15 are the results for Al and in Figure 16 are the results for both KCl and AgCl. The values of  $\sigma$  for AgCl and KCl are only 2 percent different. Thus one curve was used for both KCl and AgCl. The plots of  $A_{TDS}$  are shown only for  $T = 300^{\circ}$  K. It turns out that the temperature dependence of  $A_{TDS}$  is extremely small, e.g.  $A_{TDS}$  for Al, AgCl, and KCl changed less than 1/2 percent of the A values measured for these materials for a change in temperature from  $300^{\circ}$  to  $100^{\circ}$  K. Thus only the  $A_{TDS}$  versus  $\phi$  plot at  $300^{\circ}$  K was used to determine the TDS corrections to the A values discussed in Chapter IV.

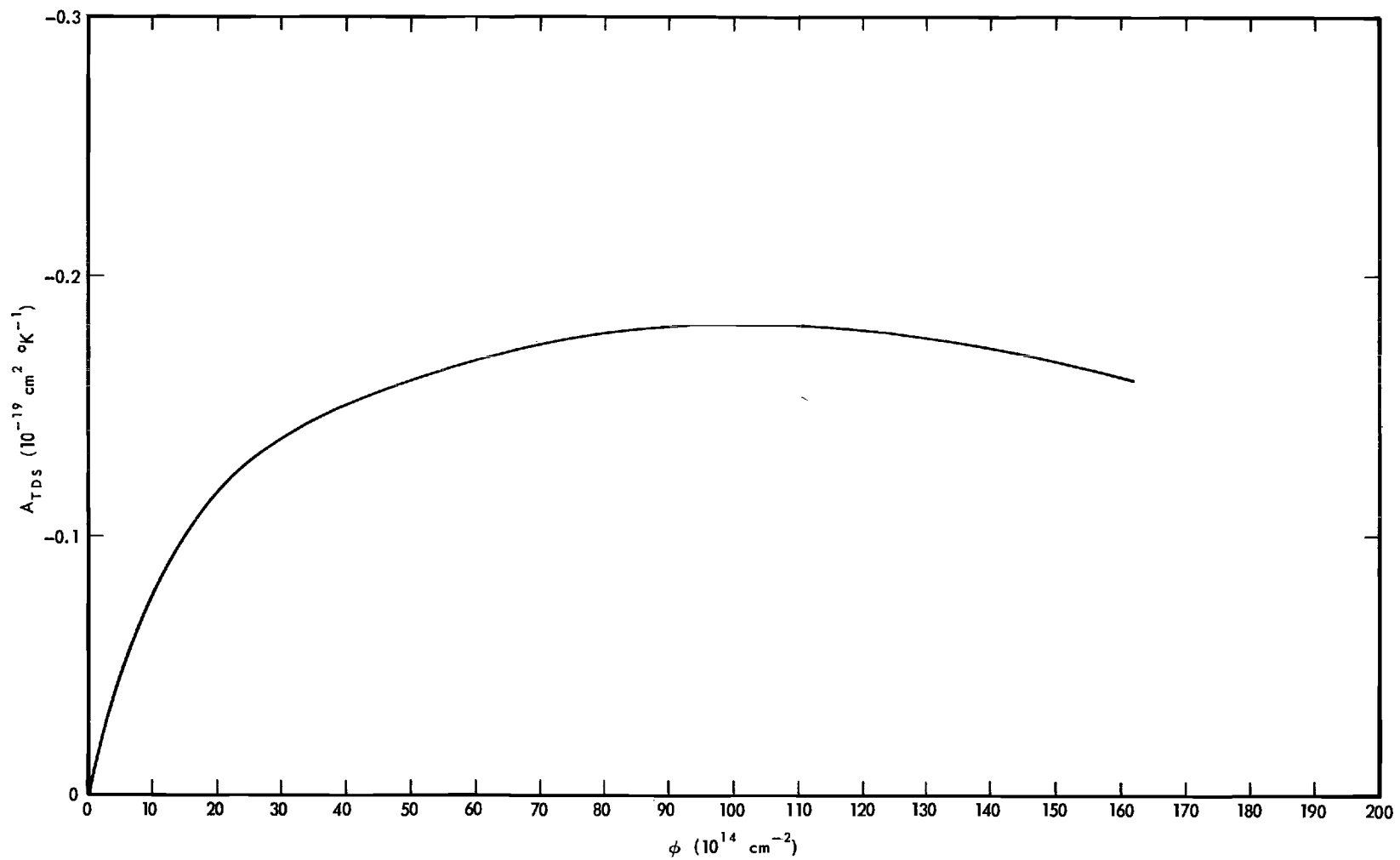


Figure 15. Dependence of  $A_{TDS}$  on  $\phi$  at 300°K for Al.

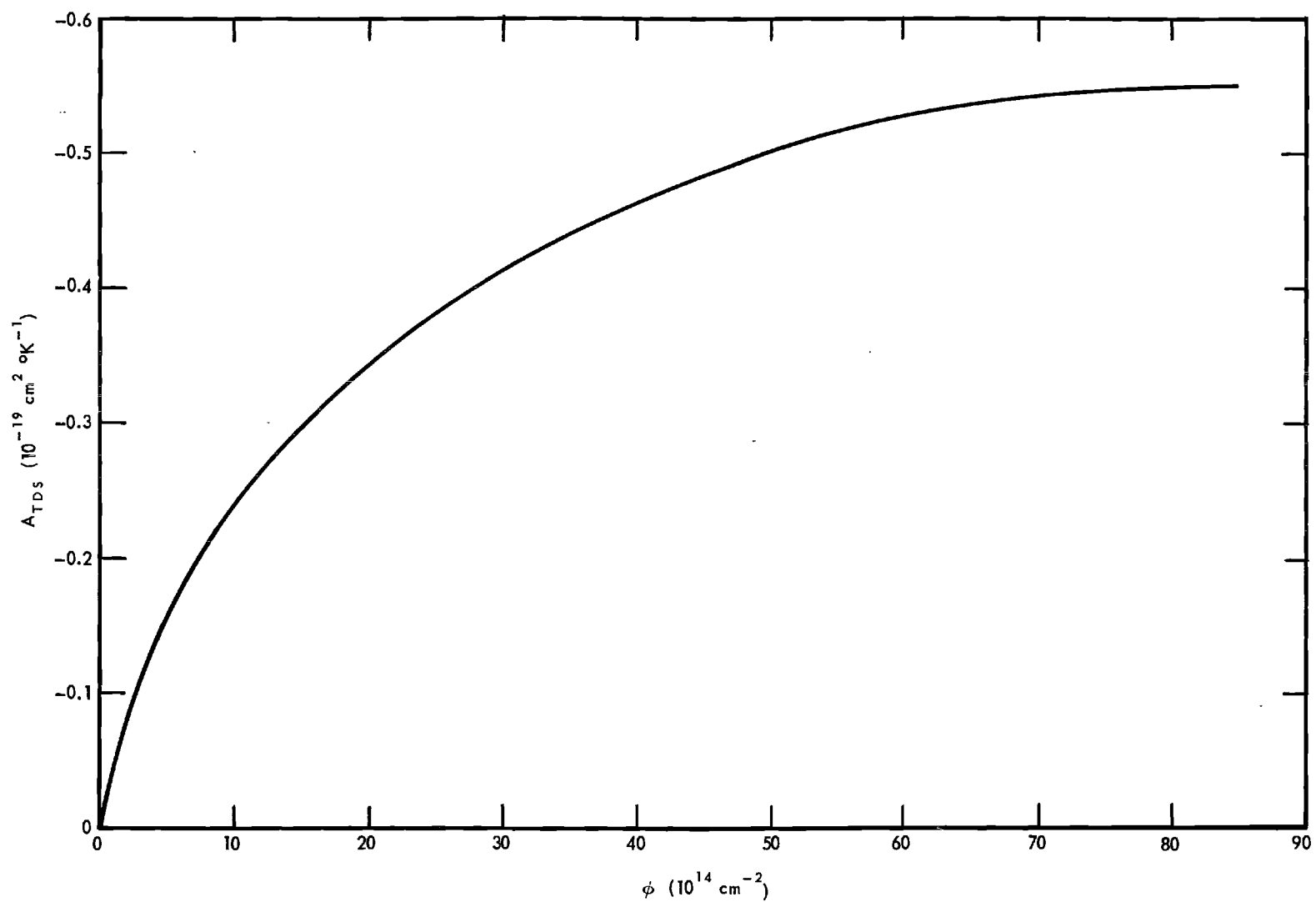


Figure 16. Dependence of  $A_{TDS}$  on  $\phi$  at  $300^{\circ}\text{K}$  for KCl and AgCl.



## CHAPTER IV

## RESULTS AND DISCUSSIONS

Some typical semilog plots of intensity versus temperature that were obtained in this work are shown in Figure 17. These data were obtained from the (h00) Bragg peaks of Al sample no. 2. The curves clearly show the expected trend with  $(hkl)$  due to the dependence of  $M$  on  $\sin^2\theta/\lambda^2$ . The non-linear dependence of  $\ln I$  on  $T$  is also apparent and agrees qualitatively with the predictions of equations (2-39) and (2-43) and the  $f(x)$  versus  $x$  plot in Figure 1. Such detail in the dependence of  $I$  on  $T$  would be completely overlooked if only the logarithm of the ratio of  $I$  at, say,  $300^\circ\text{K}$  to that at  $100^\circ\text{K}$  were determined as is often done. The scatter of the experimental points about the smooth lines drawn is small and indicates that the experimental methods used should allow meaningful determinations of the slope of  $\ln I$  versus  $T$ .

For each Bragg peak the intensity versus temperature data were plotted on a semilog scale as indicated in Figure 17. Graphically determined slopes were then used to calculate values for  $A$  at various temperatures with equation (3-1). No attempt was made to determine slopes by fitting the data with various functions or with polynomials of various degrees, with a high speed computer. It was felt that slopes so determined would be undesirably biased because of the lack of knowledge of the proper fitting function. In addition, the results of

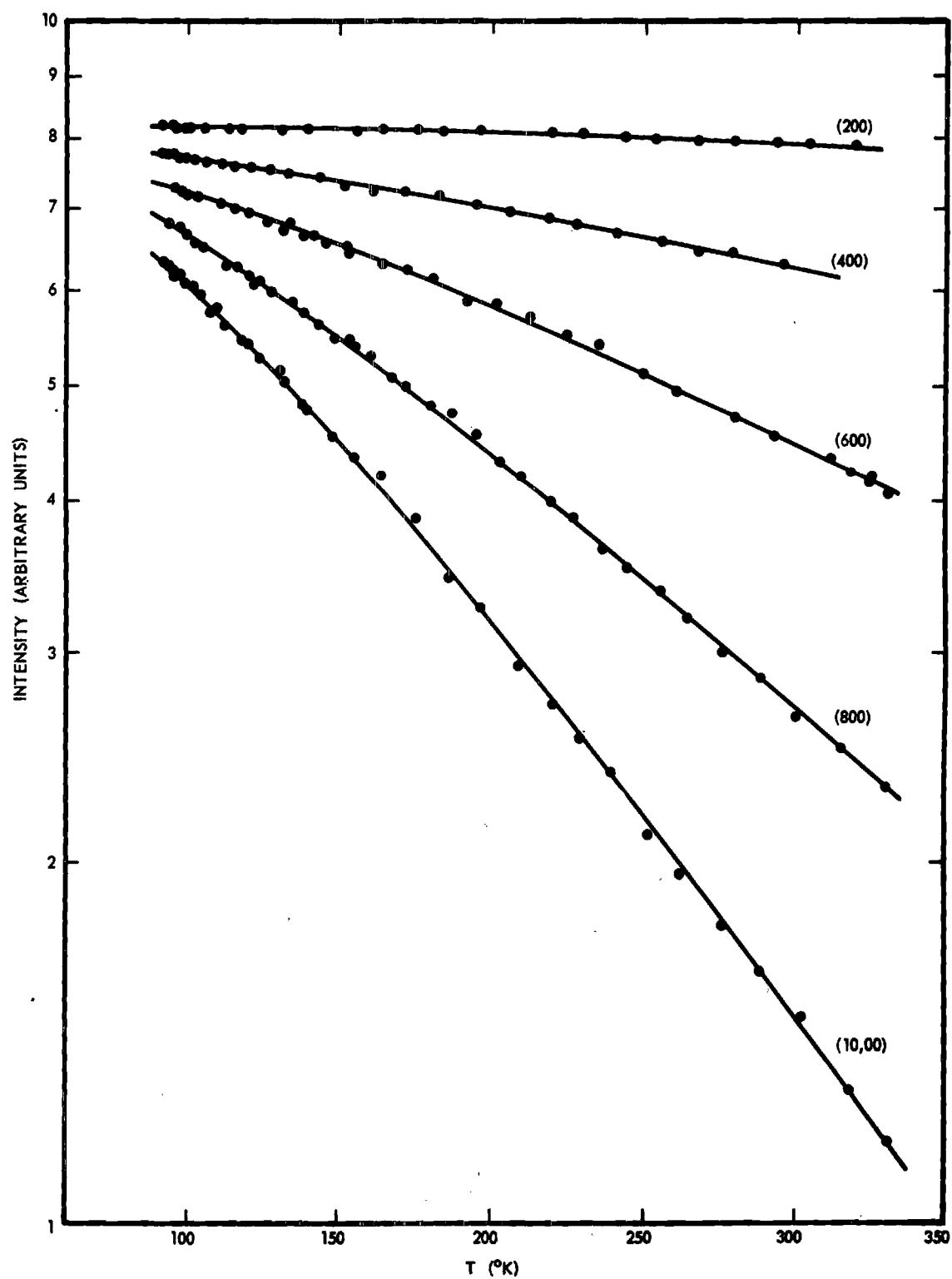


Figure 17. Dependence of Intensity on Temperature for  $(h00)$  Reflections of Aluminum Sample No. 2.

thermal expansion data which were obtained at the time of the present study<sup>25</sup>, indicated that graphically determined slopes were just as reliable as those obtained from polynomials. The results obtained for Al, KCl, and AgCl are conveniently discussed separately.

### Aluminum

The values for  $A$  determined at  $290^\circ$  K for the two Al samples used in the present study are shown plotted against  $\sin^2\theta/\lambda^2$  in Figure 18.  $A$  shows no significant variation with sample, crystallographic direction, or with angle except at small values of  $\sin^2\theta/\lambda^2$  where  $A$  decreases slightly as  $\sin^2\theta/\lambda^2$  decreases below  $25 \times 10^{14} \text{ cm}^{-2}$ . This decrease is expected and, as can be seen in Table 6, is accounted for by the  $A_{\text{LPF}}$  correction to  $A$  (also see Figure (12)). This correction varies from approximately 10 percent of  $A$  for the (220) reflection to less than 1/2 percent for the (10,00) reflection. The angular dependence of the TDS contribution,  $A_{\text{TDS}}$ , to  $A$  as shown in Figure 15 is much too small to be detected in the presence of the scatter of the data.  $A_{\text{TDS}}$  represents a significant correction, however, being between 4 and 7 percent of the  $A$  values in Figure 18.

Because of the lack of dependence on  $\sin^2\theta/\lambda^2$ , crystallographic direction, or sample,  $A_0$  at  $290^\circ$  K for Al was obtained by arithmetic averaging of the  $A_0$  values shown in Table 6 for each Bragg reflection. The mean deviation from the mean is 1.8 percent, indicating that data obtained from different Bragg reflections and different samples are in very good agreement.

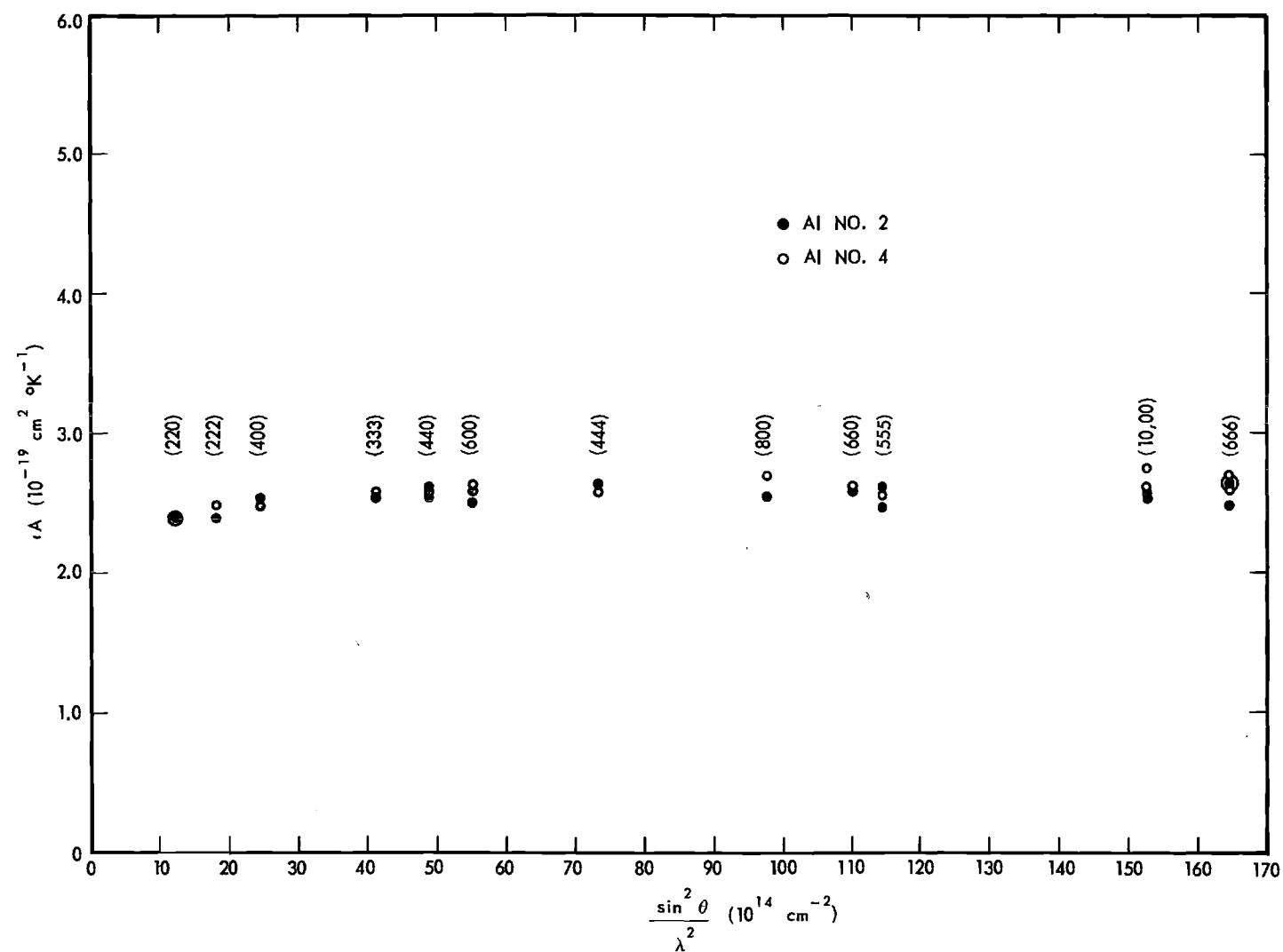


Figure 18. Dependence of A on  $\text{Sin}^2\theta/\lambda^2$  at 290°K for Al.

Table 6. Aluminum A Values and Corrections at 290° K

$$A_o = A - A_{LPf} - A_{TDS}$$

<u>hkl</u>	<u>Sample No.</u>	<u>A*</u>	<u>A<sub>LPf</sub></u>	<u>A<sub>TDS</sub></u>	<u>A<sub>o</sub></u>
220	2	2.40	-0.22	-0.10	2.72
	4	2.40	-0.22	-0.10	2.72
222	2	2.38	-0.17	-0.11	2.66
	4	2.48	-0.17	-0.11	2.72
400	2	2.53	-0.15	-0.12	2.80
	4	2.49	-0.15	-0.12	2.76
333	2	2.55	-0.11	-0.15	2.81
	4	2.57	-0.11	-0.15	2.83
440	2	2.56	-0.09	-0.15	2.80
	2	2.61	-0.09	-0.15	2.85
	4	2.58	-0.09	-0.15	2.82
	4	2.60	-0.08	-0.16	2.84
600	2	2.51	-0.08	-0.16	2.75
	4	2.58	-0.08	-0.16	2.82
	4	2.60	-0.08	-0.16	2.84
444	2	2.64	-0.06	-0.17	2.87
	4	2.58	-0.06	-0.17	2.81
800	2	2.55	-0.04	-0.17	2.76
	4	2.71	-0.04	-0.17	2.92
660	2	2.59	-0.02	-0.17	2.78
	4	2.63	-0.02	-0.17	2.82
555	2	2.47	-0.02	-0.17	2.66
	2	2.62	-0.02	-0.17	2.81
	4	2.56	-0.02	-0.17	2.75
10,00	2	2.54	+0.01	-0.15	2.68
	2	2.57	+0.01	-0.15	2.71
	4	2.75	+0.01	-0.15	2.89
	4	2.63	+0.01	-0.15	2.77
666	2	2.48	+0.02	-0.14	2.60
	2	2.64	+0.02	-0.14	2.76
	4	2.65	+0.02	-0.14	2.77
	4	2.63	+0.02	-0.14	2.75
	4	2.67	+0.02	-0.14	2.79

\*Units:  $10^{-19} \text{ cm}^2 \text{ } ^\circ\text{K}^{-1}$ 

Ave. = 2.78

Values for  $A$  for the Bragg peaks shown in Figure 18 were determined at  $240^\circ$ ,  $200^\circ$ ,  $160^\circ$ ,  $140^\circ$ ,  $120^\circ$ , and  $100^\circ$  K and are shown, along with the corrections  $A_{\text{TDS}}$  and  $A_{\text{LPf}}$ , in Tables 16 to 21 in Appendix D. At each temperature the dependence of  $A$  on  $\sin^2\theta/\lambda^2$ , sample, and crystallographic direction was as negligible as that indicated for  $290^\circ$  K in Figure 18. Thus, the  $A_0$  values obtained for different Bragg reflections were again arithmetically averaged at each temperature. The largest mean deviation from the mean obtained was 4 percent at  $100^\circ$  K. The  $A_0$  values obtained for Bragg reflections occurring at angles less than that for the (400) were not included in these averages. Although at  $290^\circ$  K the  $A$  values for these reflections show the expected trend with  $\sin^2\theta/\lambda^2$ , at lower temperatures these  $A_0$  values had considerable scatter because of the large errors in the measurement of the small slopes that these reflections have (compare, for instance, the slope for the (200) reflection in Figure 17 with that of the other reflections).

In order to compare these results with theory and with the results obtained from other experimental techniques, a Debye  $\Theta$  at each of the above temperatures was calculated from  $A_0$  with equations (3-7) and (2-43). The values used for the thermal coefficient of expansion,  $\beta$ , and the Grüneisen constant,  $\gamma$ , were those measured at the time of the present study<sup>31</sup>. The results obtained are shown in Figure 19 along with the results obtained by Sutton<sup>42</sup> from elastic constant measurements, by Chipman<sup>8</sup> from x-ray measurements, and by Walker<sup>11</sup> from the specific heat measurements of Giauque and Meads<sup>43</sup>. As can be seen, our results for  $\Theta(\text{x-ray})$  agree in most respects with those of Chipman in the  $100^\circ$  to  $300^\circ$  K temperature range. However, our results do show more detail in the dependence of  $\Theta(\text{x-ray})$  on temperature than do Chipman's.

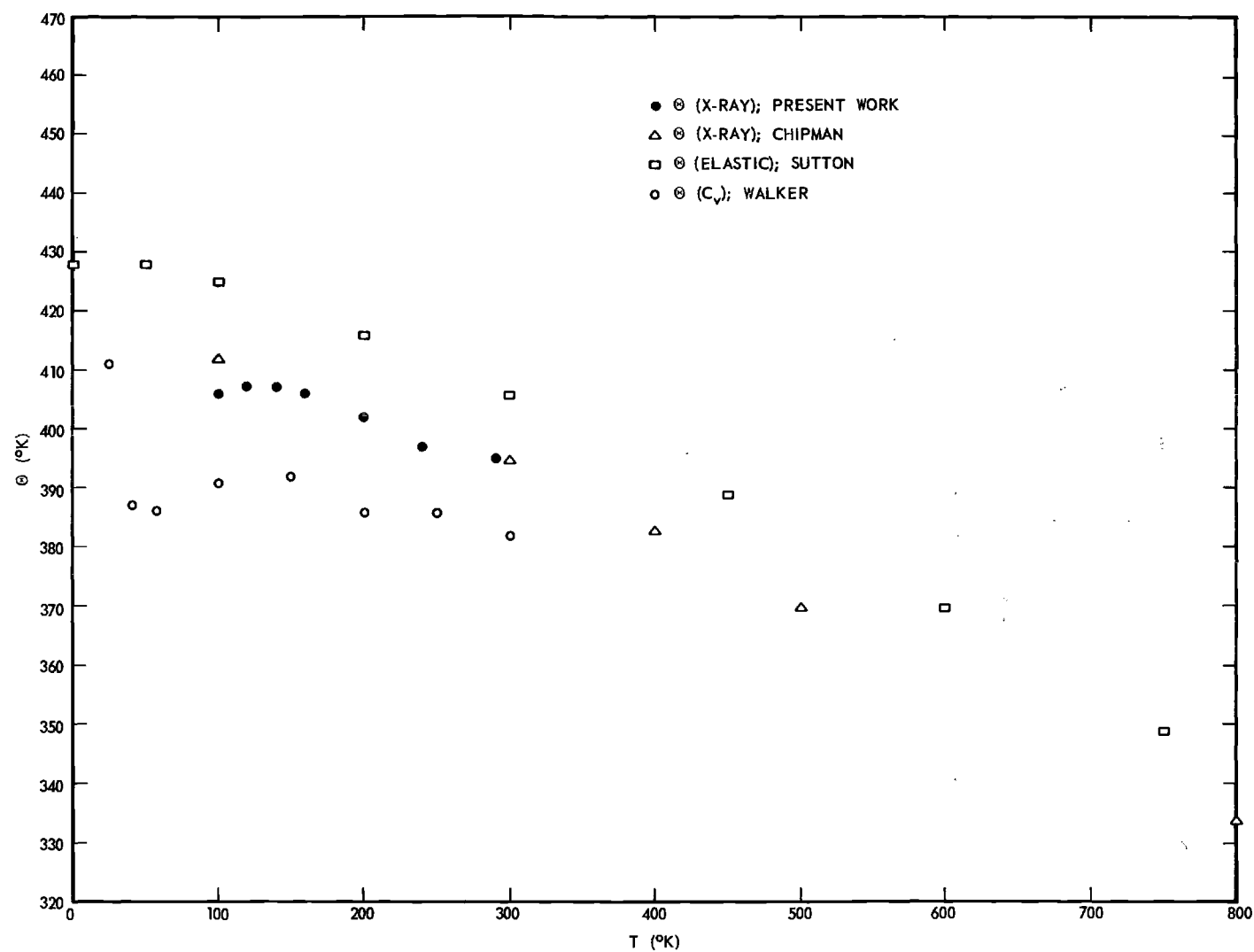


Figure 19. Dependence of Aluminum Debye  $\theta$  on Temperature.

As discussed earlier, the temperature dependence of  $\Theta(\text{x-ray})$  can be due both to anharmonic effects and to the differences between the true vibrational spectrum and the Debye parabolic approximation. In an attempt to separate these contributions to the measured  $\Theta(\text{x-ray})$  versus  $T$  results for Al, we have used the actual vibrational spectrum for Al, determined by Walker<sup>11</sup> from TDS measurements, to calculate  $(\partial B/\partial T)_V$  with equation (2-42) and a Burroughs 220 computer. These calculations are described in Appendix B where the vibrational spectrum can also be found. The resulting  $\Theta(\text{x-ray})$  versus  $T$  curve obtained from these machine calculations by iteration with equation (2-46) is shown in Figure 20 as a dot-dashed line along with our measurements. Two observations of special note can be made: (1) the calculated  $\Theta(\text{x-ray})$  versus temperature curve is essentially independent of temperature above 100° K, and (2) the magnitudes of the calculated  $\Theta$ 's are significantly smaller than those measured.

No anharmonic contributions have been included in the calculations of  $(\partial B/\partial T)_V$  and thus one might presume that the differences found between the calculated and measured sets of  $\Theta$ 's are due to anharmonic effects. Apart from the detail in the measured temperature dependence of  $\Theta(\text{x-ray})$ , the actual temperature dependence observed is larger than can be accounted for with the values used for  $\gamma$  and  $\beta$  and equation (2-32). By increasing the value of  $\gamma$ , or by assuming that there are additional anharmonic terms in the measured  $dM/dT$ , it was found that one could account for the magnitude of the measured temperature dependence of  $\Theta(\text{x-ray})$ . However, the detail in the temperature dependence still remained unaccounted for and it was not found possible for one to explain, in this manner, the differences obtained in the absolute magnitudes of the measured and calculated  $\Theta$ 's.



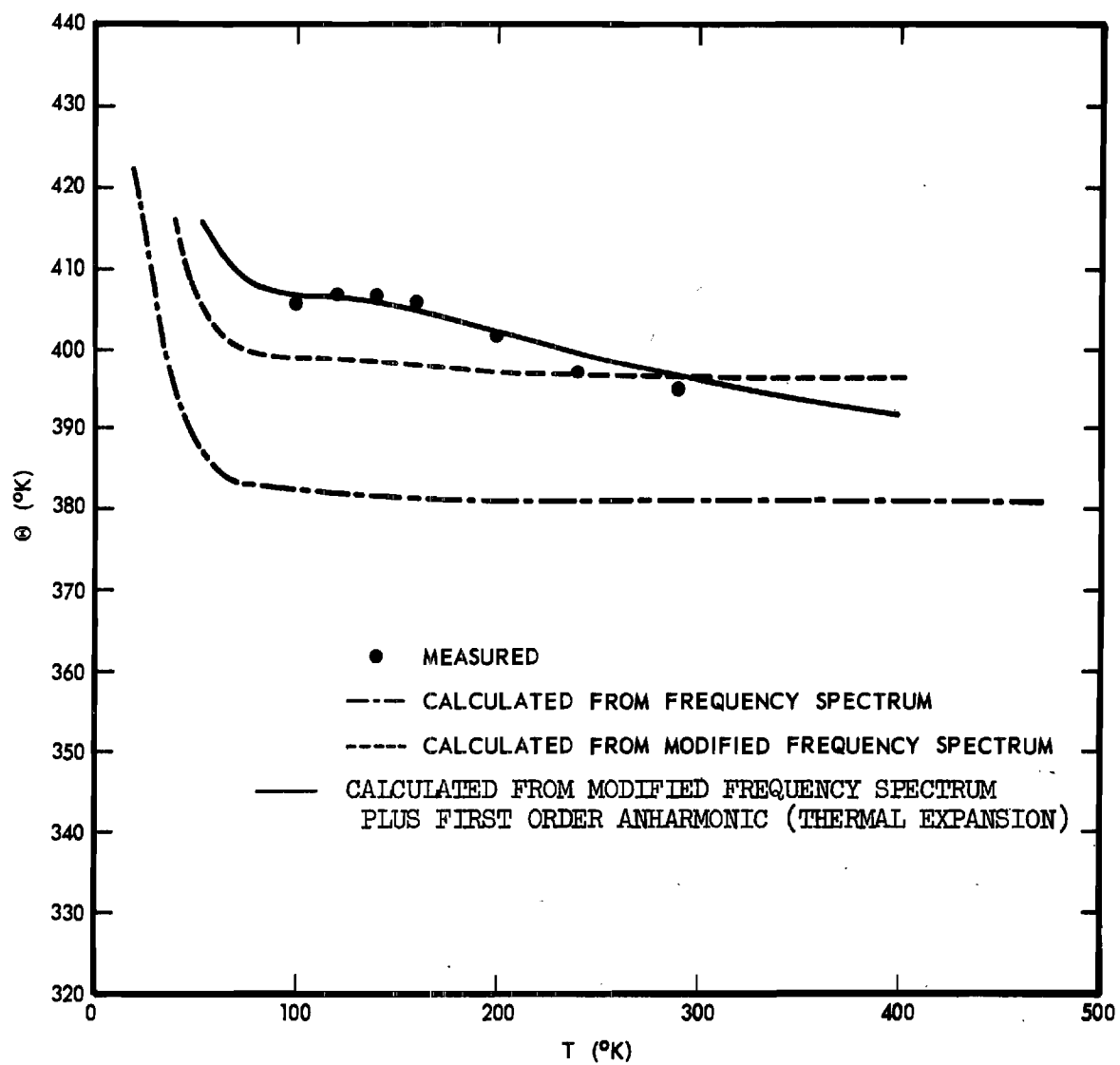


Figure 20. Comparison of Calculated and Measured Values of  $\Theta$  (x-ray) for Al.

It was therefore concluded that the source of the disagreement must lie in errors in the original data, in the subsequent corrections applied to them, or in the vibrational spectrum used. The actual measurements seem to be in good shape in view of the very good agreement obtained between  $A_0$  values determined from completely independent data obtained from different Bragg reflections and different samples. While it is always possible in principle that our TDS corrections are badly in error\*, it seems unlikely since good agreement between the calculated and measured TDS contributions to the (10,00) Bragg reflection of AgCl was obtained as discussed in Chapter III. We were thus impelled to look for errors of the size of a few percent in Walker's vibrational spectrum; presumably at low frequencies since these are the frequencies to which our type of x-ray measurements are most sensitive.

To expect such errors even in such superb work as Walker's is not unreasonable in view of the large corrections which must be applied to the original TDS measurements before the spectrum can be determined from them<sup>11</sup>. In addition, the spectrum is approximate in the sense that some force-law model must be assumed before the spectrum can be calculated even from the corrected TDS measurements. Fortunately, the thermal vibrations of Al have also been studied by Brockhouse and Stewart<sup>12</sup> by means of the inelastic scattering of cold neutrons. Although a vibrational spectrum was not determined from the neutron data, it was possible to compare the dispersion curves obtained by Brockhouse and Stewart with those obtained by Walker. Such a comparison revealed that for the

---

\*As stated in Chapter III, the TDS corrections are possibly 15% too small at most. Such an error would make  $A_0$  for Al approximately 1% too small and hence,  $\Theta$ (x-ray), one-half percent too large, whereas nearly a 4% reduction in the observed  $\Theta$ (x-ray) at 290°K is needed to bring it into agreement with that calculated.

[110] direction, the dispersion curves obtained from the neutron measurements for the transverse branch were about 10 percent higher in frequency than the corresponding curves obtained from the x-ray measurements. Since no large corrections need to be applied to the neutron data, such as those which were applied to the x-ray data, it is likely that the dispersion curves obtained from the neutron data are the more reliable and that the part of the vibrational spectrum which corresponds to the transverse branch needs to be stretched somewhat to higher frequencies. Such a change in the spectrum should have a pronounced effect on the calculated values of  $(\partial B / \partial T)_V$  since, as indicated by the histogram of the vibrational spectrum shown in Appendix B, the shape of the low frequency part of the spectrum is almost entirely determined by the transverse branch.

To determine what effect stretching the transverse branch to higher frequencies has on  $(\partial B / \partial T)_V$  and the resulting  $\Theta(\text{x-ray})$  versus  $T$  curve, we recalculated  $(\partial B / \partial T)_V$ , using the Burroughs 220 computer as before, with all the frequencies of the transverse branch of the spectrum increased by 5 percent. The 5 percent increase seemed consistent with the 10 percent difference between the [110] dispersion curves mentioned earlier, because the spectrum is an average over all directions in a solid and because 6, the multiplicity of the [110] direction, is roughly the same as 7, the sum of the multiplicities of the [100] and [111] directions, the other directions for which dispersion curves were obtained. Other details of the calculation are discussed in Appendix B.

The resulting  $\Theta(\text{x-ray})$  versus temperature curve obtained from these calculations by iteration with equation (2-46) is shown as a dotted line in Figure 20. As discussed earlier in Chapter III, the normal mode frequencies may depend on volume as shown in equation (2-32). Inclusion of that dependence of the normal mode frequencies on volume<sup>\*</sup> in these calculations yields the  $\Theta(\text{x-ray})$  versus temperature curve shown as a full line in Figure 20. The agreement between this line and the experimental  $\Theta$  versus temperature results is seen to be quite good. The small differences which remain are well within experimental error. Thus, the temperature dependence of the x-ray Debye  $\Theta$  is well accounted for by the modified vibrational spectrum and by the volume dependence of the normal mode frequencies in the 100° to 300° K temperature range. In addition, we conclude that the intensity versus temperature technique employed here provides a good method for the examination of something of the character of the low and intermediate frequency portion of the vibrational spectrum.

Had x-ray measurements been made by us at higher temperatures, it is likely that anharmonic contributions in addition to thermal expansion would have become significant in view of the strong temperature dependence of  $\Theta(\text{x-ray})$  found by Chipman<sup>8</sup>. It is noteworthy that the x-ray

---

\* This volume dependence was included by application in reverse of the method suggested earlier in the "moments expansion" discussion for the elimination of the thermal expansion contributions to an experimental  $(\partial B/\partial T)_V$ . That is, the value of  $(\partial B/\partial T)_V$  calculated for a temperature  $T$  was changed to  $(V_T/V_0)^{2\gamma} (\partial B/\partial T)_V$  and  $T$  was changed to  $T' = T(V_T/V_0)^{-\gamma}$ . The reference temperature,  $T_0$ , used with equation (2-32) was 290° K.

values for  $\Theta$  obtained by us and by Chipman are slightly less than those obtained from elastic constant measurements, as expected. The fact that  $\Theta(C_v) < \Theta(\text{x-ray})$  indicates that there is not a high density\* of high frequencies in the spectrum of Al.

### Potassium Chloride

The values for  $A$  determined at  $290^\circ \text{K}$  from the KCl samples used in this study are shown plotted against  $\sin^2 \Theta / \lambda^2$  in Figure 21. As for Al,  $A$  shows no significant variation with sample, crystallographic direction, or with angle except at the smaller values of  $\sin^2 \Theta / \lambda^2$ .  $A_0$  at  $290^\circ \text{K}$  was therefore obtained by arithmetic averaging of the  $A_0$  values obtained for each Bragg reflection (except those which occur at angles less than that for the (400)) after applying to  $A$  the  $A_{\text{LPf}}$  and  $A_{\text{TDS}}$  corrections shown in Table 7. The mean deviation from the mean is 2.1 percent, again indicating that good agreement was obtained between data obtained from different Bragg reflections and different samples. It should be pointed out that since the mass of the  $\text{K}^+$  ion is nearly the same as that for the  $\text{Cl}^-$  ion, and since both ions are isoelectronic, we have assumed that  $\Delta B$  and  $\Delta B'$  are zero\*\*. Attempts to obtain intensity versus temperature data from Bragg reflections having all odd Miller indices failed. Since  $f_1 \approx f_2$  for KCl, the intensities of these reflections were so weak that no meaningful data could be obtained.

---

\*That is, in comparison to what would be expected from a parabolic extrapolation based on the low frequency part of the spectrum.

\*\* Isothermal x-ray measurements made by Wasastjerna<sup>44</sup> indicate that  $B_{\text{K}}$  and  $B_{\text{Cl}}$  differ by only 4 percent.

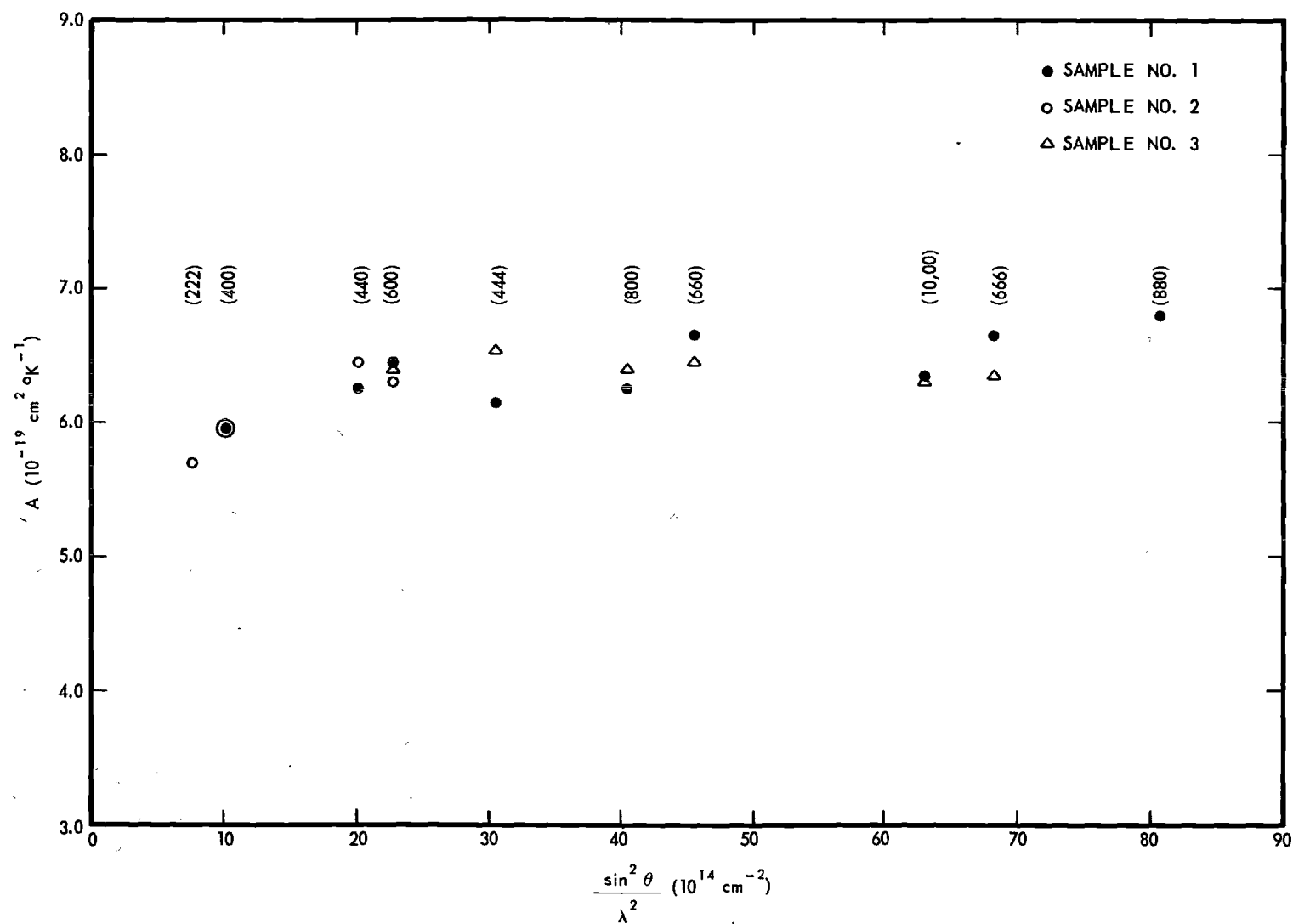


Figure 21. Dependence of A on  $\sin^2 \theta / \lambda^2$  at  $290^\circ\text{K}$  for KCl.

Table 7. Potassium Chloride A Values and Corrections at 290° K

$$A_o = A - A_{LPF} - A_{TDS}$$

<u>hkl</u>	<u>Sample No.</u>	<u>A*</u>	<u>A<sub>LPF</sub></u>	<u>A<sub>TDS</sub></u>	<u>A<sub>o</sub></u>
222	2	5.70	-0.59	-0.23	6.52
400	1	5.95	-0.44	-0.26	6.65
	2	5.95	-0.44	-0.26	6.65
440	1	6.25	-0.22	-0.35	6.82
	2	6.45	-0.22	-0.35	7.02
600	1	6.45	-0.20	-0.37	7.02
	2	6.30	-0.20	-0.37	6.87
	3	6.40	-0.20	-0.37	6.97
444	1	6.15	-0.16	-0.41	6.72
	3	6.55	-0.16	-0.41	7.12
800	1	6.25	-0.13	-0.46	6.84
	3	6.40	-0.13	-0.46	6.99
660	1	6.65	-0.11	-0.48	7.24
	3	6.45	-0.11	-0.48	7.04
10,00	1	6.35	-0.09	-0.53	6.97
	3	6.30	-0.09	-0.53	6.92
666	1	6.65	-0.08	-0.54	7.27
	3	6.35	-0.08	-0.54	6.97
880	1	6.80	-0.07	-0.54	7.41

\* Units:  $10^{-19} \text{ cm}^2 \text{ o}_K^{-1}$

Ave. = 6.98

Values for  $A$  and  $A_0$  for the Bragg peaks shown in Figure 21 were also determined at  $240^\circ$ ,  $200^\circ$ ,  $160^\circ$ ,  $140^\circ$ , and  $120^\circ$  K and are shown, along with  $A_{\text{TDS}}$  and  $A_{\text{LPF}}$ , in tables 22 to 26 in Appendix E. The  $A_0$  values obtained for different Bragg peaks were arithmetically averaged at each temperature. The largest mean deviation from the mean obtained was 3.8 percent at  $120^\circ$  K.

At each of the above temperatures, a Debye  $\Theta$  was determined from the measured  $A_0$  values by iterative calculations with equations (3-7) and (2-43). The values used for the thermal coefficient of expansion,  $\beta$ , and the Grüneisen constant,  $\gamma$ , were those measured by R. Srinivasan<sup>45</sup>. The results we obtained are shown in Figure 22 along with the results obtained from elastic constant measurements, from specific heat measurements, and from other x-ray measurements reported in the literature<sup>5</sup>.

The values for  $\Theta(\text{x-ray})$  obtained from our data decrease as the temperature increases. Above  $200^\circ$  K this decrease is well accounted for by thermal expansion contributions to  $\Theta$  (see equation (2-32)). However, below  $200^\circ$  K a small amount of temperature dependence still remains after the application of corrections to  $\Theta$  for thermal expansion modifications of the normal mode frequencies. Since anharmonic contributions are not expected to increase as the temperature is decreased, the observed temperature dependence of  $\Theta(\text{x-ray})$  is probably due to the differences between the true vibrational spectrum and the Debye approximation. (Recall that a similar result was obtained for Al.)

The  $\Theta(\text{x-ray})$  values for KCl seem to be tending toward  $\Theta(\text{elastic})$  determined at  $0^\circ$  K as one would expect. The elastic constant values for



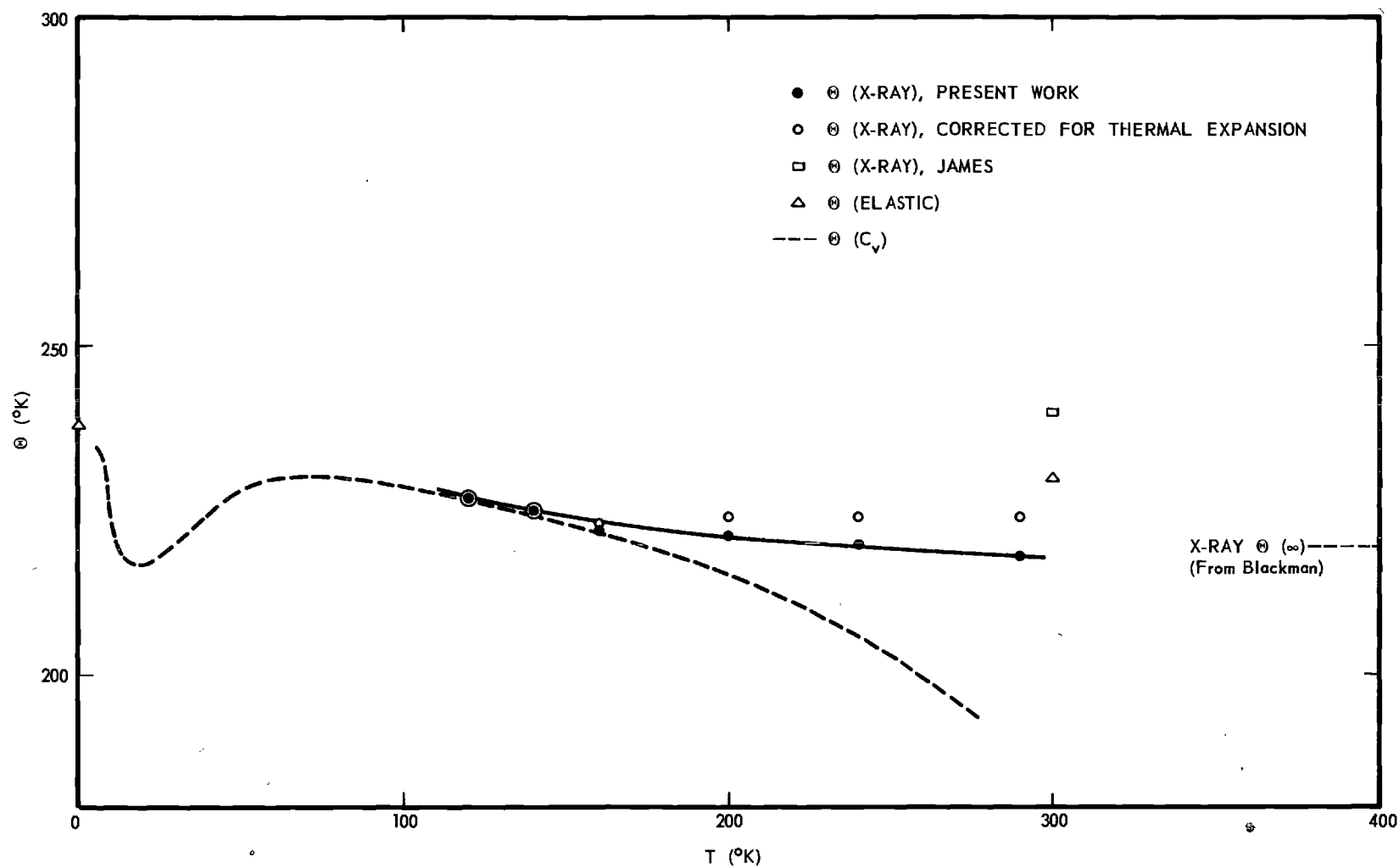


Figure 22. Dependence of Potassium Chloride Debye  $\theta$  on Temperature.

$\Theta$  are those quoted by Blackman<sup>19</sup> for room temperature and by Barron, et al<sup>13</sup>, for 0° K. As expected the value at room temperature ( $\sim 300^\circ$  K) is a little larger than our x-ray values. It is interesting to note that the  $\Theta(\text{x-ray})$  value obtained by James is larger than  $\Theta(\text{elastic})$ . Blackman<sup>19</sup> has pointed out that this does not agree with theory. Our data remove this discrepancy, presumably due to the fact that we have made corrections for TDS while James<sup>5</sup> did not. Such corrections always reduce the measured x-ray values for the Debye  $\Theta$  below the incorrect values, even though the TDS corrections do enter differently for the two x-ray methods.

The specific heat values for  $\Theta$  agree with the x-ray measurements just above  $120^\circ$  K. However, they fall off fairly rapidly as the temperature is increased. This rapid decrease of  $\Theta(C_v)$  with increasing temperature has been interpreted by Barron, et al<sup>13</sup>, as being due to anharmonic effects. It is interesting, therefore, that the  $\Theta(\text{x-ray})$  values do not show the same decrease. This may well be due to the fact that the anharmonic terms (other than thermal expansion) which apply to  $M$  do not have the same dependence on the third and fourth order derivatives of the potential energy (see equations (2-34) and (2-35)) as do those which apply to specific heats (compare reference 23 with Leibfried and Ludwig<sup>22</sup>). Therefore, comparisons of high temperature Debye  $\Theta$ 's obtained from specific heat with those obtained from x-ray measurements may provide a useful technique for the examination of anharmonicity.

The high temperature value shown for the  $\Theta(\text{x-ray})$ ,  $\Theta(\infty)$ , was calculated by Blackman from the vibrational spectrum calculated by Iona<sup>46</sup>. As can be seen in Figure 22 the values for  $\Theta(\text{x-ray})$  obtained from our data above  $200^\circ$  K agree quite well with this calculated value.

### Silver Chloride

The values for  $A$  determined at  $290^\circ \text{K}$  for the  $\text{AgCl}$  samples used in this study are shown in Table 8 along with  $A_o$  and the corrections  $A_{\text{LPf}}$  and  $A_{\text{TDS}}$ . A plot of  $A_o$  versus  $\sin^2\theta/\lambda^2$  is shown in Figure 23.  $A_o$  shows no significant variation with crystallographic direction or sample. In addition to the (333) Bragg reflection, data were also obtained from the (113), (331), (115), and (551) Bragg reflections of sample no. 18 in order to verify the result that  $A_o(\text{odd})$  is definitely larger than  $A_o(\text{even})$ . The (555) Bragg reflections were too low in intensity to allow the collection of meaningful intensity versus temperature data for them. Also the slopes of the intensity versus temperature data obtained from the (111), (200), and (220) Bragg reflections were too small to permit a meaningful determination of  $A$  for them.

According to the earlier discussion (pages 50-55) pertaining to the characteristic features of an  $A_o$  versus  $\phi$  ( $\phi = \sin^2\theta/\lambda^2$ ) plot for an  $\text{NaCl}$  type structure, the general features of the plot in Figure 23 indicate that  $\Delta B'$  and probably  $\Delta B$  are negative, i.e.  $B'_{\text{Ag}} > B'_{\text{Cl}}$  and  $B_{\text{Ag}} > B_{\text{Cl}}$ . That is, since  $A_o(\text{odd})$  is larger than  $A_o(\text{even})$ ,  $\Delta B'$  must be negative (see Figures 2 and 3 and equation (2-79)). Note that Figure 23 agrees qualitatively with the portion of Figure 3 near  $\phi = 0$  for  $\Delta B < 0$  and  $\phi < 1$ . The small increase of  $A_o(\text{odd})$  with increasing  $\phi$  indicates that  $\Delta B$  may also be negative. However, the observed increase is small and not on statistically firm ground in view of the small range in  $\phi$  over which data were obtained and in view of the small number of data obtained from Bragg reflections, other than the (333), having odd Miller indices. At least there is no strong indication that

Table 8. Silver Chloride A Values and Corrections at 290° K

$$A_o = A - A_{LPf} - A_{TDS}$$

<u>Even hkl</u>	<u>Sample No.</u>	<u>A*</u>	<u>A<sub>LPf</sub></u>	<u>A<sub>TDS</sub></u>	<u>A<sub>o</sub></u>
222	7	9.20	-0.36	-0.25	9.81
	17	9.00	-0.36	-0.25	9.61
400	7	9.15	-0.28	-0.29	9.72
	11	9.20	-0.28	-0.29	9.77
	17	9.35	-0.28	-0.29	8.92
440	7	9.00	-0.15	-0.39	9.54
	11	9.45	-0.15	-0.39	9.99
	17	9.40	-0.15	-0.39	9.94
	18	8.95	-0.15	-0.39	9.49
	18	8.65	-0.15	-0.39	9.19
600	7	8.95	-0.14	-0.40	9.49
	11	8.75	-0.14	-0.40	9.29
	17	8.55	-0.14	-0.40	9.09
444	17	9.15	-0.11	-0.46	9.72
	18	9.05	-0.11	-0.46	9.62
800	7	9.00	-0.08	-0.51	9.59
	17	8.75	-0.08	-0.51	9.34
660	17	9.30	-0.07	-0.52	9.89
	18	10.1	-0.07	-0.52	10.7
10,00	17	8.70	-0.05	-0.55	9.30
	18	9.75	-0.05	-0.55	10.4
	18	9.90	-0.05	-0.55	10.5

\*Units:  $10^{-19} \text{ cm}^2 \text{ o}_K^{-1}$

Ave. = 9.69

(Table continued on next page)

Table 8. Silver Chloride A Values and Corrections at 290° K (Continued)

<u>Odd hkl</u>	<u>Sample No.</u>	<u>A*</u>	<u>A<sub>LPf</sub></u>	<u>A<sub>TDS</sub></u>	<u>A<sub>O</sub></u>
113	18	10.2	-0.39	-0.24	10.8
331	18	10.3	-0.24	-0.31	10.9
	18	10.2	-0.24	-0.31	10.8
115	18	11.0	-0.17	-0.36	11.5
333	7	10.7	-0.17	-0.36	11.2
	11	10.9	-0.17	-0.36	11.4
	17	10.9	-0.17	-0.36	11.4
	18	10.6	-0.17	-0.36	11.1
551	18	11.1	-0.10	-0.47	11.7
	18	11.1	-0.10	-0.47	11.7

\*Units:  $10^{-19} \text{ cm}^2 \text{ } ^\circ\text{K}^{-1}$

Ave. = 11.3

Ave of (115) and (333) = 11.3

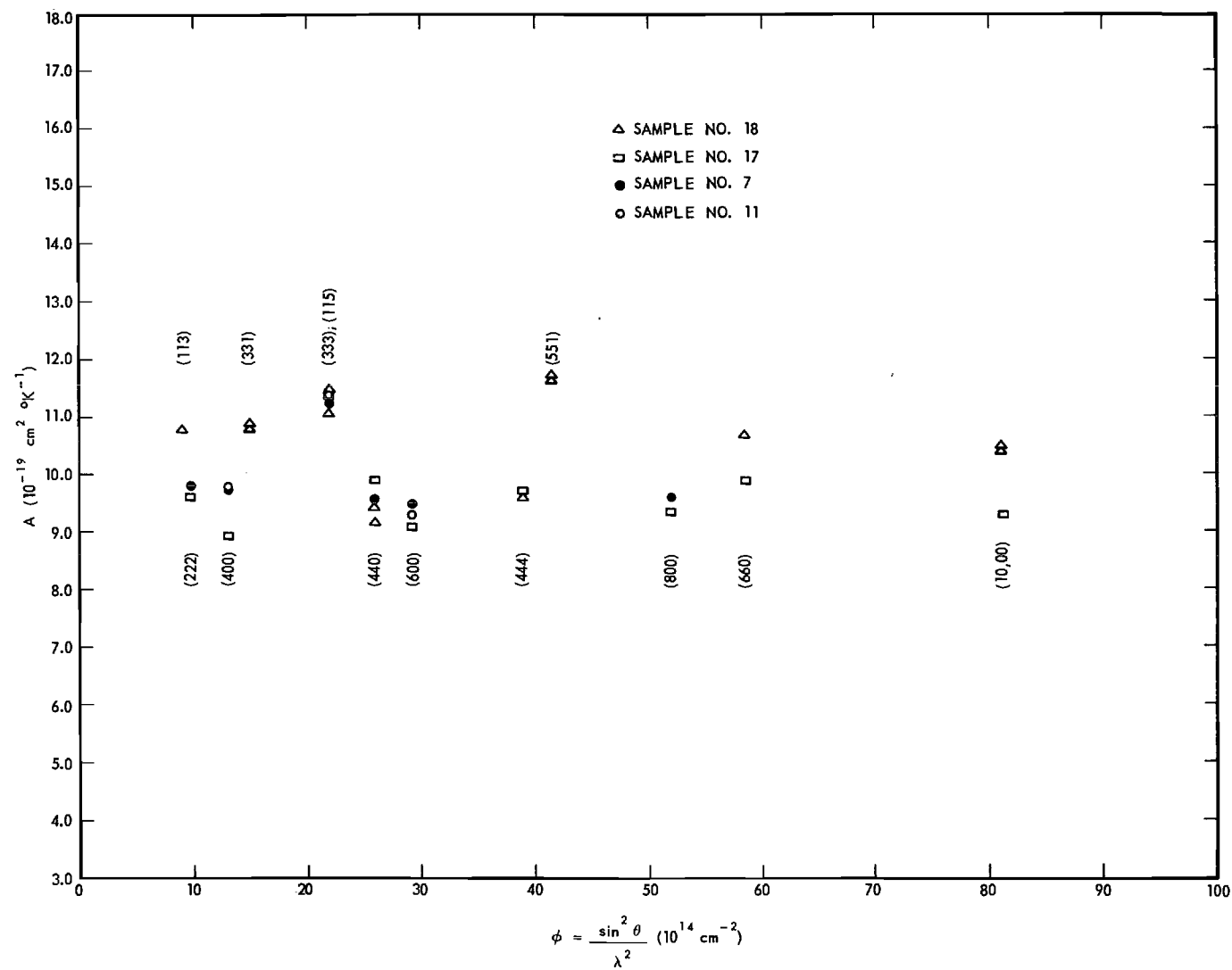


Figure 23. Dependence of  $A_0$  on  $\sin^2 \theta / \lambda^2$  at  $290^\circ \text{K}$  for  $\text{AgCl}$ .

$\Delta B$  is positive. The lack of  $\phi$  dependence for  $A_o(\text{even})$  is probably due to the fact that  $\Delta B'$  and  $\Delta B$  are small. For instance, from Figures 2 and 3, as  $\Delta B'$  gets small so does the slope of the  $A_o$  versus  $\phi$  plot except near the singularity points. Also according to these figures,  $A_o(\text{odd})$  may show a stronger dependence on  $\phi$  than  $A_o(\text{even})$ . This of course will depend on the size of  $\Delta B$  and the relationship of  $\phi = (\ln f)/(\Delta B)$  to the observable range of  $\phi$ . We are therefore led to the interesting conclusion that the vibrational amplitude of the  $\text{Ag}^+$  ion is larger than that for the  $\text{Cl}^-$  ion in  $\text{AgCl}$ .

To provide additional experimental evidence on the relative sizes of  $B_{\text{Ag}}$  and  $B_{\text{Cl}}$ , we made room temperature measurements of the integrated intensities of several Bragg reflections of  $\text{AgCl}$  sample no. 18. According to equation (2-76) the observed integrated intensity,  $I(\text{obs})$ , is proportional to  $|F(\text{obs})|^2$ , where

$$|F(\text{obs})| = |f_{\text{Ag}} e^{-B_{\text{Ag}}\phi} \pm f_{\text{Cl}} e^{-B_{\text{Cl}}\phi}| \quad (4-1)$$

If  $B_{\text{Ag}} > B_{\text{Cl}}$ , the relative decrease, with increasing  $\phi$ , of the first term in equation (4-1) is more than that of the second term. In this case values of  $|F(\text{obs})|/|F(\text{Cal})|$ , where  $|F(\text{Cal})| = |f_{\text{Ag}} \pm f_{\text{Cl}}|$ , for reflections having all odd Miller indices should decrease more with increasing  $\phi$  than those for reflections having all even Miller indices. Figure 24 shows the results obtained. As is seen these results are consistent with  $B_{\text{Ag}} > B_{\text{Cl}}$  and hence are in qualitative agreement with the intensity versus temperature results.

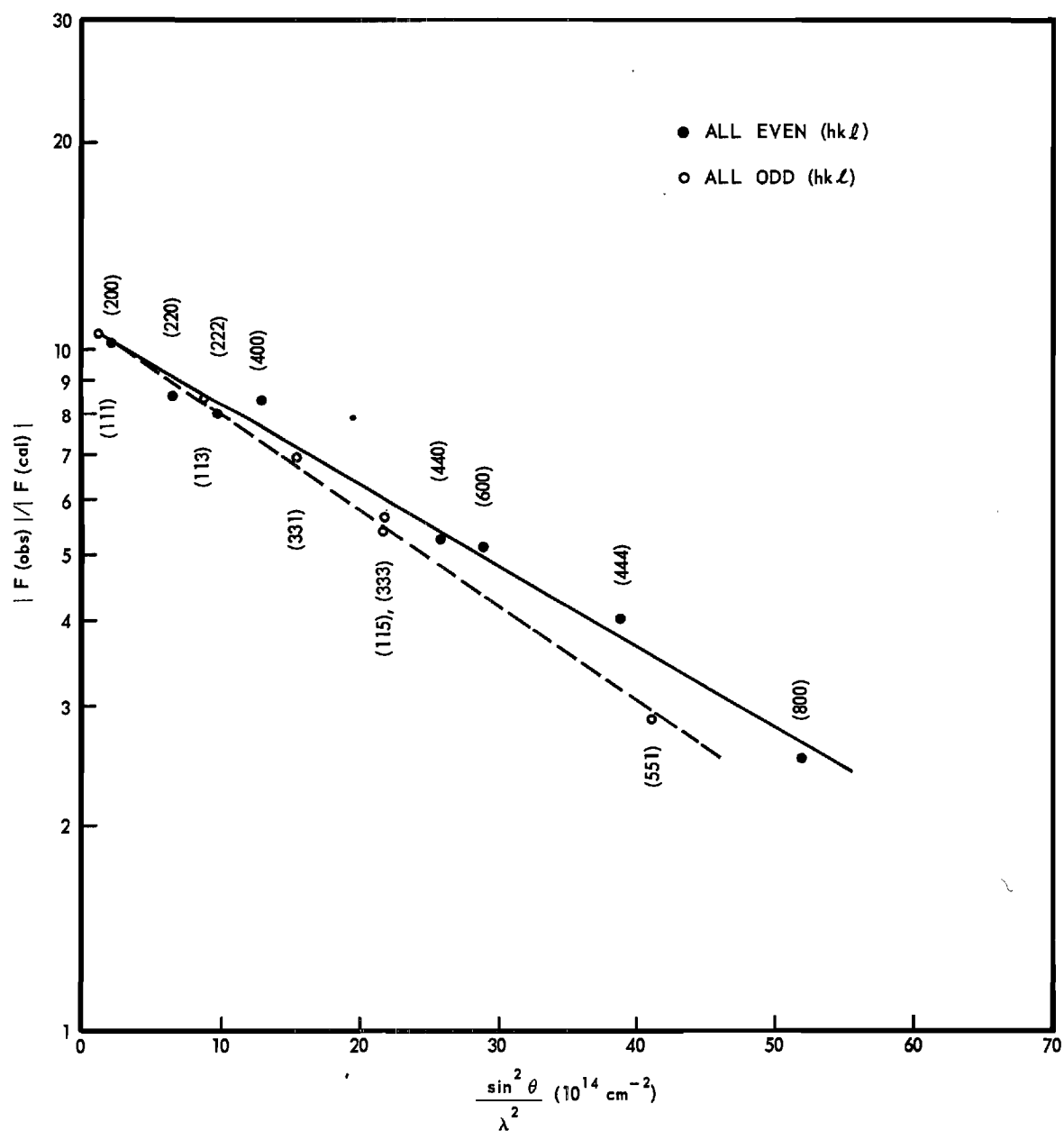


Figure 24. Dependence of  $|F(\text{obs})|/|F(\text{cal})|$  on  $\theta$  for AgCl Sample No. 18.



### Determination of Observed Values of $B'_1$ and $B'_2$

In view of the small number of  $A_o(\text{odd})$  values obtained for  $\phi$  values other than that for the (333) and (115) reflections, the method described below was used to determine  $B'_1$  and  $B'_2$  (hereafter denoted  $B'_1(\text{obs})$  and  $B'_2(\text{obs})$  respectively) from the data rather than an extrapolation procedure. The first step was to determine  $\Delta B'(\text{obs})$ . From equation (2-79) one obtains

$$A_o(\text{odd}) - A_o(\text{even}) = -f(\Delta B') \left( \frac{2e^{\Delta B\phi}}{e^{2\Delta B\phi} - f^2} \right) \quad (4-2)$$

Although there is no value of  $\phi$  for which values of both  $A_o(\text{even})$  and  $A_o(\text{odd})$  were obtained,  $A_o(\text{even})$  is independent of  $\phi$  at  $290^\circ$  K according to Figure 23. We therefore assumed that the arithmetic average of the  $A_o(\text{even})$  values shown in Figure 23 could be used in equation (4-2) with any  $\phi$  at which  $A_o(\text{odd})$  had been determined. The value used for  $A_o(\text{odd})$  was the arithmetic mean of the  $A_o(\text{odd})$  values measured for the (333) and (115) reflections. It was also assumed that  $\Delta B(\text{obs})$  was approximately given by  $\Delta B(\text{obs}) \approx \Delta B'(\text{obs})T$ . This should be a fair approximation for temperatures  $T \gtrsim \Theta$ , which is the case here for AgCl. (For these temperatures the energy per normal mode approaches  $kT$  so that  $B_1$  and  $B_2$  vary nearly linearly with temperature according to equation (2-74) and the definition of  $B$ .) Actually it turned out that  $\Delta B'(\text{obs})$  was quite insensitive to  $\Delta B(\text{obs})$  in equation (4-2). For example, in the iterative solution of equation (4-2), a 100% change in  $\Delta B(\text{obs})$  produced only a 15% change in  $\Delta B'(\text{obs})$ .

The evaluation of  $\Delta B'(\text{obs})$  by iterative solution of equation (4-2) proceeded as follows: First  $\Delta B(\text{obs})$  was set equal to zero and a trial value for  $\Delta B'(\text{obs})$  was obtained. The  $\Delta B'(\text{obs})$  value so obtained was used to calculate a trial  $\Delta B(\text{obs})$ . This  $\Delta B(\text{obs})$  was then inserted in equation (4-2) along with the value of  $\phi$  for the (333) and (115) reflections to calculate a new value for  $\Delta B'(\text{obs})$ . The calculations were repeated until successive values for  $\Delta B'(\text{obs})$  agreed to within one to two percent.  $B_1'(\text{obs})$  was determined from  $\Delta B'(\text{obs})$  and  $A_0(\text{even})$  with the following equation,

$$A_0(\text{even}) = B_1' + (\Delta B')\phi/(1 + \phi) \quad . \quad (4-3)$$

Equation (4-3) was obtained from equation (2-79) after setting  $e^{\Delta M} = e^{\Delta B\phi}$  equal to unity (because of the lack of  $\phi$  dependence of  $A_0(\text{even})$ ).  $B_2'(\text{obs})$  was then obtained from  $B_1'(\text{obs})$  and  $\Delta B'(\text{obs})$  with

$$B_2' - B_1' = \Delta B' \quad . \quad (4-4)$$

The results obtained for  $B_1'(\text{obs})$  and  $B_2'(\text{obs})$  at several temperatures are shown in Table 9 along with the results of the theoretical calculations of these quantities to be discussed later. Values obtained for  $A$  and  $A_0$  at 240, 200, 160, 140, and 120° K are shown, along with  $A_{\text{TDS}}$  and  $A_{\text{LPF}}$  in Tables 27 to 31 in Appendix F. The main characteristics of the  $A_0$  versus  $\phi$  plot as discussed above for 290° K were essentially temperature independent. The errors shown for  $B_1'(\text{obs})$  and  $B_2'(\text{obs})$  result from the propagation of the mean deviations of  $A_0(\text{odd})$  and  $A_0(\text{even})$  through the calculations carried out with equations (4-2), (4-3), and (4-4).

### Determination of Calculated Values of $B_1'$ and $B_2'$

To compare our results for AgCl with theory and with other experimental results reported in the literature for AgCl, we have made calculations of  $B_1$  and  $B_2$  (hereafter denoted as  $B_1(\text{cal})$  and  $B_2(\text{cal})$  respectively) as a function of temperature, using the Burroughs 220 computer. We have also obtained values for the Debye  $\Theta$ , at the temperatures shown in Table 9, from the experimentally determined  $B_1'(\text{obs})$  and  $B_2'(\text{obs})$ . The computer calculations will be discussed briefly first.

According to equation (2-74) the calculation of  $B_1$  (and similarly  $B_2$ ) requires a knowledge of the dependence of the normal mode frequencies,  $\nu(\vec{k}, \alpha)$ , (the dispersion curves) and the atomic vibrational amplitude ratio,  $\Gamma(\vec{k}, \alpha)$ , on the wave vector,  $\vec{k}$ , and the branch,  $\alpha$ . Cole<sup>10</sup> has determined the dispersion curves in the [100], [110], and [111] directions for the acoustic modes, transverse and longitudinal, in AgCl from TDS measurements. The determination of these curves from the TDS data was based on an assumed set of optical frequencies and on the assumption that the expression for  $\Gamma(\vec{k}, \alpha)$  obtained by Brillouin<sup>9</sup> (see Appendix B) for a one-dimensional diatomic chain was valid for a three-dimensional lattice such as AgCl.

Our calculations of  $B_1(\text{cal})$  and  $B_2(\text{cal})^*$  are based on Cole's measured dispersion curves and on the same assumptions made by Cole

---

\*  $B_1(\text{cal})$  and  $B_2(\text{cal})$  were calculated as a function of temperature rather than  $B_1'(\text{cal})$  and  $B_2'(\text{cal})$  since it was then possible to determine  $\Delta B(\text{cal})$  as well as  $B_1'(\text{cal})$  and  $B_2'(\text{cal})$  from one calculation.

concerning the form of  $\Gamma(\vec{k}, \alpha)$  and the optical frequencies in AgCl. It was felt that the subsequent comparison of these calculations with our experimental results could serve as an indication of the validity of the techniques used by Cole to interpret the TDS from a solid containing two types of atoms. In addition it was desirable to see if values for  $B_1(\text{cal})$  and  $B_2(\text{cal})$  indicate, as does our data, that the  $\text{Ag}^+$  ion has the larger vibrational amplitude in AgCl; and the use of Cole's data and of Brillouin's expression for  $\Gamma(\vec{k}, \alpha)$  seemed to provide the only method for doing so.

The calculations are described in detail in Appendix B, but it is desirable to mention here two other major assumptions on which they are based before we compare their results with experiment. For the acoustic modes the dispersion curves obtained by Cole were used to change each frequency,  $\nu(\vec{g}, \alpha)$ , where  $2\pi\vec{g} = \vec{k}$ , to a product of an appropriate phase velocity,  $V(\vec{g}, \alpha)$ , and  $|\vec{g}|$ , i.e.,  $\nu(\vec{g}, \alpha) = V(\vec{g}, \alpha)|\vec{g}|$ . We then assumed that the directionally dependent phase velocities,  $V(\vec{g}, \alpha)$  could be arithmetically averaged, after each direction had been weighted according to its multiplicity, to obtain an average isotropic phase velocity  $V(|\vec{g}|, \alpha)$ . The dependence on  $|\vec{g}|$  and the branch,  $\alpha$  was not neglected. However, the Brillouin zone was replaced by a sphere. With these assumptions the sum over wave vectors,  $\vec{g}$ , could be reduced to an integral, e.g.

$$\sum_{\vec{g}, \alpha} \longrightarrow 4\pi \sum_{\alpha} \int |\vec{g}|^2 d|\vec{g}| \quad ;$$

with a resulting great simplification of the calculation. It should be pointed out that such an averaging procedure, while hopefully not introducing great error, does neglect the fact that waves traveling in directions other than those mentioned cannot be separated into truly transverse and longitudinal modes.

The contribution to  $B_1(\text{cal})$  and  $B_2(\text{cal})$  of the optic modes was expected to be small. We therefore simplified the calculation by assuming that the optical frequencies were independent of direction, as Cole had done, and independent of wave vector. That is, single frequencies were assumed, one for the transverse modes and one for the longitudinal modes. Cole had also used a single frequency for the transverse modes but he assumed some wave vector dependence for the longitudinal mode frequencies. The resulting spread in the longitudinal mode frequencies was small, however; amounting to only 5 percent on either side of the single average frequency we used. It should be pointed out that the optic mode frequencies used are high compared to those of the acoustic modes. Thus the optic modes give rise to a high frequency peak in the vibrational spectrum of AgCl.

The results of these calculations are shown in Tables 9 and 10 along with our experimental results. Values for the calculated temperature derivatives were assumed to be adequately given by  $\Delta B_1/\Delta T$  and  $\Delta B_2/\Delta T$ , where, for example for  $290^\circ \text{ K}$ ,  $\Delta B_1 = B_1(300^\circ \text{ K}) - B_1(280^\circ \text{ K})$  and  $\Delta T = 20^\circ \text{ K}$ .

#### Comparison of Calculated and Observed Values for $B_1'$ and $B_2'$

As can be seen the calculations also indicate that both the vibrational amplitude and its temperature derivative for the  $\text{Ag}^+$  ion are

Table 9. Calculated and Measured Temperature Derivatives  
of  $B_1$  and  $B_2$  for AgCl

$T(^{\circ}\text{K})$	Calculated						Observed	
	Optic Modes		Acoustic Modes		Acoustic plus Optic Modes		$B'_1$	$B'_2$
	$\partial B_1/\partial T^*$	$\partial B_2/\partial T$	$\partial B_1/\partial T$	$\partial B_2/\partial T$	$\partial B_1/\partial T$	$\partial B_2/\partial T$		
290	0.095	3.25	10.73	4.64	10.83	7.89	10.2+0.2	8.1+0.7
240	0.091	3.18	10.71	4.63	10.80	7.81	9.8+0.2	7.7+0.7
200	0.089	3.12	10.70	4.63	10.79	7.75	9.4+0.3	7.2+0.9
160	0.087	3.03	10.66	4.61	10.75	7.64	8.7+0.2	6.7+1.3
140	0.083	2.95	10.63	4.61	10.72	7.56	8.4+0.3	6.3+1.5
120	0.078	2.83	10.58	4.59	10.66	7.42	7.9+0.3	5.7+1.5

\*Units:  $10^{-19} \text{ cm}^2 \text{ }^{\circ}\text{K}^{-1}$

Table 10. Calculated Values of  $B_1$  and  $B_2$  for AgCl

$T(^{\circ}\text{K})$	Optic Modes		Acoustic Modes		Acoustic plus Optic Modes	
	$B_1^*$	$B_2$	$B_1$	$B_2$	$B_1$	$B_2$
290	0.029	0.99	3.13	1.35	3.16	2.34
240	0.024	0.83	2.59	1.12	2.61	1.95
200	0.021	0.71	2.17	0.93	2.19	1.64
160	0.017	0.58	1.74	0.75	1.76	1.33
140	0.015	0.52	1.53	0.66	1.55	1.18
120	0.014	0.46	1.31	0.56	1.32	1.02

\*Units:  $10^{-16} \text{ cm}^2$

larger than those for the  $\text{Cl}^-$  ion; in qualitative agreement with experiment. In fact the agreement between the calculated and measured temperature derivatives of  $B_1$  and  $B_2$  is fairly good in view of the seemingly drastic approximations on which the calculations are based. It therefore appears that Brillouin's expression for the atomic vibrational amplitude ratio is at least not an extremely bad approximation for a three-dimensional lattice. Another interesting result concerning the calculations is the rather large contribution, nearly 50 percent, of the optic modes to both  $B_2(\text{calc})$  and  $B_2'(\text{calc})$ . Nearly all of the temperature dependence of  $B_2'(\text{calc})$  is due to the optic modes. On the other hand the contribution of the optic modes to  $B_1(\text{calc})$  and  $B_1'(\text{calc})$  are very small. Thus the vibrational amplitude of the  $\text{Ag}^+$  ion is due almost entirely to the acoustic modes while that for the  $\text{Cl}^-$  ion arises almost equally from the acoustic and optic modes.

Although the qualitative agreement between the calculations and the experimental results is good, there are significant differences, particularly with regard to the temperature dependences of  $B_1'$  and  $B_2'$ .  $B_1'(\text{calc})$  and  $B_2'(\text{calc})$  show very little dependence on temperature while the experimental values decrease significantly with decreasing temperature. Presumably part of the temperature dependence of the experimental values is due to anharmonic effects for which they have not been corrected. To investigate this point further,  $B_1'(\text{obs})$  and  $B_2'(\text{obs})$  were combined, as indicated in equation (2-75) for  $M_1'$  and  $M_2'$ , to give  $m_1 B_1'(\text{obs}) + m_2 B_2'(\text{obs}) = G(\text{obs})$ . The thermal expansion contribution to  $G(\text{obs})$  was eliminated in a manner analogous to that suggested in the discussion pertaining to the

expansion of  $B'(\text{obs})$  in terms of the moments of the vibrational spectrum. That is, the term proportional to  $g(x)$  in equation (2-75) was first subtracted from  $G(\text{obs})$  using the Debye  $\Theta$  values for AgCl to be discussed later. The resulting numbers were then multiplied by  $(V_0/V)^{2\gamma}$ ,  $V_0$  being the volume at  $290^\circ \text{K}$ , and plotted against  $T'$  as shown in Figure 25. The corresponding values for  $G(\text{cal})$  are shown in the same figure. As can be seen the experimental results still vary more with temperature than those calculated. There may be anharmonic contributions to  $B'(\text{obs})$  in addition to thermal expansion. However the entire temperature dependence of  $G(\text{obs})$  cannot be explained by an anharmonic term which varies only linearly with temperature as would be expected if that were the only consideration\*.

Part of the discrepancy between the measured and calculated values for  $G$  may be due to errors in the calculations which could arise both because of the grossness of the approximations made and because of some errors in the dispersion curves obtained by Cole resulting from his use of Brillouin's expression for  $\Gamma(\vec{k}, \alpha)$ . Recent theoretical calculations of the dispersion of the normal modes in the  $[100]$ ,  $[110]$ , and  $[111]$  directions in AgCl by Joshi and Gupta<sup>47</sup> show quite large discrepancies between theory and the experimental results of Cole. In particular these authors find (1) the frequencies of the longitudinal optic modes are significantly less ( $\sim 30\%$ ) than those used in our calculations and (2) the frequencies of the acoustic modes are considerably larger (as much as 100% for some values of  $|\vec{g}|$ ) than those obtained by Cole. Such a decrease in

---

\* Anharmonic terms which vary as  $T^2$  are presumably not significant since no anisotropy in  $A_0$  was observed.



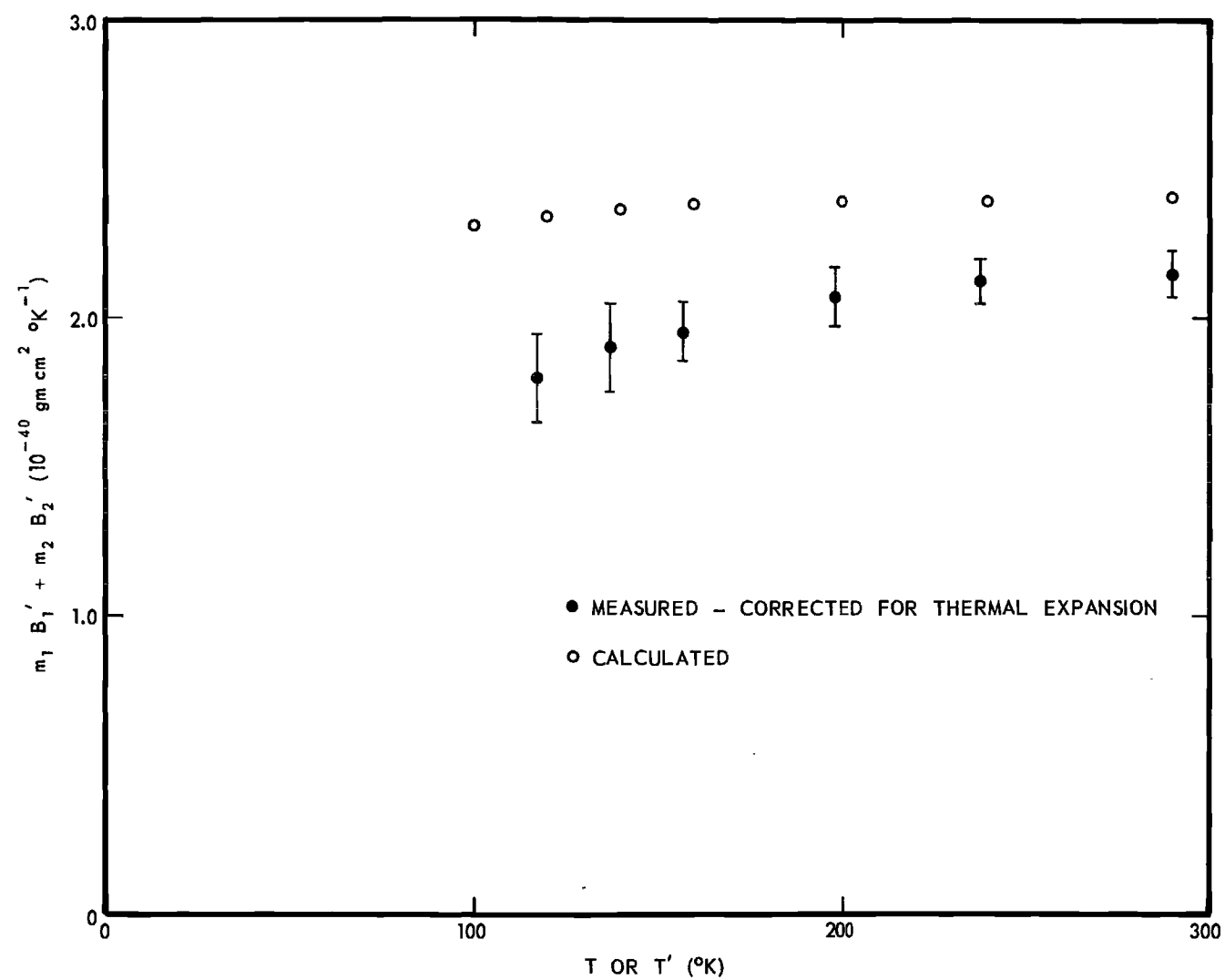


Figure 25. Dependence of  $m_1 B_1' + m_2 B_2'$  on Temperature for AgCl.

the frequencies of the optic modes would increase the contribution of these modes to  $B_1'(\text{cal})$  and  $B_2'(\text{cal})$ . Since almost all of the temperature dependence of  $G(\text{cal})$  is due to the optic modes, it is quite possible that the use of these calculated optic mode frequencies would bring the temperature dependence of  $G(\text{obs})$  and  $G(\text{cal})$  into better agreement. Also an increase in the frequencies of the acoustic modes would decrease their contribution to  $G(\text{cal})$ . Since the magnitude of  $G(\text{cal})$  is primarily determined by the acoustic modes, the use of these calculated acoustic modes would tend to improve the agreement between the magnitudes of  $G(\text{cal})$  and  $G(\text{obs})$ . Problems remain however. Joshi and Gupta find that at long wavelengths the slopes of the calculated acoustic dispersion curves do not agree with the velocities calculated from elastic constants. In any event it is clear that our data indicate that the dispersion curves calculated by Joshi and Gupta are to be preferred over those obtained by Cole.

#### Debye $\Theta$ Values

We obtained values for the Debye  $\Theta$  of AgCl from the measured values for  $B_1'$  and  $B_2'$  and equation (2-75) (divided by  $\sin^2\theta/\lambda^2$ ). The values used for the thermal coefficient of expansion,  $\beta$ , and for the Grüneisen constant,  $\gamma$ , were those measured at the time of the present study<sup>31</sup>. The results are plotted against temperature in Figure 26 along with some results obtained from other experimental techniques. Our results for  $\Theta$  show more temperature dependence than can be accounted for by thermal expansion effects alone. This may be due to additional anharmonic effects or to a contribution to  $B_1'$  and  $B_2'$  from high frequency optic modes as

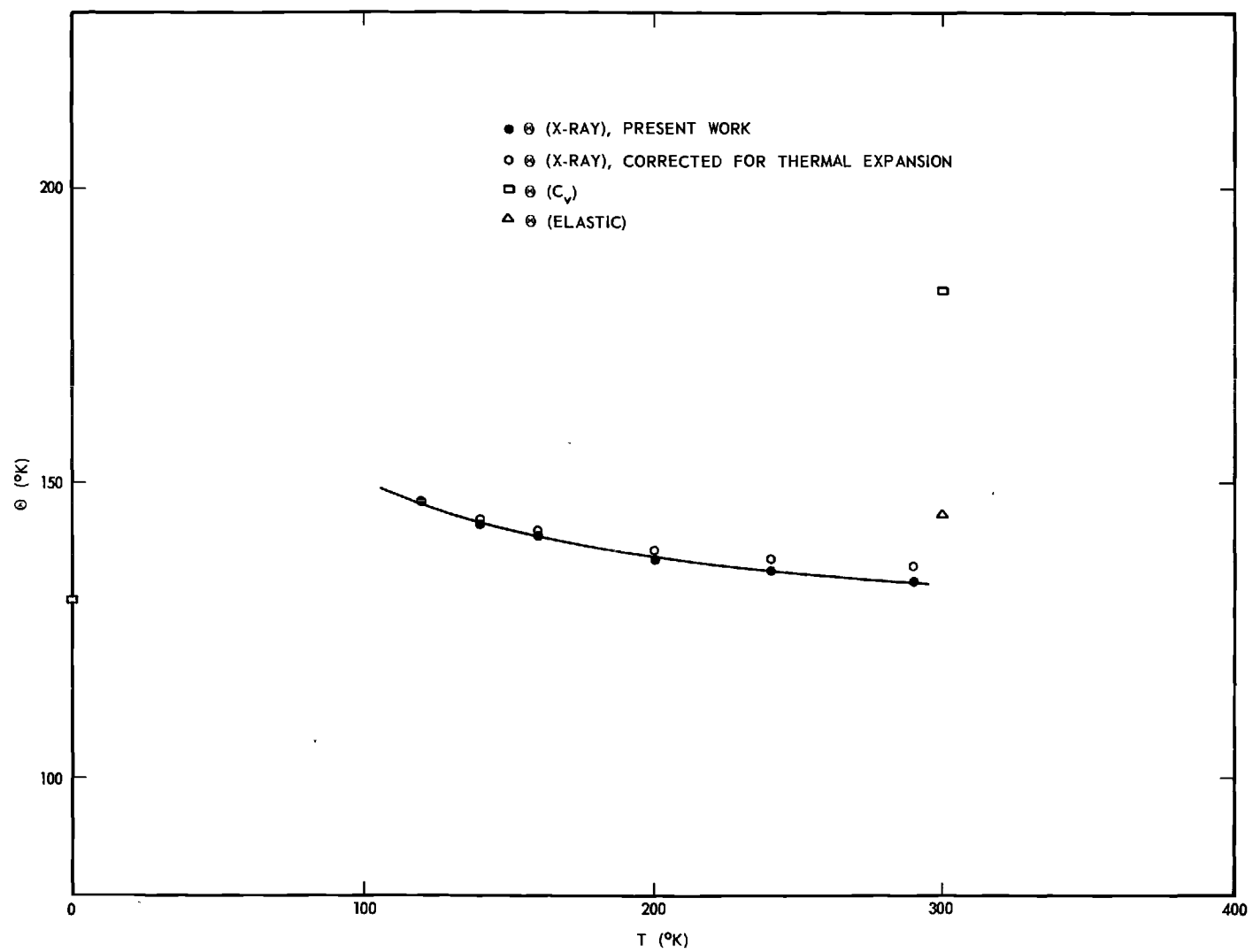


Figure 26. Dependence of AgCl Debye  $\Theta$  on Temperature.

mentioned earlier. Because the probable existence of a poorly determined contribution of the optic modes to  $B'_1$  and  $B'_2$  we have made no attempt to determine the size of anharmonic effects other than thermal expansion.

The value for  $\Theta$  determined from elastic constants was calculated by us from the room temperature elastic constant data of Arenberg<sup>48</sup> using the method suggested by Quimby and Sutton<sup>49</sup>. It is in good agreement with our x-ray values, being a little larger as expected. We were unable to find in the literature any elastic constant measurements for AgCl below room temperature. Presumably the  $\Theta$  obtained from such measurements would remain larger than the x-ray values and thus would increase as the temperature decreases.

We were unable to find in the literature very many values for  $\Theta(C_V)$ . The value shown at  $0^\circ$  K was obtained by Lonsdale<sup>50</sup> from application of the  $T^3$  law to the data of Clusius and Harteck<sup>51</sup>. No temperature was quoted by Lonsdale but since the  $T^3$  law is valid only at very low temperature we have assumed that this is the value for  $\Theta(C_V)$  which would be measured at  $0^\circ$  K. Although this assumption may not be valid, at least there is an indication that her value for  $\Theta(C_V)$  obtained from low temperature specific heat measurements is in fair agreement with those obtained from elastic constant and x-ray measurements as expected (see Chapter II). The value for  $\Theta(C_V)$  shown at  $300^\circ$  K was found in the American Institute of Physics Handbook<sup>52</sup>. Since no references or temperatures were given in the handbook, it was assumed that the  $\Theta(C_V)$  listed was determined at about room temperature. This  $\Theta(C_V)$  is considerably larger than those determined from the elastic constants or our x-ray

measurements. This difference is presumably due to the existence of relatively high frequency modes in AgCl and to the fact that  $\Theta(C_V)$  is influenced more by the high frequencies in the vibrational spectrum than are those  $\Theta$ 's obtained from either elastic constant or x-ray measurements. Thus both (1) the difference between  $\Theta(C_V)$  at  $300^\circ$  K and  $\Theta(\text{x-ray})$  and, (2) the temperature dependence of  $G(\text{obs})$ , discussed earlier, are consistent with the existence of a high frequency peak in the vibrational spectrum of AgCl.

#### Moments Expansion of Data

Considerable difficulty was encountered in our attempts to fit our x-ray data with a "moments" expansion such as that shown in equation (2-57). Most of our efforts were expended on the KCl data, primarily because the moments  $\mu_2$ ,  $\mu_4$ , and  $\mu_6$  had been determined from specific heat data by Barron, et al<sup>13</sup>. It was considered most desirable to compare their results with those obtained from x-ray measurements. Since the difficulties encountered were similar for KCl, Al, and AgCl, we shall discuss only the moments expansion work done with the KCl data.

As discussed earlier  $A_0$  values for KCl were determined at 290, 240, 200, 160, 140, and  $120^\circ$  K. It was desired that the ratio of the number of independent observations to the number of adjustable parameters in the moments expansion be made as large as conveniently possible. To increase, with a minimum of effort, the number of pieces of data to be fit, we used  $A_0$  values determined for the (800) Bragg reflection of KCl sample no. 3 at 180, 220, 260, and  $320^\circ$  K in addition to the temperatures mentioned above. At the temperatures where they

could be compared, the  $A_0$  values obtained from this particular reflection were all within 1/2% of the average  $A_0$  values determined previously for KCl. Thus, although the use of the data obtained from only one reflection would otherwise be statistically inadequate, it was felt that the agreement just cited indicated that the  $A_0$  values used adequately represented the averaged KCl data. The correction of these  $A_0$  values for thermal expansion contributions and the subsequent reduction of them to

$$(\partial E / \partial T)_V (V_0/V)^{2\gamma} + a_1(T')^{-2}$$

was accomplished as described in Chapter II (see pages 40 and 41).  $T_0$  was  $120^\circ$  K.

Two computer calculations were made. In the first the values for  $(\partial E / \partial T)_V (V_0/V)^{2\gamma} + a_1(T')^{-2}$  were fit, in a least squares sense, to the expansion  $a_0 + a_2(T')^{-4} - a_3(T')^{-6} + \dots$  (see page 41), carried out only to the  $a_3(T')^{-6}$  term, with a Burroughs 220 computer. Thus the three adjustable parameters  $a_0$ ,  $a_2$ , and  $a_3$  were determined from ten independent pieces of data. The results were then used with equation (2-58) to determine the moments  $\mu_{-2}$ ,  $\mu_2$ , and  $\mu_4$  which are shown in Table 11. The percent standard deviation in the least squares fit amounted to 1/3%.

Table 11. Vibrational Spectrum Moments for KCl

	X-ray	Specific Heat
$\mu_{-2}$	$1.4 \times 10^{-25} \text{ sec}^2$	
$\mu_2$	$27.8 \times 10^{24} \text{ sec}^{-2}$	$14.45 \times 10^{24} \text{ sec}^{-2}$
$\mu_4$	$954 \times 10^{49} \text{ sec}^{-4}$	$27.5 \times 10^{49} \text{ sec}^{-4}$

From equations (2-20), (2-46), with  $f(x) = 1$ , (2-47), and (2-54) and the value obtained for  $\mu_2$ , we obtain  $222^\circ \text{K}$  for the high temperature limit of  $\Theta(\text{x-ray})$ , i.e.  $\Theta(\infty)$ . This value agrees well with the  $\Theta(\text{x-ray})$  values determined earlier from our data for temperatures above  $200^\circ \text{K}$  and with  $\Theta(\infty)$  obtained, as discussed earlier, by Blackman<sup>19</sup>. However the values obtained for  $\mu_2$  and  $\mu_4$  are much too large when compared with the specific heat results.

In an attempt to determine if the large values we obtained for  $\mu_2$  and  $\mu_4$  were due to poor convergence of the series, we made the second calculation with the expansion carried out to the  $a_5(T')^{-10}$  term. Thus for this calculation five adjustable parameters  $a_0$ ,  $a_2$ ,  $a_3$ ,  $a_4$ , and  $a_5$  were determined from ten pieces of data. For this calculation all the parameters, except  $a_0$ , had signs which when used in equation (2-58) yielded negative values for the vibrational spectrum moments. This result is physically impossible since all the normal mode frequencies are positive.

The reason for the difficulties encountered in our attempts to fit our data to a moments expansion is not certain. However several plausible qualitative arguments come to mind:

(1) It turns out that most of the temperature dependence of  $(\partial B / \partial T)_V (V_0/V)^{2\gamma}$  comes from  $a_1(T')^{-2}$ , the term in equation (2-57) which does not depend on the moments. This is illustrated for KCl in Figure 27 where  $(\partial B / \partial T)_V (V_0/V)^{2\gamma}$  and  $(\partial B / \partial T)_V (V_0/V)^{2\gamma} + a_1(T')^{-2}$  for the (800) Bragg reflection of KCl sample no. 3 are shown plotted against  $T'$ . As is seen the temperature dependence of the points we attempted

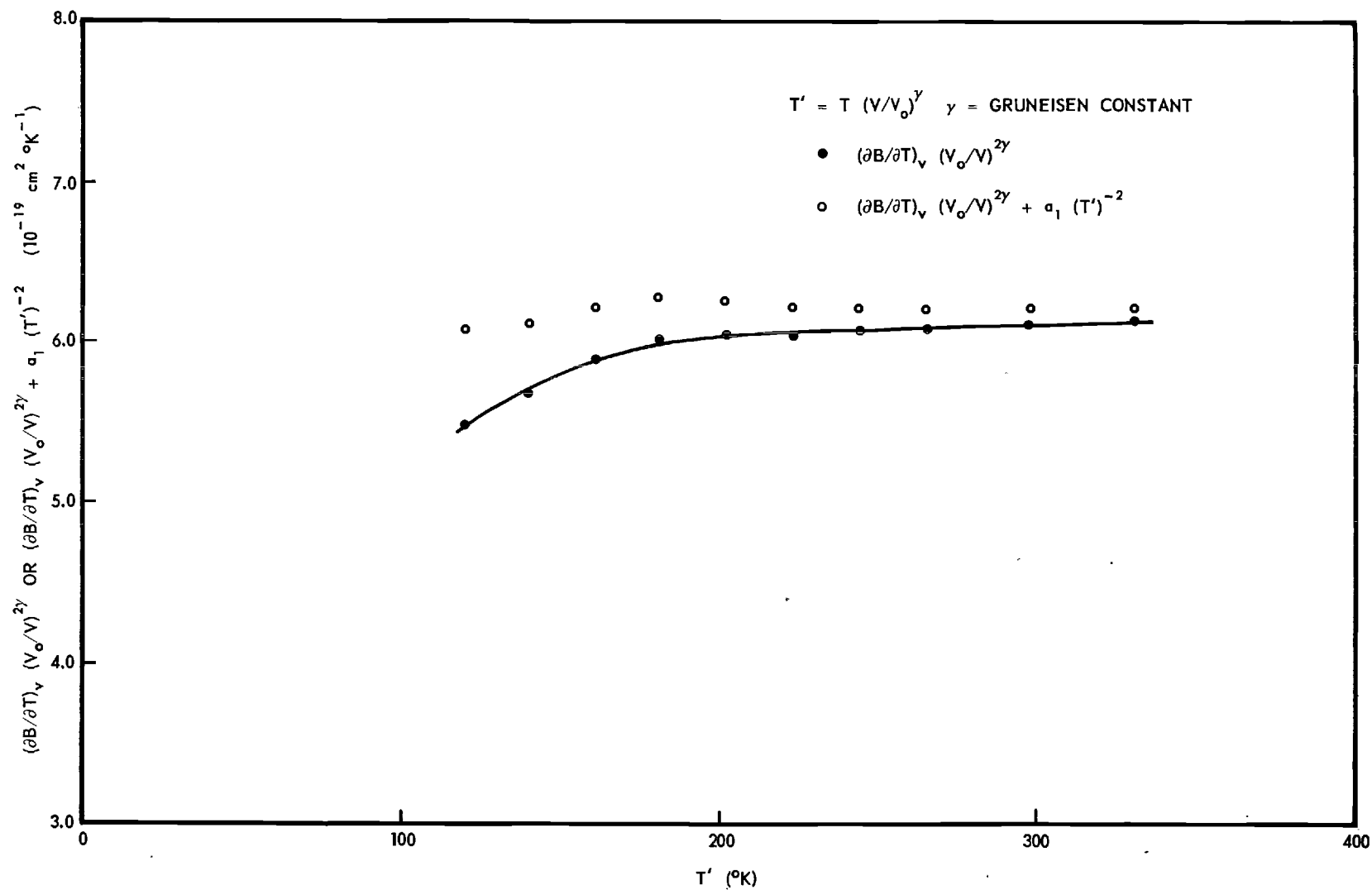


Figure 27. Dependence of  $(\partial B/\partial T)_V (V_0/V)^{2\gamma}$  and  $(\partial B/\partial T)_V (V_0/V)^{2\gamma} + a_1 (T')^{-2}$  on Temperature for KCl.



to fit with the moments expansion is quite small, possibly too small in comparison to experimental uncertainties to permit a meaningful evaluation of the coefficients of the expansion. Some evidence of this possibility was provided by the computer program that was used in the fitting procedure. This program applied a statistical t-test to the coefficients to test the hypothesis that the coefficients in the expansion were zero. For both of the above calculations, this test yielded the result that all the coefficients, except  $a_0$ , were not significantly different from zero. That is, in a statistical sense, the data which were fit to the moments expansions did not provide sufficient evidence that the coefficients were different from zero.

(2) It is possible that the thermal expansion corrections which were applied were either incorrect or did not account fully for anharmonicity. It is interesting to note that Barron, et al<sup>13</sup> state that anharmonic effects rendered their attempts to fit measured values of  $C_V$  to a moments expansion unsuccessful. They actually obtained the values for  $\mu_2$  and  $\mu_4$  shown in Table 11 from a moments expansion of  $\Theta(C_V)$  in a temperature region where  $\Theta(C_V)$  exhibits considerable temperature dependence. An expansion of  $\Theta(C_V)$  in terms of the vibrational spectrum moments is obtained by comparison of equation (2-59), written in terms of  $\mu_n$ , with the analogous equation written in terms of the moments of a Debye spectrum. A similar technique may prove successful for x-ray data.

## CHAPTER V

## CONCLUSIONS AND RECOMMENDATIONS

From the temperature slope of essentially continuous Bragg intensity versus temperature data, it is possible to obtain meaningful values of  $dB/dT$  for a cubic lattice with one atom per lattice point and of  $dB_1/dT$  for each type of atom in an NaCl type lattice as a function of temperature. These temperature derivatives of the Debye-Waller factors can be related in a straightforward way to the vibrational spectrum and, hence, can be used to determine  $\Theta(\text{x-ray})$  as a function of temperature for both the monatomic and diatomic cases. A value for  $\Theta(\text{x-ray})$  so obtained at a given temperature is absolute in the sense that it does not depend on the  $\Theta(\text{x-ray})$  values which are appropriate to other temperatures. That is, no assumptions regarding the expected shape of a  $\Theta(\text{x-ray})$  versus temperature curve are required.

The comparison of our intensity versus temperature results for Al with calculations based on Walker's vibrational spectrum for Al have shown that the temperature dependence of  $dB/dT$  is sensitive both to anharmonicity and to certain details in the character of the low and, possibly, intermediate frequency portion of the vibrational spectrum. A 5% expansion of the transverse branch of Walker's spectrum to higher frequencies, suggested by the neutron inelastic scattering results of Brockhouse and Stewart<sup>12</sup>, makes a significant improvement in the agreement between our calculated and observed results for  $\Theta(\text{x-ray})$ .

When thermal expansion effects on the frequencies are also included, the calculated  $\Theta(\text{x-ray})$  versus temperature curve is in excellent agreement with our experimental curve. Anharmonic effects other than thermal expansion are not significant in Al in the 100 to 300° temperature range. However according to the  $\Theta(\text{x-ray})$  versus temperature results obtained by Chipman, anharmonic effects probably become significant above 300° K. It would be desirable to extend our intensity versus temperature data for Al above 300° K to examine this point. It would also be desirable to extend the data below 100° K to examine experimentally the rapid increase of the calculated  $\Theta(\text{x-ray})$  versus temperature curve below 80° K (see Figure 20).

The  $A_0$  versus  $\phi$  plot was very useful in the interpretation of the intensity versus temperature results for AgCl. The results obtained show that  $d(B_{\text{Ag}})/dT$  is larger than  $d(B_{\text{Cl}})/dT$  by approximately 20 - 30% in the 100 to 300° temperature range. This result is in substantial agreement with our calculations based on Cole's<sup>10</sup> dispersion curves for AgCl and on Brillouin's<sup>9</sup> expression for the wave vector dependence of the atomic amplitude ratio in a one-dimensional lattice. This agreement indicates that (1) the experimental and analytical methods used are capable of yielding useful information about the thermal vibrations of each type of atom in an NaCl type lattice and (2) Brillouin's one-dimensional model is not completely invalid for at least one NaCl type lattice. It would be desirable to carry out new calculations based on the dispersion curves obtained by Joshi and Gupta<sup>47</sup> to determine if better agreement between theory and experiment can be obtained. According to our calculations

(1) the acoustic modes account for nearly all of  $B_{Ag}$ , (2) however, the optic modes account for nearly 50% of  $B_{Cl}$  and hence contribute significantly to the temperature dependence of  $\Theta(x\text{-ray})$  for AgCl in the 100 to 300° temperature range. Partially because of the presence of optical modes one might expect anharmonic effects in AgCl even at relatively low temperatures such as those encountered in the present study. The first order anharmonic effect, i.e. that of thermal expansion on the normal mode frequencies, accounted for a portion of the temperature dependence of  $\Theta(x\text{-ray})$ . The contributions from higher order anharmonic effects were not examined because the optic mode contributions to  $\Theta(x\text{-ray})$  were not sufficiently well known.

For KCl we find that between 200° K and 300° K  $\Theta(x\text{-ray})$  agrees well with the high temperature value calculated by Blackman<sup>19</sup> and has a temperature dependence which is fully accounted for by thermal expansion. Below 200° K  $\Theta(x\text{-ray})$  increases more than can be accounted for by thermal expansion alone as the temperature decreases. This increase is presumably due to the differences between the real vibrational spectrum and the Debye spectrum. A similar type of increase is also found at low temperatures in the calculated  $\Theta(x\text{-ray})$  versus temperature curve for Al.

For all three materials, Al, KCl, and AgCl, we have found  $\Theta(\text{elastic}) > \Theta(x\text{-ray})$  as expected. The discrepancy (according to Blackman<sup>19</sup>) between theory and experiment which once existed for KCl, viz.  $\Theta(x\text{-ray}) > \Theta(\text{elastic})$ , has been removed by our data. The large difference ( $\sim 25\%$ ) between  $\Theta(x\text{-ray})$  and  $\Theta(C_V)$  for AgCl is probably due to the existence of optic branches in AgCl which are fairly far removed from the acoustic

branches and which contribute more to  $\Theta(C_V)$  than to  $\Theta(\text{x-ray})$ . As mentioned earlier a similar effect is found in Ge and Si<sup>32</sup>.

Attempts to fit the temperature slope of intensity versus temperature data with an expansion in terms of the moments of the vibrational spectrum failed. Possible reasons for the failure are:

1. Most of the temperature dependence of  $(\partial B / \partial T)_V$  is due to a term that does not depend on any moment. The temperature dependence of the other terms is too small compared to the uncertainties in the data to be useful.

2. Thermal expansion corrections may be in error or may not fully account for anharmonicity. The advantages of the moments expansion technique are sufficiently appealing to warrant continued effort in this area of the data analysis.

We find that TDS contributions to Bragg intensities depend on various experimental parameters such as illumination gradients in the incident beam, sample size and shape, counter aperture size, etc. Expressions have been derived which can be used to determine both the one and two phonon contributions to the Bragg peak intensity. The results of specially devised experimental tests indicate that these contributions in this study probably were determined to within 5 to 15%.

On the basis of the comparisons made in this study between experiment and theory (particularly for Al and AgCl) we conclude that with the experimental and analytical techniques used in the present study, Bragg intensity versus temperature data are capable of yielding valuable information concerning (1) anharmonic effects, (2) the validity of

experimentally or theoretically determined vibrational spectra and dispersion curves for both monatomic and NaCl type lattices and (3) the validity of various theoretical models related to thermal vibrations.

## APPENDIX A

Thermal Diffuse Scattering

The general theory of thermal diffuse scattering is given by Laval<sup>17</sup> and, in somewhat different form, by James<sup>5</sup>. We shall use the form given by James, but since he considers only a monatomic cubic crystal, we shall extend his form of the theory to include diatomic cubic crystals in order to permit calculation of the TDS corrections necessary for our KCl and AgCl data.

The intensity of the thermal diffuse scattering can be expressed as a series of terms obtained by expanding in a Maclaurin series the term in equation (2-4) containing the cosine function. The linear term, called the first order or one phonon scattering, describes the scattered intensity resulting from the interaction of an x-ray photon with a single phonon\*. Similarly the nth order term describes the intensity resulting from the interaction of an incident photon with n phonons. We will be concerned only with the first two terms. The third and higher order terms are usually neglected since they are small and are quite difficult to calculate. For our purposes they will be assumed negligible. The validity of this and other assumptions to be made later are demonstrated in Chapter III where we compare with experiment our calculations based on the one and two phonon scattering. As in the discussions of M, it is convenient to consider separately those crystal structures with only one

---

\*The phonon is the quantum of vibrational energy,  $h\nu$ , where  $\nu$  is a normal mode frequency.

atom per lattice point and those with two or more. The relatively simple case of one phonon scattering from a crystal having only one atom per lattice point is described in detail. The more complex cases (e.g., two phonon scattering and/or two atoms per lattice point) are then discussed in somewhat outline form by reference to the detailed treatment of the more simple case.

### One Atom per Lattice Point

#### One Phonon Scattering Theory

If the term containing the cosine function is included when equation (2-4) is substituted into equation (2-2), equation (2-15) becomes, with  $a_j(\vec{k}, \alpha) = a_\ell(\vec{k}, \alpha) = a(\vec{k}, \alpha)$

$$\langle PP^* \rangle = e^{-2M} \sum_{n,m=1}^N \sum_{j,\ell=1}^p f_j f_\ell e^{i\vec{\kappa}\vec{S} \cdot (\vec{r}_n - \vec{r}_m)} e^{i\vec{\kappa}\vec{S} \cdot (\vec{\rho}_j - \vec{\rho}_\ell)} \exp \left[ \sum_{\vec{k}, \alpha} G(\vec{k}, \alpha) \cos\{\} \right] \quad (A-1)$$

where

$$G(\vec{k}, \alpha) = \frac{1}{2} (\vec{\kappa}\vec{S} \cdot \vec{e}(\vec{k}, \alpha))^2 \langle a^2(\vec{k}, \alpha) \rangle \quad (A-2)$$

and

$$\cos\{\} = \cos \{ \vec{k} \cdot (\vec{r}_n - \vec{r}_m) + \vec{k} \cdot (\vec{\rho}_j - \vec{\rho}_\ell) \} \quad (A-3)$$

We now expand the last term of equation (A-1) in a Maclaurin series, keep only the first two terms, and let



$$\cos\{\} = \frac{1}{2} \left( e^{i\{\}} + e^{-i\{\}} \right) \quad (\text{A-4})$$

and

$$\vec{k} = 2\pi\vec{g}, \quad |\vec{g}| = \Lambda^{-1}, \quad (\text{A-5})$$

where  $\Lambda$  is the normal mode wavelength. Equation (A-1) then becomes,

$$\begin{aligned} \langle PP^* \rangle = & I_0 \left( \vec{S}/\lambda \right) |F|^2 e^{-2M} + \\ & \frac{1}{2} e^{-2M} \sum_{\vec{g}, \alpha} (G, (\vec{g}, \alpha)) \sum_{j, \ell} f_j f_\ell \left\{ e^{2\pi i (\vec{S}/\lambda + \vec{g}) \cdot (\vec{\rho}_j - \vec{\rho}_\ell)} I_0(\vec{S}/\lambda + \vec{g}) \right. \\ & \left. + e^{2\pi i (\vec{S}/\lambda - \vec{g}) \cdot (\vec{\rho}_j - \vec{\rho}_\ell)} I_0(\vec{S}/\lambda - \vec{g}) \right\}, \quad (\text{A-6}) \end{aligned}$$

where  $I_0(\vec{S}/\lambda)$  and  $F$  are defined in equations (2-9) and (2-16) respectively and we have set

$$\sum_{n, m=1}^N e^{2\pi i (\vec{S}/\lambda \pm \vec{g}) \cdot (\vec{r}_n - \vec{r}_m)} = I_0(\vec{S}/\lambda \pm \vec{g}) \quad (\text{A-7})$$

$I_0(\vec{S}/\lambda \pm \vec{g})$  is the same function of  $\vec{S}/\lambda \pm \vec{g}$  as  $I_0(\vec{S}/\lambda)$  is of  $\vec{S}/\lambda$  and thus has appreciable values only when equation (2-10) is satisfied with  $\vec{S}/\lambda$  replaced by  $\vec{S}/\lambda \pm \vec{g}$ . For each value of  $\vec{g}$  such that  $\vec{S}/\lambda \pm \vec{g}$  is equal to a given  $\vec{H}$ , the sums over  $j$  and  $\ell$  will yield the same result,

$$\sum_{j,l} f_j f_l e^{2\pi i (\vec{S}/\lambda + \vec{g}) \cdot (\vec{p}_j - \vec{p}_l)} = \left( \sum_j f_j e^{2\pi i (\vec{S}/\lambda + \vec{g}) \cdot (\vec{p}_j)} \right)^2 = |F|^2 \quad (\text{A-8})$$

and can be taken outside the summation. Thus

$$\langle \text{PP}^* \rangle = I_0(\vec{S}/\lambda) |F|^2 e^{-2M} + \frac{1}{2} |F|^2 e^{-2M} \sum_{\vec{g}, \alpha} (G(\vec{g}, \alpha) \{ I_0(\vec{S}/\lambda + \vec{g}) + I_0(\vec{S}/\lambda - \vec{g}) \}) \quad (\text{A-9})$$

where the second term represents the first order thermal diffuse scattering. Since for each normal mode with a wave vector  $+2\pi\vec{g}$  there is a similar one with a wave vector  $-2\pi\vec{g}$ , it is easily shown<sup>5</sup> that for any given  $\vec{S}/\lambda$  the contribution to the first order scattering from the term containing  $I_0(\vec{S}/\lambda - \vec{g})$  is the same as that from the term containing  $I_0(\vec{S}/\lambda + \vec{g})$ . Thus the first order scattering is proportional to

$$J_1 = |F|^2 e^{-2M} \sum_{\vec{g}, \alpha} (G(\vec{g}, \alpha) I_0(\vec{S}/\lambda + \vec{g})) \quad (\text{A-10})$$

For convenience we also define

$$J_0 = I_0(\vec{S}/\lambda) |F|^2 e^{-2M} \quad (\text{A-11})$$

Part of the problem to be solved is the determination of how much of  $J_1$  is measured when a measurement of  $J_0$  is attempted. As one might suspect from the dependence of  $J_0$  and  $J_1$  on quantities such as  $\vec{S}/\lambda$  and  $\vec{g}$ , which have the units of reciprocal length, the solution of the problem is most easily described in terms of the reciprocal lattice.

### Reciprocal Lattice and Ewald Sphere

The reciprocal lattice and its use for the description of certain aspects of x-ray diffraction is described in detail by James<sup>5</sup>.

The general features which are of use to us are most conveniently introduced by means of a few figures. In Figure 28(a) are shown several reciprocal lattice points which lie in the plane of the page. The circle shown is the intersection of this plane with the Ewald sphere. The Ewald sphere has a radius of  $1/\lambda$ , where  $\lambda$  is the x-ray wavelength, and is situated such that the origin of the reciprocal lattice lies on its surface and such that the line connecting its center to the origin is parallel to the direction,  $\vec{S}_0$ , of the incident beam of x-rays. A diffracted beam having an intensity proportional to  $J_0$  results when the reciprocal lattice is rotated such that some reciprocal lattice point (relp), designated by the indices  $(hkl)$ , also lies on the surface. This situation is shown in Figure 28(a). The diffracted beam is in the direction along  $\vec{S}$ , and  $\vec{S}/\lambda = (\vec{S} - \vec{S}_0)/\lambda$  coincides with the position vector,  $\vec{H}$ , of the point  $(hkl)$  and thus as mentioned earlier, satisfies equation (2-10).

Similarly each term of the sum in equation (A-10) is proportional to the intensity of x-rays scattered in a direction determined by  $\vec{S}$  such that  $\vec{S}/\lambda + \vec{g}$  is equal to  $\vec{H}$ . This situation is illustrated in Figure 28(b) where only one relp is shown.

### Present Experimental Geometry in Direct and Reciprocal Space

The features of the experimental geometry necessary for the discussion of the TDS contribution to our measured intensities are illustrated

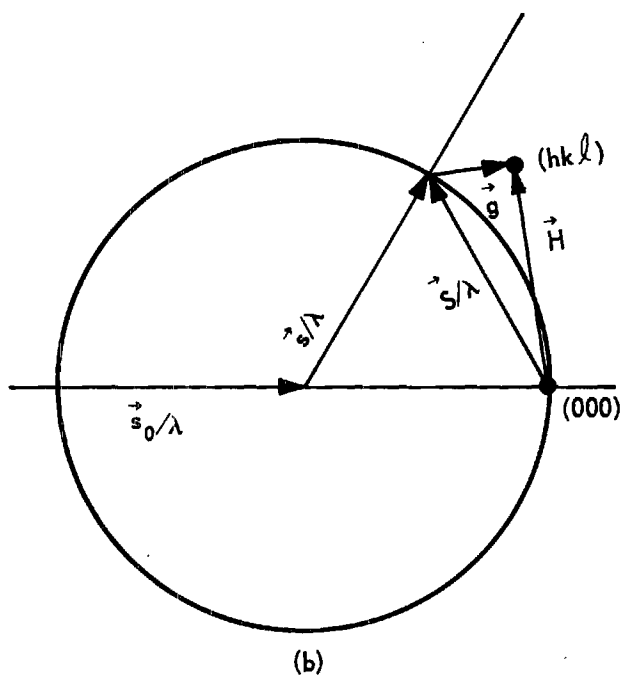
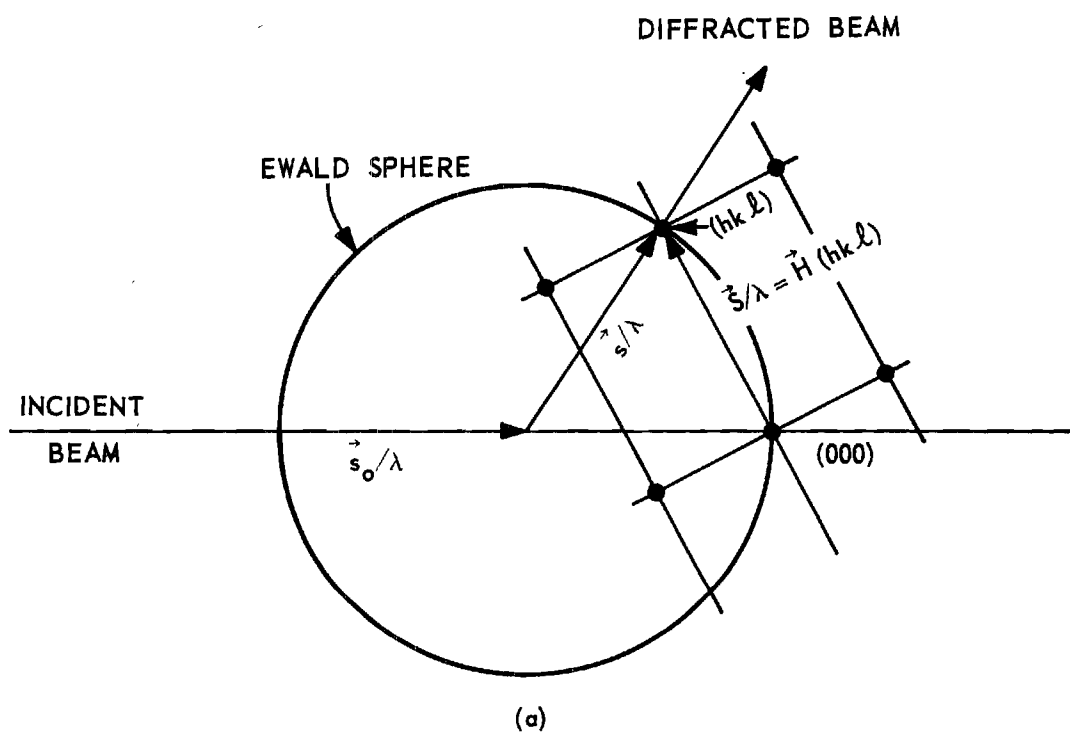


Figure 28. X-ray Scattering Viewed in Reciprocal Space.

in Figure 29. Consider two rays, A and B, in the plane of the page which have wavelength  $\lambda$ , originate at the extreme top and bottom, respectively, of the x-ray tube target projection, and travel to the volume element  $dv_1$  of an ideally perfect single crystal. Associated with these two rays, corresponding to two incident directions  $\vec{s}_0$ , are two Ewald spheres, portions of which are shown in Figure 30.

Any x-ray scattered into the counter window by the volume element  $dv_1$  whether it corresponds to a diffraction peak or TDS, has associated with it a vector  $\vec{S}/\lambda$  which terminates somewhere on or between these two spheres. We shall assume that the crystal is oriented so that all relps of interest lie in the plane of Figure 30. Similarly x-rays scattered by the volume element  $dv_2$  correspond to vectors  $\vec{S}/\lambda$  which terminate somewhere on or between the Ewald sphere associated with the rays C and D. If  $dv_1$  and  $dv_2$  are located respectively at the extreme bottom and extreme top of the sample, the entire sample can contribute to the diffracted beam only when the  $(hkl)$  relp is located in the region which is common to the two sets of Ewald spheres defined by the rays A, B, C, and D. This region is shown shaded in Figure 30.

The intensity measurements in the present study were obtained as the crystal was oscillated through the optimum diffracting position, that is, as the  $(hkl)$  relp was made to pass back and forth through the shaded region in Figure 30. The diffraction peak intensity, taken as the maximum intensity measured during such a pass, presumably corresponds to the time that the relp is in the center of the shaded region. When the crystal is so oriented, the counter detects all TDS that originates

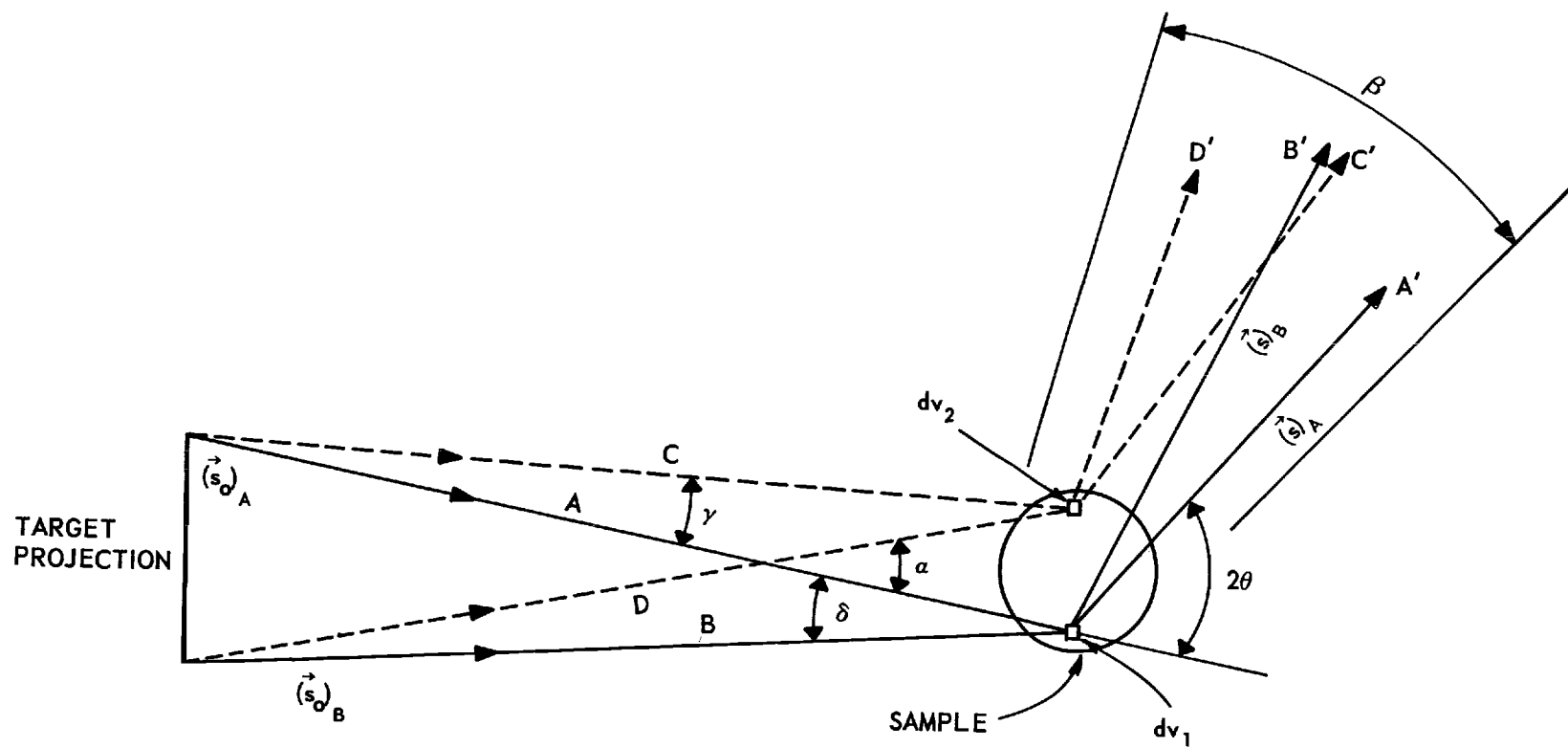


Figure 29. Present Experimental Geometry in Direct Space.



in a region surrounding the relp which, in the present experiment, is approximately coin shaped. This region has a radius determined by  $\beta$ , the angle subtended at the sample by the counter window, and a height determined by the sum of (1)  $\delta$ , the angle subtended at the sample by the x-ray target, and (2)  $\gamma$ , the angle subtended at the x-ray target by the sample (see Figure 29). The intersection of this region with the plane of incidence is illustrated in Figure 30 with the lines ab, bc, cd, and da. The x-rays which can enter the stationary counter window and which result from scattering of the incident ray A have a different average value of scattering angle  $2\theta$  than do those which result from scattering of ray D. Thus the top of the region of interest, indicated by the line ad in Figure 29, is offset from the bottom, indicated by the line bc, as shown in Figure 30<sup>\*</sup>. The amount of offset is determined by the sum of (1) the angle  $\delta$ , (2) the angle  $\gamma$ , and (3) the angle subtended at the counter by the sample. In the present experiment this offset was less than 20% of the diameter of the region of interest. Thus to simplify the calculations which are described later we assume that this offset can be neglected. In addition we assume that the curvature of the Ewald sphere within the region just described can be neglected. With these assumptions we can replace the region described above by a right circular cylinder.

The validity of these assumptions is difficult to establish theoretically. However in view of the good agreement obtained between the calculated and measured TDS contributions to the (10,00) Bragg reflection

---

\*The two lines in Figure 30 which form the angle  $\beta$  illustrate the  $2\theta$  range for the detected x-rays which result from scattering of the incident central ray which joins the center of the x-ray target with the center of the sample.



of AgCl (see Chapter III) these assumptions, and several others to be discussed later, either (1) are sufficiently valid for our purposes or (2) produce compensating errors.

A typical diffuse scattered ray is shown in Figure 30. The displacement from the reip of the associated  $\vec{S}_D/\lambda$  vector, D standing for diffuse scattering, is determined by  $\vec{g}$ . The intensity of this scattered ray can be determined from equation (A-10) by summing over  $\vec{g}$  and  $\alpha$  with  $\vec{S}/\lambda = \vec{S}_D/\lambda$ . The total diffuse intensity which is detected during a peak height measurement is then obtained by summing the contributions from all vectors  $\vec{S}_D/\lambda$  which terminate somewhere in the volume described above.

#### One Phonon TDS Contribution and Dependence on Experimental Parameters

With the use of equation (2-14) and (A-2), equation (A-10) can be rewritten as

$$J_1(\vec{S}_D/\lambda) = \frac{|F|^2 e^{-2M}}{4\pi^2 N m} \sum_{\vec{g}, \alpha} (\kappa \vec{S}_D \cdot \vec{e}(\vec{g}, \alpha))^2 \frac{E(v(\vec{g}, \alpha))}{v^2(\vec{g}, \alpha)} I_0(\vec{S}_D/\lambda + \vec{g}) \quad (A-12)$$

The sum over  $\vec{g}$  can be changed to an integral by insertion of the number of waves which have wave vectors between  $\vec{g}$  and  $\vec{g} + d\vec{g}$ . This number is independent of  $\vec{g}$  and is equal to  $V dv^{14}$ , where  $V$  is the volume of the crystal and  $dv$  is a volume element,  $dx dy dz$ , of reciprocal space. The evaluation of this integral is described in detail by James<sup>5</sup>. The result is

$$J_1(\vec{g}) = \frac{N|F|^2 e^{-2M}}{m} \frac{\sin^2 \theta}{\lambda^2} \sum_{\alpha} \cos^2(\theta(\vec{S}_D, \vec{e})) \frac{E(v(\vec{g}, \alpha))}{v^2(\vec{g}, \alpha)} \quad (A-13)$$

where we have substituted  $V = Na^3$ ,  $|\vec{S}_D| = 2 \sin \theta$ , and  $N' = 4N$ , its value for a f.c.c. crystal such as Al.  $\theta(\vec{S}_D, \vec{e})$  is the angle between  $\vec{S}_D$  and  $\vec{e}(\vec{g}, \alpha)$ .  $J_1(\vec{g})$  is the distribution function for the diffuse scattering power density in reciprocal space and  $\vec{g}$  is the vector which joins the relp with the maximum of  $I_0(\vec{S}_D/\lambda + \vec{g})$ .

The diffuse intensity will naturally depend on the intensity incident on the crystal and, according to equation (A-13), to the number of contributing unit cells in the crystal. On the basis of the discussion of Figure 30, the diffuse intensity corresponding to a particular point in the reciprocal lattice volume "seen" by the counter will depend on how much of the crystal can contribute to that point and, since the target illumination is not necessarily uniform, on the point on the target from which the scattered ray originated. For example, if the point lies on the Ewald sphere designated A in Figure 30, the diffuse scattering at that point arises only from x-rays which originate at the extreme top of the target projection and which are scattered by the extreme bottom of the sample. Thus before we can integrate  $J_1$  to obtain the total diffuse scattering observed, a function, say  $w(\vec{g})$ , must be derived which will "weight" each point in the reciprocal lattice volume of interest according to the incident intensity and the volume of the sample which contributes to the diffuse scattering at each point.

To begin we shall neglect absorption and mosaic spread and assume that volume elements in the crystal which lie on any given line perpendicular to the plane of Figure 29 and points on the target projection which lie on any other given line perpendicular to the same plane contribute

scattering to only one Ewald sphere. That is, we neglect crossfire of the beam perpendicular to the plane of incidence since rotation of an incident ray out of the plane of Figure 30 merely slides the corresponding Ewald sphere nearly along its own surface (in the vicinity of the reciprocal lattice volume of interest) in a direction perpendicular to the plane of Figure 30. We shall further assume that the crystal size is small compared to the distance of the crystal from the target, so that the angle,  $\delta$ , which defines the beam convergence for each volume element is the same for all volume elements.

The derivation of the desired weighting function will proceed most easily with the aid of several additional figures. In Figure 31 is shown an example of a target intensity distribution projected on a vertical line in the target projection. The sample will be divided into horizontal layers of thickness  $\Delta Z_1$  as shown. According to the above assumptions the volume of each layer may be projected onto a vertical line through the sample to give the sample volume distribution along the Z direction.

In Figure 32 is shown an enlarged view of the reciprocal space volume of interest. It is convenient to define a cartesian coordinate system with its origin at the  $(hkl)$  relp. The z axis is perpendicular to the surface of the Ewald sphere which passes through the center of the  $(hkl)$  relp and the x and y axes are tangent to the same sphere. Referring to Figure 32, a small rotation of an incident ray about an axis perpendicular to the page corresponds to a displacement of the surface of the Ewald sphere in a direction which makes an angle  $\theta$  with the perpendicular to the sphere's surface for  $2\theta$  angles which are not too large.

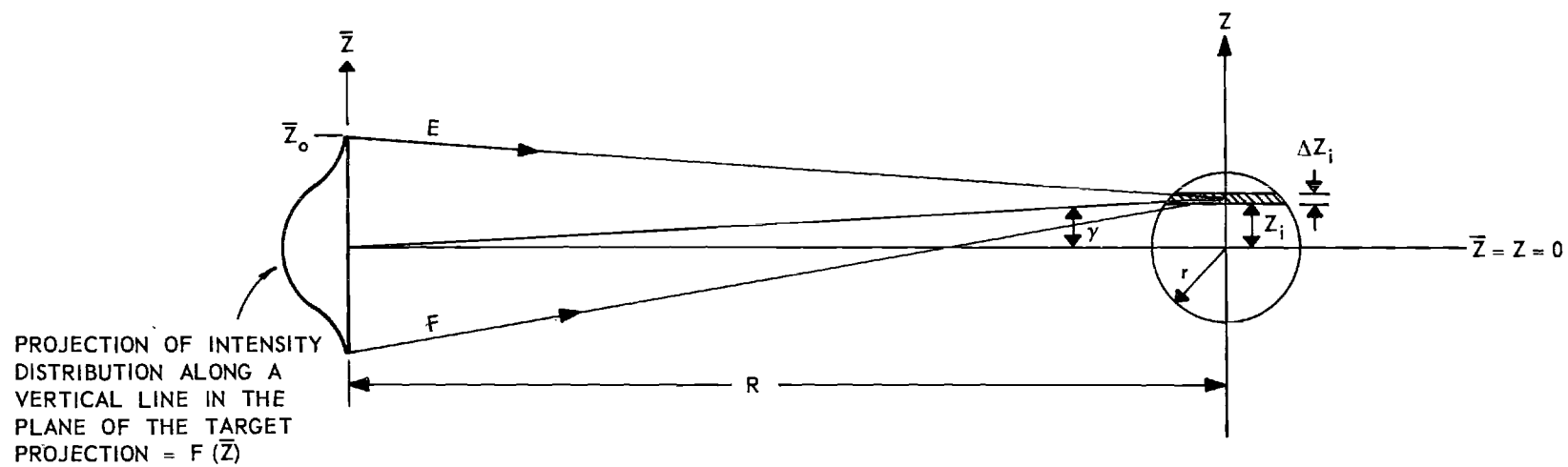


Figure 31. Direct Space Source of Typical Component of  $w(z)$ .

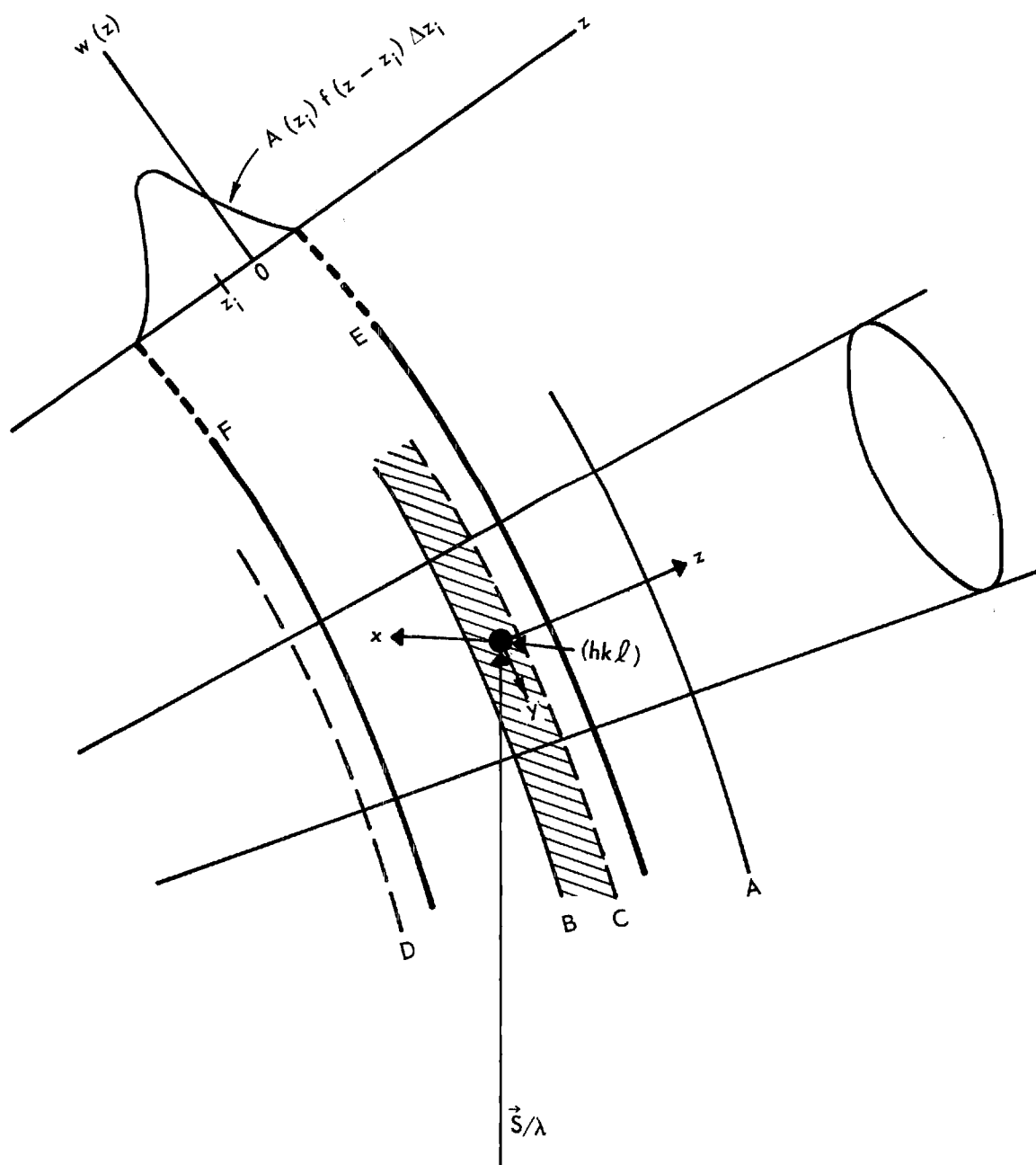


Figure 32. Typical Component of  $w(z)$ .

(Obviously this is not true for  $2\theta \rightarrow 180^\circ$  since the axis of rotation in reciprocal space passes through the origin.) If we assume that  $2\theta$  for all the Bragg peaks observed in the present study are sufficiently small, distances along  $z$  can be simply related to  $Z$  and  $\bar{Z}$ , actually  $|Z - \bar{Z}|$ , via the angle which a ray that joins  $\bar{Z}$  and  $Z$  makes with any horizontal line joining the points  $\bar{Z} = Z$ . So for  $\bar{Z} = Z$ ,  $Z = 0$ . For example, for the ray in Figure 31 which joins  $\bar{Z} = 0$  to  $Z = Z_i$ , one can easily verify that

$$z_i = (\gamma/\lambda) \sin 2\theta \quad . \quad (A-14)$$

Projection of the target intensity and the sample volume onto  $\bar{Z}$  and  $Z$  respectively results in a weighting function which depends only on  $z$ , i.e.,  $w(\vec{g}) = w(g_z) = w(z)^*$ . The contribution of the volume of the crystal within the  $\Delta Z_i$  shown in Figure 31 to the total weighting function is illustrated in Figure 32. It lies entirely between the Ewald spheres E and F, is centered about the point  $z = z_i$ , and has a shape which is related to the shape of the target intensity distribution,  $F(\bar{Z}) \rightarrow f(z-z_i)$ , multiplied by the volume of the crystal within  $\Delta Z_i$ ,  $a(Z_i)\Delta Z_i \rightarrow A(z_i)\Delta z_i$ . Thus formally we have,

$$w(z) = \sum_{i=1}^{\ell} A(z_i) f(z-z_i) \Delta z_i$$

( $\ell$  = number of sample layers) which for  $\ell \rightarrow \infty$  and  $\Delta Z_i$  or  $\Delta z_i \rightarrow 0$  can be written,

---

\* Actually we are assuming that the sample is either a sphere or a right circular cylinder with its axis perpendicular to the plane of Figure 31. Otherwise the projection of the sample volume onto  $Z$  would be dependent on  $\theta$ .

$$w(z) = \int A(z') f(z-z') dz' \quad (A-15)$$

The limits on  $z'$  will depend on the sample size.

The intensity distribution along  $\bar{Z}$  for the x-ray tube used in the present study has been experimentally determined and is shown sketched in Figure 33(a). To a good approximation this distribution could be represented by the trapezoid shown. The trapezoid could in turn be approximated by a series of rectangles stacked as shown in Figure 33(b). Actual calculation of the one phonon TDS contribution using rectangles of various widths yielded a result which was a nearly linear function of the width. This means that the TDS contribution obtained by summing  $n$  calculations based on  $n$  uniform intensity distributions each having a height  $I/n$  and appropriate widths to give a trapezoidal shape is the same as that obtained by assuming the intensity distribution to be uniform with height  $I$  over a width which is equal to the average width of the trapezoid.

If we use a uniformly illuminated target projection and assume that the sample is a sphere, the function  $w(z)$  can be determined without formally carrying out the integration as indicated in equation (A-15). In Figure 34, some of the contributions to  $w(z)$  are shown separated for the case of a uniformly illuminated target and spherical sample. Each rectangle represents the contribution from a layer of the sample such as illustrated earlier in Figures 31 and 32. For a spherical sample of radius  $r$  as shown in Figure 31, the layers are cylinders having a height  $\Delta z_i$  and a volume equal to  $\pi(r^2 - z_i^2)\Delta z_i$ . If  $\Delta z_i$  is the same for all

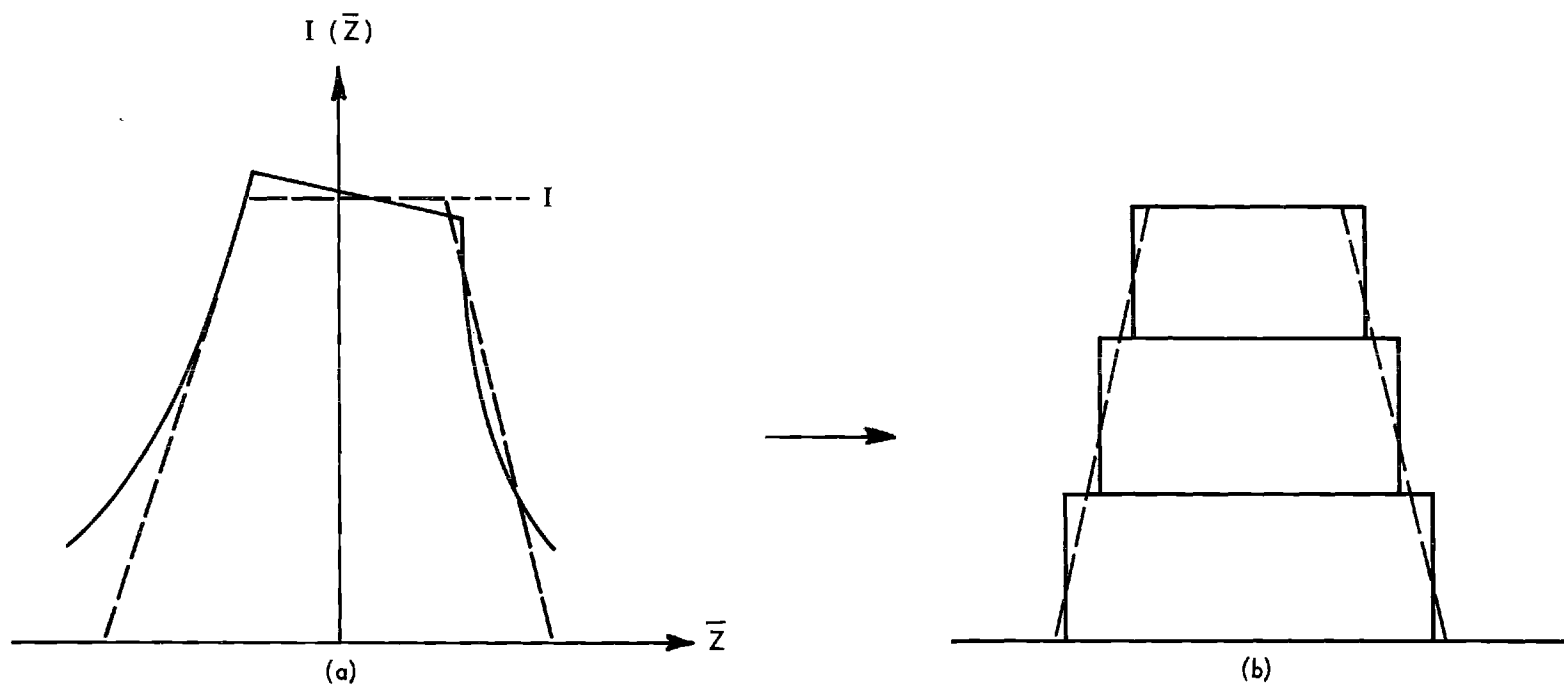


Figure 33. Intensity Distribution in X-ray Target Projection.



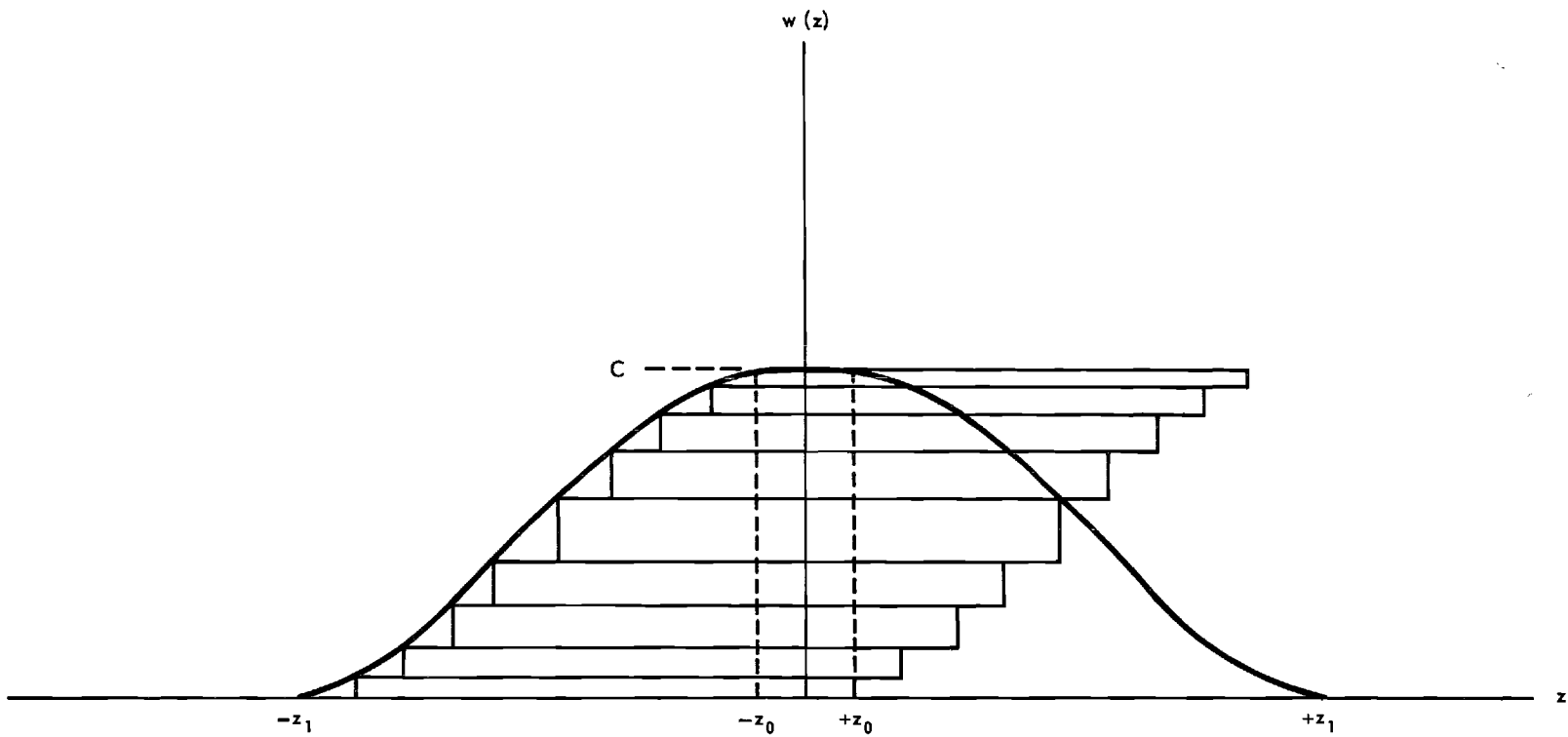


Figure 34. The Function  $w(z)$  for a Spherical Sample.

layers, the heights of the corresponding rectangles, being proportional to the layer volume, will vary as illustrated in Figure 34. Then for any  $z = z'$ ,  $w(z')$  is equal to the sum of the heights of the rectangles which can contribute to  $w(z')$ , i.e., as discussed earlier,  $w(z')$  is proportional to the volume of the crystal which can contribute diffuse scattering at  $z'$ . Between  $-z_0$  and  $+z_0$  the entire crystal contributes to  $w(z)$ ; corresponding to the shaded region of Figures 30 and 32. As  $z$  increases above  $z_0$  (or decreases below  $-z_0$ ), the decrease in  $w(z)$  from its maximum value is proportional to the volume of the sample between  $Z = r$  and  $Z = r - s$  such as indicated in Figure 35.

From equation (A-14), with  $\gamma$  expressed in terms of  $\bar{Z}$ ,  $Z$ , and  $R$ , one obtains

$$z = \frac{|\bar{Z}_0 - Z|}{R\lambda} \sin 2\theta, \text{ for } z_0 \leq z \leq z_1.$$

If  $s$  is used the absolute value signs can be removed to yield, for  $z_0 \leq z \leq z_1$ ,

$$z = \frac{(\bar{Z}_0 - r + s)}{R\lambda} \sin 2\theta = z_0 + \frac{s}{R\lambda} \sin 2\theta \quad (\text{A-16})$$

Now the volume of the sample between  $Z = r$  and  $Z = r - s$  is

$$V(s) = \pi s^2 \left( r - \frac{1}{3} s \right) \quad (\text{A-17})$$

Then for  $z \geq z_0$ ,  $w(z)$  is

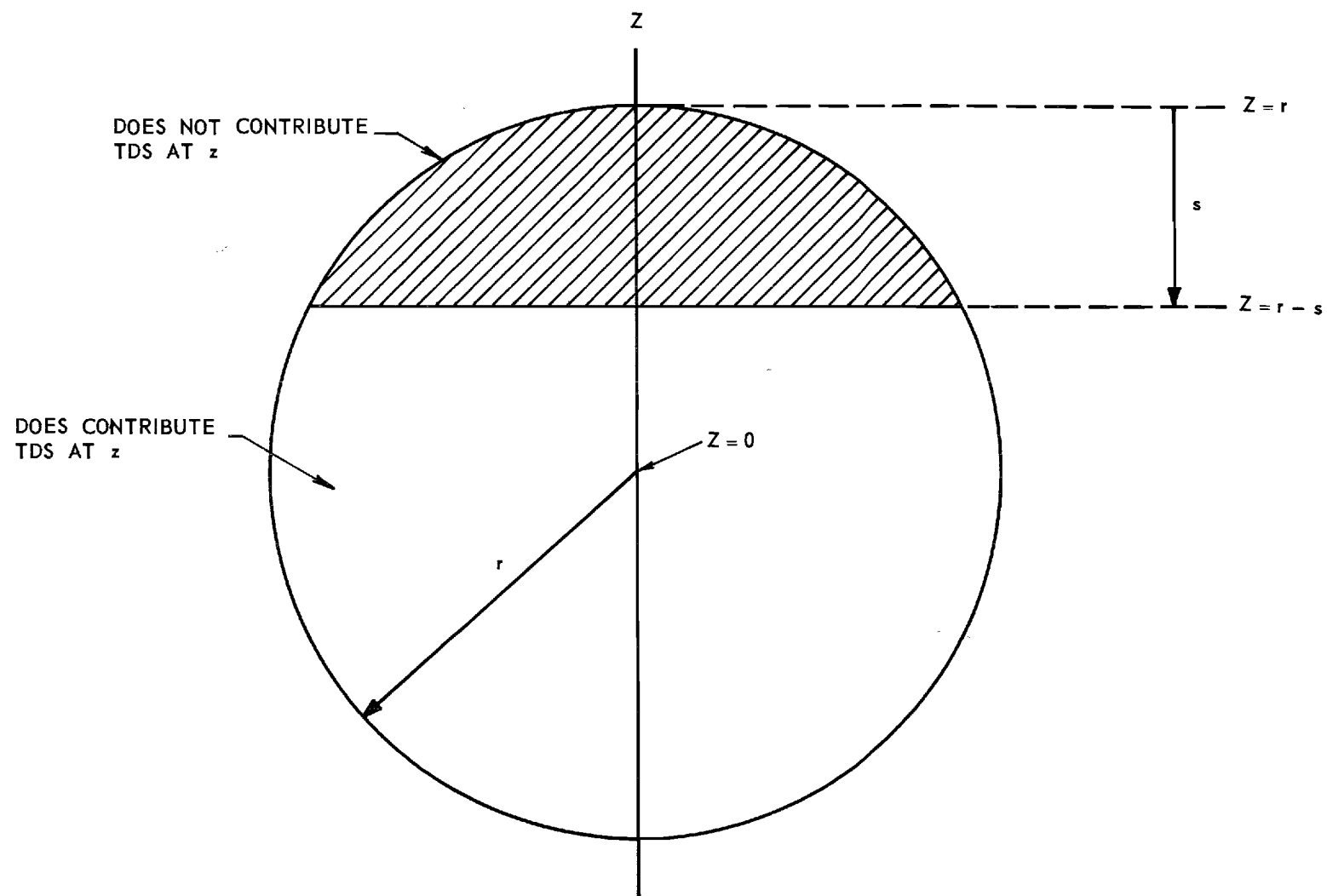


Figure 35. Fraction of Crystal Volume Which Contributes to TDS.

$$w(z) = C \left[ 1 - \frac{\pi(z-z_0)^2 \left( \frac{\lambda R}{\sin 2\theta} \right)^2 \left( \frac{\lambda R}{\sin 2\theta} (z'-z_0) - \frac{1}{3} \frac{\lambda R}{\sin 2\theta} (z-z_0) \right)}{\frac{4}{3} \pi \left( \frac{\lambda R}{\sin 2\theta} \right)^3 (z'-z_0)^3} \right], \quad (A-18)$$

or simplified,

$$w(z) = C \left\{ 1 - \frac{3}{4} \frac{(z-z_0)^2}{(z'-z_0)^3} \left[ (z'-z_0) - \frac{1}{3} (z-z_0) \right] \right\}, \quad (A-19)$$

and for  $0 \leq z \leq z_0$ ,  $w(z) = C$ , where we have used (A-17) and  $z' = z_0 + \frac{r}{R} \sin 2\theta$ . The second term in equation (A-18) is actually the fraction of the sample which does not contribute diffuse scattering at  $z$ .  $C$  can be determined by considering the fact that the integral of  $w(z)$  from  $-z_1$  to  $+z_1$  must be equal to the product  $IN$ , where  $I$  is the total intensity incident on the sample, and  $N$  is the total number of unit cells in the sample. Thus since the width of the  $w(z)$  versus  $z$  curve is directly proportional to  $(\sin 2\theta/\lambda)$  and since  $IN$  is independent of  $2\theta$ .  $C$  must be equal to  $I\lambda(\sin 2\theta)^{-1}$ .  $N$  is not included here since it is already included in equation (A-13).

To determine how much of the observed diffraction peak intensity is due to TDS, we must first determine how much of the observed intensity is due to  $J_0$ . To obtain the integrated intensity of a diffraction peak we will follow the technique described by James<sup>5</sup> for a non-absorbing crystal. Both  $J_0$  and  $J_1$  have to be multiplied by

$$\left( \frac{e^2}{mc^2} \right)^2 \frac{1 + \cos^2 2\theta}{2R^2} = \frac{B}{R^2}, \quad (A-20)$$

where  $R$  is the distance from the crystal at which the scattered intensity is measured. Since  $R^2 d\Omega$  is the area intercepted by a solid angle  $d\Omega$  on the surface of a sphere of radius  $R$ , the total energy diffracted by the sample is

$$I_o = \frac{B}{R^2} \int J_o R^2 d\Omega w(z) dz \quad (A-21)$$

If  $d\Omega$  is expressed in reciprocal space we have, on the surface of the Ewald sphere,  $d\Omega = \lambda^2 dx dy$ . As mentioned earlier, the  $x$  and  $y$  axes are tangent to the Ewald sphere. Thus we have

$$I_o = \lambda^2 B \int |F|^2 e^{-2M} I_o(\vec{S}/\lambda) w(z) dx dy dz \quad (A-22)$$

The function  $I_o(\vec{S}/\lambda)$  is sharply peaked at  $\vec{S}/\lambda = \vec{H}(hkl)$  (see equation (2-10)). The other functions in the integral vary relatively slowly with  $\vec{S}/\lambda$  so that in performing the integration we may take them as constant with values corresponding to  $\vec{S}/\lambda = \vec{H}(hkl)$ . The remaining integration of  $I_o(\vec{S}/\lambda)$  yields<sup>5</sup>  $N/a^3$ , where  $N$  is the number of unit cells in the crystal and  $a$  is the lattice parameter. Equation (A-22) then becomes

$$I_o = \lambda^2 B |F|^2 e^{-2M} w(0) N/a^3, \quad (A-23)$$

or finally,

$$I_o = \frac{I \lambda^3 B N |F|^2 e^{-2M}}{a^3 \sin 2\theta} \quad (A-24)$$

The integration of  $J_1$  proceeds similarly. The following approximations will be made:

1. The wave vectors  $\vec{g}$  which contribute to TDS in the vicinity of a relp are relatively small and correspond to long wavelength normal modes. For these modes the dispersion curves,  $v$  versus  $|\vec{g}|$ , are linear and it should be a good approximation to set  $v(\vec{g}, \alpha) = |\vec{g}|V_\alpha$ , where  $V_\alpha$  is the velocity of the waves of branch  $\alpha$ .  $V_\alpha$  will be determined from measured elastic constants.

2. Since  $|\vec{g}|$  and hence  $v$  are small,  $h\nu \ll kT$ , and hence  $E(v) \approx kT$  for temperatures between  $100^\circ$  and  $300^\circ$  K.

3. We will assume that the isofrequency contours are spherical near a relp. This assumption is quite good for many cubic solids. For example, the variation of  $V_\alpha$  with direction for the solids studied here is no greater than  $\pm 15\%$ .

4. With assumption 3 the only direction dependent quantity in equation (A-13) is  $\cos^2(\theta(\vec{S}_D, \vec{e}))$ . If we consider the total TDS intensity in a spherical shell of radius  $|\vec{g}|$ ,  $\cos^2(\theta(\vec{S}_D, \vec{e}))$  can be replaced by its average value,  $1/3$ , since in such a shell all possible orientations of  $\vec{e}(\vec{g}, \alpha)$  with respect to  $\vec{S}_D$  occur with equal probability. Unfortunately the region throughout which  $J_1$  must be integrated is not spherical. However, we will assume that for each value of  $|\vec{g}|$  in the actual region sufficiently many different orientations of  $\vec{e}(\vec{g}, \alpha)$  with respect to  $\vec{S}_D$  occur so that  $\cos^2(\theta(\vec{S}_D, \vec{e}))$  may be replaced by  $1/3$  in equation (A-13).

Equation (A-13) then becomes,

$$J_1 = \frac{N|F|^2 e^{-2M}}{3m} \frac{\sin^2 \theta}{\lambda^2} kT \sum_{\alpha=1}^3 \frac{1}{g^2 v_{\alpha}^2} \quad (\text{A-25})$$

Multiplying this expression by  $B/R^2$  and integrating, as indicated in (A-21) with  $J_0$  replaced by  $J_1$ , one obtains

$$I_1 = \frac{I \lambda^3 B N |F|^2 e^{-2M}}{\sin 2\theta} \left( \frac{\sin \theta}{\lambda} \right)^2 \frac{kT}{3m} \sum_{\alpha=1}^3 \frac{1}{v_{\alpha}^2} \int \frac{h(z) dx dy dz}{g^2} \quad (\text{A-26})$$

where we have set  $w(z) = h(z) I \lambda / \sin 2\theta$ . If we assume that the curvature of the Ewald sphere is negligible within the solid angle subtended at the crystal by the counter aperture, the region throughout which the integration must be performed can be considered a cylinder having a height determined by the maximum cross fire in the incident x-ray beam and a radius determined by the size of the counter window. It is therefore desirable to introduce cylindrical coordinates. The integral in equation (A-26) then becomes, with  $g^2 = z^2 + r^2$ ,

$$J_1 = 2\pi \int \frac{h(z) r dr dz}{z^2 + r^2} \quad (\text{A-27})$$

The radius of the cylinder is  $\beta/2\lambda$ , where  $\beta$  is the angle subtended at the crystal by the counter window. One then obtains

$$J_1 = \pi \int_{-z_1}^{z_1} [\ln(z^2 + r^2)]_0^{\beta/\lambda} h(z) dz$$

or,

$$\mathcal{J}_1 = 2\pi \int_0^{z_1} [\ln(z^2 + \beta^2/4\lambda^2) - \ln z^2] h(z) dz \quad (\text{A-28})$$

The limits for  $z$  are changed since  $h(z)$  is symmetric about  $z = 0$  and we have obtained  $h(z)$  only for  $0 \leq z$ . It turns out that for the experimental geometry used in the present study,  $z_1 \ll \beta/2\lambda$ . Thus little error (less than 1/2 percent) is introduced by neglecting  $z^2$  in the first term of the integrand. With this approximation the integration is straightforward and yields the following results,

$$\begin{aligned} \frac{1}{\pi} \mathcal{J}_1 &= \left( \frac{\delta + \gamma}{\gamma} \right)^3 (3\gamma - \delta) \frac{\sin 2\theta}{16\lambda} \ln \left[ \frac{\beta^2}{(\delta + \gamma)^2 \sin^2 2\theta} \right] \\ &+ \left( \frac{\delta - \gamma}{\gamma} \right)^3 (3\gamma + \delta) \frac{\sin 2\theta}{16\lambda} \ln \left[ \frac{\beta^2}{(\delta - \gamma)^2 \sin^2 2\theta} \right] \\ &+ \frac{\delta + \gamma}{\gamma} \left[ \frac{19}{6} \delta^3 - \frac{101}{12} \delta^2 (\delta - \gamma) + \frac{145}{24} \delta (\delta - \gamma)^2 - \frac{21}{16} (\delta - \gamma)^3 \right] \frac{\sin 2\theta}{2\lambda} \\ &+ \left( \frac{\delta - \gamma}{\gamma} \right)^3 \left[ \frac{11}{6} \delta - \frac{21}{16} (\delta - \gamma) \right] \frac{\sin 2\theta}{2\lambda} \end{aligned} \quad (\text{A-29})$$

where  $\delta$  is the angle subtended at the sample by the target and  $\gamma$  is the angle subtended at the target by the sample (see Figure 29).

Equation (A-29) is rather unwieldy and hence we found it desirable to investigate the possibility of obtaining a simpler expression for  $\mathcal{J}_1$  which is adequate for our purposes. A surprisingly good approximation



to  $\mathcal{Q}_1$  is obtained by setting  $h(z)$  equal to 1 over the range  $-z'$  to  $z'$ . With regard to the form of  $h(z)$ , this is equivalent to neglecting the effect of the sample's size and shape\*. The expression obtained for  $\mathcal{Q}_1$  is then,

$$\mathcal{Q}_1 = \pi \left\{ \frac{\delta \sin 2\theta}{\lambda} \ln \left( 1 + \frac{\beta^2}{\delta^2 \sin^2 2\theta} \right) + \frac{2\beta}{\lambda} \tan^{-1} \left( \frac{\delta \sin 2\theta}{\lambda} \right) \right\} \quad (\text{A-30})$$

For  $\beta = 7.0 \times 10^{-2}$  rad.,  $\delta = 7.6 \times 10^{-3}$  rad.,  $\gamma = 3.8 \times 10^{-3}$  rad. and  $\sin 2\theta \cong 1$ , values which apply to our experimental geometry and the (800) reflection of aluminum, the following results are obtained: for equation (A-29),  $\mathcal{Q}_1 = \pi 6.7 \times 10^6$ ; for equation (A-30),  $\mathcal{Q}_1 = \pi 6.9 \times 10^6$ . The simplified equation seems adequate, therefore.

Some experimental measurements, which were described in Chapter III were made to check the validity of TDS calculations which were based on the one phonon contribution described above and on the two phonon contribution to be discussed later. The measurements include the determination of the intensity scattered by the sample when it is rotated a few degrees from the diffraction peak. Thus it is necessary to calculate  $\mathcal{Q}_1$  for the case when  $h(z)$  is symmetrically situated about some point, say  $z''$ , rather than  $z = 0$ . For the case of the simplified  $h(z)$  used to obtain equation (A-29) we merely have to change the integration limits of equation (A-28) to go from  $z'' - z'$  to  $z'' + z'$ . The result, written

---

\* Another effect of the sample's size and shape on the TDS calculations was neglected earlier. Recall that in Figure 29 the offset of the line ad from the line bc depends on the angle subtended by the sample at the counter and that this offset has been neglected.

in terms of  $\delta$  and  $\Delta$ , the angle in radians through which the sample is rotated off the diffraction peak, is

$$\begin{aligned} \frac{1}{\pi} \mathcal{J}_1(\Delta) = & \frac{\sin 2\theta}{\lambda} (\Delta + \delta/2) \ln \left[ 1 + \frac{\beta^2}{4(\Delta + \delta/2)^2 \sin^2 2\theta} \right] \\ & - \frac{\sin 2\theta}{\lambda} (\Delta - \delta/2) \ln \left[ 1 + \frac{\beta^2}{4(\Delta - \delta/2)^2 \sin^2 2\theta} \right] \\ & + \frac{\beta}{\lambda} \tan^{-1} \left[ \frac{2\beta\delta \sin 2\theta}{\beta^2 + 4(\Delta + \delta/2)(\Delta - \delta/2) \sin^2 2\theta} \right] \quad (\text{A-31}) \end{aligned}$$

In addition, since a measurement of the background intensity is required to determine the true diffraction peak intensity, it is necessary to calculate the TDS contribution to a background measurement. This could be done with equation (A-31) by inserting the appropriate  $\Delta$ . It is, however, expected that the TDS contribution to the background will be small. Thus for the purpose of simplification it will be assumed that the background contribution can be obtained by considering the solid angle subtended at the relp by the cylindrical region used above when it is a distance, say  $\bar{z}$ , from the relp, where  $\bar{z}$  is determined by the angle through which the sample is rotated for a background measurement. Thus

$$\mathcal{J}_1(B_g) = \int_{\bar{z}-z'}^{\bar{z}+z'} \left( \frac{1}{g^2} \right) g^2 d\Omega \quad (\text{A-32})$$

where  $d\Omega$  is the solid angle. Now  $d\Omega = (\text{area of the cylinder's base})/\bar{z}^2 = \pi(\beta/2\lambda)^2/\bar{z}^2$ . In terms of  $\Delta$ , one obtains

$$\oint_1(B_g) = \frac{\pi\delta\beta^2}{8\lambda\Delta^2} \cot \theta \quad (\text{A-33})$$

### Two Phonon TDS Contributions

For the case of one atom per lattice point, the two phonon scattering is proportional to<sup>39</sup>

$$J_2 = \frac{1}{2} |F|^2 e^{-2M} \sum_{\vec{g}, \alpha} \sum_{\vec{h}, \delta} G(\vec{g}, \alpha) G(\vec{h}, \delta) I_0(\vec{S}/\lambda + \vec{g} + \vec{h}) \quad (\text{A-34})$$

where  $\vec{h}$  and  $\delta$  denote the wave vector and branch respectively. If the same assumptions are made which lead to equation (A-25), one obtains

$$J_2 = \frac{1}{2} |F|^2 e^{-2M} \left( \frac{\sin \theta}{\lambda} \right)^4 \left( \frac{kT}{3mN} \sum_{\alpha} \frac{1}{v_{\alpha}^2} \right)^2 \int \frac{d\vec{h}}{|\vec{h}|^2} \int \frac{I_0(\vec{S}/\lambda + \vec{g} + \vec{h}) d\vec{g}}{|\vec{g}|^2} (Na^3)^2 \quad (\text{A-35})$$

According to Paskin<sup>39</sup> the integration yields  $N \pi^3/a^3 \rho$ , where  $\rho$  is the distance in reciprocal space from the reip nearest the point at which the diffuse scattering is measured. Integration of  $J_2$  throughout the volume described above in the one phonon calculation then yields

$$I_2 = \frac{I\lambda^3 B Na^3 |F|^2 e^{-2M}}{\sin 2\theta} \left( \frac{\sin \theta}{\lambda} \right)^4 \left( \frac{kT}{3m} \sum_{\alpha} \frac{1}{v_{\alpha}^2} \right)^2 \frac{J_2}{2} \quad (\text{A-36})$$

where

$$\mathcal{Q}_2 = \pi^3 \int \frac{h(z) dx dy dz}{\rho} \quad (\text{A-37})$$

Assuming again, that  $h(z)$  can be replaced by 1 between  $-z'$  and  $+z'$  and changing to cylindrical coordinates, one obtains

$$\begin{aligned} \mathcal{Q}_2 = \pi^4 \left\{ \frac{\delta \sin 2\theta}{2\lambda} \left( \beta^2 + \delta^2 \sin^2 2\theta \right)^{1/2} \right. \\ \left. + \frac{\beta^2}{4\lambda^2} \ln \left[ \frac{(\beta^2 + \delta^2 \sin^2 2\theta)^{1/2} + \delta \sin 2\theta}{(\beta^2 + \delta^2 \sin^2 2\theta)^{1/2} - \delta \sin 2\theta} \right] \right\} . \quad (\text{A-38}) \end{aligned}$$

When  $h(z)$  is symmetric about  $z'' = (\Delta \sin 2\theta)/\lambda$ ,

$$\begin{aligned} \mathcal{Q}_2 = \pi^4 \left\{ \frac{\sin 2\theta}{2\lambda^2} (\Delta + \delta/2) A - \frac{\sin 2\theta}{2\lambda^2} (\Delta - \delta/2) B \right. \\ \left. + \frac{\beta^2}{4\lambda^2} \ln \left[ \frac{2(\Delta + \delta/2) \sin 2\theta + A}{2(\Delta - \delta/2) \sin 2\theta + B} \right] - \frac{\sin^2 2\theta}{\lambda^2} \delta \Delta \right\} , \quad (\text{A-39}) \end{aligned}$$

where

$$A = [\beta^2 + (2(\Delta + \delta/2) \sin 2\theta)^2]^{1/2} ,$$

and

$$B = [\beta^2 + (2(\Delta - \delta/2) \sin 2\theta)^2]^{1/2} .$$

And finally for the two-phonon contribution to the background,

$$J_2(\text{Bg}) = \frac{\pi^4 \delta \beta^2}{4 \Delta \lambda^2} \cos \theta \quad . \quad (\text{A-40})$$

### Total Observed Intensity

The total intensity observed at the diffraction peak is obtained by adding  $I_0$ ,  $I_1$  and  $I_2$ , which gives

$$I(\text{obs}) = I_0 \left( 1 + \sigma^2 J_1 + \frac{1}{2} \sigma^2 J_2 \right) \quad , \quad (\text{A-41})$$

where

$$\sigma = \frac{a^3 k}{3m} \sum_{\alpha=1}^3 \frac{1}{v_{\alpha}^2} \quad , \quad (\text{A-42})$$

$$\phi = \frac{\sin^2 \theta}{\lambda^2} \quad ,$$

and  $I_0$  is given in equation (A-24). The intensity above background is obtained by subtracting from  $J_1$  and  $J_2$ ,  $J_1(\text{Bg})$  and  $J_2(\text{Bg})$  respectively. The value of  $\sigma$  will depend on the material studied and is discussed later. The contribution of TDS to the temperature derivative of  $\ln I(\text{obs})$  has been discussed in Chapter III.

### Two Atoms per Lattice Point

#### One Phonon Scattering Theory

One phonon scattering theory for a crystal with two atoms per lattice point is very similar to the theory discussed above for the case of

one atom per lattice point. The difference arises from the facts (1) that the vibrational amplitudes and phases for the two atoms are not necessarily the same and (2) that there are optic vibration modes which have to be considered.

If we let (see equation (2-69)),

$$a_j(\vec{g}, \alpha) = c_j(\vec{g}, \alpha) a(\vec{g}, \alpha) \quad ,$$

then for two atoms per lattice point one obtains

$$J_1 = \frac{1}{2} \sum_{\vec{g}, \alpha} G(\vec{g}, \alpha) \left[ \left( \sum_j f_j c_j(\vec{g}, \alpha) e^{-M_j} e^{2\pi i (\vec{S}/\lambda + \vec{g}) \cdot \vec{\rho}_j} \right)^2 I_0(\vec{S}/\lambda + \vec{g}) \right. \\ \left. + \left( \sum_j f_j c_j(\vec{g}, \alpha) e^{-M_j} e^{2\pi i (\vec{S}/\lambda - \vec{g}) \cdot \vec{\rho}_j} \right)^2 I_0(\vec{S}/\lambda - \vec{g}) \right] \quad . \quad (A-43)$$

We consider now only the term multiplying  $I_0(\vec{S}/\lambda + \vec{g})$  and multiply it by two since the second term will give the same contribution as for the monatomic case. Performing the sum over  $j$  for a f.c.c. lattice such as AgCl and KCl one obtains

$$16 \sum_{\vec{g}, \alpha} G(\vec{g}, \alpha) \left( c_1(\vec{g}, \alpha) f_1 e^{-M_1} + c_2(\vec{g}, \alpha) f_2 e^{-M_2} \right)^2 \quad , \quad (A-44)$$

where the subscript 1 refers to  $Ag^+$  (or  $K^+$ ) and the subscript 2 refers to  $Cl^-$ . With the use of equation (2-11) and (A-2), equation (A-44) becomes

$$16 \sum_{\vec{g}, \alpha} \frac{E(v(\vec{g}, \alpha)) c_1^2(\vec{g}, \alpha) (\kappa \vec{S} \cdot \vec{e}(\vec{g}, \alpha))^2}{4\pi^2 N v^2(\vec{g}, \alpha) \sum_j m_j c_j^2(\vec{g}, \alpha)} \left( f_1 e^{-M_1} \pm \Gamma(\vec{g}, \alpha) f_2 e^{-M_2} \right)^2 \quad (\text{A-45})$$

where  $\Gamma(\vec{g}, \alpha) = (c_2(\vec{g}, \alpha)/c_1(\vec{g}, \alpha))$  is the ratio of the vibration amplitude of the  $\text{Cl}^-$  ion to that of the  $\text{Ag}^+$  (or  $\text{K}^+$ ) ion. For acoustic modes  $\Gamma(\vec{g}, \alpha)$  is positive and for optic modes it is negative<sup>10</sup>. Now

$$\sum_j m_j c_j^2(\vec{g}, \alpha) = 4(m_1 c_1^2(\vec{g}, \alpha) + m_2 c_2^2(\vec{g}, \alpha))$$

and

$$(\kappa \vec{S} \cdot \vec{e}(\vec{g}, \alpha))^2 = 16\pi^2 \frac{\sin^2 \theta}{\lambda^2} \cos^2(\theta(\vec{S}, \vec{e}))$$

So for  $J_1$  one finally obtains,

$$J_1 = 16 \left( \frac{\sin \theta}{\lambda} \right)^2 \sum_{\vec{g}, \alpha} \frac{E(v(\vec{g}, \alpha)) \cos^2(\theta(\vec{S}, \vec{e}(\vec{g}, \alpha)))}{N v^2(\vec{g}, \alpha) (m_1 + |\Gamma(\vec{g}, \alpha)|^2 m_2)} \left( f_1 e^{-M_1} \pm \Gamma(\vec{g}, \alpha) f_2 e^{-M_2} \right)^2 I_0(\vec{S}/\lambda + \vec{g}) \quad (\text{A-46})$$

The amplitude ratio  $\Gamma(\vec{g}, \alpha)$  is a function of the mode and has been calculated<sup>9</sup> only for a one-dimensional diatomic chain with nearest neighbor interactions. For this particular case  $\Gamma(\vec{g}, \alpha)$  approaches unity for

acoustic waves and small  $|\vec{g}|$ . To simplify  $J_1$  the following assumptions will be made:

1. For the region throughout which  $J_1$  must be integrated  $v^{-2}(\vec{g}, \alpha)$  for the optic modes is negligible compared to that for the acoustic modes.

2. For the acoustic modes of interest  $\Gamma(\vec{g}, \alpha) = 1$ .

3. For the acoustic modes of interest  $v(\vec{g}, \alpha) = |\vec{g}|V_\alpha$  where  $V_\alpha$  is the average wave velocity calculable from elastic constants.

4.  $E(v(\vec{g}, \alpha)) = kT$ .

5.  $\cos^2(\theta(\vec{S}, \vec{e})) = 1/3$ .

One then obtains for  $J_1$

$$J_1 = |\vec{F}|^2 \left( \frac{\sin \theta}{\lambda} \right)^2 \frac{kT}{3N(m_1 + m_2)} \sum_{\vec{g}, \alpha} \frac{I_o(\vec{S}/\lambda + \vec{g})}{V_\alpha^2 |\vec{g}|^2}, \quad (\text{A-47})$$

where the sum over  $\alpha$  includes only the acoustic modes. If the same assumptions are made for two phonon scattering, the derivation of the total intensity observed at the diffraction peak proceeds identically to that already discussed for the monatomic case. We can therefore use equation (A-41) for both monatomic and diatomic crystals except that for the diatomic case  $m$  must be replaced by  $m_1 + m_2$  and  $e^{-2M}$  cannot be taken out of  $|\vec{F}|^2$ .

#### Calculation of $\sigma$ for Al, AgCl, and KCl

We now calculate the  $\sigma$  defined by equation (A-42) for waves traveling in the [100], [110], and [111] directions in a cubic crystal



the velocities of both the longitudinal and transverse polarizations are related to the elastic constants  $C_{11}$ ,  $C_{12}$ , and  $C_{44}$  as follows<sup>5</sup>,

$$\begin{aligned}
 [100]: \quad \rho V_\ell^2 &= C_{11} \\
 \rho V_t^2 &= C_{44} \\
 [110]: \quad 2\rho V_\ell^2 &= C_{11} + C_{12} + 2C_{44} \\
 2\rho V_{t1}^2 &= C_{11} - C_{12} \quad ; \quad 2\rho V_{t2}^2 = C_{44} \\
 [111]: \quad 3\rho V_\ell^2 &= C_{11} + 2C_{12} + 4C_{44} \\
 2\rho V_t^2 &= C_{11} - C_{12} + C_{44}
 \end{aligned} \tag{A-48}$$

where  $\rho$  is the density and  $\ell$  and  $t$  refer to longitudinal and transverse polarizations respectively. For the  $[110]$  direction the velocities of the two transverse polarizations are not the same as for the other directions. For most cubic solids,  $V_\alpha$ , as determined from equations (A-48) and measured elastic constants, is direction dependent with  $V_\ell \approx 2V_t$  for each of the above three directions. The dependence of  $V_\alpha$  on direction is small however, the variation being only about  $\pm 10$  percent for Al, so that we will assume  $\sum_\alpha V_\alpha^{-2}$  to be adequately given by

$$\sum_\alpha V_\alpha^{-2} = V_\ell^{-2} + 2V_t^{-2} = 3V^{-2} \tag{A-49}$$

with  $V_\ell$  and  $V_t$  being arithmetic averages of the velocities corresponding to the  $[100]$ ,  $[110]$ , and  $[111]$  directions. Other averaging procedures

could be used such as weighting the velocity of a wave in a given direction in proportion to the multiplicity of that direction or the method described by Quimby and Sutton<sup>49</sup> for calculating the Debye  $\Theta$  from elastic constants. However, since the TDS correction is expected to be small, the use of a more elaborate averaging procedure does not seem to be worth the effort. The data used to calculate  $\sigma$  and the values obtained are listed in Table 12.

Table 12. Data Used to Calculate  $\sigma$ 

	<u>Aluminum</u>	<u>Silver Chloride</u>	<u>Potassium Chloride</u>
$C_{11}$ ( $10^{12}$ dyne/cm <sup>2</sup> )	1.118 <sup>a</sup>	0.605 <sup>b</sup>	0.407 <sup>c</sup>
$C_{12}$ ( $10^{12}$ dyne/cm <sup>2</sup> )	0.660 <sup>a</sup>	0.364 <sup>b</sup>	0.066 <sup>c</sup>
$C_{44}$ ( $10^{12}$ dyne/cm <sup>2</sup> )	0.276 <sup>a</sup>	0.0624 <sup>b</sup>	0.063 <sup>c</sup>
$\rho$ (gm/cm <sup>3</sup> )	2.697	5.56	1.98
$V^{-2}$ ( $10^5$ cm/sec) <sup>-2</sup>	0.079	0.473	0.165
$m$ or $(m_1+m_2)(10^{-24}$ gm)	44.8	238.	124.
$a(10^{-8}$ cm)	4.04	5.55	6.29
$\sigma(10^{-27}$ cm <sup>3</sup> o <sub>K</sub> <sup>-1</sup> )	1.60	4.68	4.58

a see reference 42

b see reference 48

c see reference 22

The values used for  $\beta$ ,  $\delta$ , and  $\Delta$  are  $7.0 \times 10^{-2}$  rad.,  $0.76 \times 10^{-2}$  rad. and  $8.7 \times 10^{-2}$  rad. respectively.

## APPENDIX B

Calculation of  $(\partial B / \partial T)_V$  for Aluminum Using the  
Frequency Spectrum Determined by Walker

According to equations (2-20) and (2-42),  $(\partial B / \partial T)_V$  is given by

$$(\partial B / \partial T)_V = \frac{2h^2}{mkT^2} \int_0^{\nu_m} \frac{e^{h\nu/kT} g(\nu) d\nu}{(e^{h\nu/kT} - 1)^2} \bigg/ \int_0^{\nu_m} g(\nu) d\nu \quad (B-1)$$

Walker<sup>11</sup> has determined the frequency spectrum for Al in the form of a histogram. This histogram is shown plotted in Figure 36 and in tabular form in Table 13\*. The designation  $T_H$ ,  $L$ , and  $T_L$  refer to the contributions to the total spectrum,  $g$ , from the "high transverse", the "longitudinal", and the "low transverse" branches respectively (see Walker<sup>11</sup>). In order to compute  $(\partial B / \partial T)_V$  with this spectrum, the range of integration in equation (B-1),  $\nu = 0$  to  $\nu = \nu_m$ , was subdivided into intervals of width  $\Delta\nu = 0.01 \times 10^{13} \text{ sec}^{-1}$  to agree with the frequency intervals used by Walker. The calculation required is therefore

$$(\partial B / \partial T)_V = \frac{2h^2}{mkT^2} \sum_{i=1}^N e^{h\nu_i/kT} \left( e^{h\nu_i/kT} - 1 \right)^{-2} g(\nu_i) \Delta\nu \quad (B-2)$$

---

\*This table is included here because it is not given in Walker's publication. We wish to thank Dr. Walker for kindly furnishing us with the information shown in the table.

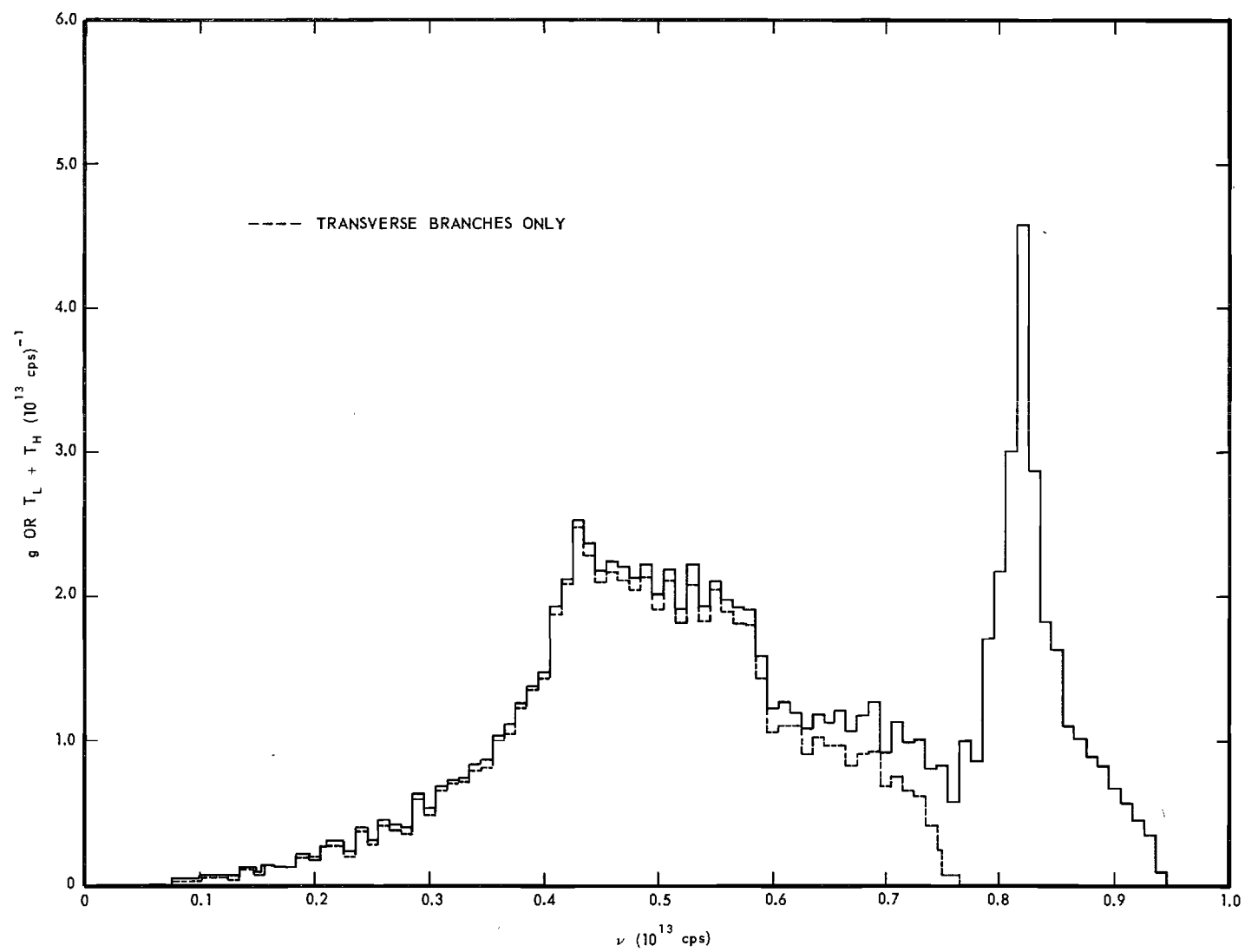


Figure 36. Aluminum Vibration Spectrum.

Table 13. Frequency Spectrum of Aluminum in Tabular Form

$\nu$ ( $10^{13}$ cps)	$g$ ( $10^{-3}$ cps) $^{-1}$	$T_H$ ( $10^{13}$ cps) $^{-1}$	$L$ ( $10^{13}$ cps) $^{-1}$	$T_L$ ( $10^{13}$ cps) $^{-1}$
0.01	0.0	0.0	0.0	0.0
0.02	0.0	0.0	0.0	0.0
0.03	0.007348	0.001845	0.0	0.005503
0.04	0.008597	0.006151	0.0	0.002446
0.05	0.005529	0.001845	0.001850	0.001834
0.06	0.029437	0.014763	0.0	0.014674
0.07	0.011005	0.0	0.0	0.011005
0.08	0.040507	0.20299	0.003700	0.016508
0.09	0.036765	0.009842	0.002467	0.024456
0.10	0.049718	0.029526	0.001850	0.018342
0.11	0.066154	0.020299	0.0	0.045855
0.12	0.073655	0.036907	0.007401	0.029347
0.13	0.056383	0.011687	0.007401	0.037295
0.14	0.132420	0.059052	0.0	0.073368
0.15	0.088319	0.040598	0.003700	0.044021
0.16	0.163782	0.075660	0.009251	0.078871
0.17	0.144682	0.054131	0.007401	0.083150
0.18	0.139910	0.073815	0.007401	0.058694
0.19	0.211931	0.049825	0.009867	0.152239
0.20	0.198802	0.095959	0.014801	0.088042
0.21	0.27525	0.10765	0.00925	0.15835
0.22	0.28330	0.11810	0.01480	0.15040
0.23	0.23181	0.08858	0.01850	0.12473
0.24	0.40210	0.14824	0.01480	0.23906
0.25	0.30521	0.11072	0.00740	0.18709
0.26	0.43210	0.14209	0.02405	0.26596
0.27	0.41574	0.16977	0.02220	0.22377
0.28	0.40101	0.17593	0.00987	0.21521
0.29	0.63606	0.19376	0.02960	0.41270
0.30	0.51704	0.22883	0.02775	0.26046
0.31	0.68862	0.17962	0.03700	0.47200
0.32	0.73947	0.30818	0.02960	0.40169
0.33	0.74264	0.23621	0.02220	0.48423
0.34	0.84317	0.27004	0.02960	0.54353
0.35	0.86985	0.31002	0.04625	0.51358
0.36	1.04527	0.32540	0.02960	0.69027
0.37	1.12399	0.36169	0.05747	0.70433
0.38	1.25854	0.40844	0.02960	0.82050
0.39	1.39328	0.43735	0.03700	0.91893
0.40	1.49194	0.44909	0.05365	0.98925

(Continued on next page)

Table 13. Frequency Spectrum of Aluminum in Tabular Form (Continued)

$\nu$ ( $10^{13}$ cps)	$g$ ( $10^{13}$ cps) $^{-1}$	$T_H$ ( $10^{13}$ cps) $^{-1}$	$L$ ( $10^{13}$ cps) $^{-1}$	$T_L$ ( $10^{13}$ cps) $^{-1}$
0.41	1.95280	0.52101	0.05920	1.37259
0.42	2.12474	0.67541	0.03700	1.41233
0.43	2.55740	0.60344	0.06290	1.89106
0.44	2.38761	0.70493	0.08326	1.59942
0.45	2.17524	0.69940	0.06167	1.41417
0.46	2.22736	0.62743	0.05920	1.54073
0.47	2.21383	0.78428	0.08141	1.34814
0.48	2.13057	0.67172	0.07586	1.38299
0.49	2.23577	0.77321	0.09141	0.38115
0.50	2.02270	0.68648	0.10731	1.22891
0.51	2.19959	0.83595	0.09621	1.26743
0.52	1.91076	0.71047	0.08326	1.11703
0.53	2.24072	0.89131	0.14801	1.20140
0.54	1.95589	0.75291	0.11347	1.08951
0.55	2.12302	0.91715	0.09251	1.11336
0.56	1.99682	0.94668	0.11286	0.93728
0.57	1.95794	0.84887	0.14061	0.96846
0.58	1.93152	1.06017	0.11841	0.75294
0.59	1.60546	1.05555	0.17206	0.37785
0.60	1.23436	0.97067	0.16281	0.10088
0.61	1.27249	0.11091	0.16158	0.0
0.62	1.20552	1.01126	0.19426	
0.63	1.10401	0.91900	0.18501	
0.64	1.29241	1.04079	0.25162	
0.65	1.15013	0.97067	0.17946	
0.66	1.22597	0.97805	0.24792	
0.67	1.08573	0.83411	0.25163	
0.68	1.18727	0.91900	0.26827	
0.69	1.27296	0.93007	0.34289	
0.70	0.92327	0.69755	0.22572	
0.71	1.14326	0.76398	0.37928	
0.72	1.00484	0.63481	0.37003	
0.73	1.03263	0.61635	0.41628	
0.74	0.81302	0.40229	0.41073	
0.75	0.84363	0.25282	0.59081	
0.76	0.59559	0.05905	0.53654	
0.77	1.03047	0.01845	1.101202	
0.78	0.87881	0.0	0.87881	
0.79	1.70952		1.70952	
0.80	2.18500		2.1850	
0.81	3.10513		3.10513	
0.82	4.59202		4.59202	

(Continued on next page)

Table 13. Frequency Spectrum of Aluminum in Tabular Form (Continued)

$\nu$ $(10^{13} \text{ cps})$	$g$ $(10^{13} \text{ cps})^{-1}$	$T_H$ $(10^{13} \text{ cps})^{-1}$	$L$ $(10^{13} \text{ cps})^{-1}$	$T_L$ $(10^{13} \text{ cps})^{-1}$
0.83	2.86955		2.86955	
0.84	1.83810		1.83810	
0.85	1.44557		1.44557	
0.86	1.10268		1.10268	
0.87	1.01387		1.01387	
0.88	0.90286		0.90286	
0.89	0.83133		0.83133	
0.90	0.68825		0.68825	
0.91	0.56984		0.56984	
0.92	0.47610		0.47610	
0.93	0.35522		0.35522	
0.94	0.09991		0.09991	
0.95	0.0		0.0	

Here  $N$  is the number of frequency intervals, which depends on the branch (see Table 13), and  $\nu_i = (i)\Delta\nu$ . It should be noted that  $g(\nu_i)$  is a function of  $i$  only, i.e.,  $g(\nu_i) = g(i)$ . Also the spectrum is normalized so that

$$\sum_i^N g(\nu_i) \Delta\nu = 1$$

with each branch contributing  $1/3$ .

The computation indicated in equation (B-2) was carried out on the Burroughs 220 computer. Four separate calculations were made; one with the entire spectrum  $g$ , one with only the longitudinal branch  $L$ , one with the high transverse branch  $T_H$ , "stretched" 5% to higher frequencies (see A1 results discussion), and one using the low transverse branch,  $T_L$ , stretched 5% to higher frequencies. The resulting contributions to  $(\partial B / \partial T)_V$  are shown in Table 14.

When the stretched transverse branches were used, each frequency  $\nu_i = (i)\Delta\nu$  of the unstretched transverse branches was replaced by  $\nu'_i = (i)\Delta\nu'$ , where  $\nu' = (1.05)\Delta\nu$ . Thus although the number of frequency intervals remains unchanged by this stretching process the width of each interval is increased by 5%. In order for the spectrum to remain normalized, the product  $g(\nu'_i)\Delta\nu'$  for each  $i$  must be equal to  $g(\nu_i)\Delta\nu = g(i)\Delta\nu$ . This could have been accomplished by setting  $g(\nu'_i) = g(i)/(1.05)$ . However, since

$$g(\nu'_i)\Delta\nu' = \left(\frac{g(i)}{1.05}\right) (1.05\Delta\nu) = g(i)\Delta\nu$$

and since  $g(i)$  always occurs multiplied by  $\Delta\nu$ , normalization was assured merely by not changing  $\Delta\nu$  to  $\Delta\nu'$  where it multiplied  $g(i)$ .



Table 14. Calculated Values for  $(\partial B/\partial T)_V$  for Aluminum

$T(^{\circ}\text{K})$	$^*$ $g$ (Unmodified)	$L$ (Unmodified)	$T_H$ (Modified)	$T_L$ (Modified)
10	0.14969	0.005499	0.052777	0.069435
20	0.36921	0.016233	0.130010	0.171028
30	0.62354	0.027933	0.212165	0.294587
40	0.90545	0.041698	0.300006	0.436756
50	1.18349	0.059334	0.388188	0.577231
60	1.43537	0.081237	0.470492	0.701528
70	1.65301	0.106103	0.543339	0.805192
80	1.83663	0.132061	0.605756	0.889338
90	1.98989	0.157534	0.658397	0.957004
100	2.11737	0.181503	0.702203	1.011421
110	2.22352	0.203445	0.738802	1.055399
120	2.31219	0.223183	0.769370	1.091204
130	2.38662	0.240752	0.795001	1.120597
140	2.44945	0.256295	0.816599	1.144937
150	2.50279	0.270006	0.834904	1.165264
160	2.54834	0.282090	0.850508	1.182380
170	2.58747	0.292747	0.863889	1.196905
180	2.62127	0.302158	0.875429	1.209319
190	2.65064	0.310488	0.885438	1.220005
200	2.67627	0.317878	0.894165	1.229260
210	2.69877	0.324452	0.901812	1.237323
220	2.71861	0.330318	0.908546	1.244387
230	2.73617	0.335567	0.914503	1.250708
240	2.75179	0.340277	0.919794	1.256113
250	2.76573	0.344517	0.924514	1.261006
260	2.77823	0.348343	0.928740	1.265373
270	2.78947	0.351806	0.932537	1.269286
280	2.79961	0.354948	0.935961	1.272806
290	2.80878	0.357806	0.939057	1.275982
300	2.81711	0.360413	0.941867	1.278858
310	2.82470	0.363796	0.944423	1.281470
320	2.83162	0.364980	0.946756	1.283849
330	2.83796	0.366985	0.948889	1.286021
340	2.84377	0.368831	0.950845	1.288010
350	2.84911	0.370532	0.952643	1.289836
360	2.85403	0.372104	0.954299	1.291516
370	2.85858	0.373559	0.955828	1.293065
380	2.86279	0.374908	0.957241	1.294496
390	2.86669	0.376161	0.958551	1.295821
400	2.87031	0.377327	0.959767	1.297050

\*Units for all entries:  $10^{-19} \text{ cm}^2 \text{ } ^{\circ}\text{K}^{-1}$

## APPENDIX C

Calculation of Individual Temperature Factors forSilver and Chlorine in AgCl

According to equation (2-74)  $M_1$  is given by

$$M_1 = \frac{1}{6N} \left( \frac{\sin \theta}{\lambda} \right)^2 \sum_{\vec{k}, \alpha} \frac{E(v(\vec{k}, \alpha))}{(m_1 + |\Gamma(\vec{k}, \alpha)|^2 m_2) v^2(\vec{k}, \alpha)} \quad (C-1)$$

As before the subscripts 1 and 2 refer to silver and chlorine respectively. In equation (C-1)  $\Gamma(\vec{k}, \alpha)$  is the ratio of the  $\text{Cl}^-$  vibrational amplitude to that for the  $\text{Ag}^+$  ion. A similar equation can be obtained for  $M_2$ , namely,

$$M_2 = \frac{1}{6N} \left( \frac{\sin \theta}{\lambda} \right)^2 \sum_{\vec{k}, \alpha} \frac{E(v(\vec{k}, \alpha))}{(|\delta(\vec{k}, \alpha)|^2 m_1 + m_2) v^2(\vec{k}, \alpha)} \quad (C-2)$$

Here  $\delta(\vec{k}, \alpha)$  is the ratio of the  $\text{Ag}^+$  ion vibrational amplitude to that for  $\text{Cl}^-$  ion. Obviously,

$$|\delta(\vec{k}, \alpha)|^2 = |\Gamma(\vec{k}, \alpha)|^2$$

For a diatomic linear chain having only nearest neighbor forces, Brillouin<sup>9</sup> obtained

$$\delta(g) = \frac{m_1 - m_2 \pm \left[ m_1^2 + m_2^2 + 2m_1m_2 \cos(2\pi ga) \right]^{1/2}}{2m_1 \cos(\pi ga)}, \quad (C-3)$$

where  $g = 1/\Lambda$ ,  $\Lambda$  is the normal mode wavelength, and  $a$  is the repeat distance in the chain. The plus sign in front of the square root in the numerator is used for the acoustic branch and the minus sign is used for the optic branch. Now for AgCl,  $m_1 \approx 3m_2$ , then

$$\delta(g) = \frac{2 \pm \left[ 10 + 6 \cos(2\pi ga) \right]^{1/2}}{6 \cos(\pi ga)} \quad (C-4)$$

For the one-dimensional lattice the maximum value of  $g$  is  $(2a)^{-1}$ . In a three-dimensional lattice the maximum value for  $\vec{g}$  depends somewhat on direction, however, for simplicity one often neglects this direction dependence and replaces the Brillouin zone by a sphere of equal volume. The maximum value for  $|\vec{g}|$  then becomes, for a f.c.c. Bravais lattice such as AgCl,

$$|\vec{g}|_m = (3/\pi)^{1/3}/a,$$

where  $a$  is the lattice parameter. We then have for AgCl,

$$\delta(|\vec{g}|) = \frac{2 \pm \left[ 10 + 6 \cos(\pi |\vec{g}|/|\vec{g}|_m) \right]^{1/2}}{6 \cos(\pi |\vec{g}|/2|\vec{g}|_m)} \quad (C-5)$$

It turns out that

for the optic branch:  $\Gamma(|\vec{g}|) \rightarrow \infty$  as  $|\vec{g}| \rightarrow |\vec{g}|_m$

and for the acoustic branch:  $\delta(|\vec{g}|) \rightarrow \infty$  as  $|\vec{g}| \rightarrow |\vec{g}|_m$

In view of the computer calculation to be made it is necessary that infinities be avoided. We therefore break up the sums for  $M_1$  and  $M_2$  into two parts; one for the acoustic modes and one for the optic modes, and replace  $\delta(g)$  by  $\Gamma(g)^{-1}$ , or vice versa, where infinities would occur. We then have for  $B_1$  and  $B_2$ ,

$$\begin{aligned}
 B_1(\text{acoustic}) &= \frac{1}{6N} \sum_{\vec{g}, \alpha}^{\text{acoustic}} \frac{E(v(\vec{g}, \alpha))}{(m_1 + \Gamma(|\vec{g}|)^2 m_2) v^2(\vec{g}, \alpha)} , \\
 B_1(\text{optic}) &= \frac{1}{6N} \sum_{\vec{g}, \alpha}^{\text{optic}} \frac{E(v(\vec{g}, \alpha)) \delta(|\vec{g}|)^2}{(\delta(|\vec{g}|)^2 m_1 + m_2) v^2(\vec{g}, \alpha)} , \\
 B_2(\text{acoustic}) &= \frac{1}{6N} \sum_{\vec{g}, \alpha}^{\text{acoustic}} \frac{E(v(\vec{g}, \alpha)) \Gamma(|\vec{g}|)^2}{(m_1 + \Gamma(|\vec{g}|)^2 m_2) v^2(\vec{g}, \alpha)} , \\
 B_2(\text{optic}) &= \frac{1}{6N} \sum_{\vec{g}, \alpha}^{\text{optic}} \frac{E(v(\vec{g}, \alpha))}{(\delta(|\vec{g}|)^2 m_1 + m_2) v^2(\vec{g}, \alpha)} . \quad (C-6)
 \end{aligned}$$

By the insertion of the appropriate density,  $\rho$ , of wave vectors,  $\vec{g}$ , in reciprocal space, the above sums over  $\vec{g}$  can be changed to integrals. The value for  $\rho$  is  $Na^3 = V^*$ . With  $\rho$  written in terms of  $|\vec{g}|_m$  and dropping vector notations, one obtains

---

\*See Appendix A

$$B_1(\text{acoustic}) = \frac{2}{g_m^3} \sum_{\alpha=1}^3 \int_0^{g_m} \frac{E(v(g,\alpha))g^2 dg}{(m_1 + \Gamma(g)^2 m_2)v^2(g,\alpha)} , \quad (C-7)$$

for example.

For the acoustic modes we used the dispersion curves obtained by Cole<sup>10</sup> for acoustic waves traveling in the [100], [110], and [111] directions to change each frequency to an appropriate phase velocity,  $V(g,\alpha)$ , times  $g$  such that

$$v(g,\alpha) = gV(g,\alpha) . \quad (C-8)$$

Cole has already obtained plots of  $V(g,\alpha)$  versus  $g$  and for each direction mentioned above they are essentially straight lines. We assumed that an appropriate average\*, linear  $V(g,\alpha)$  versus  $g$  relationship for both the longitudinal and transverse branches could be obtained from these plots in the following manner. For each branch we arithmetically averaged the values of  $V(0,\alpha)$  for the individual  $V(g,\alpha)$  versus  $g$  plots, after weighting each direction according to its multiplicity, to give an average isotropic value for  $V(0,\alpha)$ . An average value for  $V(g_m,0)$  was obtained similarly. An average, linear  $V(g,\alpha)$  versus  $g$  relationship was then obtained for each branch by passing a straight line through the appropriate average values obtained for  $V(0,\alpha)$  and  $V(g_m,\alpha)$ .

In order that the calculation indicated in equation (C-7) could be performed by the computer, the range 0 to  $g_m$ ,  $g_m = 1.77 \times 10^7 \text{ cm}^{-1}$ , was divided into 177 intervals all of width  $\Delta g = 0.01 \times 10^7 \text{ cm}^{-1}$ . The

---

\*That is, averaged over the above crystallographic direction.

integral was thereby changed to a sum over an integer  $i$  such that  $g_i = (i)\Delta g$  and  $i$  ranged from 0 to 177 as shown below,

$$B_1(\text{acoustic}) = 2 \left( \frac{2h}{g_m} \right) \sum_{i=0}^{177} \frac{g_i}{v_t(g_i)} \left[ \frac{1}{2} + \frac{1}{e^{h v_t(g_i) g_i / kT} - 1} \right] \frac{\Delta g}{(m_1 + \Gamma(g_i)^2 m_2)} \\ + \left( \frac{2h}{g_m} \right) \sum_{i=0}^{177} \frac{g_i}{v_\ell(g_i)} \left[ \frac{1}{2} + \frac{1}{e^{h v_\ell(g_i) g_i / kT} - 1} \right] \frac{\Delta g}{(m_1 + \Gamma(g_i)^2 m_2)} \quad , \quad (C-9)$$

and

$$B_2(\text{acoustic}) = 2 \left( \frac{2h}{g_m} \right) \sum_{i=0}^{177} \frac{g_i}{v_t(g_i)} \left[ \begin{array}{l} \text{same as for trans-} \\ \text{verse mode contribu-} \\ \text{tion to } B_1(\text{acoustic}) \end{array} \right]_t \frac{\Delta g \Gamma(g_i)^2}{(m_1 + \Gamma(g_i)^2 m_2)} \\ + \left( \frac{2h}{g_m} \right) \sum_{i=0}^{177} \frac{g_i}{v_\ell(g_i)} \left[ \begin{array}{l} \text{same as for longitu-} \\ \text{dinal mode contribution} \\ \text{to } B_1(\text{acoustic}) \end{array} \right]_\ell \frac{\Delta g \Gamma(g_i)^2}{(m_1 + \Gamma(g_i)^2 m_2)} \quad (C-10)$$

where we have introduced equations (2-12) and (2-13) for  $E(v)$ . The  $t$  and  $\ell$  subscripts represent the transverse and longitudinal modes respectively. The factor two in front of the transverse mode contribution arises from there being two transverse modes for each value of  $g$ .

For the optic modes we have assumed that  $v(g, \alpha)$  is independent of  $g$ . Thus  $E(v(g, \alpha))/v^2(g, \alpha)$  can be taken outside the summation in equation (C-6). The value used for the transverse frequency is that used by Cole,  $v_t = 3.1 \times 10^{12} \text{ sec}^{-1}$ . Cole assumed some dependence of  $v_\ell$  on  $g$  such that

$\nu_\ell$  went from  $7.0 \times 10^{12} \text{sec}^{-1}$  for  $g = 0$  to  $6.0 \times 10^{12} \text{sec}^{-1}$  at  $g = g_m$ . We have used the arithmetic average of these two frequencies, viz.  $\nu_\ell = 6.5 \times 10^{12} \text{sec}^{-1}$ . The equations obtained for the optic mode contributions to  $B_1$  and  $B_2$  are analogous to equations (C-9) and (C-10) are

$$B_1(\text{optic}) = \left[ \left( \frac{4h}{g_m \nu_\ell} \right) \left( \frac{1}{e^{h\nu_\ell/kT} - 1} + \frac{1}{2} \right) + \left( \frac{2h}{g_m \nu_\ell} \right) \left( \frac{1}{e^{h\nu_\ell/kT} - 1} + \frac{1}{2} \right) \right] \sum_{i=0}^{177} \frac{\delta(g_i)^2 g_i^2 \Delta g}{(\delta(g_i)^2_{m_1+m_2})} \quad (\text{C-11})$$

$$B_2(\text{optic}) = \left[ \text{same as for } B_1(\text{optic}) \right] \sum_{i=0}^{177} \frac{g_i^2 \Delta g}{(\delta(g_i)^2_{m_1+m_2})} \quad (\text{C-12})$$

The results of these calculations are shown in Table 15.

Table 15. Calculated Values for  $B_{Ag}$  and  $B_{Cl}$  for AgCl

T( $^{\circ}$ K)	Optic Modes		Acoustic Modes	
	$B_{Ag}^*$	$B_{Cl}$	$B_{Ag}$	$B_{Cl}$
100	0.011998	0.40962	1.10329	0.47138
110	0.012789	0.43662	1.20848	0.51716
120	0.013607	0.46452	1.31408	0.56305
130	0.014445	0.49313	1.41999	0.60902
140	0.051300	0.52233	1.52613	0.65505
150	0.016170	0.55202	1.63247	0.70113
160	0.017051	0.58212	1.73897	0.74726
170	0.017943	0.61255	0.84561	0.79342
180	0.018843	0.64328	1.95235	0.83961
190	0.019750	0.67426	2.05917	0.88582
200	0.020664	0.70544	2.16609	0.93206
210	0.021583	0.73682	2.27307	0.97831
220	0.022507	0.76836	2.38011	1.02458
230	0.023434	0.80003	2.48719	1.07086
240	0.024366	0.83184	2.59433	1.11715
250	0.025301	0.86375	2.70150	1.16346
260	0.026238	0.89576	2.80871	1.20977
270	0.027179	0.92786	2.91595	1.25609
280	0.028121	0.96004	3.02321	1.30242
290	0.029066	0.99224	3.13050	1.34875
300	0.030013	1.02461	3.23782	1.39510

\*Units for all entries:  $10^{-16} \text{ cm}^2$



## APPENDIX D

## ALUMINUM A VALUES AND CORRECTIONS

Table 16. Aluminum A Values and Corrections at 240° K

$$A_o = A - A_{LPf} - A_{TDS}$$

hkl	Sample No.	A*	A <sub>LPf</sub>	A <sub>TDS</sub>	A <sub>o</sub>
400	2	2.22	-0.14	-0.12	2.48
	4	2.25	-0.14	-0.12	2.51
333	2	2.47	-0.10	-0.15	2.72
	2	2.46	-0.10	-0.15	2.71
440	2	2.42	-0.09	-0.15	2.66
	2	2.49	-0.09	-0.15	2.73
600	4	2.45	-0.09	-0.15	2.69
	2	2.39	-0.08	-0.16	2.63
	4	2.41	-0.08	-0.16	2.65
444	4	2.46	-0.08	-0.16	2.70
	2	2.54	-0.06	-0.17	2.77
	4	2.47	-0.06	-0.17	2.70
800	2	2.44	-0.03	-0.17	2.64
	4	2.60	-0.03	-0.17	2.80
660	2	2.48	-0.02	-0.17	2.67
	4	2.55	-0.02	-0.17	2.74
555	2	2.39	-0.02	-0.17	2.58
	2	2.52	-0.02	-0.17	2.71
	4	2.48	-0.02	-0.17	2.69
10,00	2	2.43	+0.01	-0.15	2.57
	2	2.43	+0.01	-0.15	2.57
	4	2.59	+0.01	-0.15	2.73
	4	2.55	+0.01	-0.15	2.69
666	2	2.37	+0.02	-0.14	2.49
	2	2.46	+0.02	-0.14	2.58
	4	2.50	+0.02	-0.14	2.62
	4	2.53	+0.02	-0.14	2.65
	4	2.56	+0.02	-0.14	2.68

\* Units:  $10^{-19} \text{ cm}^2 \text{ } ^\circ \text{K}^{-1}$

Table 17. Aluminum A Values and Corrections at 200° K

$$A_o = A - A_{LPf} - A_{TDS}$$

hkl	Sample No.	A*	A <sub>LPf</sub>	A <sub>TDS</sub>	A <sub>o</sub>
400	2	2.16	-0.13	-0.12	2.41
	4	2.13	-0.13	-0.12	2.38
333	2	2.20	-0.10	-0.15	2.45
	4	2.30	-0.10	-0.15	2.55
440	2	2.31	-0.08	-0.15	2.54
	2	2.26	-0.08	-0.15	2.49
	4	2.30	-0.08	-0.15	2.53
600	2	2.25	-0.07	-0.16	2.48
	4	2.19	-0.07	-0.16	2.42
	4	2.31	-0.07	-0.16	2.54
444	2	2.42	-0.06	-0.17	2.65
	4	2.37	-0.06	-0.17	2.60
800	2	2.36	-0.03	-0.17	2.56
	4	2.32	-0.03	-0.17	2.52
660	2	2.32	-0.02	-0.17	2.51
	4	2.40	-0.02	-0.17	2.59
555	2	2.31	-0.02	-0.17	2.50
	2	2.32	-0.02	-0.17	2.51
	4	2.27	-0.02	-0.17	2.46
10,00	2	2.25	+0.01	-0.15	2.39
	2	2.33	+0.01	-0.15	2.47
	4	2.42	+0.01	-0.15	2.56
	4	2.43	+0.01	-0.15	2.57
666	2	2.34	+0.02	-0.14	2.46
	2	2.29	+0.02	-0.14	2.41
	4	2.38	+0.02	-0.14	2.50
	4	2.32	+0.02	-0.14	2.44
	4	2.38	+0.02	-0.14	2.50

\*Units:  $10^{-19} \text{ cm}^2 \text{ } ^\circ \text{ K}^{-1}$

Table 18. Aluminum A Values and Corrections at 160° K

$$A_o = A - A_{LPf} - A_{TDS}$$

hkl	Sample No.	A*	A <sub>LPf</sub>	A <sub>TDS</sub>	A <sub>o</sub>
400	2	2.05	-0.11	-0.12	2.28
	4	2.00	-0.11	-0.12	2.23
333	2	1.96	-0.08	-0.15	2.19
	4	2.09	-0.08	-0.15	2.32
440	2	1.98	-0.07	-0.15	2.20
	2	2.22	-0.07	-0.15	2.44
	4	2.07	-0.07	-0.15	2.29
600	2	2.01	-0.06	-0.16	2.23
	4	2.00	-0.06	-0.16	2.22
	4	1.98	-0.06	-0.16	2.20
444	2	2.17	-0.04	-0.17	2.38
	4	2.09	-0.04	-0.17	2.30
800	2	2.27	-0.02	-0.17	2.46
	4	2.11	-0.02	-0.17	2.30
660	2	2.08	-0.01	-0.17	2.26
	4	2.20	-0.01	-0.17	2.38
555	2	2.21	-0.01	-0.17	2.39
	2	2.10	-0.01	-0.17	2.28
	4	2.11	-0.01	-0.17	2.29
10,00	2	2.11	+0.01	-0.15	2.25
	2	2.22	+0.01	-0.15	2.36
	4	2.13	+0.01	-0.15	2.27
	4	2.16	+0.01	-0.15	2.30
666	2	2.08	+0.01	-0.14	2.21
	2	2.16	+0.01	-0.14	2.29
	4	2.17	+0.01	-0.14	2.30
	4	2.13	+0.01	-0.14	2.26
	4	2.13	+0.01	-0.14	2.26

\*Units:  $10^{-19} \text{ cm}^2 \text{ } ^\circ \text{ K}^{-1}$

Table 19. Aluminum A Values and Corrections at 140° K

$$A_o = A - A_{LPf} - A_{TDS}$$

hkl	Sample No.	A*	A <sub>LPf</sub>	A <sub>TDS</sub>	A <sub>o</sub>
400	2	1.94	-0.11	-0.12	2.17
	4	1.80	-0.11	-0.12	2.03
333	2	1.94	-0.08	-0.15	2.17
	4	1.94	-0.08	-0.15	2.17
440	2	1.92	-0.07	-0.15	2.14
	2	1.86	-0.07	-0.15	2.08
	4	2.12	-0.07	-0.15	2.34
600	2	1.90	-0.06	-0.16	2.12
	4	1.88	-0.06	-0.16	2.10
	4	1.90	-0.06	-0.16	2.12
444	2	2.08	-0.05	-0.17	2.30
	4	2.02	-0.05	-0.17	2.24
800	2	2.08	-0.02	-0.17	2.27
	4	1.94	-0.02	-0.17	2.13
660	2	1.98	-0.02	-0.17	2.17
	4	2.08	-0.02	-0.17	2.27
555	2	2.17	-0.01	-0.17	2.35
	2	1.92	-0.01	-0.17	2.10
	4	1.94	-0.01	-0.17	2.12
10,00	2	2.09	+0.01	-0.15	2.23
	2	2.04	+0.01	-0.15	2.18
	4	1.98	+0.01	-0.15	2.12
	4	2.08	+0.01	-0.15	2.22
666	2	2.05	+0.01	-0.14	2.18
	2	1.97	+0.01	-0.14	2.10
	4	2.01	+0.01	-0.14	2.14
	4	2.01	+0.01	-0.14	2.14
	4	2.03	+0.01	-0.14	2.16

\*Units:  $10^{-19} \text{ cm}^2 \text{ } ^\circ \text{ K}^{-1}$

Table 20. Aluminum A Values and Corrections at 120° K

$$A_o = A - A_{LPF} - A_{TDS}$$

hkl	Sample No.	A*	A <sub>LPF</sub>	A <sub>TDS</sub>	A <sub>o</sub>
400	2	1.80	-0.10	-0.12	2.02
	4	1.70	-0.10	-0.12	1.92
333	2	1.86	-0.07	-0.15	2.08
	4	1.81	-0.07	-0.15	2.03
440	2	1.75	-0.06	-0.15	1.96
	2	1.98	-0.06	-0.15	2.19
	4	1.88	-0.06	-0.15	2.09
600	2	1.80	-0.06	-0.16	2.02
	4	1.84	-0.06	-0.16	2.06
	4	1.74	-0.06	-0.16	1.96
444	2	1.90	-0.04	-0.17	2.11
	4	1.82	-0.04	-0.17	2.03
800	2	1.94	-0.02	-0.17	2.13
	4	1.73	-0.02	-0.17	1.92
660	2	1.82	-0.01	-0.17	2.00
	4	1.93	-0.01	-0.17	2.11
555	2	2.04	-0.01	-0.17	2.22
	2	1.77	-0.01	-0.17	1.95
	4	1.81	-0.01	-0.17	1.99
10,00	2	1.92	+0.01	-0.15	2.06
	2	1.99	+0.01	-0.15	2.13
	4	1.79	+0.01	-0.15	1.93
	4	1.96	+0.01	-0.15	2.10
666	2	1.98	+0.01	-0.14	2.13
	2	1.82	+0.01	-0.14	1.95
	4	1.88	+0.01	-0.14	2.01
	4	1.88	+0.01	-0.14	2.01
	4	1.91	+0.01	-0.14	2.04

\* Units:  $10^{-19} \text{ cm}^2 \text{ } ^\circ \text{ K}^{-1}$

Table 21. Aluminum A Values and Corrections at 100° K

$$A_o = A - A_{LPF} - A_{TDS}$$

hkl	Sample No.	A*	A <sub>LPF</sub>	A <sub>TDS</sub>	A <sub>o</sub>
400	2	1.59	-0.09	-0.12	1.80
	4	1.51	-0.09	-0.12	1.72
333	2	1.63	-0.06	-0.15	1.84
	4	1.70	-0.06	-0.15	1.91
440	2	1.83	-0.05	-0.15	2.03
	2	1.49	-0.05	-0.15	1.69
	4	1.66	-0.05	-0.15	1.86
600	2	1.66	-0.05	-0.16	1.87
	4	1.55	-0.05	-0.16	1.76
444	2	1.67	-0.03	-0.17	1.87
	4	1.76	-0.03	-0.17	1.96
800	2	1.87	-0.02	-0.17	2.06
	4	1.54	-0.02	-0.17	1.73
660	2	1.63	-0.01	-0.17	1.81
	4	1.78	-0.01	-0.17	1.96
555	2	1.95	-0.01	-0.17	2.13
	2	1.56	-0.01	-0.17	1.74
	4	1.63	-0.01	-0.17	1.81
10,00	2	1.81	+0.01	-0.15	1.95
	2	1.73	+0.01	-0.15	1.87
	4	1.63	+0.01	-0.15	1.77
	4	1.77	+0.01	-0.15	1.91
666	2	1.74	+0.01	-0.14	1.87
	2	1.67	+0.01	-0.14	1.80
	4	1.81	+0.01	-0.14	1.94
	4	1.70	+0.01	-0.14	1.83
	4	1.66	+0.01	-0.14	1.79

\* Units:  $10^{-19} \text{ cm}^2 \text{ } ^\circ \text{K}^{-1}$

## APPENDIX E

## POTASSIUM CHLORIDE A VALUES AND CORRECTIONS



Table 22. Potassium Chloride A Values and Corrections at 240° K

$$A_o = A - A_{LPf} - A_{TDS}$$

hkl	Sample No.	A*	A <sub>LPf</sub>	A <sub>TDS</sub>	A <sub>o</sub>
400	1	5.35	-0.42	-0.26	6.03
	2	5.75	-0.42	-0.26	6.43
440	1	6.00	-0.21	-0.35	6.56
	2	6.15	-0.21	-0.35	6.71
600	1	6.30	-0.19	-0.37	6.86
	2	6.10	-0.19	-0.37	6.66
	3	6.15	-0.19	-0.37	6.71
444	1	5.90	-0.15	-0.41	6.46
	3	6.20	-0.15	-0.41	6.76
800	1	6.00	-0.12	-0.46	6.58
	3	6.15	-0.12	-0.46	6.73
660	1	6.35	-0.11	-0.48	6.94
	3	6.10	-0.11	-0.48	6.69
10,00	1	6.15	-0.08	-0.53	6.76
	3	6.05	-0.08	-0.53	6.66
666	1	6.35	-0.08	-0.54	6.97
	3	6.15	-0.08	-0.54	6.77
880	1	6.60	-0.07	-0.54	7.01

\* Units:  $10^{-19} \text{ cm}^2 \text{ } ^\circ \text{ K}^{-1}$

Table 23. Potassium Chloride A Values and Corrections at 200° K

$$A_o = A - A_{LPf} - A_{TDS}$$

hkl	Sample No.	A*	A <sub>LPf</sub>	A <sub>TDS</sub>	A <sub>o</sub>
400	2	5.40	-0.40	-0.26	6.06
440	1	5.85	-0.20	-0.35	6.40
	2	5.95	-0.20	-0.35	6.50
600	1	6.05	-0.18	-0.37	6.60
	2	5.90	-0.18	-0.37	6.45
	3	5.90	-0.18	-0.37	6.45
444	1	5.70	-0.15	-0.41	6.26
	3	6.05	-0.15	-0.41	6.61
800	1	5.80	-0.11	-0.46	6.37
	3	5.95	-0.11	-0.46	6.52
660	1	6.10	-0.10	-0.48	6.68
	3	5.90	-0.10	-0.48	6.48
10,00	1	5.90	-0.08	-0.53	6.49
	3	5.75	-0.08	-0.53	6.34
666	1	6.15	-0.07	-0.54	6.76
	3	6.00	-0.07	-0.54	6.61
880	1	6.40	-0.06	-0.54	7.00

\*Units:  $10^{-19} \text{ cm}^2 \text{ } ^\circ \text{ K}^{-1}$

Table 24. Potassium Chloride A Values and Corrections, at 160° K

$$A_o = A - A_{LPf} - A_{TDS}$$

hkl	Sample No.	A*	A <sub>LPf</sub>	A <sub>TDS</sub>	A <sub>o</sub>
400	2	5.35	-0.37	-0.26	5.98
440	1	5.50	-0.18	-0.35	6.03
	2	5.70	-0.18	-0.35	6.23
600	1	5.60	-0.17	-0.37	6.14
	2	5.55	-0.17	-0.37	6.09
	3	5.30	-0.17	-0.37	5.84
444	1	5.45	-0.13	-0.41	5.89
	3	5.85	-0.13	-0.41	6.39
800	1	5.60	-0.10	-0.46	6.16
	3	5.65	-0.10	-0.46	6.21
660	1	5.70	-0.10	-0.48	6.28
	3	5.65	-0.10	-0.48	6.23
10,00	1	5.65	-0.07	-0.53	6.25
	3	5.65	-0.07	-0.53	6.25
666	1	5.85	-0.07	-0.54	6.46
	3	5.80	-0.07	-0.54	6.41
880	1	5.95	-0.06	-0.54	6.55

\* Units:  $10^{-19} \text{ cm}^2 \text{ } ^\circ \text{ K}^{-1}$

Table 25. Potassium Chloride A Values and Corrections at 140° K

$$A_o = A - A_{LPf} - A_{TDS}$$

hkl	Sample No.	A*	A <sub>LPf</sub>	A <sub>TDS</sub>	A <sub>o</sub>
400	2	5.05	-0.34	-0.26	5.65
440	1	5.05	-0.17	-0.35	5.57
	2	5.50	-0.17	-0.35	6.02
600	1	5.25	-0.15	-0.37	5.77
	2	5.30	-0.15	-0.37	5.82
	3	5.05	-0.15	-0.37	5.57
444	1	5.20	-0.12	-0.41	5.73
	3	5.55	-0.12	-0.41	6.08
800	1	5.35	-0.10	-0.46	5.91
	3	5.35	-0.10	-0.46	5.91
660	1	5.45	-0.09	-0.48	6.02
	3	5.40	-0.09	-0.48	5.97
10,00	1	5.40	-0.07	-0.53	6.00
	3	5.45	-0.07	-0.53	6.05
666	1	5.55	-0.06	-0.54	6.15
	3	5.70	-0.06	-0.54	6.30
880	1	5.60	-0.05	-0.54	6.19

\* Units:  $10^{-19} \text{ cm}^2 \text{ } ^\circ \text{K}^{-1}$

Table 26. Potassium Chloride A Values and Corrections at 120° K

$$A_o = A - A_{LPf} - A_{TDS}$$

hkl	Sample No.	A*	A <sub>LPf</sub>	A <sub>TDS</sub>	A <sub>o</sub>
400	2	4.75	-0.28	-0.26	5.29
440	1	4.75	-0.14	-0.35	5.24
	2	5.25	-0.14	-0.35	5.74
600	1	4.95	-0.13	-0.37	5.45
	2	4.85	-0.13	-0.37	5.35
	3	4.80	-0.13	-0.37	5.30
444	1	4.85	-0.10	-0.41	5.36
	3	5.25	-0.10	-0.41	5.76
800	1	5.20	-0.08	-0.46	5.74
	3	5.10	-0.08	-0.46	5.64
660	1	5.20	-0.08	-0.48	5.76
	3	5.10	-0.08	-0.48	5.66
10,00	1	5.10	-0.06	-0.53	5.69
	3	5.25	-0.06	-0.53	5.84
666	1	5.25	-0.05	-0.54	5.84
	3	5.55	-0.05	-0.54	6.14
880	1	5.20	-0.04	-0.54	5.78

\*Units:  $10^{-19} \text{ cm}^2 \text{ } ^\circ \text{K}^{-1}$

## APPENDIX F

SILVER CHLORIDE A VALUES AND CORRECTIONS

Table 27. Silver Chloride A Values and Corrections at 240° K

$$A_o = A - A_{LPf} - A_{TDS}$$

Even hkl	Sample No.	A*	A <sub>LPf</sub>	A <sub>TDS</sub>	A <sub>c</sub>
222	7	8.85	-0.34	-0.25	9.44
	17	8.70	-0.34	-0.25	9.29
400	7	8.80	-0.26	-0.29	9.34
	11	8.75	-0.26	-0.29	9.29
	17	7.90	-0.26	-0.29	8.44
440	7	8.65	-0.14	-0.39	9.18
	11	9.15	-0.14	-0.39	9.68
	17	9.00	-0.14	-0.39	9.53
	18	8.45	-0.14	-0.39	8.98
	18	8.35	-0.14	-0.39	8.88
600	7	8.60	-0.13	-0.40	9.13
	11	8.40	-0.13	-0.40	8.93
	17	8.10	-0.13	-0.40	8.63
444	17	8.80	-0.10	-0.46	9.36
	18	8.70	-0.10	-0.46	9.26
800	7	8.75	-0.08	-0.51	9.34
	17	8.45	-0.08	-0.51	9.04
660	17	8.90	-0.07	-0.52	9.49
	18	9.80	-0.07	-0.52	10.39
10,00	17	8.20	-0.05	-0.55	8.80
	18	9.45	-0.05	-0.55	10.05
	18	9.35	-0.05	-0.55	9.95

\*Units:  $10^{-19} \text{ cm}^2 \text{ } ^\circ \text{K}^{-1}$

(Continued)

Table 27. Silver Chloride A Values and Corrections at 240° K (Continued)

$$A_o = A - A_{LPf} - A_{TDS}$$

Odd hkl	Sample No.	A*	A <sub>LPf</sub>	A <sub>TDS</sub>	A <sub>o</sub>
113	18	9.40	-0.36	-0.24	10.0
331	18	9.80	-0.22	-0.31	10.3
		9.80	-0.22	-0.31	10.3
115	18	10.6	-0.36	-0.36	11.1
333	18	10.1	-0.16	-0.36	10.6
	7	10.4	-0.16	-0.36	10.9
	11	10.4	-0.16	-0.36	10.9
	17	10.5	-0.16	-0.36	11.0
551	18	10.6	-0.10	-0.47	11.2
		10.7	-0.10	-0.47	11.3

\*Units:  $10^{-19} \text{ cm}^2 \text{ }^\circ \text{K}^{-1}$



Table 28. Silver Chloride A Values and Corrections at 200° K

$$A_o = A - A_{LPf} - A_{TDS}$$

Even hkl	Sample No.	A*	A <sub>LPf</sub>	A <sub>TDS</sub>	A <sub>o</sub>
222	7	8.65	-0.31	-0.25	9.21
	17	8.40	-0.31	-0.25	8.96
400	7	8.50	-0.24	-0.29	9.03
	11	7.85	-0.24	-0.29	8.38
	17	7.65	-0.24	-0.29	8.18
440	7	8.40	-0.13	-0.39	8.92
	11	8.70	-0.13	-0.39	9.22
	17	8.70	-0.13	-0.39	9.22
	18	7.75	-0.13	-0.39	8.27
	18	7.85	-0.13	-0.39	8.37
600	7	8.30	-0.12	-0.40	8.82
	11	7.75	-0.12	-0.40	8.27
	17	7.60	-0.12	-0.40	8.12
444	17	8.40	-0.10	-0.46	8.96
	18	8.30	-0.10	-0.46	8.86
800	7	8.45	-0.07	-0.51	9.03
	17	8.20	-0.07	-0.51	8.78
660	17	8.65	-0.07	-0.52	9.24
	18	9.35	-0.07	-0.52	9.94
10,00	17	7.90	-0.05	-0.55	8.50
	18	9.15	-0.05	-0.55	9.75
	18	9.10	-0.05	-0.55	9.70

\*Units:  $10^{-19} \text{ cm}^2 \text{ }^\circ \text{K}^{-1}$

(Continued)

Table 28. Silver Chloride A Values and Corrections at 200° K (Continued)

$$A_o = A - A_{LPf} - A_{TDS}$$

Odd hkl	Sample No.	A*	A <sub>LPf</sub>	A <sub>TDS</sub>	A <sub>o</sub>
113	18	8.90	-0.33	-0.24	9.47
331	18	9.30	-0.21	-0.31	9.82
		9.10	-0.21	-0.31	9.62
115	18	9.90	-0.15	-0.36	10.4
333	18	9.70	-0.15	-0.36	10.2
	7	9.95	-0.15	-0.36	10.5
	11	10.1	-0.15	-0.36	10.6
	17	10.1	-0.15	-0.36	10.6
551	18	10.3	-0.09	-0.47	10.8
		10.2	-0.09	-0.47	10.7

\* Units:  $10^{-19} \text{ cm}^2 \text{ } ^\circ \text{ K}^{-1}$

Table 29. Silver Chloride A Values and Corrections at 160° K

$$A_o = A - A_{LPf} - A_{TDS}$$

Even hkl	Sample No.	A*	A <sub>LPf</sub>	A <sub>TDS</sub>	A <sub>o</sub>
222	7	7.95	-0.30	-0.25	8.50
	17	7.55	-0.30	-0.25	8.10
400	7	7.85	-0.23	-0.29	8.37
	11	6.90	-0.23	-0.29	7.42
	17	7.20	-0.23	-0.29	7.72
440	7	8.15	-0.12	-0.39	8.66
	11	8.05	-0.12	-0.39	8.61
	17	8.15	-0.12	-0.39	8.66
	18	7.00	-0.12	-0.39	7.51
	18	7.15	-0.12	-0.39	7.66
600	7	7.75	-0.11	-0.40	8.26
	11	7.05	-0.11	-0.40	7.56
	17	6.90	-0.11	-0.40	7.41
444	17	8.10	-0.09	-0.46	8.65
	18	7.40	-0.09	-0.46	7.95
800	7	7.95	-0.07	-0.51	8.53
	17	7.75	-0.07	-0.51	8.33
660	17	8.20	-0.06	-0.52	8.78
	18	8.50	-0.06	-0.52	9.08
10,00	17	7.50	-0.04	-0.55	8.09
	18	8.60	-0.04	-0.55	9.19
	18	8.65	-0.04	-0.55	9.24

\*Units:  $10^{-19} \text{ cm}^2 \text{ } ^\circ \text{K}^{-1}$

(Continued)

Table 29. Silver Chloride A Values and Corrections at 160° K (Continued)

$$A_o = A - A_{LPf} - A_{TDS}$$

Odd hkl	Sample No.	A*	A <sub>LPf</sub>	A <sub>TDS</sub>	A <sub>o</sub>
113	18	8.45	-0.31	-0.24	9.00
331	18	8.25	-0.20	-0.31	8.76
		8.15	-0.20	-0.31	8.66
115	18	8.80	-0.14	-0.36	9.30
333	18	8.65	-0.14	-0.36	9.15
	7	9.15	-0.14	-0.36	9.65
	11	9.80	-0.14	-0.36	10.3
	17	9.35	-0.14	-0.36	9.85
551	18	9.75	-0.08	-0.47	10.30
		9.40	-0.08	-0.47	9.95

\*Units:  $10^{-19} \text{ cm}^2 \text{ } ^\circ \text{ K}^{-1}$

Table 30. Silver Chloride A Values and Corrections at 140° K

$$A_o = A - A_{LPf} - A_{tds}$$

Even hkl	Sample No.	A*	A <sub>LPf</sub>	A <sub>TDS</sub>	A <sub>o</sub>
222	7	7.75	-0.28	-0.25	8.28
	17	6.90	-0.28	-0.25	7.43
400	7	7.40	-0.22	-0.29	7.91
	11	6.40	-0.22	-0.29	6.91
	17	6.80	-0.22	-0.29	7.31
440	7	7.85	-0.11	-0.39	8.35
	11	7.55	-0.11	-0.39	8.05
	17	7.20	-0.11	-0.39	7.70
	18	6.40	-0.11	-0.39	6.90
	18	6.70	-0.11	-0.39	7.20
600	7	7.55	-0.11	-0.40	8.06
	11	6.55	-0.11	-0.40	7.06
	17	6.65	-0.11	-0.40	7.16
444	17	7.80	-0.08	-0.46	8.34
	18	7.05	-0.08	-0.46	7.59
800	7	7.75	-0.06	-0.51	8.32
	17	7.50	-0.06	-0.51	8.07
660	17	7.80	-0.06	-0.52	8.38
	18	8.15	-0.06	-0.52	8.73
10,00	17	6.65	-0.04	-0.55	7.24
	18	8.40	-0.04	-0.55	8.99
	18	8.25	-0.04	-0.55	8.84

\* Units:  $10^{-19} \text{ cm}^2 \text{ } ^\circ \text{ K}^{-1}$

(Continued)

Table 30. Silver Chloride A Values and Corrections at 140° K (Continued)

$$A_o = A - A_{LPf} - A_{TDS}$$

Odd hkl	Sample No.	A*	A <sub>LPf</sub>	A <sub>TDS</sub>	A <sub>o</sub>
113	18	7.85	-0.30	-0.24	8.39
331	18	7.85	-0.18	-0.31	8.34
		7.80	-0.18	-0.31	8.29
115	18	8.55	-0.13	-0.36	9.04
333	18	8.30	-0.13	-0.36	8.79
	7	8.80	-0.13	-0.36	9.29
	11	9.55	-0.13	-0.36	10.04
	17	8.95	-0.13	-0.36	9.44
551	18	9.30	-0.08	-0.47	9.85
		8.90	-0.08	-0.47	9.45

\* Units:  $10^{-19} \text{ cm}^2 \text{ }^\circ \text{K}^{-1}$

Table 31. Silver Chloride A Values and Corrections at 120° K

$$A_o = A - A_{LPf} - A_{TDS}$$

Even hkl	Sample No.	A*	A <sub>LPf</sub>	A <sub>TDS</sub>	A <sub>o</sub>
222	7	7.25	-0.26	-0.25	7.76
	17	6.25	-0.26	-0.25	6.76
400	7	6.80	-0.20	-0.29	7.29
	11	5.85	-0.20	-0.29	6.34
	17	6.30	-0.20	-0.29	6.79
440	7	7.30	-0.11	-0.39	7.80
	11	7.10	-0.11	-0.39	7.60
	17	7.40	-0.11	-0.39	7.90
	18	6.40	-0.11	-0.39	6.90
600	7	7.05	-0.10	-0.40	7.55
	11	6.15	-0.10	-0.40	6.65
	17	6.10	-0.10	-0.40	6.60
444	17	7.35	-0.08	-0.46	7.89
	18	6.55	-0.08	-0.46	7.09
800	7	6.50	-0.06	-0.51	7.07
	17	6.70	-0.06	-0.51	7.27
660	17	7.45	-0.06	-0.52	8.03
	18	7.70	-0.06	-0.52	8.28
10,00	17	6.35	-0.04	-0.55	6.94
	18	8.00	-0.04	-0.55	8.59
	18	7.75	-0.04	-0.55	8.44

\* Units:  $10^{-19} \text{ cm}^2 \text{ } ^\circ \text{ K}^{-1}$

(Continued)

Table 31. Silver Chloride A Values and Corrections at 120° K (Continued)

$$A_O = A - A_{LPf} - A_{TDS}$$

Odd hkl	Sample No.	A*	A <sub>LPf</sub>	A <sub>TDS</sub>	A <sub>O</sub>
113	18	7.15	-0.28	-0.24	7.67
331	18	7.45	-0.17	-0.31	7.93
		7.05	-0.17	-0.31	7.53
115	18	8.05	-0.13	-0.36	8.54
333	18	7.95	-0.13	-0.36	8.44
	7	8.45	-0.13	-0.36	8.94
	11	9.30	-0.13	-0.36	9.79
	17	8.50	-0.13	-0.36	8.99
551	18	8.85	-0.07	-0.47	9.39
		8.45	-0.07	-0.47	8.99

\*Units:  $10^{-19} \text{ cm}^2 \text{ } ^\circ \text{ K}^{-1}$



## GLOSSARY

$\alpha$	linear coefficient of thermal expansion
$\alpha$	dispersion curve branch
$\beta$	volume coefficient of thermal expansion
$\beta$	$(\sin \theta)/\lambda$
$\gamma$	Grüneisen constant
$\Gamma$	vibrational amplitude ratio of two different types of atoms
$\delta$	phase angle of normal mode wave
$\delta$	$\Gamma^{-1}$
$2\theta$	angular deflection of scattered x-rays from the incident direction
$\Theta$	Debye characteristic temperature
$\Theta(\text{elastic})$	$\Theta$ determined from elastic constants
$\Theta(\text{x-ray})$	$\Theta$ determined from x-ray measurements
$\Theta(C_V)$	$\Theta$ determined from specific heat measurements
$\lambda$	x-ray wavelength
$\Lambda$	normal mode wavelength
$\mu_n$	nth moment of vibration spectrum
$\nu$	normal mode frequency
$\nu_m$	cut off frequency of the Debye vibrational spectrum
$\vec{\xi}_j$	position vector of the jth atom in a Bravais unit cell referred to some point in the cell
$\varnothing$	$(\sin^2 \theta)/\lambda^2$

## GLOSSARY (Continued)

$\omega$	$2\pi\nu$
A	absorption factor
A	$-(2\phi)^{-1} \frac{d}{dT} \ln I(\text{obs})$
$A_{\text{LPf}}$	contribution to A from thermal expansion
$A_{\text{TDS}}$	contribution to A from TDS
$A_0$	$A = (A_{\text{LPf}} + A_{\text{TDS}})$
$a_j$	amplitude of normal mode wave
$B_0$	ratio of integrated intensity to peak height
B	$8\pi^2 \overline{u_n^2}$
$B_1$	B for $\text{Ag}^+$ ion or for $\text{K}^+$ ion
$B_2$	B for $\text{Cl}^-$ ion
$B(\text{cal})$	calculated value of B
$B(\text{obs})$	observed value of B
$B'$	temperature derivative of B
$C_V$	specific heat measured at constant volume
E	mean energy of simple harmonic oscillator
E	extinction factor
$\vec{e}$	polarization vector of normal mode wave
f	atomic scattering factor
$f_1$	atomic scattering factor of $\text{Ag}^+$ ion or of $\text{K}^+$ ion
$f_2$	atomic scattering factor of $\text{Cl}^-$ ion
$f$	$f_2/f_1$
F	structure factor
$\vec{g}$	$\vec{K}/2\pi$
G	$m_1 B'_1 + m_2 B'_2$
g	frequency distribution function
h	Miller index

## GLOSSARY (Continued)

$h$	Planck's constant
$\vec{H}$	reciprocal lattice vector
$I_0$	x-ray intensity diffracted in the absence of thermal vibrations
$I_0$	interference function
$I$	observed x-ray intensity
$I(\text{obs})$	observed x-ray intensity
$k$	Boltzman's constant
$k$	Miller index
$\vec{k}$	wave vector of normal mode wave
$l$	Miller index
$m$	atomic mass
$m_1$	mass of silver atom or of potassium atom
$m_2$	mass of chlorine atom
$M$	Debye-Waller factor
$M'$	temperature derivative of $M$
$M_1$	$M$ for $\text{Ag}^+$ ion or for $\text{K}^+$ ion
$M_2$	$M$ for $\text{Cl}^-$ ion
$N$	number of Bravais unit cells in crystal
$N'$	number of atoms in crystal
$p$	number of atoms in Bravais unit cell
$q$	number of lattice points in Bravais unit cell
$\vec{r}_n$	position vector of $n$ th Bravais cell
$\vec{R}_{nj}$	position vector of the $j$ th atom in the $n$ th Bravais unit cell
$s$	number of atoms per lattice point
$\vec{s}$	unit vector in the direction of the scattered x-rays
$\vec{s}_0$	unit vector in the direction of the incident x-rays
$\vec{S}$	diffraction vector; equals $\vec{s} - \vec{s}_0$
$T$	absolute temperature
TDS	thermal diffuse scattering

## GLOSSARY (Continued)

$\vec{u}_{nj}$	instantaneous displacement of the jth atom in the nth Bravais unit cell
$\overline{u_n^2}$	mean square displacement of an atom normal to the Bragg planes
V	crystal volume
V	phase velocity of normal mode wave
x	$\Theta/T$

## REFERENCES

1. M. Born and T. von Kármán, *Physikalische Zeitschrift* 13, 297 (1912); 14, 15 (1913)
2. M. Born and G. H. Begbie, *Proceedings of the Royal Society (London)* A188, 179 (1946)
3. F. H. Herbstein, *Advances in Physics* 10, 313 (1961)
4. P. Debye, *Annalen der Physik* 43, 49 (1914)
5. R. W. James, "The Optical Principles of the Diffraction of X-rays" (G. Bell and Sons, London, 1948)
6. N. Nilsson, *Arkiv för Fysik* 12, 247 (1957)
7. M. Renninger, *Acta Crystallographica* 5, 711 (1952)
8. D. R. Chipman, *Journal of Applied Physics* 31, 2012 (1960)
9. L. Brillouin, "Wave Propagation in Periodic Structures" (McGraw-Hill Book Company, Inc., New York, 1946)
10. H. Cole, *Journal of Applied Physics* 24, 482 (1953)
11. C. B. Walker, *Physical Review* 103, 547 (1956)
12. B. N. Brockhouse and A. T. Stewart, *Reviews of Modern Physics* 30, 236 (1958)
13. T. H. K. Barron, W. T. Berg, and J. A. Morrison, *Proceedings of the Royal Society* A242, 478 (1957)
14. M. Born and K. Huang, "Dynamical Theory of Crystal Lattices" (Oxford University Press, London, 1954)
15. J. M. Ziman, "Electrons and Phonons" (Clarendon Press, Oxford, England, 1960)
16. M. Born and K. Sarginson, *Proceedings of the Royal Society (London)* A179, 69 (1941)
17. J. Laval, *Bulletin of the Société Française de Minéralogie* 64, 1 (1941)

## REFERENCES (Continued)

18. W. H. Zachariasen, "Theory of X-ray Diffraction in Crystals" (John Wiley and Sons, Inc., New York, 1945), p. 208
19. M. Blackman, *Acta Crystallographica* 2, 734 (1956)
20. P. Debye, *Annalen der Physik* 39, 789 (1912)
21. M. Blackman, "Handbuch der Physik", edited by S. Flugge (Springer-Verlag, Berlin, 1955), Vol. 7, Part I, p. 325
22. G. Leibfried and W. Ludwig, "Solid State Physics", edited by F. Seitz and D. Turnbull (Academic Press Inc., New York, 1961), Vol. 12, pp. 276-444
23. Harro Hahn and Wolfgang Ludwig, *Zeitschrift für Physik* 161, 404 (1961)
24. A. A. Maradudin and P. A. Flinn, *Physical Review* 129, 2529 (1963)
25. Harro Hahn, *Zeitschrift für Physik* 165, 569 (1961)
26. A. A. Maradudin, *Physica Status Solidi* 2, 1493 (1962)
27. A. Paskin, *Acta Crystallographica* 10, 667 (1957)
28. C. Zener and S. Belinsky, *Physical Review* 50, 101 (1936)
29. M. Blackman, *Proceedings of the Physical Society (London)* B70, 827 (1957); B74, 17 (1959)
30. T. H. K. Barron, *Annals of Physics* 1, 77 (1957)
31. Robert M. Nicklow and R. A. Young, *Physical Review* 129, 1936 (1963)
32. Boris W. Batterman and David R. Chipman, *Physical Review* 127, 690 (1962)
33. John C. Slater, *Reviews of Modern Physics* 30, 197 (1958)
34. R. A. Young, "Advances in X-ray Analysis" (Plenum Press, New York, 1961), Vol. 4, pp. 219-232
35. R. A. Young, "Mechanism of the Phase Transition in Quartz", AFOSR Document No. 2569, Final Report, Contract No. AF 49(638)-624, Project A-447, Engineering Experiment Station, Georgia Institute of Technology, 1962, ASTIA Document AD-276235

## REFERENCES (Continued)

36. R. A. Young, "Background Intensities in Single Crystal Diffractometry" Technical Report No. 2, ONR Contract NONr 991(00) and 991(06); NR 017-623, Georgia Institute of Technology, Atlanta, Georgia, Project A-389, July, 1961, ASTIA Document AD 262912
37. R. A. Young, Zeitschrift für Kristallographie 118, 233 (1963)
38. R. A. Young, Annual Report No. 1, ONR Contract NONr 991(00) and 991(06); NR 017-623, Project A-389, Engineering Experiment Station, Georgia Institute of Technology, 1959, ASTIA Document
39. Arthur Paskin, Acta Crystallographica 11, 165 (1958)
40. D. R. Chipman and A. Paskin, Journal of Applied Physics 30, 1998 (1959)
41. Shoichi Annaka, Journal of the Physical Society of Japan 17, 846 (1962)
42. P. M. Sutton, Physical Review 91, 816 (1953); (Errata, Ibid. 112, 2139 (1958))
43. W. F. Giaque and P. F. Meads, Journal of the American Chemical Society 63, 1897 (1941)
44. J. A. Wasastjerna, Comment. Phys.-Math., Helsingf. 13, No. 5 (1945)
45. R. Srinivasan, Journal of the Indian Institute of Science 37A, 232 (1955)
46. M. Iona, Physical Review 60, 823 (1941)
47. S. K. Joshi and R. Gupta, Physical Review 126, 933 (1961)
48. D. L. Arenberg, Journal of Applied Physics 21, 941 (1950)
49. S. L. Quimby and Paul M. Sutton, Physical Review 91, 1122 (1953)
50. Kathleen Lonsdale, Acta Crystallographica 1, 144 (1948)
51. K. Clusius and P. Harteck, Zeitschrift für Physikalische Chemie A134, 243 (1928)
52. American Institute of Physics Handbook (McGraw-Hill Book Company, Inc., New York, 1957) pp. 4-47

## VITA

Robert Merle Nicklow was born in St. Petersburg, Florida on October 11, 1936. He graduated from Hillsborough High School in Tampa, Florida in 1954. He received the degree of Bachelor of Science with honor in Physics from the Georgia Institute of Technology in 1958. Since 1958 he has been associated with the Engineering Experiment Station at the Georgia Institute of Technology. He received the degree of Master of Science in Physics from the Georgia Institute of Technology in 1960. He is a member of the American Crystallographic Association, the American Physical Society, and the honor societies Sigma Pi Sigma and Phi Kappa Phi. He was elected a full member of Sigma Xi in 1963. He married Marilyn Meadows in 1958 and they now have three children.